UNIVERSITAT DE BARCELONA

Memòria de Tesi presentada per

Judit Torner Perez

Paleoclimatic reconstruction of past interglacial periods and their transitions in the Iberian Peninsula and its surrounding seas

Reconstruccions paleoclimàtiques dels interglacials recents i les seves transicions a la Península Ibèrica i mars circumdants

Programa de Doctorat de Ciències del Mar

Departament de Dinàmica de la Terra i de l'Oceà, Facultat de Ciències de la Terra

Sota la direcció de la Doctora

Isabel Cacho Lascorz

Barcelona, Juny de2020

Ph.D. Thesis

JUDIT TORNER

PALEOCLIMATIC RECONSTRUCTION OF PAST INTERGLACIAL PERIODS AND THEIR TRANSITIONS IN THE IBERIAN PENINSULA AND ITS SURROUNDING SEAS

Reconstruccions paleoclimàtiques dels interglacials recents i les seves transicions a la Peninsula Ibèrica i mars circumdants

Potograph: Vallgornera cave, Mallorca
courtesy of Toni Merino

UNIVERSITAT DE BARCELONA

A l'Alicia

A les meves altres mares

This research was financially supported by HIDROPAST (ref. CGL2010-16376), OPERA (ref. CTM2013-48639-C2-1-R) and CHIMERA (ref. CTM2016-75411-R) projects. It was accomplished at the GRC Geociències Marines, awarded with the Generalitat de Catalunya Grups de Recerca Consolidats grant (ref. 2017 SGR 315). Judit Torner benefited from a pre-doctoral FPI-fellowship of the Ministerio de Ciencia, Innovación y Universidades (MINECO) (ref. A-20149185).

Acknowledgements

Agradecimientos

Agraïments

Divisa

A l'atzar agraeixo tres dons: haver nascut dona,
de classe baixa i nació oprimida.

I el tèrbol atzur de ser tres voltes rebel.

Maria-Mercè Marçal i Serra
Cau de Llunes, 1977

Vull començar agraint a la Isabel Cacho la oportunitat que m'ha donat. Ella es la persona que va confiar en mi i em va animar a fer el doctorat. La Isa s'ha convertit possiblement en l'única mentora que he tingut a la vida. Tres voltes rebel, així la veig. Lluitant sempre per allò que vol, si cal a contracorrent, segura de si mateixa i victoriosa en un món d'homes. Gràcies Isa per tot el temps invertit en mi, pel temps que hem passat juntes. Sobretot el de campanyes a coves, que vist amb perspectiva, és del més divertit i enriquidor que he fet al llarg d'aquests anys de tesi.

De la misma manera también os quiero agradecer a vosotras, Ana Moreno y Heather Stoll. Para mí sois el espejo de Isa en diferentes localidades. Las mujeres 3 veces rebeldes están por todas partes! Vosotras también habéis hecho posible de forma activa que haya podido hacer el doctorado. Gracias por compartir vuestros proyectos.

Vull agrair el recolzament que sempre he rebut del Grup de Recerca Consolidat de Geociències Marines (GRCGM). A en Miquel Canals per tirar del carro i fer que el GRCGM sigui una realitat. I bé, en general, a tots els integrants actuals i passats, amb els que hem compartit tantíssimes coses; campanyes, calçotades, dinars de carmanyola, xerrades apassionants sobre ciència, xerrades igual d'apassionants però no científiques, coffee breaks, classes, pràctiques de laboratori, organització d'esdeveniments a la facultat... Si es

que al GRCGM no parem! Companyes i companys del GRCGM i del departament de Dinàmica de la Terra i de l'Oceà, gràcies per fer-me la vida més senzilla i enriquidora; Anna Sanchez, Toni Calafat, Jose Luis, Galderic, David Amblàs, Liam, Marta, Edu, Andrea, Andreu, Sergi Tries, Maria Jaume, Helena, Aitor, miniRut , Xavi Rayo, Lluis Valero, Olaia, Jaime, Leo, Ester, Maria de la Fuente, Patri, Itxaso, Mercè, Marc, Jose Noel, Albert, Montse Guart, Montse Errea, Montse Roca Plana i Magda. De tots vosaltres he après i m'enduc alguna cosa. Com per exemple del Leo, que sempre fa que em qüestioni les dades i, per que no? Tot en general... aportant l'esperit crític tant necessari en ciència. O la Ester, que sempre m'ajuda en tots els dubtes que sorgeixen inesperadament allí a la sala. Sempre fent de "supporter". Gràcies a tots i totes.

El Jaime Frigola va ser el primer que em va fer embrutar les mans amb sediments marins. Recordo perfectament aquell dia. Em va ensenyar com "maquillar" els cores a la sala del XRF. Jaime, es nota que gaudeixes molt amb el que fas. De tu he aprés sobretot a ser organitzada, sistemàtica, meticulosa i rigorosa. Qualitats que et caracteritzen i que des del meu punt de vista són imprescindibles per fer investigació. Ja saps com és el meu cap, mentalment em veig a mi mateixa dins aquella pel·lícula… m'aixeco, pujo sobre la taula, i crido, Ooh capitán! Mi capitán!. És la meva manera d'agrair-te la teva passió, gràcies.

A les Maries, quin parell! A les dues les vaig conèixer al principi d'estar jo al grup d'investigació. Després van volar i voltar per altres mons. Finalment, no fa gaire, han tornat a la meva vida, ara que jo estic acabant la tesi. Maries, gràcies per fer sempre que els meus petits problemes i les moltes queixes que tinc es converteixin en unes bones rialles. M'ha ajudat moltíssim. Per això, Maria de la Fuente, Maria Jaume Seguí, us desitjo que *el eterno sol os ilumine y el amor os rodee*!!

També voldria agrair detingudament a la Mercè i en Marc, ja que han sigut les dues persones amb les que he viscut tot el procés de la tesi en paral·lel. Mercè, no em crec que ja faci tant de temps de la nostra escapada a la summer school de Miami. Una multitud de flashbacks passen ara mateix pel meu cap, quantes aventurilles hem compartit eh? I per diferents climes, des del clima tropical de Miami (Aw) al màxim fred del clima continental d'Amèrica del Nord (Dfa). Només vull dir-te que espero veure't riure sota la pluja púrpura, com diu aquella cançó, d'aquell cantant de Minneapolis que tant ens hagués agradat veure. Amb el Marc vàrem començar exactament el mateix dia la tesi, i també la dipositarem junts. Increïble eeh?. Poques vagades deu haver passat que dues persones comparteixin tant estretament l'experiència de fer la tesi. Marc, moltes mercès pel teu suport infinit, l'ajuda i el temps que has perdut amb les meves preguntes sobre tota la burocràcia i papers varis que hem fet. Gràcies també per ser company de lluita pels nostres drets aquest últim any, estic segura que vàrem guanyar gracies als teus dots de paraula. No se

explicar el suport que ha sigut tenir-te al meu costat. Poder compartir l'angoixa, el patiment i l'estrès màxim del últims mesos a sigut terapèutic. Voto SI a la paella a Castefa per celebrar el nostre dipòsit, ens ho hem guanyat!

De ti Jose ya se me podría haber pegado más la verdad. Eres la persona más previsora y organizada que conozco. Escribiendo estas líneas no paro de pensar que esto tu haría semanas que lo tendrías terminado. Gracias por aceptarme tal como soy, lo haces sin prejuicios. Gracias por tu ayuda y consejos estos años. Ha sido un placer trabajar junto a ti. Estoy muy feliz que hayas escogido Barcelona y sus gentes como segundo hogar y familia. Se te echa de menos.

Voldria fer una menció especial a la Olaia Cerdeira i a la Patricia Povea, els meus dos grans pilars. Olaia, de ti he aprendido sobre todo a tener una visión estética y artística, ¡incluso para la representación de los datos científicos! Además, la gran curiosidad y respeto que sientes por la vida me inspiró, me convertiste en una naturalista desenfrenada. Aunque estoy a años luz de ti, maestra Oliwan Kenobi. Amb la Patri vàrem compartir moltes hores de laboratori. Ho recordes Patri? Pràcticament em vas ensenyar tot el que sé del funcionament del laboratori, de metodologies analítiques i del processament de dades. Gràcies per ensenyar-me tot el que necessitava per poder fer aquesta tesi, la llista es inacabable. Ets l'ésser més entranyable que existeix en tot el Paleozoo sencer. Però noies, no només us vull agrair per inspirar-me durant els meus inicis com a jove investigadora. També us vull agrair pel que avui en dia continueu fent per mi en el terreny personal. Gràcies per ser fortes, valentes, lluitadores i posar seny a la vida. M'heu ensenyat a ser una mica més forta, independent, feminista i "ecofriendly". Gràcies per ser part del meu món i per deixar que jo formi part del vostre. Gràcies de tot cor per ser les meves amigues, amb certesa d'aquelles que duren tota la vida encara que els nostres camins es separin.

Benvolgut Català! sembla *impossible que pugui acabar.* Tinc molt clar que no ho podria haver fet tota sola. Crec que hauríem de compartir el premi, llàstima que els títols son unipersonals. No sé ni per on començar, hi ha tantes coses que recordo, que estan *ressonant com un exèrcit de timbals* dins el meu cap. Començaré agraint que m'hagis deixat inflar-te taaant el cap. Et prometo que quan arribi el teu *últim tram final*, que arribarà, tindré les *tres portes de ca meua obertes a tots els vents* per tu. Ets una persona extraordinària Xixo, sempre feliç i alegre, aquest viatge hauria sigut molt avorrit sense tu. Després, està la teva capacitat per ajudar als altres sense esperar res a canvi, totalment altruista, està clar que *depèn de gent com tu la sort del món.* Gràcies per estar sempre al meu costat quan més ho necessito i per compartir tantes hores de feina junts. En definitiva*, no puc explicar el plaer indescriptible que és estar amb tu avui que em faig gran.*

També li estic molt agraïda a la Montse Guart, la tècnica més xixaraxera del la Facultat i la persona que revisarà les faltes d'ortografia d'aquest apartat. Gràcies per aguantar-me tots aquest anys, entrant i sortint del lab, molestant, imprimint en color, deixant coses pel mig, etc.. i tu sempre amb un somriure i de bon humor. Donat la quantitat d'hores que he passat al laboratori, t'agraeixo de tot cor l'atmosfera de bon rotllo que has creat. Importantíssim!, Gràcies per estar sempre ajudant i per fer dinàmiques de grup, creant Team Building, saps que m'encanta.

M'agradaria agrair també l'ajuda de tots els tècnics de laboratori dels quals he requerit la seva ajuda. Gràcies Joaquim, Maite, Toni, Barbara i Susana dels serveis científics i tecnològics de la UB. També als tècnics de la facultat, la Montse del Servei de Lamina Prima, la Fàdua encarregada de la litoteca i l'Alejandro del Laboratori de Paleontologia, per tots els mals de cap relacionats amb els espeleotemes.

També he compartit experiències molt enriquidores amb el Carles, l'Eva Calvo, l'Ari i la Lucia de l'Institut de Ciències del Mar o amb la Belen Martrat, l'Annuar i l'Oscar del IDAEA-CSIC. Amb totes elles he compartint les paleotrobades, on la discussió de temes científics era l'excusa perfecte per estrènyer llaços. I què dir de l'ajuda rebuda de la gent de Mallorca! En Joan Fornós, el Toni Merino i l'Alejandro. Gràcies per tot l'assessorament i per haver compartit els vostres coneixements geològics de les coves. Recordo amb molta estima aquell dia sencer que vàrem passar dins de Vallgornera flotant entre llacs i fent fotografies a *la sala que no té nom*. Toni ets el millor guia d'espeleo de la història. Gràcies pel vostre temps invertit en ajudar-nos. Ah! I gràcies també a la Joana per acollir-nos a casa seva sempre que ho necessitàvem.

Emparados bajo el ala del proyecto OPERA también aparecieron muchas otras personas. Con todas ellas he compartido reuniones de proyecto donde la transmisión de conocimientos me ha sido de mucha utilidad. Gracias Julio Lázaro de la Universidad del País Vasco y a Miguel Iglesias de la Universidad de Oviedo. A la gente del Instituto Pirenaico de Ecología y la Universidad de Zaragoza, por acogerme cálidamente siempre que les he visitado y por los buenos momentos compartidos en las salidas de campo a cuevas. Gracias, Ana Moreno, Carlos Sancho, Graciela, Penélope, Arsenio, Cinta, Miguel Bartolomé y Carlos Pérez. Precisamente con este último, Carlos, junto con Miguel Iglesias tuve el enorme placer de compartir estancias breves en la Universidad de Minnesota.

Life is what goes between uranium samples

Para no perder la tradición Carlos! Chicos, cada vez que recuerdo el tiempo que pasamos en MN se me dibuja una sonrisa en la cara. Este tipo de experiencias le marcan a uno la vida, gracias por estar ahí! Sí Michu, recuerdo el mejor pastel de Zanahoria de la historia entre infinitas explicaciones sobre nubes. Y Carlos, gracias por cuidar de mí y ponerme siempre las cosas lo más fáciles posible. Recuerdo todos esos pequeños detalles, como hacías la "acid party" por mí o el colchón pinchado. Incluso me organizaste una cena de bienvenida.

Thank you Carlos and Michu,
master and padawan of the state-of-the-art in U-Th dating.

Larry Edwards and Hai Cheng, thank you to bring me the opportunity to work in your laboratory. I met incredible friendly people in Minnesota. Thanks to Yanbin Lu and Pu Zhang for all your help at the clean laboratory and the machine, even in unearthly hours. Thank you to the entire local people but also the visitors to offer me the opportunity to know and enjoy local traditions, especially the happy hours (burger and beer) and Halloween parties. Thanks Katee, Mathieu, Yves, Julia, Akemi, Valdir, Pablo and Eline.

Finally it is time to talk about Phillis. I do not have enough words to thank you all your hospitality. You were always sharing all your stuff and time with me to make my live more comfortable and fun. And you did it! I am forever indebted to you. I won an American mum. I do not forget Laurie, my aunt. The three of us spent grate time in concerts, road trips, Thai dinners, beers, several Thanksgiving Day experiences, whatever necessary to distract me. I'm waiting you here in Barcelona.

Finalment, fora de l'ambient científic-laboral hi ha molta gent a la que estic altament agraïda. Al *Love Machine* i les *Dones Rebels* per estar sempre allà i donar-nos suport mutu. D'allà he tret grans consells com.. *No levantes el pie del acelerador*. Al Nacho i la Claudia per deixar-me la seva caseta aïllada del món, on he pogut escriure part d'aquestes paraules. I sobretot al clan! Gràcies per fer-me sentir protegida i que formo part d'això tant increïble que tenim, la Family . Us estimo.

Contents

Chapter III- Results

Chapter IV- Discussion

Chapter V- Conclusions

List of Figures

Chapter I- Introduction

Chapter II- Methodology

Chapter III- Results

Chapter IV- Discussion

List of Tables

Ph.D. thesis structure

This Ph.D. thesis is presented in the format of a “classic volume style” structured in five chapters as follow:

- Chapter I provides a general introduction to the Earth climate system, including the foundations of the paleoclimate sciences. It also introduces the climatic archives used, the speleothems and marine cores, describing their potential for the application of different climate proxies. A brief review of the knowledge of interglacial paleoclimatic reconstructions is also provided with a next description of the main current and past features of the marine and climate conditions of the studied area. This section ends with the presentation of the objectives of this Ph.D. thesis.
- Chapter II presents the methodology. This includes a description of the used material, information about field and laboratory work, and the applied analytical techniques. This section ends with the descriptions for the proxy calculations and the bases for their interpretation.
- Chapter III presents the obtained results. This chapter is subdivided in two sections according to the nature of the studied archives. First, it presents the speleothem age models and their geochemical results. This first part also includes an evaluation of the suitability of the produced proxy records as a reliable climate signal and indicates those speleothems that will be further considered in the discussion. The second section concentrates on the marine sediment cores results, starting with their chronologies, then the foraminifera geochemical results and finally the sedimentological results. This second section ends with a comparison among the studied marine cores highlighting their regional differences.
- Chapter IV includes the discussion of the results. This chapter starts with a discussion about the hydroclimate interpretation of the geochemical proxies applied in the speleothems. Next, the discussion is focussed on the speleothem records covering four interglacial periods. The next section is dedicated to a detailed discussion of the last interglacial, the last glacial inception and the early glacial period, the MIS 5, where both speleothem and marine records are integrated. Finally the discussion is centred in some of the glacial termination periods.
- The Chapter V presents the major conclusions.

Abstract

This study combines cave speleothems and marine sediments to gain an insight into the climate variability of the Iberian Peninsula (IP) and its surrounding seas associated with previous warm interglacial periods. In particular, it centres in the time period from 530 to 65 kyr BP, thus covering the interglacials comprised within the Marine Isotopic Stages (MIS) 13, 11, 9, 7, and 5, and their associated transitions such as glacial terminations and also the onset of the last glaciation. The speleothems are used as archives for changes in atmospheric moisture availability by means of stable isotopes and Mg/Ca analysis. The studied speleothems correspond mostly from the Balearic Islands (Minorca and Mallorca) but also from the Pyrenees. Marine conditions for the penultimate termination (T-II) and the MIS 5 have been reconstructed in the base to three sediment cores from three different marine locations around the IP: the Cantabrian Sea, the Alboran Sea, and the Balearic Sea. Surface conditions were explored by means of pair analyses of $\delta^{18}O$ and Mg/Ca ratios measured in carbonate shells of the planktonic foraminifera *Globigerina bulloides*. These measurements let to the reconstruction of Sea Surface Temperatures (SST) and sea water $\delta^{18}O_{sw}$ values as a proxy of major changes in the regional precipitation/evaporation balance or, during some brief intervals, as an indicator of the arrival of melting waters. In addition, changes in the intensity of western Mediterranean deep convection are explored through additional measurements of grain size distribution and XRF-geochemical ratios performed in the Balearic core (MD99-2343).

The studied speleothem collection provides a nearly continuous 450 kyr record, unique for the Mediterranean region, that allows, for the very first time, to reconstruct the hydroclimate of several interglacial periods (MIS 13, 11, 9, 7, and 5). Interglacial periods are characterized by light $\delta^{13}C$ and low Mg/Ca ratios pointing to enhanced precipitation and climate amelioration that allowed the expansion of the vegetation cover. On the contrary, heavier/higher $\delta^{13}C$ and Mg/Ca ratios during glacial stages highlight their dry conditions with reduced vegetation activity. The $\delta^{18}O_{speleo}$ records reveal also the overall dominance of lighter values during interglacial periods in contrast to the glacial periods but with a strong 23-kyr (precessional) imprint in the signal. The extraordinary resemblance between the cave and marine $\delta^{18}O$ records support a strong influence of Mediterranean source rains over the studied caves whose $\delta^{18}O$ signal was dominated by the precession control on the evaporation/precipitation ratio on the Mediterranean basin.

The MIS 11 appears in the studied speleothem $\delta^{13}C$ and Mg/Ca records as a long and stable interglacial with rather constant water availability over the Balearic Islands. The MIS 9 and partially MIS 7 are represented by the speleothem RAT (Minorca) with an exceptionally accurate absolute chronology due to the low errors of its U/Th dates. The Mg/Ca record of this speleothem allows identifying the sub-stage structure of both MIS 9 and 7 with wetter conditions associated with the warm periods. This record presents extraordinary resemblance to previously published pollen sequences from the Mediterranean region and they agree in suggesting comparable wet conditions for both MIS 9e and 9a sub-stages. The MIS 7e clearly shows an increment in the water availability.

Glacial terminations (T-III, IV, and V) appear as periods of low rates in speleothem growth while T-II is only represented by growth interruptions. The marine $\delta^{18}O_{sw}$ for the T-II supports the occurrence of a major freshening event with comparable light values in the Cantabrian and Mediterranean Sea in correspondence to the Heinrich Event (HE) 11. This major and rapid melt event should have caused major distortions in the hydrological conditions of the Balearic Islands, stopping speleothem growths. Previous terminations are represented by an early light $\delta^{18}O_{speleo}$ anomaly, likely reflecting that this early deglacial major melting over the Atlantic Ocean was a rule for deglacial initiations.

The MIS 5 is studied in detail through the integrated study of marine and speleothem records. During the Last Interglacial (LIG), the sea surface temperature evolution was heterogeneous around the IP with gradients among the three studied seas larger than those from today. The LIG ended earlier in the Cantabrian Sea than in the western Mediterranean Sea, which was coincident with an accelerated aridification phase that marked the glacial inception in a Minorca speleothem at 116.5 kyr BP and preceding the Greenland Stadial 25 (GS). This was the first of a series of stadials that punctuated the early glaciation and where the sea thermal gradient almost disappeared around the IP. These intense coolings during stadials led the development of drier but intense westerlies over southern European latitudes that favoured deep convection in the western Mediterranean Sea. In contrast to this regional homogeneity among the studied records during stadial periods, the interstadials periods were rather heterogeneous pointing to much complex ocean-atmosphere interconnections during these warm intervals.

Chapter I

Introduction

1.1 Paleoclimatology

Paleoclimatology is the science that studies past climate evolution of the Earth. It allows identifying the range of natural climate variability when anthropogenic interference did not exist (PAGES, 2016; Tzedakis *et al*., 2009). Under the ongoing climate change situation where we are experimenting a worldwide climate warming and several associated environmental changes, the study of past warm interglacial periods brings the opportunity to improve our understanding of the climate system operation in a warmer Earth (IPCC, 2013).

Climate is defined as the statistical average of the predominant meteorological variables in a given region and over a given period (usually 30 years). It describes the average conditions and the range of variability of different weather variables such as temperature, precipitation and wind patterns (IPCC-2013). In a broad sense, the climate is a specific state of the climatic system. This extraordinary system is composed by the hydrosphere, the atmosphere, the cryosphere, the lithosphere and the biosphere, which are interconnected and where complex interactions among them are constantly taking place (Ruddiman, 2001).

The first theories on past climate changes dated from the 19Th century. Louis Agassiz was one of the first scientists using the term "glaciation" to describe a past period of colder conditions and enhanced extension of ice sheets. During the 20Th century, the perspective that climate changed cyclically during the past time was progressively accepted by the scientific community (Ruddiman, 2005). The paleoclimatology investigates this past climate variability (at Earth time-scale), addressing the triggering factors and analysing the climate system response to these forcings. Different natural processes can be the driving force for climatic variability. While external forcings are mainly related to Earth orbital changes and solar activity, the internal forcings concerns to a large number of inherent processes within the Earth Climate System (Cronin, 1999) (Table 1). When one of these forcing factors produce a change in the climate system, even a small one, can trigger disequilibrium within the internal components of the climate system, they will act as climate feedbacks that ultimately will intensify (positive feedback) or weaken (negative feedback) the effect of the original forcing. Feedbacks can act as great amplifiers of climate changes but their operation adds big complexity within the climate system (Alley *et al*., 2003). For example, one feedback that has acted in the past time as a great amplifier is the albedo. When large ice sheets start to grow the incoming solar radiation is increasingly reflected by this white surface and further reinforcing the original cooling (Fig. 1).

External Earth forcings	
Solar radiation	Sunspot variation and irradiance changes
	Solar diameter
	Solar ultraviolet wavelength variability
	Magnetic variation
Earth's orbital changes	Eccentricity
	Obliquity (tilt)
	Precession
Asteroid impacts	

Internal Earth forcings	
Plate tectonics	Mountain building
	Ocean-volume changes
Volcanism	Aerosols
	Gases

Climate system internal forcings and feedbacks	
Ice sheets and sea ice	Albedo
	Meltwater
	Atmospheric circulation
Ocean-atmosphere feedbacks	Thermohaline circulation
	Internal dynamics (El Niño–Southern Oscillation)
Biosphere-atmosphere gas exhanges	Dimethylsulfide (DMS–cloud condensation nuclei)
	Carbon dioxide (biological pump)
	Methane (wetlands)

Antropogenic forcings and feedbacks	
Anthropogenic emissions	Carbon dioxide (CO_2)
	Methane (CH_4)
	Nitrous oxide (N_2O)
	Carbon monoxide (CO)
	Sulfate aerosols

Table.1. Left) External and internal Earth forcings list, Right) Climate system processes and anthropogenic origin emissions which act as forcings and/or feedbacks. (source: Adapted from Cronin, 1999)

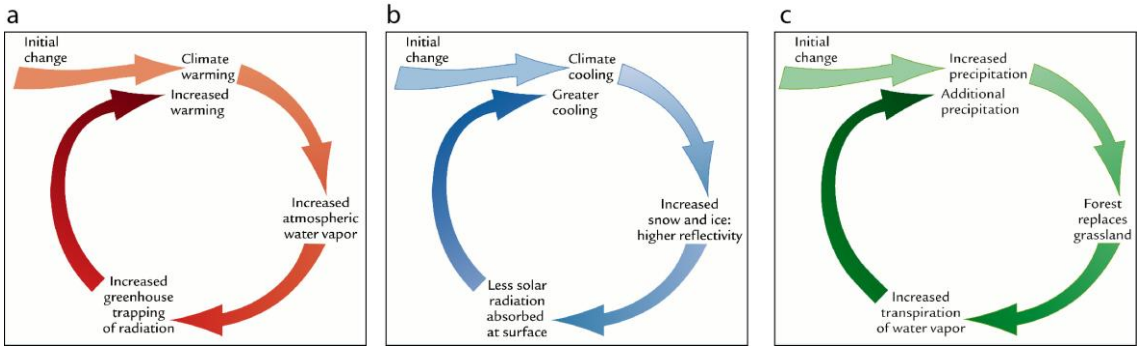

Figure 1: Example of three climate feedbacks, a) greenhouse-warming, b) ice-volume-cooling and c) vegetation-precipitation (Source: Ruddiman, 2001)

The paleoclimatology is based in the study of climatic archives that can be of different nature: ice-cores, marine and lake sediment cores, speleothems, death corals and tree rings among others. These archives contain different physical, chemical or biological properties that indirectly stored climatic conditions from the time when the archive was formed. The measured properties that can be related to climatic conditions are called proxies (Bradley, 1999). Several of the applied proxies in paleoclimatology are geochemical parameters; such as elemental composition of the bulk sediment (Mg/Ca, Sr/Ca, Zr/Al), stable isotopes and trace elements in biogenic carbonates ($\delta^{18}O$, $\delta^{13}C$, Mn/Ca) and radiogenic isotopes in carbonates (U/Th, ^{14}C). But several other proxies from different nature also exist: faunal assemblages, pollen distribution, foraminifera counting or sediment grain size distribution among others.

One of the most critical tasks of the paleoclimatologists consists on elucidating the climatic processes controlling the proxy variability and its evolution along time. Three elements set the basis in this research: 1) the climate system itself and the dynamic interrelationships among its components and processes, 2) chronologies, which provide a timeframe to the studied climate variability, and 3) the climate proxies that are the tools that allow reconstructing climate-related parameters. Thus, in the process to achieve reliable climate interpretations several disciplines need to be combined, mostly atmospheric physics, oceanography, geology, biology and chemistry. Consequently the paleoclimatology is indeed an interdisciplinary science where multi-archive and multi-proxies approaches are required for unravel the Earth climate history at different time scales.

1.2 Speleothems as climatic records

Speleothems have become a very valuable paleoclimatic archive from the continental realm since they have the potential to record key elements from the climatic system with exceptional accurate chronologies. Besides many different kinds of speleothems can be distinguished, flowstones and stalagmites are the most common used for paleoclimate reconstructions. This study is focused on the analysis of stalagmites which usually provide records at higher resolution than flowstones. Stalagmites are mineral deposits of calcite and/or aragonite ($CaCO_3$) that grew over time from dripping water within caves in karstic systems (Gunn, 2004) (Fig 1.1). When rain waters enter through the soil into the karstic system, as a result of organic matter respiration and decomposition, it increases its carbon dioxide partial pressure (pCO_2) becoming more acid. When this groundwater, with high pCO_2, percolates through pores, fissures or conduits of the karst bed-rock, it dissolves carbonate, generally limestones ($CaCO_3$) or dolomites ($CaMg(CO_3)_2$). Hence the calcium concentration and other elements increase in the water solution. While the ground water enters deeper in the karst, it may found air with lowest pCO_2 that led to water CO_2 degassing, a process that may increase when the ground water reaches the cave chamber. During this CO_2 lost, the solution becomes oversaturated in calcium inducing carbonate precipitation (McDermott, 2004; Fairchild and Baker, 2012). Therefore, degassing process led by different pCO_2 between the dripping water and the cave is one of the controlling factors on the fluid calcium concentration and thus the carbonate precipitation (Fig 1.1). Usual ranges of pCO_2 are 0.1-3.5% in the soil and 0.06-0.6% in caves (Fairchild and Baker, 2012). Hence the speleothem growth is controlled by the water availability but also by the cave-aire contidions (temperature and pCO_2) (Kowalczk and Froelich, 2010). Speleothems can reach growth rates of the order of millimetre per year in humid and warm areas whereas in cool temperate regions the growth rates are usually less than 100µm per year (McDermott, 2004).

Speleothems can be studied in base to a broad number of proxies: stable and radiogenic isotopes, clumped isotopes, fluid inclusion, trace elements, thickness of laminae, growth-rate, pollen, organic acid contents and petrology. They provide information about environmental variables such as rainfall variability, atmospheric circulation changes, annual mean temperature, vegetation response and cave ventilation changes in a variety of timescales (Fairchild *et al*., 2006; McDermott, 2004). However, several competing factors, at local, regional and global scale, can directly or indirectly influence the same proxy signal thereby challenging its interpretation.

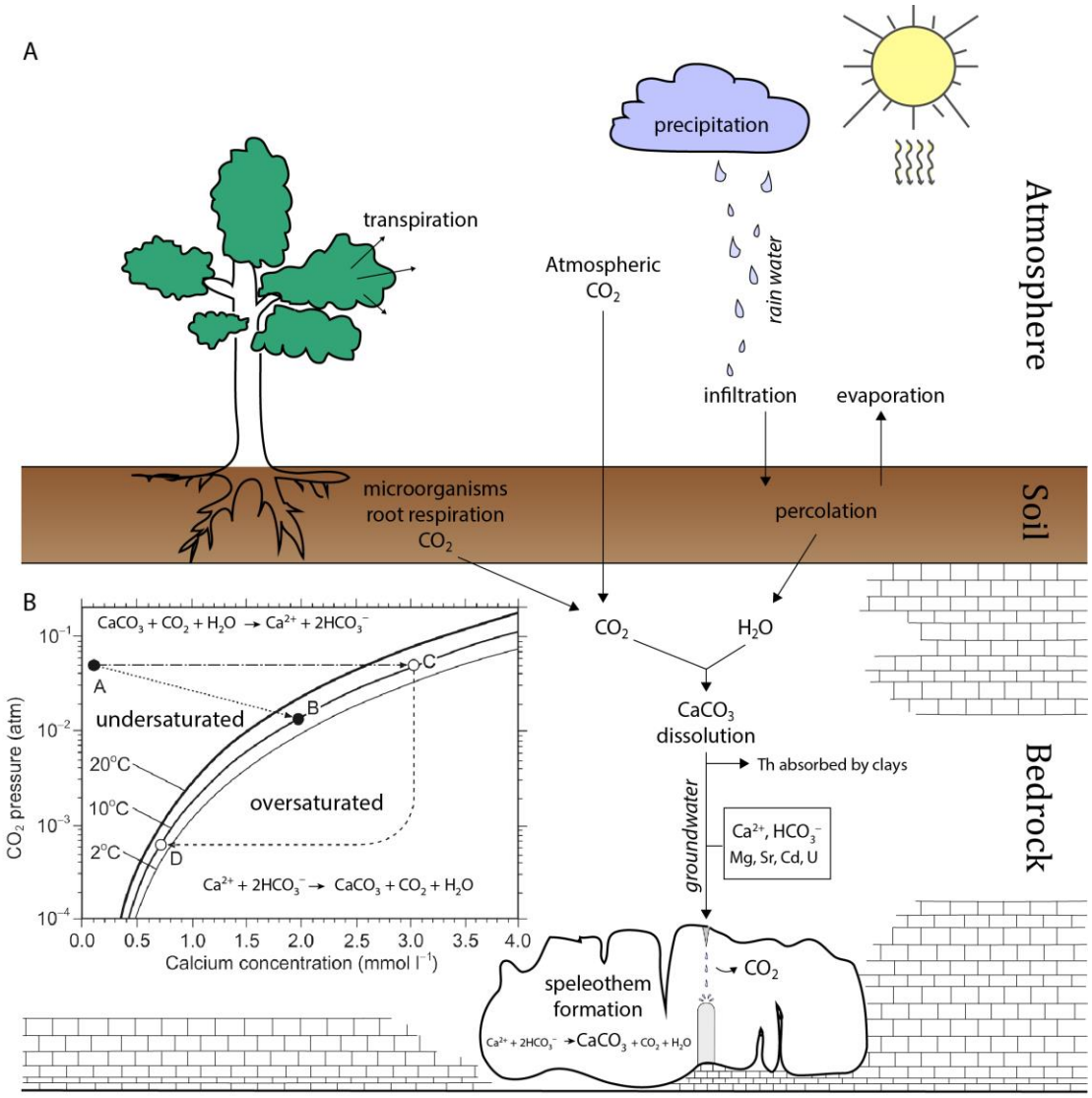

Figure 1.1. A) Speleothem formation scheme and processes involved. B) Chemical pathway leading to $CaCO_3$ precipitation. Point A indicates high $_PCO_2$ in the soil owing to respiration and decomposition of organic matter. When percolating water with high $_PCO_2$ reaches carbonates they will be dissolved, increasing the calcium solution (point B and C where it has been no renewal and restock of CO_2 respectively.). When water encounters an air space with lower $_PCO_2$, it degasses the CO_2 and precipitate $CaCO_3$ within the oversaturated zone (point D). (source: Fairchild and Baker 2012)

Speleothems have been applied on paleoclimate studies since late 60's (Hendy and Wilson, 1968; Thompson *et al*., 1974). However, improvements in analytical techniques, especially related to the U-Th dating, have determined a major development in the application of speleothems science during the recent years (Edwards *et al*., 1987; Hoffman *et al*., 2007). The pioneer analytical technique applied to speleothem studies was the measurement of oxygen isotopes as paleothermometer, with a subsequent shift of its interpretations towards hydroclimate processes and applying additional proxies (Baker *et al*., 1993; Bar-Matthews *et al.,* 1997; Ludwing *et al.,* 1992; McDermott *et al*., 1999)

including carbon isotopes (Bar-Matthews *et al*., 1997 and 1999; Dorale *et al*., 1992; Genty *et al*., 2006). More recently, the use of trace elements has rapidly widespread (Fairchild and Treble, 2009; Borsato *et al*., 2007; Treble *et al*., 2003). Oxygen and carbon isotopes together with Mg/Ca ratios are the main proxies used in this thesis and their theoretical bases are presented in detail in section 2.5.

One of the great strength of the speleothem records lies in their suitability to obtain independent absolute chronologies (Cheng *et al*., 2009; Fairchild and Baker, 2012). The assignation of absolute ages in speleothems is performed by radiometric methods due to the decay of radioactive species (e.g.: ^{14}C, ^{234}U). The most broadly used is the uranium-thorium disequilibrium method (see section 2.5.1). In addition, speleothems also give the opportunity to obtain high-resolution records; allowing even the detection of short-lived and low-amplitude climatic events when speleothems with rapid growth rates are chosen (McDermott *et al*., 2001).

The proxy interpretation in speleothems can significantly benefit from the development of detailed cave-monitoring exercises of present-day conditions that bring the opportunity to validate and calibrate the paleo-data with current conditions. However, when cave-monitoring efforts are not possible, multiproxy approaches applied over several speleothem records from the same cave or region, and overlapping on time, can provide the opportunity to obtain replicated signals establishing confidence in their interpretations as robust climatic records.

1.3 Paleoclimate reconstructions on sediment cores

Marine sediment cores provide the bases to reconstruct past ocean conditions ultimately reflecting climate conditions. These records have become a key in paleoclimatic studies for their value providing long and continuous climatic records with a rich variety of proxies. These proxies are based in the analysis of both lithogenic and biogenic components from the sediments. On one hand, the lithogenic particles can provide information of sediment transport processes (e.g. wind, riverine inputs or oceanic currents) that often offer a diagnosis of atmospheric conditions. On the other hand, biogenic particles are mostly carbonate or silicic shells from both planktonic and benthic organisms that are preserved in deep sediments (e.g. corals, foraminifera, coccolitophores or diatoms). Assemblage distribution and also chemical signal of these biogenic remains provide information about chemical or physical properties of the sea water.

Usually the first analytical technics to be applied in a sediment core are those non-destructive with multisensor core-loggers or with X-ray fluorescence core-scanners that provide physical and chemical properties of the sediments. One of the great advantages of these non-destructive techniques is their capacity to provide simultaneously information of several parameters at high resolution with a relatively low time and cost. Sediment cores are then studied with other destructive analytical techniques that include micro-fossil characterization, geochemistry, biomarkers, grain size, carbonate opal or even plastics content among several others. From both non-destructive and destructive analyses it is possible to obtain an important variety of proxies (e.g. $U^{37'}_{k}$, $\delta^{18}O$, Mg/Ca or pollen characterization). In some cases the proxy can be calibrated and quantitatively transformed into an environmental variable by means of a transfer function. An example is the case of Mg/Ca ratios measured in planktonic foraminifera to reconstruct sea surface temperature which is used in this study (Elderfield and Ganssen, 2000; Cisneros *et al.,* 2016). The applied proxies in this thesis include the analysis of both lithogenic and biogenic particles although the major effort has concentrated in geochemical analysis, stable isotopes and Mg/Ca ratios, of foraminifer shells. Specific information of the theoretical basis of each proxy utilized in this study is detailed in section 2.5.

Foraminifera are unicellular organisms which species are adapted to different habitats, including planktonic (free floating in the water column) and benthic (on and within the sediments) ecosystems. Geochemical analyses in foraminifera are usually concentrated in one specific species that represents the environment targeted by the study (Rosenthal *et al.,* 1997; Lea *et al*., 1999, 2000; Elderfield and Ganssen, 2000; Barker

et al., 2003). These technics have been largely applied in paleoceanographic studies demonstrating their suitability to reconstruct chemical and thermal conditions during past climate fluctuations (e.g. Cacho *et al*., 1999 and 2000; Elderfield and Ganssen, 2000; Elderfield *et al*., 2006; Lea *et al*., 1999, 2000; Martrat *et al.,* 2004; Nürnberg *et al*., 1996; Sierro *et al*., 2005) In particular, in this thesis the effort has concentrated in the analysis of planktonic foraminifera *Globigerina bulloides* for two independent proxies, $\delta^{18}O$ and Mg/Ca ratio. This foraminifer is a planktonic spinose spice which lives in a wide range of water temperatures, from tropical to sub-Antarctic waters (Hembleben *et al*., 1989; Sen Gupta, 1999). It is abundant in eutrophic conditions and it is strongly associated with phytoplankton blooms in the ocean (Mortyn and Charles, 2003).

The first large scientific effort to produce a global record for the Quaternary climate cycles provided the so called SPECMAP stacked curve, which was based in the integration of several worldwide records of $\delta^{18}O$ measured on planktonic foraminifera (Imbrie *et al*, 1984; Martinson *et al*., 1987). More recently, a stack record covering the last 5 million years has been produced in base to several worldwide distributed $\delta^{18}O$ records in benthic foraminifera (Lisiecki and Raymo, 2005). These two stack records have become fundamental tools for the study of glacial/interglacial cycles and their chronologies are in part determined by the orbital cycles. They also provide the bases to produce age models in marine sediment cores by means of the isotopic chronostratigraphy. The principle to allow their use as global chronological markers is their global signal driven by changes in the ice-sheet build-up, which is the main control factor in the benthic $\delta^{18}O$ signal. However this assumption could be challenged due to regional temperature or hydrographic changes that can overprint the isotopic signal particularly in planktonic $\delta^{18}O$ records. Thus the marine records are mostly dated by relative chronologies that ultimately have been constructed by astronomical tuning. This complicates any interpretation in terms of orbital forcing in base to the marine record and this has been one of the reasons why absolute dated speleothem records have become highly valuable in paleoclimate studies.

1.4 Climatic cycles: The 100kyr world

Earth climate has oscillated at different time-scales from million years to multidecadal scales (Fig. 1.2a). The available paleoclimate records covering the last ~50 Ma BP have shown that since the Early Eocene Climatic Optimum, when continental ice-sheets were absent on Earth, climate has been progressively cooled in part due to important reductions of atmospheric pCO_2 (Zachos *et al.*, 2008). During this general cooling trend the south hemisphere ice-sheets were the first ones in develop at ~40 Ma ago, while the north hemisphere ice-sheets started also to build up far later, at ~2.6 Ma ago (Fig. 1.2b). Since the glaciation of the NH a sequence of glacial/interglacial cycles have succeed (Emiliani, 1955; Lisiecki and Raymo, 2005; Shackleton *et al.*, 1984; Shackleton, 1967), initially every ~41 kyr, but a shift to longer cycles of ~100 kyr occurred during the so-called Mid-Pleistocene Transition, between 1-0.8Ma (Fig. 1.2c). The ultimate reason for this major climate re-organization is still a matter of intensive research, several hypothesis exist but remain an open question why the Earth Climate entered in the ~100 kyr cycles, which have dominated for the last 800 kyr (PAGES, 2016).

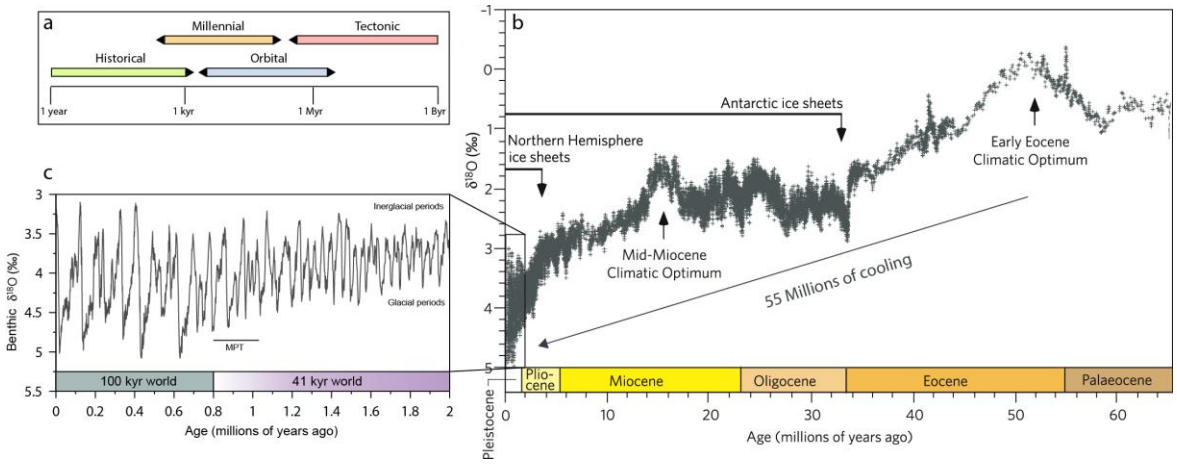

Figure 1.2. A) Different time scales of the climatic variability (source: adapted from Ruddiman 2001). B) A stacked deep-sea benthic foraminiferal oxygen-isotope curve that clearly shows an increment in the $\delta^{18}O$ values highlighting a general cooling trend over the last 65 millions of years. The onset of the glaciations on the Antarctica and the Northern Hemisphere are emphasised (modified from Zachos *et al.*, 2008). C) The LR04 stack of benthic $\delta^{18}O$ records from 57 globally distributed sites where the glacial/interglacial marine isotopic stages can be observed (Lisiecki and Raymo 2005)

The trigger of this glacial/interglacial climate variability was proposed to respond to astronomical forcing led by changes in the insolation distribution associated to the earth orbit changes (Shacleton, 1967, Imbrie and Imbrie, 1979). The combination of three astronomical parameters (precession, obliquity and eccentricity), which oscillate at

different period, control the incoming solar radiation on the Earth (Fig. 1.3) (Berger, 1988; Imbrie *et al.*, 1992). Indeed, according to the Milankovitch theory (Milankovitch, 1941) it was proposed that the summer insolation at high northern latitudes would drive the growth and reduction of the ice-sheets and hence inducing glacial/interglacial cycles. But pioneer paleoceanographic studies based on marine records identified that the Earth Climate had a nonlinear response to orbital forcing, recognizing the operation of climate feedbacks inherent to the earth climate system to account for the actual intensity and patterns of the glacial/interglacial cycles (Hays, Imbrie, & Shackleton, 1976). In this regard, CO_2 was proposed as a key positive feedback that causes non-linear growth of large ice sheets (Ruddimman, 2006). Non-orbitally forced climate fluctuations have also been observed during rapid cooling events associated to ice rafting events in the North Atlantic Sea, the so-called Heinrich events (Bond *et al*., 1992, 1993). Therefore this non-linear response of the Earth Climate System is ascribed to several internal forcing or feedbacks (e.g. CO_2, ocean circulation, and albedo) (PAGES, 2016). Understanding their role in the modulation of glacial/interglacial cycles and also shorten climate oscillations involves comprehensive studies of high-resolution multi-proxy and multi-archive paleoclimate studies at millennial time scale.

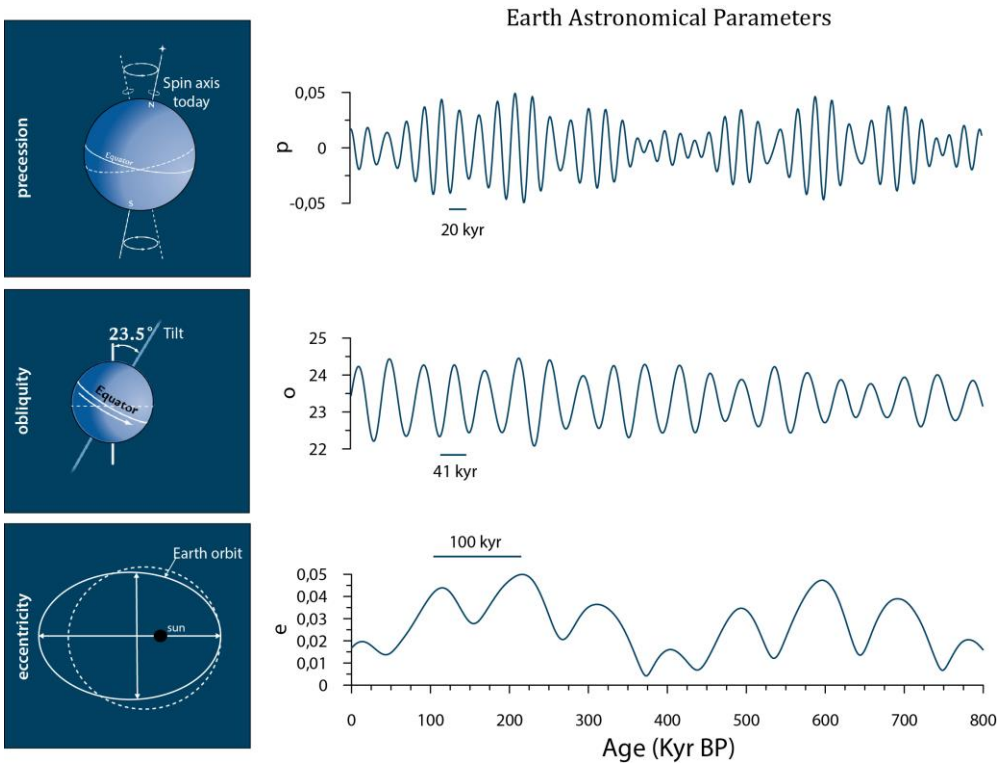

Figure 1.3. Orbital parameters scheme at the left panels with their respectively periodicities over the last 800 kyr in the right (source: modified from Ruddiman 2001)

1.4.1 Interglacial periods

Interglacial periods can be defined as short warm intervals with low ice volume which have commonly been described as less climatically unstable than the glacial periods. However an exact definition remains under discussion and several definitions have been described depending on the parameter used (PAGES, 2016).

In the marine realm, glacial/interglacial cycles were defined as Marine Isotopes Stages (MIS) in the base to the foraminifera $\delta^{18}O$ records which were initially interpreted to reflect changes in global temperature (Emiliani, 1955), although later was recognized the global effect of continental ice volume in the ocean $\delta^{18}O$ composition (Shackleton, 1967). In this regard, light $\delta^{18}O$ intervals correspond to interglacial periods and they were classified with odd-numbered stages which were further divided into substages (Emiliani, 1955) (Fig. 1.4).

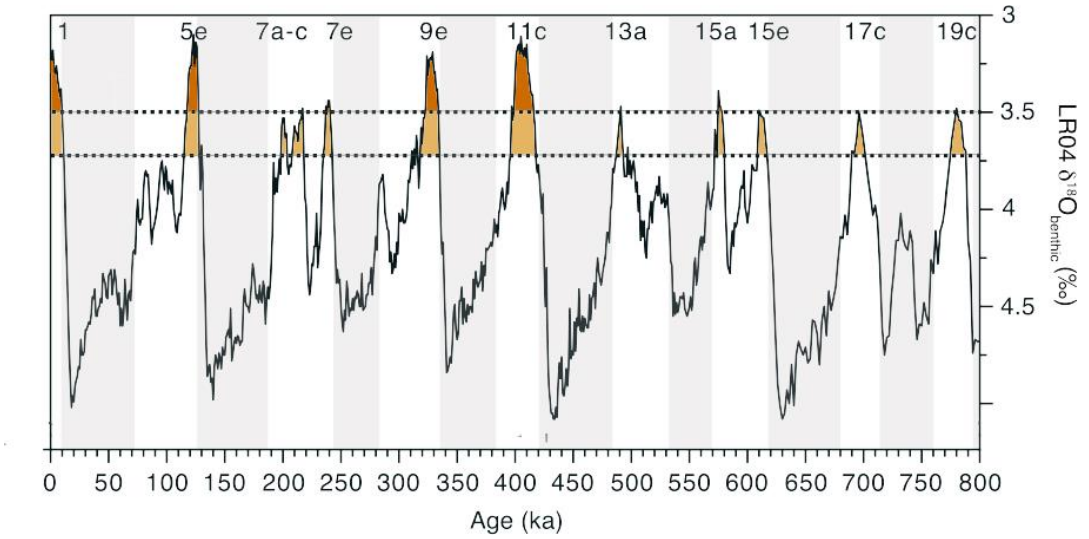

Figure 1.4. The $\delta^{18}O$ benthic foraminifera of the LR04 stack (Lisiecki and Raymo 2005) with the interglacial marine isotope acmes highlighted in orange (source: modified from PAGES, 2016)

Paleoclimatological studies based on pollen sequences from terrestrial archives from mid-latitudes regions defined the interglacial periods by the development of temperate deciduous forest on land (West 1984; Gibbard and West, 2000). Depending on the region and the period, these interglacials were named by a specific nomenclature. For instance, the Last Interglacial (LIG) in the continental Western Europe is defined as the Eemian (Otvos, 2015). A detailed comparison of pollen and foraminiferal isotopic composition revealed that interglacial periods on land were equivalent to MIS's substages rather than whole MIS's (Shackleton, 1969). Furthermore, further marine-terrestrial

comparisons also allowed recognizing time and geographical asynchronies of the climatic response between the terrestrial and marine realms (Sanchez-Goñi *et al*., 1999; Shackleton, 1969 and 2002; Tzedakis *et al*., 2004). This asynchrony in the boundaries of interglacial periods between marine and terrestrial records or even different proxies within the same archives has challenged the interglacial definition. Recently the concept of the interglacial "acme" term has been introduced. It is defined as the interval containing a plateau or peak values in a given record (Govin *et al*., 2015). Different attempts have been accomplished in order to achieve an unambiguous definition for interglacial or the "acme" period based on a single climate proxy.

Tzedakis *et al.,* 2009 described the interglacial as the most prominent temperate interval (low $\delta^{18}O$) within odd-numbered marine isotopic stages of the LR04 benthic $\delta^{18}O$ stack of Lisiecki and Raymo, 2005. Consequently, this definition comprises the MIS 5e, 7e, 9e, 11c, 13a, 15a, 15e, 17 and 19 as interglacial periods besides the MIS 1. When the traditional expectation of the 100 kyr periodicity is assumed, the 7e and MIS 15a could be also justified with the exception of the MIS 3 (PAGES, 2016; Yin and Berger, 2010 and 2012) (Fig 1.4).

On the other hand, the *Past Interglacial working group of PAGES* defined the interglacial as the interval where sea level resembled the present level (0± 20m) in contrast to periods of significantly enhanced ice volume and lower sea level. And therefore there is not substantial NH ice extent outside Greenland during interglacials. This definition was applied on different sea level reconstructions (Elderfield *et al*., 2012; Rohling *et al*., 2009 and 2014; Shakun *et al*., 2015) and the MIS 1, 5e, 7a-c, 7e, 9e, 11c, 13a, 15e, 17c, and 19c were defined as interglacial periods (Fig 1.4).

However, each interglacial period is singular and presents several differences among the others in terms of strength/intensity, duration and internal climate variability (Table 1.1) (Tzedakis *et al.,* 2009). The strength of each of these interglacial periods apparently is not related to the force of its associated insolation maximum (phases of minimum precession and maximum obliquity) (Yin and Berger 2010). Since the interglacial strength is not tied to the astronomical forcing, it has been proposed that the atmospheric CO_2 concentration could have a relevant influence (Ruddiman, 2006). Traditionally the duration of the past interglacial periods was defined as a half-precession cycle (~10 kyr) on average, but the increasing availability of paleoclimatic records of improved resolution and chronologies have proved the existence of exceptions to this erroneous "duration rule", as is the case of the MIS 11 and 19 which extended

approximately half-obliquity cycle (~20 kyr). But, in any case, any interstadial end is always determined by a millennial-scale event (Tzedakis *et al.,* 2004). Therefore, the intensity, duration, the precise timing, and even internal variability that characterize an interglacial period is besides the astronomical forcing and result from the interaction of several internal forcings and feedbacks (such as CO_2, ice-volume or the thermal bipolar seesaw) which are the ultimately cause of the existing interglacial diversity (Tzedakis *et al.,* 2009).

Table 1.1. Key features of the past interglacial periods (source: Tzedakis *et al.,* 2009)

Interglacial diversity				
Interglacials	**Intensity***	**Duration**	**Instability**	**CO_2 overshoot**
MIS 1	Warm	?	Yes	No
MIS 5e	Warm	S	Yes	Yes
MIS 7e	Warm?	S	NE	Yes
MIS 9e	Warm	S	NE	Yes
MIS 11c	Warm	L	NE	No
MIS 13a	Cool	S	NE	No
MIS 15a	Cool	S	NE	No
MIS 15c	Cool	S	NE	No
MIS 17	Cool	S	NE	No
MIS 19	Cool	L	NE	?

The diversity of past interglacial periods provide us different climatic scenarios with different combinations of boundary conditions. The MIS 5e, 9e, and MIS 11c are important focuses of ongoing research due to they were commonly considered strong interglacials based on SST records (Table 1.1). The MIS 11c was a long interglacial period that has been considered as the closest analog to MIS 1 in relation to its astronomical configuration (Tzedakis *et al*., 2009). Several studies highlight that the current interglacial period will remain warm for many millennia and it is going to be exceptionally long not only due to industrial accelerated greenhouses emissions if not also human activity influences since the early Holocene (Ganopolski *et al.,* 2016, IPCC, 2013; Ruddiman, 2005). Hence research on MIS 11 records may provide interesting information about long interglacials climate variability as expected for the current one. Nevertheless, the MIS 9e was the interglacial with the highest CO_2 concentration peak (~300ppmv) over a relatively short period of a few centuries. Hence it becomes the perfect candidate to elucidate how the climatic system could respond in the future due to extremely increased anthropogenic greenhouse emissions. Particularly, the MIS 5e, the Last Interglacial period (LIG), is one of the best targets due to the good preservation of the geological records that allows to obtain high resolution records of temperatures, ice-sheet extent and sea level proxies among others (Bardají *et al*., 2009; Dutton and Lambeck, 2012; Martrat *et al*., 2014). Detailed studies of high-resolution records allow identifying global but also regional climatic feedbacks that

in addition to the thermal inertia of the oceans also contribute to elucidate geographical and temporal differences in the response and the magnitude of the climatic variability at millennial/centennial time scale (Bakker *et al*., 2014).

1.4.2 Interglacial transitions

Deglaciations led to the onset of interglacial periods and are always characterized by sea level rise due to ice-sheet melting (PAGES 2016). Deglaciations, also called glacial terminations, are fast and intense transitions that contrast with the slower and more progressive character of the glaciations. The increasing NH summer insolation is considered to be the main driver of the deglaciations (Past Interglacials Working Group of PAGES, 2016, Cheng *et al*., 2009; Drysdale *et al*., 2009; Tzedakis *et al*., 2012). However, due to the slow response of the ice sheets, the peak of the sea level highstand, represented by minimum $\delta^{18}O$ values that define the interglacial acme or plateau, occurred systematically few thousand years after the maximum in NH summer insolation (precession minimum) (PAGES, 2016; Yin and Berger 2010). Hence glacial terminations are determined by the interaction between the insolation rise and the actual state of ice build-up extent during the preceding glacial period (Tzedakis *et al.,* 2009, 2012). Interestingly, an essential feedback for glacial terminations appears to be the intense North Atlantic freshening by iceberg melting due to increasing NH summer insolation. This freshwater discharge disturbed the Atlantic Meridional Overturning Circulation (AMOC) and changed the interhemispheric heat transport. In consequence, a rapid cooling occurred in the North Atlantic region while the Antarctica gradually warmed up. This asymmetry in the hemispheric heath transport is known as the bipolar-seesaw. These changes trigger other secondary feedbacks such as the albedo due to the reduction in the ice sheets extension and also an increase in atmospheric CO_2 in part due to southern ocean circulation changes related to the bipolar-seesaw dynamics. In consequence, the current scientific evidences point to this bipolar see-saw process as a fundamental requirement to enter in a deglaciation transition (Barker *et al*., 2011; Cheng *et al*., 2009; Tzedakis *et al*., 2012)

On the contrary, glacial inceptions symbolize the end of the full Interglacial conditions and the onset of a rather long transition toward full glacial conditions that involved continental ice growth and atmospheric CO_2 reductions (Ganopolski *et al*., 2016). They were driven by decreases in NH summer insolation in polar and subpolar regions and always occurred when obliquity was decreasing. However, the ice growth and the CO_2 concentration changes were non-linear to this external forcing. Several studies point to the high sensitivity of the glacial inceptions to the atmospheric CO_2 concentration (Berger and

Loutre, 2002; Ganopolski *et al.,* 2016). It has even been reported that the next glacial inception could be delayed due to currently anomalously high CO_2 concentrations (Fig 1.5). High resolution paleoclimatic records also reveal that the glacial inception result from a complex interaction between orbital and millennial-scale changes that led the planet to enter into a new glacial state although this interplay is not yet fully understood (Drysdale *et al.,* 2007; Tzedakis *et al.,* 2009). For example, the earth entered into the last ice age after MIS 5e (the Last Interglacial) and, although other comparable large maxima in NH summer insolation occurred (MIS 5a and c) the earth was able to build up sufficient ice-sheet to go back to full glacial conditions (PAGES, 2016). The currently used Marine Isotopic Stages were initially defined by Emiliani (1955) and he established the even/odd number to refer to warm/cold periods. The improvement in the paleoclimatic resolutions and in the number of proxy reconstructions has allowed to better characterize these climatic periods, this has shown that the full glacial conditions were not developed only during the entire even isotopic stages initially defined (Fig 1.4). In consequence, the Last Interglacial refers only to the MIS 5e and not to the entire MIS 5, where the MIS 5a-d is considered the early glacial.

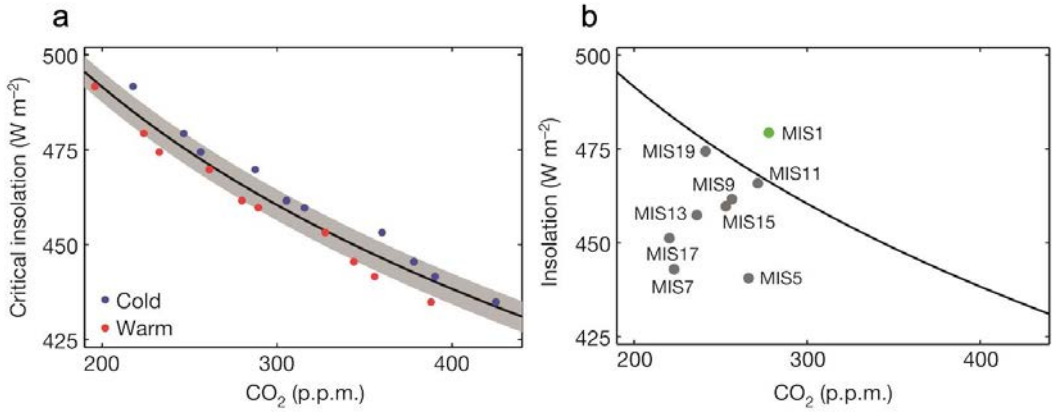

Figure 1.5. A) Modelled critical functional relationship between boreal summer insolation and global CO_2 concentration. The best fit-logarithmic relation (black line) shows the CO_2 threshold for glacial inceptions. The blue dots correspond to the coldest model and red dots to the warmest model. B) Location of previous glacial inceptions respect to the modelled insolation-CO_2 threshold. Glacial inception only is possible when the point is below the modelled curve. (source: Ganopolski *et al.,* 2016). This study suggests that the current CO_2 levels would probably postpone the next glacial inception.

Overall, the interglacial ends are fascinating examples of non-linear behaviour of the Earth system. Despite that, glacial inceptions and early glacial periods have often received less attention than glacial periods, glacial terminations and interglacial periods, although they are often associated with large-scale but also rapid climatic changes (Dorale *et al*., 2010; Drysdale *et al*., 2007).

1.5 The Iberian Peninsula and its surrounding seas

1.5.1 Current oceanographic conditions

The Ocean is an essential component of the Earth climate system. It absorbs most of the solar radiation and distributes the heat around the world. Ocean and atmosphere interactions are key elements controlling climate evolution in past, present and future times (Bigg *et al*., 2003). The North Atlantic Ocean is a key factor in the Earth climate system. The importance of the surface North Atlantic Current (NAC) remains on its northward heat and salt transport into the Nordic Sea, where deep-water formation occurs (Fig. 1.6). (McCartney and Mauritzen, 2001). Expansions and contractions of the subtropical and the subpolar gyres control the NAC heat and salinity supply to high latitudes, finally influencing the AMOC dynamics and the global oceanic circulation and climate (Mary *et al.,* 2017; Pérez-Brunius *et al*., 2004). In addition, North Atlantic surface water enters into the Mediterranean Sea while Mediterranean deep waters supply salinity to the Atlantic intermediates waters, overall establishing ocean and climatic links. The Iberian Peninsula and the Balearic Islands in the western Mediterranean Sea are in a strategic geographical area to evaluate teleconnections between the North Atlantic and the Mediterranean regions. In this sense, the climatic conditions over the IP are very much linked to the conditions in its surrounding seas. This thesis explores the past variability of two remote marine regions, the Cantabrian and the Mediterranean Sea to evaluate their connections to the atmospheric changes recorded in the speleothem records.

The Cantabrian Sea

The Cantabrian Sea is located north of the IP at the southern part of the Bay of Biscay, which opens westward to the North Atlantic Ocean (Fig. 1.6). The surface water mass in the Cantabrian Sea is characterized by the Eastern North Atlantic Central Water (ENACW), which is the result of winter mixing of surface waters from the northeast Azores to the European margin, mainly driven to this location by the North Atlantic Current (NAC) via the subtropical gyre (STG) (Pollard *et al.,* 1996). The Iberian Poleward Current (IPC) is an additional current that flows seasonally every winter eastward along the IP shelf into the Cantabrian Sea (Pingree and Le Cann, 1990). Freshwater runoff from Spanish and French rivers can produce variations in the IPC salinity, and therefore in its density (Ferrer *et al*., 2009).

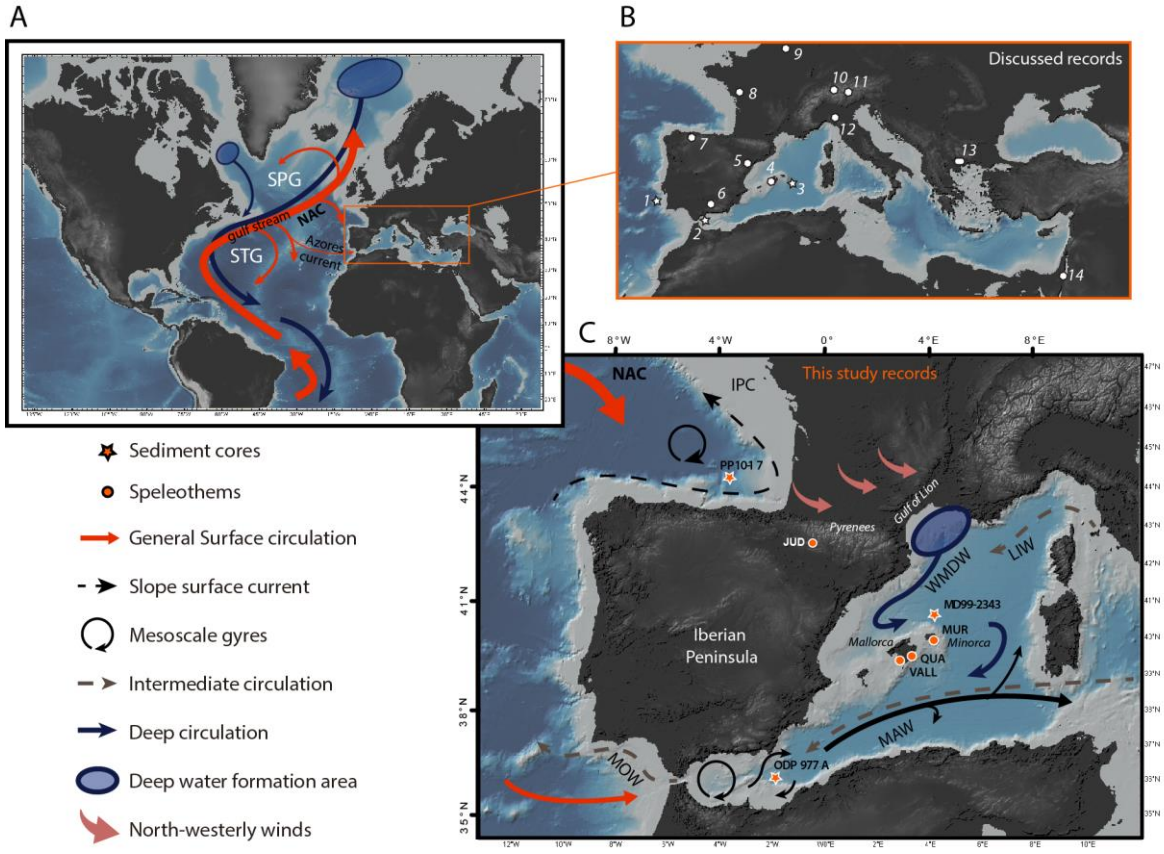

Figure 1.6. A) Schematic North Atlantic water circulation. NAC: North Atlantic Current, SPG: Subpolar gyre, STG: Subtropical gyre. B) European map showing the location of several sites discussed in the text: 1) MD01-2444 core (Tzedakis *et al*., 2018), 2) ODP Site 976 (Jiménez-Amat and Zahn, 2015), 3) ODP site 975 (Marino *et al.,* 2015) 4) Campanet cave (Dumitru *et al*., 2018) and Cala Falcó cave (Hodge *et al*., 2008b), 5) Ejulve cave (Pérez-Mejias *et al.,* 2017), 6) Gitana cave (Hodge *et al*., 2008a), 7) Cantabrian caves (Stoll *et al*., 2015), 8) Villars cave (Genty *et al.,* 2003), 9) Han-sur-Lesse cave (Vansteenberge *et al*., 2016), 10) Alps caves (Moseley *et al*., 2015), 11) Spannagel cave (Spötel *et al*., 2008), 12) Corchia cave (Drysdale *et al*., 2007; Tzedakis *et al*., 2018), 13) Tenaghi Philippon arboreal pollen record (Tzedakis *et al*., 2006) and 14) Soreq cave (Bar-Matthews *et al.,* 2000, 2003). C) Map showing the location of four caves (Pot-au-feu cave (JUD), Murada, Es Quartó, and Vallgornera caves) from which several speleothems have been selected for further discussion. This study marine sediment cores location are also indicated. Main circulation patterns: North Atlantic Current (NAC); Iberian Poleward current (IPC); Mediterranean Outflow Water (MOW); Levantine Intermediate Water (LIW); Modified Atlantic Water (MAW); Western Mediterranean Deep Water (WMDW).

The Western Mediterranean

The Mediterranean is a semi-enclosed sea where freshwater inputs, as rainfall and fluvial discharge, are exceeded by evaporation leading to a high salinity basin. The western Mediterranean circulation is mostly determined by three major water masses: surface, intermediate and deep (Fig. 1.6) (Lionello, 2012; Rohling *et al.*, 2009). Less saline water enters at surface through the Strait of Gibraltar to compensate the negative water balance caused by excessive evaporation in the Mediterranean. This surface water mass flow eastward while progressively increases its salinity and temperature creating the Modified Atlantic Water (MAW) (Pastor *et al.,* 2017; Pierre, 1999; Pinardi and Masetti, 2000;

Vargas-Yáñez *et al*., 2017). The Mediterranean Intermediate Water (MIW) spreads westwards, while mixing with regional waters, to finally outflow through the Strait of Gibraltar (Pinardi and Masetti, 2000). The deepest water mass in the western basin is the Western Mediterranean Deep Water (WMDW) (Millot *et al*., 1999). During winters, the north and northwestern winds cause strong cooling and evaporation of surface waters in the Gulf of Lion, increasing its density, and consequently mixing and sinking it into the deep basin (Fig. 1.6). Therefore, the density of this deep-water mass is determined by the temperature and salinity of both the local surface water and the MIW, and also the wind features (Millot *et al*., 1999; Rohling *et al*, 2009). The WMDW flows southwards collecting the continental sediment discharges, mainly from the Rhone and Ebro rivers, and depositing approximately the 10% of them in the deep basin (Martin *et al.,* 1989). In the Balearic Promontory, the currents associated to the WMDW accelerate and induces a re-working, transport and classification of the sediment particles (Cisneros *et al.,* 2019; Frigola *et al.,* 2008; Millot *et al.,* 1999; Velasco *et al.,* 1996) (Fig. 1.6).

1.5.2 Current climatology

The Mediterranean region is a transitional zone between subtropical and midlatitude temperate regimens, which exerts an important climate contrast among different nearby areas, even over time (Lionello, 2012). While the northern part of the Mediterranean region and also the Cantabrian Sea are strongly linked to midlatitude variability mostly characterized by the North Atlantic Oscillation, the southern and eastern parts are exposed to the influences of the Inter-Tropical Convergence Zone dynamics (ITCZ). The ITCZ is a circum-global atmospheric belt of intense moist convection and rainfall that controls the hydrologic cycle over the tropical continents (Fig. 1.7) (Koutavas and Lynch-Stieglitz, 2004; Wang, 2001). Latitudinal shifts of the ITCZ and its related precipitation changes over time strongly influences African monsoon patterns that are tightly linked with changes in the Mediterranean Sea water composition due to river runoff along the North African coast (Rohling *et al.,* 2014; Grant *et al*., 2016). Therefore atmospheric circulation, in both, the North Atlantic but also in the inter-tropical convergence zone, controls the precipitation patterns and regional temperature over the studied region. The Mediterranean Sea morphology with several subbasins, islands and peninsulas with narrow straits and the presence of mountains close to the sea, also allow producing spatial heterogeneities and regional climates.

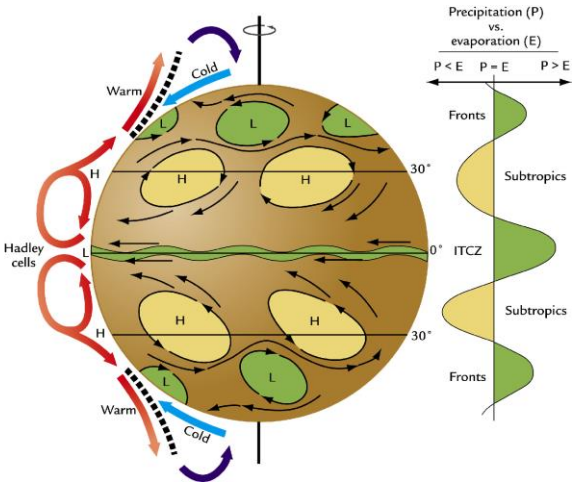

Figure 1.7. Scheme of the general atmospheric circulation on Earth and the ITCZ position. The enhanced solar radiation in the equatorial zone produces transport of heat and moisture to higher latitudes by means of the atmospheric cells (Hadley cell). In to the right it can be observed the precipitation-evaporation balance depending on the latitude. (source: Ruddiman 2001)

The studied cave locations are mostly dominated by the Mediterranean climate conditions which according to the traditional Köppen classification it is defined as a midlatitude temperate climate with a dry summer season. Besides this general context, the studied speleothems were collected from three different locations with their own local climate (Fig.1.8). One speleothem was collected at the central southern Pyrenees where the mountain relief strongly influences the local climate dominated by humid temperate conditions (Cfa), with an annual rainfall around 1000-1200 mm that mostly occurs as snow. The annual mean temperature is 4-5°C (AEMET-IM 2011). On another hand, the other studied speleothems correspond to the Balearic Islands located in the middle of the Mediterranean Sea. Here the climatic conditions are warmer with seasonal rainfall, intense storms in autumn and dry summers causing the lack of permanent watercourses. Therefore the Minorca and Mallorca islands present temperate with dry/hot summer climates (Csa) except for a small area in south Mallorca were the climate is like steppe (Bsk) according to the Köppen climate classification (Fig.1.8). The annual rainfall average in both Balearic island is similar, around 500-600 mm and the annual mean temperatures around 16-17°C (AEMET-IM 2011).

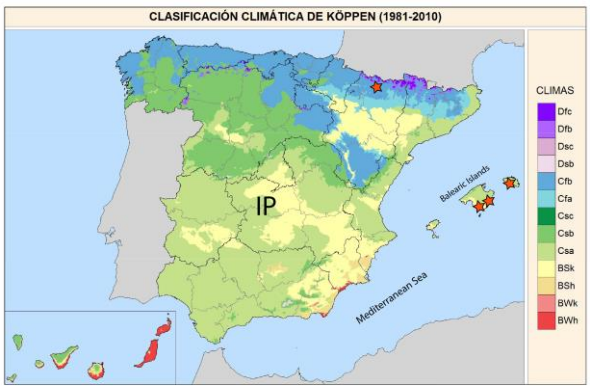

Figure 1.8. Climate types in the Iberian Peninsula and the Balearic Islands according to the Köppen classification. Orange starts point to this study cave locations. (source: Modified from AEMET, 2011)

Nowadays, the main areas of moisture source that affect the IP and the Balearic Islands are the tropical–subtropical North Atlantic corridor, the IP itself and the Mediterranean Sea via the dominant eastward atmospheric circulation (Krklec and Domínguez-Villar 2014; Nieto *et al*., 2010 and Gimeno *et al*., 2010). The eastern IP region is more dominated by Mediterranean moisture source than the Atlantic one (Dumitru *et al.*, 2017; Gimeno *et al.,* 2010).

1.6 Paleoclimate background

Paleoclimate reconstructions by means of speleothem records are found worldwide, however continuous speleothem records spanning several glacial/interglacial cycles are restricted to a few studies such as those focused on the Asian monsoon in China (Yuan et al., 2004; Cheng *et al*., 2006, 2009, 2016), the American monsoon in Brazil (Cruz *et al*., 2005, 2009) or the classic speleothem record of the Devil's hole in North America (Moesley *et al.,* 2016). Usually, speleothems spans shorter periods, but in contrast, they provide high resolution allowing carefully analysis and comparison at millennial or even centennial time scales, being extraordinary archives to resolve abrupt climate changes. Concerning to interglacial periods and its transitions a great variety of European speleothem records reveal climate variability during the MIS 5, spanning the penultimate termination (T-II), the LIG-acme and the early glacial period (e.g. Couchoud *et al*., 2009; Demény *et al*., 2017; Drysdale *et al*., 2005, 2007, 2009; Meyer *et al*., 2008; Moseley *et al*., 2015; Vansteenberge *et al*., 2016). Several of these records indicate enhanced moisture availability during the LIG-acme and show regional heterogeneity in the hydrological patterns during the glacial inception which is associated with AMOC changes. In the context of the Mediterranean Sea, an exceptional effort has performed in speleothem records from Soreq cave, in the Near East, which have allowed identifying rainfall changes associated to the timing of sapropels in the eastern Mediterranean, but records only arrive to the LIG (Bar-Matthews *et al*., 1999, 2000, 2003). In contrast, well-resolved paleoclimate records from previous interglacial periods remain elusive in Europe. Few examples are the speleothem record from Austria that grew during the penultimate interglacial (MIS 7) (Spötl *et al.,* 2008), the Antro del Corchia speleothem record from Italy that covers intermittently some interglacials, mainly the MIS 9 and 5 (Drysdale *et al.,* 2004), and other from the IP covering the T-III (Pérez-Mejias *et al.,* 2017). In base to the $\delta^{13}C$ records, this last record recovered from Ejulve cave in the eastern IP indicates that the T-III involved an increment in both temperature and precipitation that led to higher vegetation activity at the beginning of the MIS 7e (Pérez-Mejias *et al.,* 2017).

Besides the Ejulve cave record, all the other IP speleothem records from interglacial periods grew during the MIS 5-1. Regarding the MIS 5, the available information is limited to a stacked-speleothem reconstruction from the north-western IP, which recorded changes in water source properties at orbital scale (Stoll *et al*., 2015) and to a low-resolution record from southern IP that shows increased effective precipitation during the MIS 5 (Hodge *et al*., 2008a). Moreover, two speleothem records from Mallorca Island, partially cover the MIS 5 and indicate dry periods within the warm interstadials (Dumitru

et al., 2018; Hodge *et al*., 2008b). Additionally, speleothem encrustations records from several coastal Mallorca caves have been the base of a sea level reconstruction for the MIS 5e and 5a highstand (Dorale *et al*., 2010).

In the marine realm Martrat *et al.,* (2004 and 2007) provided continuous high-resolution paleoclimate records from the Western Iberian margin and the Alboran Sea encompassing several glacial/interglacial cycles. Paleoceanographic studies from the Western Mediterranean Sea have dedicated far more attention to the rapid climate variability of the last glacial period, focussing for instance in changes in deep water conditions. These studies described an antiphase behaviour between the deep overturning cells of the North Atlantic and the Mediterranean (Cacho *et al*., 2000, 2006; Frigola *et al.,* 2008, 2007; Sierro *et al*., 2005). Several studies also reveal that the injection of large volumes of water from melting icebergs (Henrich events) reached the western Mediterranean over the last glacial period but even in glacial terminations (T-I and T-II) (Jiménez-Amat and Zahn 2015; Marino *et al*., 2015; Sierro *et al*., 2005). Furthermore, variability in the north-westerly belt and precipitation patterns were highlighted as the main forcing mechanism to explain western Mediterranean climate variability on a millennial time-scale during glacial periods (Moreno et al., 2002, 2005). Overall, these paleo-oceanographic studies have already proved the strong impact of past AMOC changes into the IP climatology and surrounding marine regions (Cacho *et al*., 2001, 1999; Martrat *et al.,* 2015, 2014, 2007, 2004; Mary *et al.,* 2017; Rodríguez-Sanz *et al.,* 2017).

1.7 Objectives

The main objective of this Ph.D. thesis is to gain an insight into the climate variability associated with past interglacial periods and their accompanying transitions around the Iberian Peninsula. A particular emphasis is addressed to decipher the interplay of marine and atmospheric processes that operated during these past climate oscillations and to better understand interregional teleconnections responsible to transfer those climate oscillations. In order to accomplish this general objective, several specific goals should be accomplished:

- Compile a collection of speleothems and evaluate its suitability to provide paleoclimatic records of hydrological changes in the IP
- Construct solid accurate U-Th chronologies for those key speleothems that grew during interglacial periods.
- Understand the processes that explain the geochemistry variability in the speleothems.
- Provide the first comparison of Mediterranean climate conditions among the most recent Quaternary interglacial periods by means of terrestrial records.
- Identify possible links between ocean-atmosphere processes associated with Interglacial climate instability with particular attention to their beginning and end transitions.
- Evaluate the role that North Atlantic circulation changes had into determining past millennial time-scale variability in the region.
- Produce a detailed analysis of the Mediterranean and Atlantic changes associated with the last interglacial end or the initiation of the last glaciation, contrasting patterns among different marine locations around the IP, and identifying the hydrological impact in the northwestern IP.

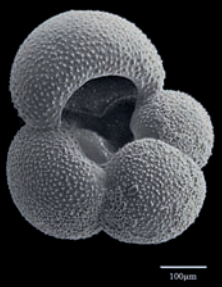

Yo nunca he creído que debamos renunciar a las visiones a largo plazo [..] pero lo lógico es comenzar por lo que tenemos a mano. Es como el chiste del borracho que se ha detenido junto a una farola, mirando el suelo. Llega un tipo y le pregunta:

-¿Qué buscas?
- Un lápiz que se me ha caído- le dice
-¿Y dónde se te ha caído? – pregunta el tipo
-Al otro lado de la calle- contesta el borracho
-Entonces, ¿por qué lo estás buscando aquí?
Y el borracho le responde – Porque aquí hay luz

Así es como trabajan las ciencias. A lo mejor el problema que a uno realmente le interesa está al otro lado de la calle, pero sólo se puede buscar donde hay luz. Si tratamos de desplazarla poco a poco, a lo mejor llegamos al otro lado de la calle.

Noam Chomsky

Chapter II

Methodology

2.1 Material recovery

2.1.1 Cave sampling

Speleothems used in this study were collected in caves from three different areas; two caves in the eastern Iberian Peninsula, 5 caves from Minorca Island and 5 from Mallorca Island. JUD is the speleothem studied more in detailed from the eastern Iberian Peninsula and it was collected from a Central Pyrenees cave during a field work previous to this thesis and organized by the Scientific Speleological Association of Cotiella (ACEC) in collaboration with the Pyrenean Institute of Ecology (IPE). The studied speleothems from Minorca were also recovered previously, in November 2011 in the context of the *HIDROPAST Project* and in collaboration within the University of Barcelona, University of Oviedo and the Institute of Environmental Assessment and Water Research (IDAEA-CSIC) and the Municipal Museum of Ciutadella. The speleothems from Mallorca were recovered during different field trips performed in the context of *OPERA Project* and in collaboration within the University of Barcelona and University of the Balearic Islands. These caves belong to private properties or are managed by public administrations. All of the activities performed during cave expeditions were correctly informed to the properties or the designed representatives and under permission. The speleothem archives used for this thesis were mainly broken at the floor and they did not present modern growth. All the activities were performed avoiding major impact on the environment and the ornamental forms in the caves. The *OPERA project* also dedicated a significant effort on monitoring environmental conditions in few caves from Mallorca from November of 2014 until April of 2018 on seasonal basis. Among the routinely data collection of different environmental parameters, samples of drip waters and farmed carbonates, a collection of speleothems was also recovered. Part of these speleothem archives are used for this thesis, while the monitoring data acquisition is the focus of ongoing parallel publications. The monitoring surveys, together with characterization of soil, vegetation and geology in the surrounding cave areas are relevant to better understand speleothem genesis and the complexity of their geochemical signal. Here is provided detailed information for those caves whose speleothems were chosen in this study to analyse their paleoclimatic signature.

Pyrenees- Pot au Feu cave

Pot au Feu cave is located at southern Central Pyrenees at the Cotiella massif into the Sobrarbe geopark (42°31.48' N; 0°14.26' W) at 997 m a.s.l. (Fig. 1.6 C). It is located at the Irués river valley and represents a fossil level of the high mountain karst aquifer Cotiella-Turbón of the Ebro watershed although it is vertically connected to another cave which sporadically floods. This karstic system, that still currently active, began to develop in the Miocene, eroding and dissolving the cave host rock which correspond to cretaceous packstones with miliolids (upper Turonian-lower Coniacian)(Lopez, 2013). Vegetation around the cave consists of mid-mountain forests and shrubbery in the valleys whereas the highlands are characterized by exposed bed-rock with sparse vegetation such as pastures. The annual rainfall is above 1000-1200 mm mostly as snow. *Judit* speleothem (JUD) was collected in situ and it is the only stalagmite used from this cave in this study.

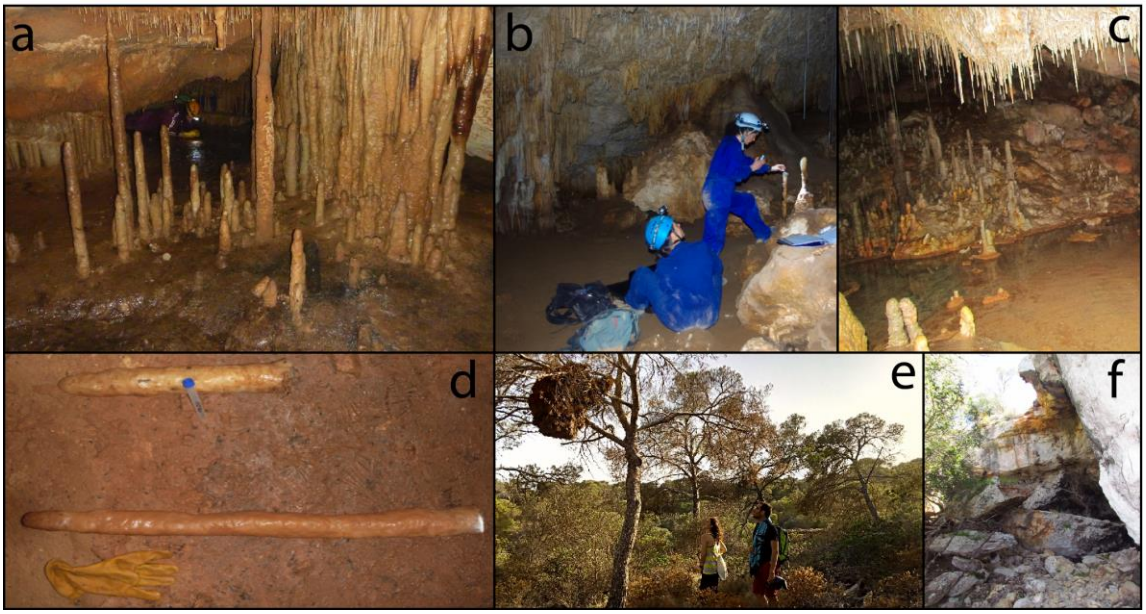

Figure 2. a) Interior of the Murada cave (Menorca). B) Sampling into the Sa Balma des Quarto cave (Mallorca). C) Vallgornera cave (Mallorca). D) IND ad RAT speleothems collected in the Murada Cave (Menorca). E) Vegetation cover over Sa Balma des Quartó cave. (Mallorca). F) Entrance to the Sa Balma des Quartó cave (Mallorca).

Minorca- Murada cave

Murada cave is located at southwest Minorca Island (39°57'58''N; 3°57'53''W) at 80 m a.s.l. (Fig. 1. 6 C), in the western edge of the *Barranc d'Algendar*, which is a canyon carved by a torrent. Minorca is characterized by the lack of permanent watercourses in the surface network and with irregular regime of torrents especially in autumn when intense storms causes sporadic high flows. This cave is the biggest of the canyon and represents a fossil level of karst drainage conduit. This karstification began to develop in the upper Miocene and affect the Miocene calcarenites (Helvecià-Tortonià) that are deeply karstified

forming a porous mixed aquifer. The scarce vegetation over the cave is composed by Mediterranean shrubland. The annual mean temperature is 16-17°C and the annual rainfall average is above 500-600mm (Jansà, 2014). Although 3 speleothems are dated and analysed from this cave only 2 stalagmites were analysed at high resolution, Indiana (IND) and Ratpenat (RAT). All the speleothems from this cave were inactive and both speleothem were fallen on the floor (Fig. 2a and d).

Mallorca- Sa Balma des Quartó, Pas de Vallgornera and Campanet caves

Sa Balma des Quartó cave is located at the eastern part of the Mallorca Island (39°51 N; 3°30' W, at 10 m a.s.l.) (Fig. 1.6 C). The host rock corresponds to upper Miocene coralline limestone were the cave was developed in a littoral cliff carved by a torrent. The karstification processes and the Mallorca coastal geomorphology has been further controlled by sea level oscillations during Pliocene and the Quaternary (Ginés *et al.,* 2012) and the development of the fluvial network. The cave is formed by one unique chamber with collapsed blocks above which several speleothem developed and several of them are still active. The annual mean temperature in Mallorca is ~17°C and average annual precipitation is ~500 mm with most of the rainfall in autumn (Guijarro, 1986, Jansà, 2014). Vegetation above the cave consists of evergreen forest and shrubland (Fig. 2 b, d and f). QUA14 was the only speleothem used from this cave and it was collected from the floor.

El Pas de Vallgornera cave is located in the south region of the Mallorca Island (39° 22' 00'' N, 2° 52' 25'' E) (Fig. 1.6 C). The host rock and the climatic conditions are the same to those of the *Sa Balma des Quartó* cave, with typically Mediterranean climate and vegetation. This cave consists of a more than 67 km of conduits and chambers flooded (Fig. 2 c). The cartography of this cave is not completed due to several conduits and chambers are not yet explored. Sea level reconstruction by means of phreatic overgrowths on speleothems has been previously studied in this cave (Dorale *et al*., 2010). Speleothems from that cave were recovered close to the entrance in the first big chamber highly ornamented with a permanent water pool.

Campanet cave is located in the northern part of Mallorca, into the *Serra de Tramuntana* (39°47′32″ N, 2°58′9'' E, at 65 m a.s.l.). The cave was developed on dolomites from the Upper Triasic and it has 397 m of length divided in several galleries. The vegetation over the cave mainly consists on *Quercus ilex* and *Cyclamen balearicus*, which both are Mediterranean subhumid-humid species. The mean annual temperature inside the cave is 18.8 °C, mainly constant throughout the year (Dumitru *et al.*, 2018).

2.1.2 Oceanographic cruises

The three marine sediment cores used in this study were recovered in different oceanographic cruises performed previously to the beginning of this thesis. All three cores were the subject of previous paleoceanographical studies performed by different national and international institutions and applying a wide range of micropaleontological, geochemical and sedimentological proxies. Therefore, this thesis has added a further contribution to this intensive scientific collaboration.

Sediment core PP10-17 was collected in 2010 during SARGASS oceanographic cruise on board *R/V Pourquoi Pas?,* that was organized by the Bordeaux I University. It consists in a calypso long-piston core of 17.92 m length retrieved from the Cantabrian Sea. More specifically, from the Bay of Biscay at the southwestern part of the Landes Plateau at 43° 58.91' N and 03°14.02' W, from a water depth of 2280 m b.s.l. (Fig. 1.6 C). The Bay of Biscay is a deep basin that opens westward to the Atlantic Ocean and is under the influence of the river systems that drain the Cantabrian Mountains and the Pyrenees. Landes Plateau sediment facies represents a hemipelagic environment (Brocheray *et al.,* 2014).

ODP Site 977A was retrieved on June 1995 during LEG 161 of the Ocean Drilling Program (ODP) on board *JOIDES Resolution*. It was located at halfway between the Spanish and Algerian coasts, in particular, at south of Cabo de Gata in the eastern sub-basin of the Alboran Sea, at 36°01.92'N and 1°57.32'W, from a water depth of 1984 m b.s.l. (Fig. 1.6 C). The drill penetrates into Pliocene-Pleistocene sediments that are filling a wide structural graben. The total length of the sediment core was 545.49 m from an open-marine hemipelagic environment (Comas *et al.,* 1996).

Sediment core MD99-2343 was collected in summer 1999 during LEG 5 of the International Marine Past Global Changes Study program (IMAGES) on board *R/V Marion-Dufresne and* conducted by the French Institute for Polar Research and Technology (IFRTP). This core was retrieved in the Balearic Sea with a calypso piston system obtaining a total length of 32.44 m. It was located NE of Minorca Island, at 40°29.84' N and 04°01.69' E, from a water depth of 2391 m b.s.l. (Fig. 1.6 C). In particular, it was obtained from N-NE Minorca peripheral contourite drift environment. Contourite systems are formed by bottom currents but they also depend of bottom morphology, intensity of currents, Coriolis Effect or even volume of sediment inputs. All contourite systems are characterized by a depression zone with erosive character where currents induce to re-working, transport and classification of sediment particles, and conversely, a sedimentary

drift that reaches high accumulation rates, where potentially continuous and high resolution records could be found. Therefore, these sediment drifts are valuable archives for paleoceanography studies since they could inform about ocean circulation patterns, current velocities and oceanographic processes (Rebesco *et al*., 2014). The Minorca contourite drift was genetically related to the southward flow of the WMDW (Velasco *et al.,* 1996). This current transports and deposits approximately the 10% of continental sediments discharge, mainly inputs from the Ebro and Rhone rivers, in the deep basin (Martin *et al.,* 1989), however the Minorca contourite drift receives sediments by means of deep currents eroding and transporting sediment particles from the drift margins and surrounding basins rather than direct riverine supplies (Frigola *et al.,* 2008). The oligotrophic character of most of the western Mediterranean Sea restricts pelagic carbonate contribution and therefore spillover processes from the nearby Balearic shelf edge should also be considerate as sediment source (Maldonado and Canals, 1982).

2.2 Material description and sampling

2.2.1 Speleothems

In order to perform the geochemical measurements, all speleothems were longitudinally cut with a saw taking into account the morphology and the growth axis. Subsequently they were polished at the lamina prima survey in the University of Barcelona. Among all the collected speleothems, 48 were dated during three research stays at the University of Minnesota. A total of 16 speleothem were selected for further geochemical analyses since they cover the targeted time intervals by the objectives of this study (Annex 1). Among all these speleothems, the description bellow focuses on those included in the discussion section and selected in base to their precise chronology or quality of their geochemical records.

JUD speleothem from *Pot au Feu* cave (Pyrenees) is a 55 cm length stalagmite and it has an internal banded structure formed by white-grey crystalline calcite alternated with brown-orange detrital enriched layers. The identification of some detrital layers and changes in the axial growth direction has allowed identifying three discontinuities (Fig. 2.1). These discontinuities are located at 35, 406 and 448 mm from the top and divide JUD in four growing phases. Such visible discontinuities in speleothems could be associated with changes in the growth rate or even with growth hiatuses which are often related to changes in the cave environment and ultimately to climate variability.

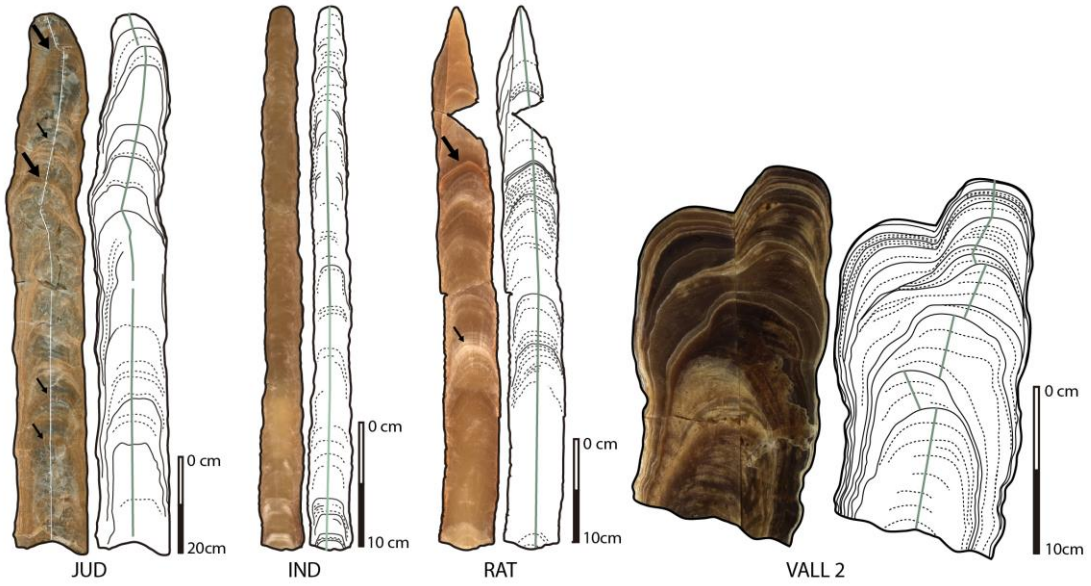

Figure 2.1. Images of JUD, IND, RAT and VALL2 stalagmites and a scheme of the identified layers and direction of the growth axis.

IND speleothem from *Murada* cave (Minorca) is 88 cm length (Fig. 2.1) and presents an internal banded structure with white-grey crystalline calcite. This speleothem does not present irregularities or discontinuities and the growth axis shows a continuous path without any direction change. RAT speleothem is from the same Minorca cave and presents a very similar white-grey crystalline calcite to IND speleothem. It is a 50 cm long speleothem that shows several white layers and shows a prominent orange-brown layer at 14 cm depth from the top. RAT is broken at the top of the speleothem where a 2cm calcite piece was lost.

VALL2 speleothem from *Vallgornera* cave (Mallorca) is a wide dark-brown speleothem of 22 cm long. The colour at the bottom of the speleothem is light brown with a porous texture that towards the top it becomes darker and less porous. The growth axis presents several changes in direction associated to different discontinuities represented by light layers. After the last main discontinuity the speleothem presents two independent growths (Fig. 2.1). The axis selected to accomplish the geochemical analysis has 22 cm length and follows the most developed axis of the last two growths.

2.2.2 Marine sediment cores

Core PP10-17 from the Cantabrian Sea was formed by olive grey silty clay, except for few coarser grained layers which are distinguished by magnetic susceptibility peaks (Brocheray *et al.,* 2014). These sediments present pervasive bioturbation and dynamic sedimentary structures are absent. A completed taxonomic study of ostracods and foraminifers was performed in this sediment core by Rodriguez-Lazaro *et al.,* (2017). Only 5 sections from the completed core sequence were used in this thesis (sections Tr-14 to Tr-18).

The dominant lithology for the ODP 977 Site from the Alboran Sea is olive-grey clay with nannofossil and nannofossil-rich silty clay moderately bioturbated. Several green organic-rich layers (ORLs) are present and characterised by low magnetic susceptibility values (Comas *et al.,* 1996). Carbonate fraction consists of nannofossils (70%), micrite (19%), bio-clasts (6%), and foraminifers (5%). Sedimentary structures are variables along the core from not recognized to cross-laminated structures. The sections used in this thesis were from 3H-5W to 4H-2W. A previous SST record exists for this site but based on alkenone measurements (Martrat *et al*., 2004).

Core MD99-2343 from the Balearic Sea was studied on the lower 11.4 m (section 15 to 22) which were grey silty clay, moderately bioturbated with high presence of coloured layers (greyish orange, yellowish brown, light olive brown and brownish black). Fine levels of pyrite, organic matter, nannofossil shell fragments and foraminifera are also observed throughout this level. This sediment core has been intensely studied for the upper sections corresponding to the last glacial and Holocene periods (Frigola *et al*., 2007 and 2008; Sierro *et al*., 2005) but this is the first study dedicated to the oldest sections.

Every sediment core was first divided in 1 or 1.5m sections and then longitudinally split in two halfs, the working and the archive half. The working sections were sampled into 1 cm thick slides in order to perform destructive analyses. These samples have been studied at different resolution for the three cores depending of their sedimentation rates and sample availability (Table 2). Geochemical analysis in the planktic foraminifera *G. bulloides* were performed in all three cores at different resolutions while the Balearic core (MD99-2343) was also analysed to determine the lithic grain size distribution (Table 2). In addition, the archive sections of this last core were subsampled to perform non-destructive core-scanner X-ray fluorescence analysis in order to determine sediment elemental composition.

Location	Sediment core	Mg/Ca		$\delta^{18}O$		Grain size		XRF
		sample num.	resolution (cm)	sample num.	resolution (cm)	sample num.	resolution (cm)	
Balearic Sea	MD99-2343	116	10	219	5	116	10	YES
Alboran Sea	ODP 977A	163	5	p.p	p.p	n	n	n
Cantabrian Sea	PP10-17	220	2	219	2	n	n	n

Table 2. Summary of the analyses performed in the studied sediment cores indicating its resolution. (p.p: previous published, Martrat *et al*., 2004)(n: none)

The sample treatment previous to the instrumental analysis was the same for the three cores (Fig.2.2). Samples were first frozen and lyophilized to eliminate water content but favouring the sample disintegration. Samples were then introduced into 100 ml vials with distilled water and agitated for 2-6 hours to allow sample suspension. In the case of samples from core MD99-2343 about 0.5 g of bulk sediment sample was reserved for grain size analysis before sample agitation. After agitation, sediment samples were washed over a 63 μm sieve with pressurized distiller water to separate silt and clay from sand fraction and then dried in an oven at 60°C. When samples were dry they were further dry-sieved and reserved the 250-355 μm fraction to examine under the binocular loupe. The foraminifera *G. bulloides* was handpicked with a fine brush in order to be used for geochemical analysis. After this step, the procedures for sample preparation were specific

for each chemical measurement and they are described in next section. It is important to mention that the sample fraction used for the foraminifera picking was kept narrow to obtain a homogenous population. This is relevant since the used specie changes its water depth habitat along its life cycle and this strategy minimize the intraspecific variability of the chemical signal associated to these depth changes. A schematic diagram for the followed sample pre-treatment is shown at Fig. 2.2.

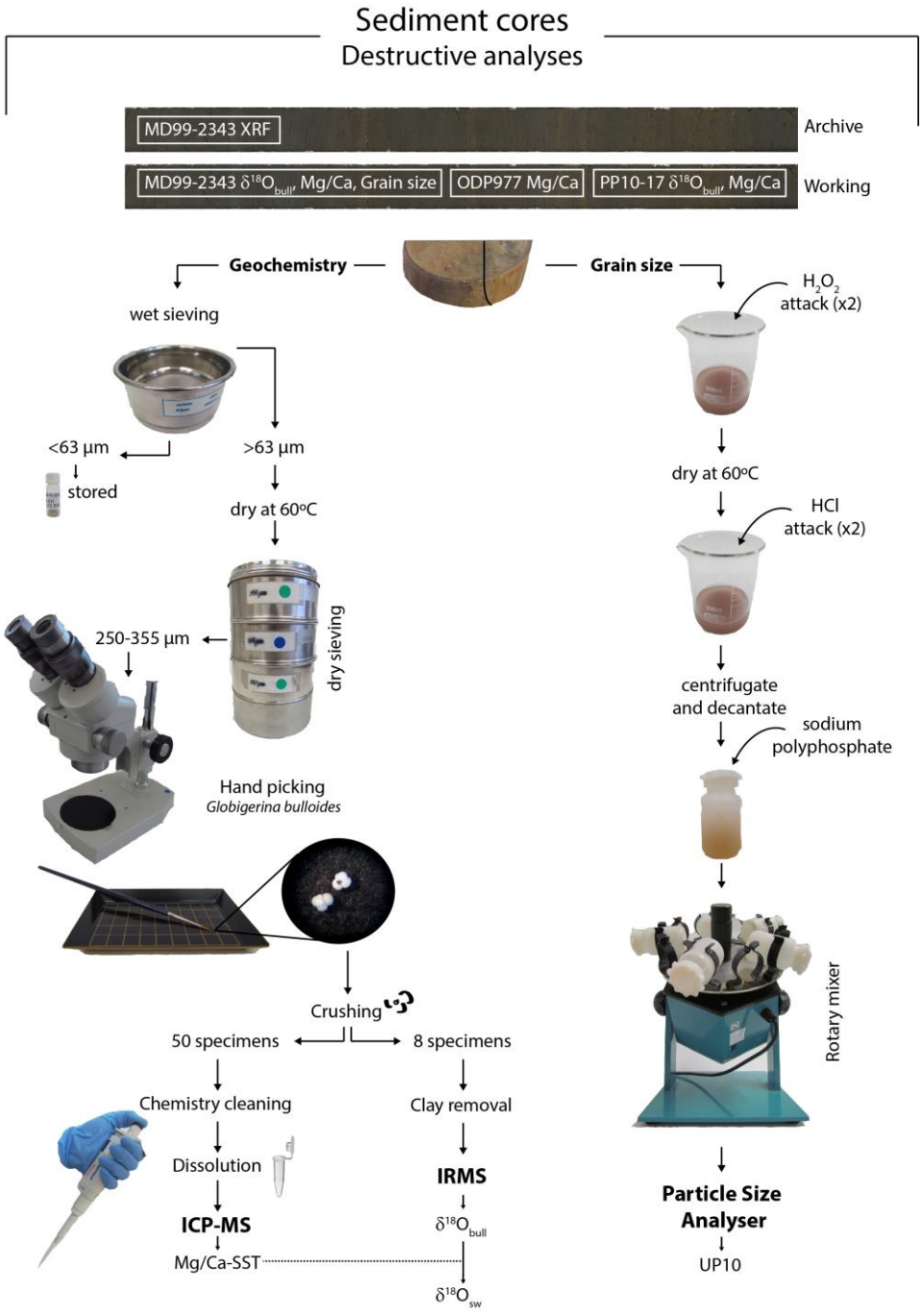

Figure 2.2. Illustration for the followed protocols for the sample treatments previous to instrumental analysis of sediment cores

2.3 Laboratory work

2.3.1 Uranium and thorium on speleothems

A total of 298 samples of speleothems were selected for measuring uranium and thorium isotopes in order to determine their absolute ages. The sampling was designed taking into account the speleothem morphology and its layering in order to detect possible hiatuses and changes in growth rates. A first quick identification of the speleothem age range was performed by analysing samples from the top and the bottom. Accordingly to these preliminary results, the dating effort concentrated on those speleothems more suitable to achieve the objectives of this thesis. Samples for absolute dating were then prepared following the next methodology.

Samples were milled with 2 mm diameter tungsten carbide micro-drill under a laminar air flow cabinet to prevent any contamination. It was obtained about 100-200 mg of carbonate powder for each sample. The chemical procedure was performed into the ultra-clean laboratory at the University of Minnesota and applying the methodology previously described by (Cheng *et al*., 2009; Shen *et al*., 2002) for isolating uranium and thorium elements. The completed protocol can be found at Annex 2. To summarize, sample powders were dissolved in 7N HNO_3 and spiked with an in-house solution with known ^{233}U, ^{236}U and ^{229}Th concentrations. After that, few drops of concentrated $HClO_4$ were added in order to attack and remove organic matter. After one hour refluxing, the samples were completely dried and re-dissolved in 2N HCl. The U and Th were isolated from Ca and several trace elements by means of an iron co-precipitation. Then, 1-2 drops of $FeCl_2$ were added and in order to induce the Fe precipitation together with U and Th several NH_4OH drops are added continuously. After that, samples were centrifuged and rinsed with super-clean water three times while overlying liquid was being removed. In order to separate Fe from U and Th, iron samples were dissolved and loaded in anion exchange resin columns. While Fe was removed with 7N HNO_3, Th was collected with 6N HCl and separated from U, which was recovered ultimately with super-clean water. Finally each pair of samples were dried and dissolved in a low-concentrated nitric acid and analysed by means of multi collector inductively coupled plasma mass spectrometry at the University of Minnesota.

2.3.2 Stable isotopes on speleothems

A total of 926 samples from 15 speleothems were sampled. Around 50 μg of carbonate was drilled along the speleothem growth axis using a 0.5 mm diameter tungsten carbide dental bur in order to determine the stable isotopes (oxygen and carbon). Carbonate powders were introduced in clean vials and analysed by means of isotope ratio mass spectrometry at the scientific and Technological Centres of University of Barcelona (CCiT-UB). Generally, speleothems were firstly analysed at low-resolution and only few speleothems were selected to improve it attending to the quality of their age models for this thesis objective.

2.3.3 Calcium, magnesium and trace elements on speleothems

Around 3 mg of carbonate were drilled with a 0.5 mm diameter tungsten carbide dental bur generally on same centimetres as isotopes analyses. A total of 930 measurements were carried out from 11 speleothems. Carbonate powder was directly introduced in clean vials, dissolved with 3 ml of ultra-pure 2% HNO_3 and centrifuged in order to prevent possible detritic particles or impurities in the solution before the analyses. All the samples were analysed by means of inductively coupled plasma mass spectrometry at the CCiT-UB.

2.3.4 Oxygen isotopes in foraminifera

Stable isotopes on planktic foraminifer were performed on about 8 specimens of handpicked *G. bulloides*. A total of 219 samples for the MD99-2343 and the PP10-17 cores were obtained, while the ODP Site 977A data belongs to a previous study (Martrat *et al.,* 2004). Shells were crushed between two glass plates to open the chambers and favour clay removal and then cleaned in methanol. After few seconds of sonication, the supernatant solution was removed with a micropipette and samples dried (Fig. 2.2), the detailed protocol is provided at Annex 3. The measurements were accomplished by an isotope ratio mass spectrometry at the CCiT-UB.

2.3.5 Calcium, magnesium and trace elements in foraminifera

A total of 216, 116 and 163 samples were selected for cores PP10-17 (2 cm resolution), MD99-2343 (10 cm resolution) and ODP Site 977 (5 cm resolution). The elementary analysis were performed using 40-50 specimens of *G. bulloides* handpicked from a size range of 250-355 μm and carefully crushed in order to open the chambers to

favour contamination removal (Fig. 2.2). Samples were cleaned by means of a full chemical cleaning procedure based on the last modifications on trace elements cleaning protocols developed by Barker *et al.,* (2003) and Pena *et al.,* (2005). The detailed protocol can be seen in the Annex 4, and it consist on four main steps. The first step is designed to remove clay minerals and consists on several rinses with ultrapure water and methanol. The second step uses a reductive reagent attack to remove potential Mn-Fe oxide contaminant phases. After that, the third step is a further attack but with an oxidative solution of NaOH and H_2O_2 to promote the removal of organic matter. The last step is a weak acid leaching to eliminate potential secondary carbonates adhered on the carbonate shells. The reductive attack step was only performed on ODP Site 977A since a preliminary test indicated that these samples could have potential contamination problems associated to high manganese values, a problem which was not detected in the other cores. Before the analysis, all samples were dissolved with 3 ml of ultra-pure 1 % HNO_3, centrifuged to avoid possible remained solid particles and transferred into clean vials. Additionally, in order to monitor the any potential contamination during the laboratory procedure, chemistry blanks were performed on random days. All the samples were analysed with an inductively coupled plasma mass spectrometry at the CCiT-UB.

2.3.6 Sediment grain-size distribution

The grain-size distribution of terrigenous-sourced particles was measured only on the Balearic sediment core (MD99-2343), expanding the previous available record of Frigola *et al*. (2007) and according to the same methodology (Fig. 2.2). Previous to the instrumental measurements, organic matter was attacked twice by adding 50 ml of 10 % H_2O_2 during 24 h in order to avoid aggregated particles which can distort the measurements. Once the samples were dried in an oven (60°C) they were attacked with 50 ml of HCl 1 M for 12 h to remove carbonate shells fragments. The exceeding HCl solution was removed after samples were centrifuged. Then, in order to avoid clay flocculation, the samples were treated with 30-40 ml of a dispersant solution of sodium polyphosphate and agitated during few hours before they were analysed (detailed protocol at Annex 5). A total of 116 measurements from the Balearic sediment core (MD99-2343) have been measured at 10 cm resolution with a Coulter LS 230 Laser Particle Size Analyser at the Sedimentology Laboratory of the University of Barcelona.

2.3.7 Elemental composition of sediments

Variations in elemental composition of sediments were determined only in the Balearic sediment core at 10 mm resolution. Analyses were performed on the surface of the split archive core sections that were previously smoothed carefully with a glass plate to remove any irregularities and roughness. Sediment surface was covered with a 4 μm-thick Ultralene film with the aim of 1) eliminating air presence between sediment and the analyser prism, 2) prevents possible contamination and 3) avoid desiccation of sediments (Richter *et al.,* 2006; Tjallingii *et al.,* 2007). Following, the split core was introduced into an Avaatech III Core Scanner system (Serial No. 21) at the CORELAB laboratory of the University of Barcelona in order to perform high quality photographs and the elemental measurements of the sediments by means of X-Ray Fluorescence analysis.

2.4 Analitical tecniques

2.4.1 Mass spectrometry

There are several varieties of mass spectrometers and all of them are stablished on the same bases, ionization of the samples and selection according to the mass/charge ratio before the measurement in the detector. In this study, three different varieties of mass spectrometers have been used due to important differences among the specific techniques. The Isotope-Ratio Mass Spectrometry (IRMS) was used to measure stable isotope ratios, the Inductively Coupled Plasma Mass Spectrometry (ICP-MS) for elementary ratios and, the Multi-Collector Inductively Coupled Plasma Mass Spectrometry (MC-ICP-MS) to measure the radiogenic U and Th isotopes.

Inductively Coupled Plasma- Mass Spectrometry

Calcium, magnesium and trace elements from both marine cores and speleothems were analysed with a Inductively Coupled Plasma Mass Spectrometer (ICP-MS), Perkin-Elmer Elan-6000 model at the CCiT-UB (Fig 2.3). Measurements are performed throughout different steps. The first one is the introduction of the sample into the mass spectrometer. Dissolved samples are pumped into the introduction system, which contains the spray chamber and the nebulizer that converts the sample into an aerosol. In the second step, the aerosol finds a high temperature plasma of argon that dry and vaporize the sample generating posetively charged ions. Then, a representative number of excited ions are transported through two cones and the ion optics system, at vacuum conditions, in order to focusing them into the mass separation device, where the ions are separated according to their mass-to-charge ratio by the mass analyzer. Generally the ICP-MS uses a standard quadrupole mass analyzer. Employing specific selected currents and radio frequency fields the ions of a selected mass are allowed to pass through the mass analyzer while the other ions are repeled. Finally the selected ions achive the detector where they are converted to an electronic signal. This selective process through the mass analyzer is repeated using diferent configurations until all the desired elements have been measured in the ICP-MS.

Possible contamination was controlled by means of chemistry blanks analyses in random days. An in-house high purity standard solution was measured routinely every four samples to control the accuracy. According to the in-house standard analysis the external reproducibility (%, 2-sigma) obtained for the speleothem analyses was 11.01% for IND , 2.39 % for JUD , 0.86% for RAT and as much 0.66% for all the other ones. The external reproducibility for the sediment cores was 6.59 % for core PP10-17, 5.7 % for

ODP Site 977A and 3.21 % for MD99-2343. All samples were corrected using a sample-standard bracketing method (SSB) in order to correct the analytical drift. Moreover, an internal rhodium standard was also added into each sample to control the analytical sensibility loss of the spectrometer due to cone clogging.

Concentrations of Sr, Cd and Ba in this study speleothems were too low for satisfactory quantification, hence they are not used in this study and the discussion will be focused in the Mg and Ca fluctuations along the speleothem.

Multi-Collector Inductively Coupled Plasma Mass Spectrometry

The radiogenic isotopes of U and Th for speleothem dating were analysed using the parallel ion-counting Multi Collector Inductively Coupled Plasma Mass Spectrometry (MC-ICP-MS) with a *Finnigan Neptune* model at the University of Minnesota. Several blanks were performed routinely for each laboratory set.

This instrument allows low detection limits, acquiring an exceptional accuracy and sensitivity in detect low abundant isotopes in nature. The introduction system is the same used for ICP-MS although in this case is previously used an Aridus II desolvating nebulizer that allow reducing the solvent-based interferences such as oxides and hydrides. After vaporize the sample into the argon plasma the ions are transported into the mass analyzer like in the ICP-MS. However the MC-ICP-MS use a retarding potential quadrupole that improves abundance sensitivity by an order of magnitude, to accurate the quantification of minor isotopes. The ions selected and classified according to their mass-to-charge finally reache the detector. In this case, the system is equipped with a multicollector detector array allowing multiple measurements at the same time. Moreover, the MC-ICP-MS also has a flexible system that permits switches between detector systems (Faraday cup to SEM ion counter) providing low and high isotopes concentrations measurements at the same time with the same instument.

Isotope-Ratio Mass Spectrometry

The stable isotopes measurements in both marine cores and speleothems were accomplished on a Finnigan-MAT 252 mass spectrometer at CCiT-UB (Fig 2.3). This mass spectrometer is coupled in a single acid bath CarboKiel-III carbonate preparation device in order to convert solid carbonate samples in simple gas (CO_2) before entering into the ion source of the IRMS. Therefore the stable isotope measurements were performed from gas source, in contrast to the radiogenic isotope measurements which are performed by ionization of a liquid source. An isotopically representative amount of gas is ionized afterwards via electron impact in the ion source. The ion stream is then accelerated and

separated in the analyzer by a magnetic field according to their mass-to-charge ratio. Hence, the IRMS mass analyzer is provided by a magnetic device instead of the quadrupole for ICP-MS. Light and heavy ions can be classified due to they are bended at different radius along a circular path by the magnetic field. After the ion separation, the current of each ion beam is detected by the Faraday cups. Ions hit the cups, where the transference of their electric charge into an electric current is finally converted to a digital signal. The IRMS allows detecting two ionic beams at the same. Therefore, it directly determines isotope ratios with great precision and accuracy in contrast to the ICP-MS which acquire absolute isotope values.

Analytical uncertainties were obtained by means of two in-house carbonate standards that were calibrated to NBS-19 international standard (Coplen, 1996). The uncertainties were ≤ 0.04 ‰ VPDB for $\delta^{13}C$ and 0.08 ‰ VPDB for $\delta^{18}O$.

2.4.2 Particle Size Analyser

Measurements of particles size distribution on sediment core MD99-2343 were performed with a Coulter LS 230 Laser Particle Size Analyser at the Sedimentology Laboratory of the University of Barcelona (Fig 2.3). This technique measures the diffraction angle of a laser beam when impacts with sample particles. The Coulter LS 230 analyser can detect particles from 0.4 μm to 2000 μm. It is composed by two bench top systems: 1) the fluid module and 2) the optical module. The fluid module allows introducing samples suspended in a liquid that together with a sonicator device helps to disperse sample particles. Particles circulate at variable speed through a sample cell untill the optical module. In the optical module there are a light source, lenses and a diffraction detector assembly containing a photodetector array. The laser, that it is a monochromatic light beam, reaches the suspended particles and is diffracted in different degrees according to the grain size of each particle as outlined in the Fraunhofer theory (Hodkinson, J., 1966). The lens set concentrates the diffracted beams towards the detectors. High particles supply low diffracted degree and then, high light intensity arrives at the detectors and vice versa for small particles. This measurement, performed during several seconds, allow finally obtain the amount of different particle sizes in percentage of volume and therefore the grain size distribution for each sample.

The precision and accuracy were tested performing several control runs using the LS size control G15, which gave a coefficient of variation of 0.03%.

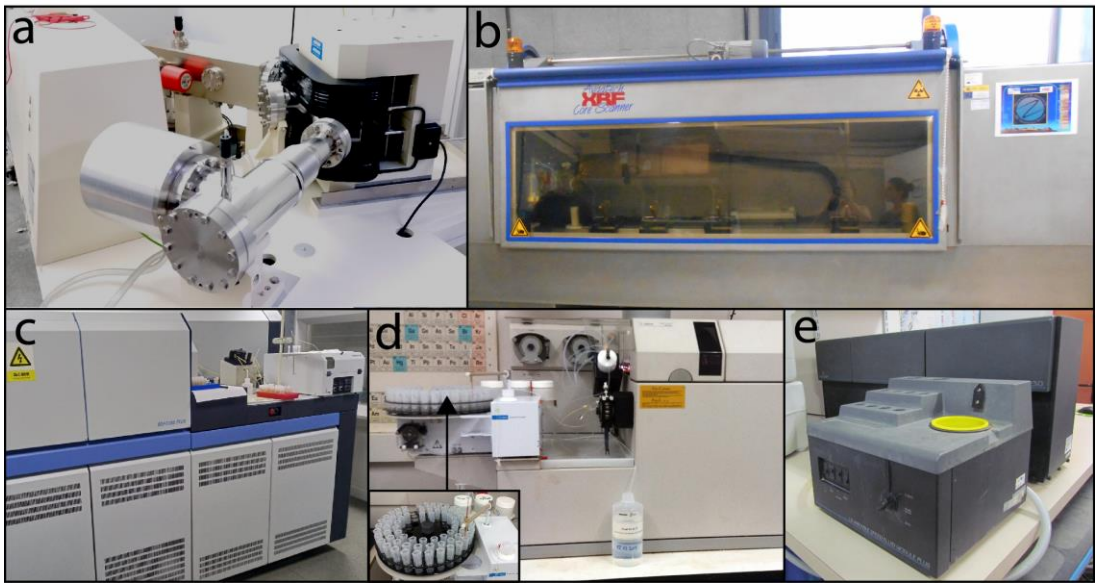

Figure 2.3. Images of the used instruments in this study. A) IRMS, Finnigan-MAT 252. B) Avaatech III Core Scanner system (picture courtesy of A. Baza). C) MC-ICP-MS, Finnigan Neptune (picture courtesy of C. Pérez). D) ICP-MS, Perkin-Elmer Elan-6000. E) Coulter LS 230 Laser Particle Size Analyser.

2.4.3 XRF-Core Scanner

Measurements of the sediment elemental composition of the Balearic core (MD99-2343) were performed by X-Ray Fluorescence analysis using an Avaatech III Core Scanner system (Serial No. 21) at the CoreLab in the Geoscience Faculty of the University of Barcelona (Fig. 2.3). Although the first X-Ray fluorescence logging was developed at 1988 the Avaatech generation of XRF-core scanners has been operating since 2002 (Jansen *et al*., 1998; Richter *et al*., 2006). This method is advantageous over discrete conventional geochemical methods because it allows rapid, non-destructive and high-resolution analysis (10 mm in this study) of long sediment sequences (Richter *et al.,* 2006; Rothwell and Rack, 2006). Also provides us a large range of elements to be analysed (Al-U atomic weight range) by qualitative approach.

The scanning took place directly at the split core surface which is completely introduced into the scanner. The entire circuit is filled with helium in order to remove air absorption. When the prism rests on the sediment, the X-ray tube generates incoming radiation over a 1.2cm^2 area. Hence, atoms of different chemical elements from the sediments are ionized. During ionization, one or more electrons bombarded with the X-Ray are excited and ejected from the inner orbitals of the atom generating electronic structure instability. The resulting vacancy is afterwards replaced by electrons falling back from outer orbitals, releasing energy in form of photons (X-Ray fluorescence, Potts and Webb, 1992). This secondary radiation emitted is characteristic according to the distance

between orbitals for each atom existing in the sediment and therefore different for each chemical element. Finally the detector measures the intensity of the emitted radiation. The wavelength is characteristic for each element and the amplitudes of the XRF-peaks are proportional to the concentration, allowing thus determining the elementary composition when data is adjusted with a calibration line (Rothwell, 2006). Several elements were measured in three separate runs with different excitation conditions in order to improve the sensitivity of the scanner. The excitations conditions and the elements measured for each run were:

1) Conditions: voltages of 10 KV, currents of 0.5 mA and excitation times of 10s. Elements: Al, Si, P, S, Cl, K, Ca, Sc, Ti, V, Cr, Mn, Fe
2) Conditions: voltages of 30 KV (Pd-thick filter), currents of 2.0 mA and excitation times of 25s. Elements: : Ni, Cu, Zn, Br, Rb, Sr, Y, Zr, Mo, Pb
3) Conditions: voltages of 50 kV (Cu filter), currents of 2.0 mA, and excitation times of 35s. Elements: Ag, Cd, Sn, Te, I, Ba

This procedure was repeated along the entire sediment core and finally the element intensities were obtained by post-processing of the of X-ray spectra by Iterative Least square software (WIN AXIL) package from Canberra Eurisys. Therefore the relative elemental composition variability along the sediment cores can be known although preventing direct concentration correspondence.

Furthermore, with a spectrophotometer mounted into the Avaatech III Core Scanner system also has been performed colour reflectance analysis. The colour spectrum for each measurement was recorded using three axis parameters: the lightness (L*), the red to green axis (a*) and the yellow to blue axis (b*). In parallel to this measurements high resolution photographs of the sediment core MD99-2343 and all the speleothems were performed.

2.5 Proxy calculations and basis for their interpretation

2.5.1 Radiogenic isotopes: $^{230}Th/^{234}U$ ages

Isotopes are varieties of a given chemical element with different number of neutrons in their nucleus and thus different atomic mass number. Isotopes can be stables (e.g ^{18}O and ^{13}C) or radiogenic (e.g. ^{234}U and ^{230}Th), these last ones associated to radioactive decay processes. Radiogenic isotopes become an excellent radiometric dating tool due to the isotopic composition of a sample evolve along time by radioactive decay. In speleothems science the uranium-thorium disequilibrium dating is the most appropriated tool allowing determining the timing and duration of geological events with a method limit of approximately 600 kyr (Edwards *et al*., 1987). Generally, radiogenic isotopes are reported relative to that of a stable, non-radiogenic isotope of the same element as isotope ratios. Despite that, in the case of the U-series decay, isotope ratios are usually expressed relative to the ^{238}U, because it is assumed that it is constant along time due to their relative long half-live ($4.47x10^6$ kyr). Currently, variations in the abundance of these radiogenic isotopes ratios are measured directly by isotope ratio mass spectrometry although the first efforts in radiometric dating for speleothem dating were performed by alpha-spectrometry which was progressively replaced by TIMS, improving the U-series dating, reducing the amount of sample necessary to perform the analyses and highly improving the precision (Edwards *et al*., 1987). After that, TIMS was substituted by MC-ICP-MS technique, decreasing even more the sample amount and wastage, reducing also the analysis time, simplifying chemistry procedures and allowing further reliable dates (Cheng *et al*., 2013; Hellstrom *et al*., 2003). Since then U-Th dating by MC-ICP-MS is the most widely used technique for speleothems radiometric dating.

The U-Th dating method is based in the high contrast in the solubility of the uranium and thorium in water. Uranium is transported via groundwater until the speleothem, where it is incorporated in the carbonate, whereas there is no transport of thorium according to its very low solubility. Assuming a closed system, uranium radioactively decays after the speleothem calcite precipitation to thorium, from the parent isotope (^{238}U), abundant in nature, to their daughter isotopes (^{243}U and ^{230}Th). The ^{238}U decay serie is shown in Fig. 2.4 with the half-life times for interesting radiogenic isotopes used in the age calculation (Edwards *et al*., 1987 and 2003, Cheng *et al.*, 2006 and 2000).

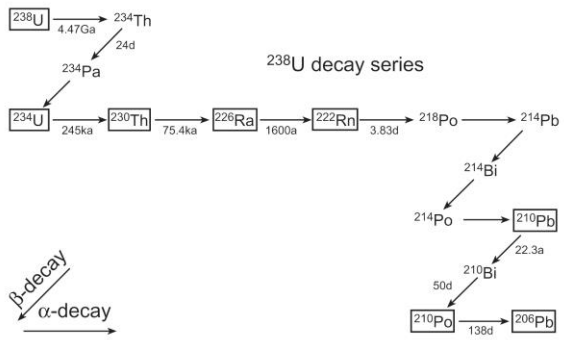

Figure 2.4. Principal decay series for uranium and thorium nuclides. (source: Fairchild and Baker 2012)

Due to faster decay of the ^{234}U respect to the ^{238}U, the initial $^{234}U/^{238}U$ ratio from the speleothem progressively falls over time and consequently the $^{230}Th/^{238}U$ increases (Fig 2.5 a). The relationship of both activity ratios allow to achieve the time elapsed by means of the standard $^{230}Th/^{238}U$ age equation (Fig. 2.5 b) from Kaufman and Broecker (1965) and Edwards *et al*., (1987). The activity between parents and daughters get closer along time, consequently the precision of the method very rapidly deteriorates beyond 400 kyr and finally the secular equilibrium is reached indicating the limit of the method (Fig. 2.5 a).

a)

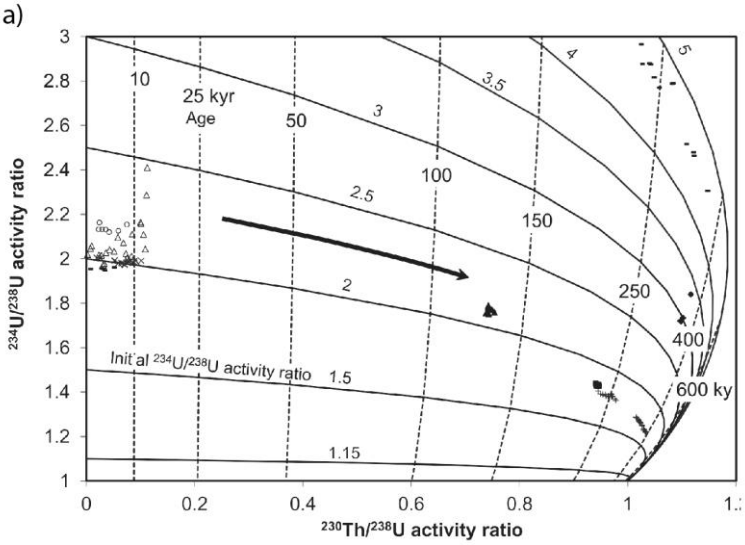

b)

$$\left(\frac{^{230}\mathrm{Th}}{^{238}\mathrm{U}}\right)_A = 1 - e^{-\lambda_{230}T} + \left(\frac{\delta^{234}\mathrm{U}(T)}{1000}\right)\left(\frac{\lambda_{230}}{\lambda_{230}-\lambda_{234}}\right)\left(1 - e^{(\lambda_{234}-\lambda_{230})T}\right)$$

where:

$$\delta^{234}\mathrm{U}(T) = \delta^{234}\mathrm{U}(0)e^{-\lambda_{234}T}$$

$$\delta^{234}\mathrm{U} = 1000*[(^{234}\mathrm{U}/^{238}\mathrm{U})_m/(^{234}\mathrm{U}/^{238}\mathrm{U})_{eq} - 1]$$

mass ratio measured at sample / mass ratio at secular equilibrium

Figure 2.5. a) Principles of U-Th disequilibrium calculated from the decay equation. For a given speleothem sample, the initial calcite $^{234}U/^{238}U$ ratio (y-axis) starts to evolve following the black arrow direction over time. Consequently, the $^{230}Th/^{238}U$ ratio increases. Measuring both ratios and using the age equation (b) the final age of the speleothem sample is known. Several measured ratios of Sanbao cave samples from Cheng *et al*., (2009), are plotted as example. The ultimate end-point is secular equilibrium, when both ratios are one. (Source: Fairchild and Baker, 2012). b) Decay equation developed by Kaufman and Broecker (1965) and Edwards *et al*., (1987).

The major source of uncertainty in the U-Th ages is due to speleothems remain susceptible to incorporate detrital transported ^{230}Th within fine sediments. This detrital ^{230}Th is always accompanied by higher amount of ^{232}Th and therefore with an initial activity ratio ($^{230}Th/^{232}Th$) that it is variable depending on the bed-rock and soil characteristic (Drysdale *et al*., 2006; Hellstrom *et al.*, 2006). In order to distinguish between ^{230}Th detrital and those from the U-decay and not overestimate U-Th dates, ^{230}Th corrections must be performed for speleothems containing ^{232}Th (Hellstrom *et al.*, 2006).

Summarizing, three requirements are important in order to obtain absolute radiometric dates:

1) Enough amount of initial ^{238}U in the samples to perform the analysis.
2) A closed system since the carbonate precipitation formation.
3) Insignificant or known amount of detrital ^{230}Th at the formation time.

Synthetic isotopes (^{233}U, ^{236}U and ^{229}Th) are incorporated into the samples (spike), before the chemistry in order to control lost sample and fractionation processes during the chemistry procedure and also as a reference for the measurements. All this synthetics isotopes and also the natural ones (^{238}U, ^{235}U, ^{234}U and ^{230}Th and ^{232}Th) were measured in order to determine the $^{234}U/^{238}U$, the $^{230}Th/^{238}U$ and the $^{230}Th/^{232}Th$ radiogenic ratios necessary to calculate the age of each sample.

Thus, the $^{230}Th/^{234}U$ absolute ages were used for the construction of age-depth model, which is fundamental to frame in a time scale the generated geochemical proxy records. In the elaboration of speleothem age-depth models often are applied Bayesian approaches that are believed to be more reliable than simple linear interpolation methods (Breitenbach *et al*., 2012; Ramsey, 2008; Scholz *et al.,* 2012). Here the age modelling was determined by StalAge packaging software (Scholz and Hoffmann, 2011) in all the speleothems except TER speleothem whose chronology was estimated by linear interpolation due to the few available dates in this case.

2.5.2 The δ notation on stable isotopes

Stable isotopes can be classified as lighter or heavier depending on their mass number. For example, there are three stable isotopes of oxygen (^{16}O, ^{17}O, and ^{18}O), and two of carbon (^{12}C and ^{13}C) with the lighters ones occurring most abundant (Table 2.1). Although they still have the same number of protons and electrons and thus the same electronic configuration, isotopes differ in the number of neutrons. Due to these atomic differences, the physicochemical properties among isotopic spices of the same chemical

element are slightly different. In consequence, during chemical reactions, these different characters can generate isotopic effects.

Element	Isotope	Abundance (%)	Ratio measured	Reference standard
Carbon	^{12}C	98.89	$^{13}C/^{12}C$	VPDB
	^{13}C	1.11		
Oxigen	^{16}O	99.763	$^{18}O/^{16}O$	SMOW / VPDB
	^{17}O	0.0375		
	^{18}O	0.1995		

Table 2.1. Information on the measured stable isotopes. Natural isotopes abundances, and most standard ratios used.

For example, during water evaporation, the light oxygen isotope (^{16}O) is more prompt to evaporate. Therefore, the amount of isotopic species for each chemical element in a given substances or compounds is usually different. Consequently, substances or compounds have a specific relation according to the abundance of each isotope, generally expressed as the ratio between the heaviest and the lightest isotope (e.g. $^{18}O/^{16}O$). During a given reaction, the isotopic behaviour can produce preferential distribution of isotopes by isotopic exchange between two compounds or phases of substances, changing its isotopic ratio and generating the so-called isotopic fractionation.

The fractionation factor is described as:

$$\alpha_{A/B=} R_A/R_B$$

Where:

R_A= isotopic ratio of compound A

R_B= Isotopic ratio of compound B

Due to the fractionation factor is always close to one with a small positive or negative deviation, the isotopic fractionation is usually expressed in units per mil (‰):

$$\varepsilon(‰)= (\alpha\text{-}1)10^3$$

The absolute abundance of stable isotopes is difficult to achieve with enough accuracy, in contrast, the relative differences between two samples can be measured with high precision. Due to the interest in geoscience research is focused in the relative changes rather than absolute values, the isotope ratio of an unknown sample is compared with the

known ratio of a standard substance and thus the isotopic fractionation is expressed in terms of delta values (δ).

$$\delta_{(‰)} = ((R_{sample}/R_{standard}) - 1) \times 10^3 = \frac{(R_{sample} - R_{standard})}{R_{standard}} \times 10^3$$

As the δ value informs us about the difference between the sample and the standard, they can be either positive or negative, depending if the sample ratio is higher or lower than that of the standard substance. Consequently, a positive δ values means that the measured sample is enriched in the heavy isotope respect to the standard (higher isotopic ratio). While a negative δ values means that the measured sample is depleted in the heavy isotope respect to the standard (lower isotopic ratio).

There are several different standards. The VSMOW (Vienna standard Mean Oceanic Water) is used in water analyses while the VPDB (Vienna Pee Dee Belemnite) is used for carbonates. Usually, stable isotope laboratories routinely use in-house standards which are already calibrated to the homologated standards (NBS 19, NBS 18 used in this study).

2.5.3 $\delta^{18}O$ and $\delta^{13}C$ on speleothems

Several processes control the geochemistry signal in speleothems, starting from the early step when water is evaporating from oceans, until the calcite precipitates as speleothem forms inside caves. Thus, several processes along the water and carbon cycles can induce oxygen or carbon isotopic fractionation which ultimately would influence the speleothem isotope signal and complicates the interpretation of past hydrological and climate changes (Fairchild and McMillan, 2007; Fairchild and Treble, 2009; Mc Dermont, 2004; Wong and Breecker, 2015).

The speleothem science during the late 20th century focussed the $\delta^{18}O$ speleothem interpretation as cave temperature proxy since temperature control on oxygen fractionation is relevant when the system remains in isotopic equilibrium (Hendy and Wilson, 1968; Tremaine *et al*., 2011). But more recent studies have recognized the relevance of changes in cave $\delta^{18}O$ drip-waters ($\delta^{18}O_{dw}$) which often are larger than cave temperature changes (McDermott, 2004). Calcite is often deposited out of isotopic equilibrium, although very close, maintaining changes in the $\delta^{18}O_{dw}$ despite a further temperature dependence fractionation can occur within the cave. In turns, the $\delta^{18}O_{dw}$ reflects the $\delta^{18}O$ of precipitation ($\delta^{18}O_p$) and other fractionation processes that can occur into the soil and the karst system (McDermott, 2004). During evaporation, lighter isotopes

are preferentially incorporated into the vapour due to lower atomic mass. On the contrary, during condensation, heavy isotopes are preferentially incorporated to the liquid state. Consequently, $\delta^{18}O_p$ will be lighter respect to the ocean and even more after precipitation (Lachinet, 2009). Evaporation processes occurs all through the hydrological cycle; in oceans, atmosphere, at soil zones, vadose zones and also inside caves (Fig. 2.6).

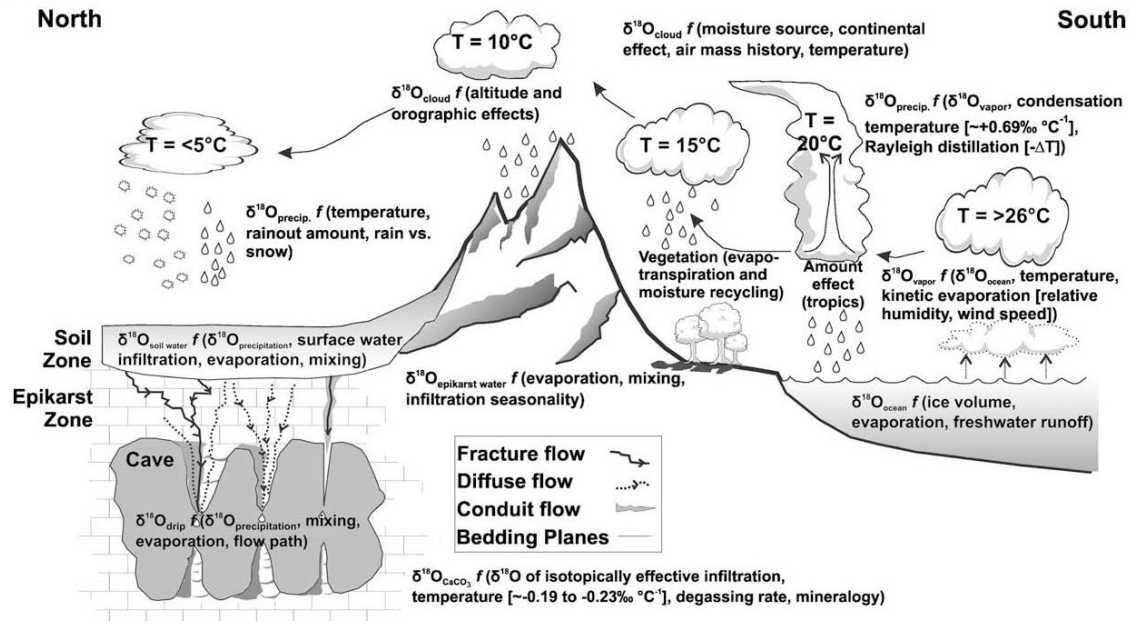

Figure 2.6. Primary processes related to $\delta^{18}O$ variations in cave speleothems. Relative humidity changes and temperature-related processes, such as phase changes, occur all through the hydrosphere, the atmosphere, the soil and epikarst zones which control $\delta^{18}O$ variations. (Source: Lachinet *et al*., 2009)

Repeated evaporation-condensation processes combined with temperature changes along the rainfall path produce the so-called Rayleigh distillation (Clark and Fritz 1997), which not only affects the $\delta^{18}O_p$ but also the isotopic composition of the sea waters ($\delta^{18}O_{sw}$). At glacial-interglacial time-scale, the dimensions of the continental ice sheets controlled the accumulation of light isotopes previously evaporated from the ocean and thus the global $\delta^{18}O_{sw}$ signal during glacial periods was enriched. This influence in the isotopic records is the so-called "ice volume effect" (Genty *et al*., 2003; Lachinet, 2009). Two additional effects related to evaporation-temperature processes affect the $\delta^{18}O_p$ signal: the "source effect" that reflects regional $\delta^{18}O_{sw}$ differences from the oceanic moisture origin (Bar-Matthews *et al*., 1999; Rozanski *et al*., 1993), and the "amount effect", especially in tropical regions, where the large precipitation amounts associated with monsoon dynamics strongly decreases the $\delta^{18}O_p$ signal (Cai *et al*., 2012; Cheng *et al.,* 2009; Rozanski et al., 1993). Likewise, other evaporative fractionation processes have also been reported for clouds dynamics (Araguás-Araguás *et al.,* 2000), by the atmospheric addition

to recycled humidity over continents (Koster *et al*., 1993; Krklec and Domínguez-Villar 2014), in the soil wherein infiltrated water becomes ^{18}O-enriched with increased dryness (Ayalon *et al.*, 1998; Clark and Fritz 1997; Gazis and Feng, 2004; Tang and Feng, 2001), or even in drip-waters when cave air allows humidity uptake (Feng *et al*., 2012). There are several other effects related with the Rayleigh distillation that also induce isotopic fractionation as: cave latitude and altitude, the continental character or distance from sea and air temperature when precipitation forms (Boch *et al*., 2011; Moseley *et al.,* 2014; Rozanski *et al*., 1982, 1993). These factors are considered to be dominant modulating the $\delta^{18}O_p$ signal in mid-latitude areas and thus the speleothem $\delta^{18}O$ reflect a mixture of ocean water source ($\delta^{18}O_{sw}$), the atmospheric air temperature and the rainfall patterns (Fairchild *et al.,* 2006 and 2007; McDermott *et al*., 2001; McDermott, 2004; Lachniet 2009; Rozanski *et al*., 1993; Wang *et al*., 2001).

Once rain-water enters into the karst system, other isotopic fractionation processes could change the original $\delta^{18}O_p$, thus affecting the $\delta^{18}O_{dw}$ signal; the amount of water infiltrating into the karst, seepage or fracture flows, mixture of different ground waters or the water-rock interaction (Hendy 1971; Cobb *et al*., 2007; Lachinet 2009; Mattey *et al*., 2008). Furthermore changes into the pCO_2 inside cave, changes in the drip rate, the speleothem growth rate, carbonate mineralogy and kinetic effects could also induce further fractionation at the moment of calcite precipitation, affecting another time the isotopic signature when is transmitted from $\delta^{18}O_{dw}$ to the speleothem $\delta^{18}O$ (Baldini *et al*., 2006; Sharp, 2007; Spötl *et al.*, 2005; Stoll *et al*., 2015).

Therefore in most cases, the $\delta^{18}O$ signal in speleothems is too complex to be ascribed to one simple fractionation process and thus it is necessary to recognize the site-specific characteristics in order to correctly interpret the speleothem $\delta^{18}O$ fluctuations at different time scales; seasonal, millennial or orbital scales. In this regard, this study discusses the interpretation of the obtained speleothems $\delta^{18}O$ records in a dedicated part (Section 4.1 and 4.2).

On the other hand, the speleothem $\delta^{13}C$ proxy is also a useful tool to reconstruct climate-driven changes. The carbon cycle adds several fractionation processes that also need to be considered with attention (Mc Dermont, 2004). There are different possible sources for speleothem carbon, the host carbonate rock and the soil CO_2, which in turn, consists in a mixing of the atmospheric CO_2 and biogenic CO_2, (Hellstrom *et al*., 1998, Genty *et al*., 2001). During percolation the seepage water is in continuous equilibration with the soil CO_2 (mostly biogenic) but in closed systems also from the carbonate bed-

rocks (McDermott *et al.,* 2006). The inorganic carbon contribution from the bed-rock would result in elevated $\delta^{13}C$ value in the drip water, while the soil/biogenic carbon source in lower $\delta^{13}C$ values (Breecker *et al*., 2012; Wong and Breecker, 2015). However, it was reported that the relationship between biogenic and inorganic source is 9:1 in temperate areas (Genty *et al*., 2001). Due to most natural systems are partially open and assuming that the bed-rock source is limited and do not changes along time, the $\delta^{13}C$ of the dissolved carbon in drip waters closely reflects changes in soil CO_2 mostly from the biogenic source. The type of vegetation C3/C4 plants (Dorale *et al.,* 1992; Genty *et al*., 2003 and 2006) and the intensity of vegetation activity above the cave site (Baldini 2006; Gently *et al*., 2001, 2003; Moreno *et al*., 2010) would be the two main biogenic processes affecting the $\delta^{13}C$ of the soil CO_2. Due to temperate regions are dominated by C3-vegetation, and there is no changes between C3 and C4 plants, the vegetal root respiration and microbial activities mainly control the $\delta^{13}C$ changes into the soil. Less biogenic CO_2 production due to reductions in the biological activity increases the relative proportion of atmospheric CO_2, leading to higher δ13C values. On the contrary, enhanced vegetation activity due to more plant root respiration and microbial activity let lighter soil $\delta^{13}C$. Additional effects on $\delta^{13}C$ changes of the biogenic CO_2 are related to photosynthetic discrimination in C3 plants (Schubert and Jahren, 2012) and atmospheric pCO_2 changes, such as happened during glacial-interglacial or stadial-interstadial transitions (Wong and Breeker, 2015). Therefore, variations in the soil CO_2 productivity, and consequently in the $\delta^{13}C$ signal of the dissolved carbon in drip waters, is ultimately influenced by climate-driven changes. By changes in temperature and water availability which hardly controls the vegetation activity (Fairchild and Baker 2012), as well as atmospheric CO_2 isotopic composition changes at different time scales (Baker *et al.,* 1997; Genty *et al.,* 2003).

As in the case of the $\delta^{18}O_{dw}$, some kinetic effects can affect the isotopic composition of the dissolved carbon of drip-waters (Richards and Dorale 2003; Fairchild and McMillan, 2007). The CO_2 degassing from seepage waters through the karst leads to $CaCO_3$ supersaturated waters than induce calcite precipitation. The isotopically light carbon (^{12}C) is removed from the drip-waters during degassing, hence enriching the residual water solution in ^{13}C (Dulinski and Rozanski 1990; Hendy 1971; Mickler *et al*., 2006; Spötl *et al*., 2005). When this isotopic fractionation processes occur along the hydrological flow-path before the speleothem formation is called the prior calcite precipitation effect (PCP). PCP is related with changes in the pCO_2 and the water availability (Fairchild and McMillan 2007) and it could control the speleothem $\delta^{13}C$ signal. Generally, less infiltration and long water resident times influence the extent of PCP (Wong and Barnner 2010, McDonal *et al*., 2007).

Overall, temporal changes in speleothem $\delta^{13}C$ can offer a potential tool to reconstruct past climate conditions when assuming that dry/cold conditions drive to less water availability, less vegetal activity and enhanced PCP. However distinguish among temperature, precipitation or PCP effect is far from being a simple issue. For that reason should be appropriated to interpret the isotopic signal in parallel to trace elements ratios in order to evaluate the possible causes for temporal changes in $\delta^{13}C$. In that sense, strongly $\delta^{13}C$ and Mg/Ca ratios may point to water availability or PCP rather than temperature effect (Fairchild and McMillan 2007). In this study, the interpretation of the produced speleothem $\delta^{13}C$ records is discussed in detail together with the Mg/Ca records at section 5.2.

2.5.4 Mg/Ca on speleothem

The primary source of calcium, magnesium and other trace elements in speleothems is from the bed-rock and its dissolution occurs in areas of maximum pCO_2 (Fairchild and Treble 2009). The infiltration of these elements into the karst is dependent of their chemical mobilization and hydrological processes during infiltration (Fig. 2.7).

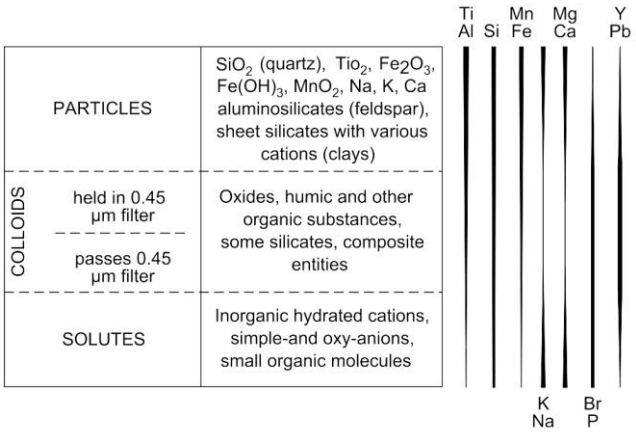

Figure 2.7. Modes of transport of the Ca, Mg and trace elements in the karstic waters. (Source: Fairchild and Treble, 2009)

The Mg cation of the drip water solution is incorporated in the $CaCO_3$ cristals at the speleothem surface according to:

$$\left(\mathrm{Tr/Ca}_{\mathrm{CaCO_3}}\right) = K_{\mathrm{Tr}}(\mathrm{Tr/Ca})_{\mathrm{solution}} \quad \text{(Fairchild and Treble, 2009)}$$

where K_{Tr} is the partitioning coefficient which is temperature dependent.

The rate of CO_2 degassing and consecuently the calcite precipitation increase in warmer temperatures (Day and Henderson, 2011). However, temperature was proved to be insuficient to explain the main reason for equilibrium partitioning of Mg into calcite

(Fairchild *et al.,* 1996). Hence, speleothem Mg/Ca ratio reflects other factors besides temperature: 1) speleothem growth rate controlled by the cave-aire contidions (temp and pCO_2) (Kowalczk and Froelich, 2010) and 2) other processes which endure changes in the drip-water composition proceding from the bed-rock, mostly related to water availability (Gascoyne, 1983; Huang and Fairchild, 2001; Morse and Bender, 1990). Changes in groundwater residence time produce more water-rock contact time, affecting the dolomite dissolution (magnesium enriched) relative to the calcite dissolution and incrementing the speleothem Mg/Ca ratio (Fairchild *et al.,* 2000 and 2006; Fairchild and McMillan, 2007). Moreover, as commented previously, PCP can occur during the infiltration and dripping, removing cations from the groundwater and reducing Ca respect to others trace elements (Fairchild and McMillan, 2007; Fairchild and Treble 2009). When PCP is an important process, it results in stronger Mg enrichment of the residual waters solution compared with the bed-rock signal (Fairchild and Treble 2009) (Fig. 2.8). Consequently, variations in the precipitation–evaporation balance over the cave should be related to the amount of water infiltrating into the karst system and affecting the water residence time, the PCP, the drip rate and the speleothem growth rate, that finally, increase the Mg/Ca ratio in the speleothem due to this preferential calcium lost.

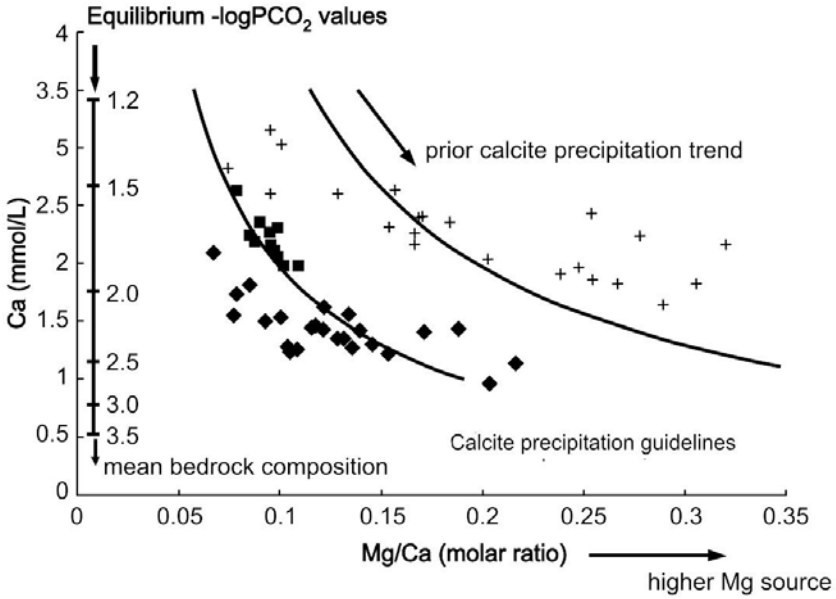

Figure 2.8. When PCP increases (black line and arrow direction) the Ca concentration decreases in the solution and finally the Mg/Ca in speleothems becomes higher due to this premature Ca lost. (Source: Fairchild and Tremble, 2009)

Several previous studies inferred hydrological changes using the Mg/Ca ratio in speleothems where high Mg/Ca ratios suggest arid conditions and vice versa (Moreno *et al.,* 2010; Fairchild *et al.,* 2000). A strong co-variation between Mg/Ca and $\delta^{13}C$ in speleothem records reinforces the interpretation of water availability in the soil thus reflecting atmospheric moisture variability (Fairchild and Treble, 2009)

2.5.5 $\delta^{18}O$ on foraminifera

The first record of $\delta^{18}O$ mesured in planktonic foraminifera was performed by Cesare Emiliani. He documented cyclyc $\delta^{18}O$ variations in Caribean cores, which were interpreted as temperature changes (Emiliani, 1955). This first aplication of oxygen isotopes in foraminifera as a paleotemperature proxy was in agreement with previous findings from Epstein *et al*., (1953) that could determine a temperature equation for marine carbonates. Later, Shackleton (1967) was the first to recognize that changes in sea water $\delta^{18}O$ composition ($\delta^{18}O_{sw}$) associated to the development or decay of continental ice sheets had a dominant imprint in the foraminifera $\delta^{18}O$ signal. These changes were the result of the Rayleigh distillation process of water from the ocean to the ice-sheets. Lighter isotopes are preferentially evaporated and transported until the ice-sheets while the oceans are enriched in heavy isotopes. If the isotopically depleted snow remains stored in the ice sheets for a long time, the global isotopic composition of sea water will be modified, and finally, becomes heavier (Fig. 2.6).

In addition to the global changes associated to ice sheet volume, the $\delta^{18}O_{sw}$ also depend of other more local or regional hydrographic processes (Lea, 2003; Rohling *et al*., 1999). Regional evaporation-precipitation balance (E-P) plays an important role controlling the $\delta^{18}O_{sw}$ of sea surface waters. E-P balance also controls surface water salinity and this co-variance with $\delta^{18}O_{sw}$ has allowed the use of this geochemical ratio as a salinity proxy although their relationship varies considerably among regions. In the case of the Mediterranean Sea, variations in the inflow water volume through the strait of Gibraltar due to changes in the relative sea level resulted on an amplified effect of the E-P balance in the $\delta^{18}O_{sw}$ during glacial times (Rohling *et al*., 2014, 1999). Here, the $\delta^{18}O_{sw}$ evolution is investigated in records from the Mediterranean and Cantabrian Sea and it is interpreted in terms of regional E-P changes but also enhance surface freshening associated to N Atlantic iceberg melting (Ferrer *et al*., 2009; Pierre, 1999; Sierro *et al*., 2005) plus this amplification effect of sea-level changes in the Mediterranean Sea (Rohling *et al.,* 2014). Overall, heavy/light $\delta^{18}O_{sw}$ values correspond to saltier/fresher sea surface water properties (Pierre, 1999) although the complexity of the factors prevents the

application of a simple linear function for paleosalinity reconstructions (Rohling *et al.,* 1999).

There are other factors that can also produce a further imprint of the foraminifera $\delta^{18}O$ signal as the so-called "vital effect" related to symbiont influences, growth phases and migrations in the water column along the live cycle (Urey, 1947). In order to reduce those interferences is convenient to select adequate species, properly know the environment along their cycle of live and homogenize growth phase sizes of the selected specimens. Moreover, benthic and planktic foraminifera can occupy several ecological niches, from surface to deep water environments, allowing isotopic reconstructions from different parts of the water column.

Overall, oxygen isotopic ratios are widely used as climate proxy in paleoceanography since they are enable to reconstructs past global ice volume, ocean temperatures, relative sea level changes, iceberg melting, ocean circulation, water column structure, surface water salinity, river discharge, monsoonal intensity and other factors related with the hydrological cycle including E-P changes. In this study it has been measured the $\delta^{18}O$ from the planktic foraminifera *G. bulloides* and used as a chronostratigraphic tool among the sediment cores but also as a proxy of surface waters properties.

Since the $\delta^{18}O$ signal from *G. bulloides* shells represents a combined signal of surface water temperature and the original seawater $\delta^{18}O_{sw}$ (Waelbroeck *et al.,* 2002), when an independent sea surface temperature estimation is available, it can be applied to elucidate variations in the $\delta^{18}O_{sw}$ (Mashiotta *et al*., 1999; Elderfield and Ganssen, 2000). This study has estimated the $\delta^{18}O_{sw}$ by using the Shackleton palaeotemperature equation (Shackleton, 1974) where the temperature has been isolated by the use of the Mg/Ca-SST estimates. Finally, the $\delta^{18}O_{sw}$ was converted in Standard Mean Ocean Water (SMOW) after the correction of Craig (1965) and used as indicator of regional E-P balance, freshening events due to N Atlantic iceberg melting and global sea-level changes.

2.5.6 Mg/Ca-SST on foraminifera

The Mg/Ca ratio measured in carbonate shells of planktic foraminifera is a frequently used proxy for sea surface temperature (SST) reconstructions (Barker *et al*., 2005; Lea, 2003; Elderfield and Gansen, 2000). During carbonate precipitation, Mg can replace Ca within the structure of calcite because these two elements have the same oxidation state and similar atomic radius. The Mg/Ca ratio as a paleothermometer is on

the basis that this substitution is favored at higher temperatures due to it is an endothermic reaction (Chave 1954). Therefore, the rate of incorporation of Mg in carbonate shells is temperature dependent and, it is consequently controlled by the sea water temperature (Elderfield and Gansen, 2000). Several attempts to calibrate temperature changes with the Mg/Ca ratios allowed to discovered 1) the Mg/Ca ratio increases exponentially with increments in SST (Lea *et al.,* 1999) and 2) its relationship is different depending on the foraminifera species (Nürnberg, 1995; Nürnberg *et al.,* 1996; Lea *et al*., 1999; Toyofuku *et al*., 2000). By means of culture experiments Lea *et al*. (1999) found a general calibration that relates temperature and Mg/Ca ratios, using an exponential equation (Mg/Ca (mmol/mol)= be^{mT}; where b is the pre-exponential constant, m the exponential constant, and T the water temperature). Afterwards, Elderfield and Gansen (2000) proposed a specific calibration for *G. bulloides* among other species and based on core-tops from the N Atlantic Ocean. More recently, using western Mediterranean core-tops, Cisneros *et al*., (2016) expanded the temperature sensitivity range of the original calibration of Elderfield and Gansen, (2000) towards the warm end that characterize Mediterranean waters (Fig. 2. 9).

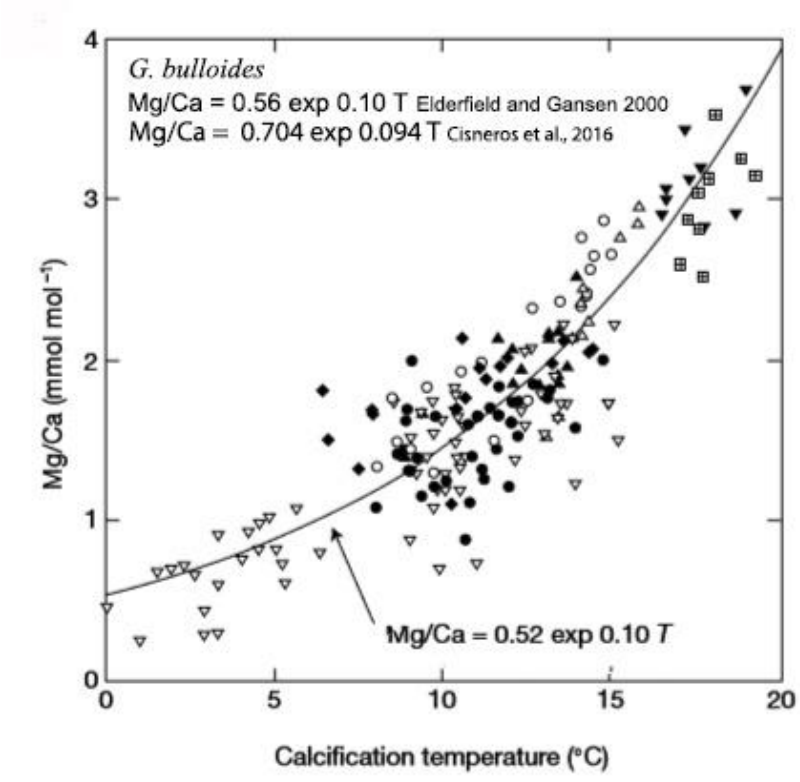

Figure 2.9. General calibration curve for Mg/Ca vs. temperature for eight different species of planktic foraminifera. (Source: Elderfield and Gansen, 200). On the top are the specific equations for *G. bulloides* specie developed by Elderfiend and Gansen, (2000), and Cisneros *et al*., (2016).

This study has applied the calibration of Cisneros *et al.,* (2016) to transfer the measured Mg/Ca ratios into SST. The Mg/Ca-SST has been interpreted to reflect spring temperatures in the Mediterranean Sea, since sediment trap fluxes of *G. bulloides* are maximum during this bloom season (Bárcena *et al.,* 2004; Cisneros *et al*., 2016; Rigual-Hernández *et al.,* 2012).

The foraminifera–Mg/Ca ratios have been proposed to be affected by other factors like high-salinity conditions, which is the case of the Mediterranean Sea (Ferguson *et al*., 2008), but more recent culture experiments appears to not support it (Hönisch *et al*., 2013). In contrast, diagenetic overprints have been proposed as the main cause of anomalous high foraminifera-Mg/Ca ratios (Hoogakker *et al*., 2009). Despite that, secondary high-Mg-calcite overgrowths in foraminiferal shells is lower in deep western Mediterranean samples than in eastern locations due to the presence of less calcite supersaturated waters (van Raden *et al*., 2011). Furthermore, both reductive and weak acid leaching steps applied in the cleaning procedure have been proved to be efficient removing secondary overgrowths (Pena *et al*., 2005). Overall, the Mg/Ca ratios obtained in this study appear not to be anomalous high ratios since they are coherent with other studies for the same location (Català *et al.,* 2019; Jiménez-Amat and Zahn 2015) and within the ranges of the calibration used to transfer ratios into SST (Cisneros *et al.,* 2016).

Previous studies have demonstrated that the reductive step dissolves preferably Mg rich calcite and consequently the Mg/Ca ratio estimation become lower. Consequently, Mg/Ca ratios of the reductively cleaned samples are systematically lowered by about 10–15% (Barker *et al*., 2003, 2005; Yu *et al*., 2007). Accordingly, the estimated Mg/Ca ratios of the ODP Site 977A were corrected with an increase of 15% as it is suggested by Barker *et al.,* (2003) due to the reductive attack step was applied in this case.

Moreover, in order to identify potential contaminated samples and avoid overestimated Mg/Ca–SST, Al/Ca and Mn/Ca ratios were also measured controlling thus the presence of manganese oxides and/or aluminosilicate (Barker *et al.,* 2003; Lea *et al.,* 2005; Pena *et al.,* 2008, 2005). Few samples were discarded according to values above 2σ of each ratio (ODP site 977A: Mn/Ca ≥ 0.41 and Al/Ca ≥ 0.46; MD99-2343: Mn/Ca ≥ 0.82 and Al/Ca ≥ 0.32; PP10-17: Mn/Ca ≥ 0.49 and Al/Ca ≥ 0.33). Furthermore, no co-variations of Al/Ca and Mn/Ca with Mg/Ca ratios were found (Fig. 2.10).

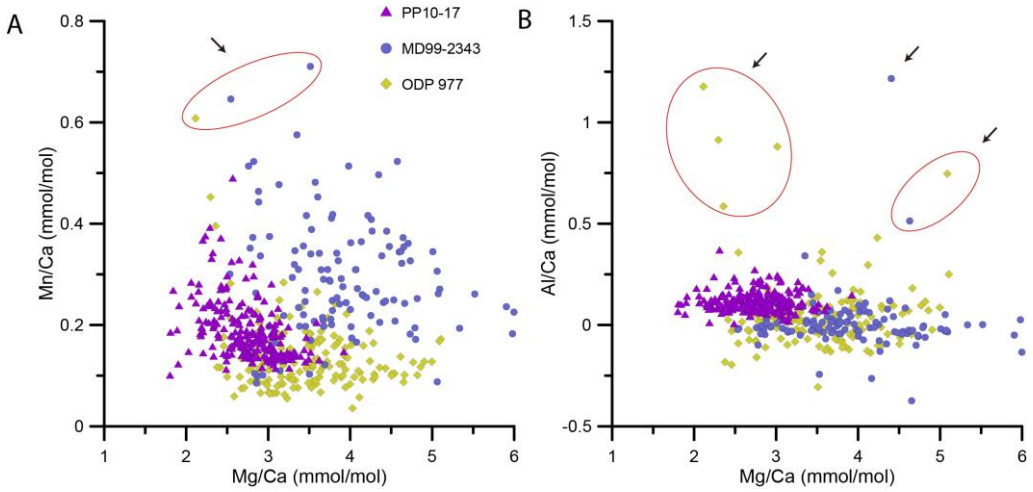

Figure 2.10. Measured Mn/Ca and Al/Ca ratios plotted versus the Mg/Ca ratios of the three sediment cores. Red circles highlight those samples discarded duo to possible contamination.

2.5.7 UP10 index

Deep-water current intensity directly affects the proportion and grain-size of non-cohesive particles (McCave and Hall, 2006; Mulder *et al.,* 2013; Rebesco *et al.,* 2014). In this sense, the grain-size distribution of the non-carbonate fraction of sediments represents the intensity of bottom currents (McCave *et al.*, 1995). Several paleoceanographic studies in sediment cores have been carried out using the sortable silt (SS) and/or silt/clay proxies (Robinson and McCave, 1994; McCave *et al.*, 1995; Bianchi *et al.*, 1999; Hall and McCave 2000; McCave and Hall 2006; Frigola *et al.*, 2008). While the silt/clay ratio directly compares the relationship between silt (>2 μm) and clay (2-63 μm) of the sediments, the SS encompasses the lithic fraction between 10 and 63 μm (McCave *et al.*, 1995). The SS proxy assumes that 1) fine sediment behavior is dominantly cohesive below <10 μm grain size and therefore they are not being able to be transported individually by currents and 2) particles with grain sizes <63 μm from deep hemipelagic sediments corresponds mainly to biogenic fragments (McCave *et al.,* 1995). However in contourite drifts lithic particles >63 μm can be eroded, suspended and transported by contour currents (Rebesco *et al.*, 2014). These sediment deposits are characterized by very high sedimentation rates providing information about terrigenous inputs at high-resolution (Hodell *et al.,* 2009; Oppo *et al.,* 2001; Robinson and McCave, 1994). A new developed proxy that represents all the particles higher than 10 μm (UP10) was developed by Frigola *et al.*, (2007) on the same core used in this study, hence encompassing also possible fine sandy particles. This UP10 record from core MD99-2343, linked deep-water currents intensity changes with climate oscillations controlling the deep-water formation in the western Mediterranean during the last 50 kyr (Frigola *et al.*, 2008, 2007). Moreover,

this UP10 index was recently validated with instrumental measurements from the western Mediterranean (Cisneros *et al*., 2019). For these reasons the UP10 proxy was calculated from the addition of all the lithic particles higher than 10 μm as volume percentage.

Furthermore, the suitability of the UP10 proxy was validated performing also a clustering statistical analysis of the grain-size modal distributions based on a k-means method (McQueen, 1967; Povea *et al*., 2015). This statistical method allows to classified all the samples in *n* clusters (4 in this study) according to their modal distribution similarity with a prototype sample, which it is obtained by several iterations and defined by the mean of all the samples belonging to the cluster (Davis, 2002).

2.5.8 The Zr/Al: XRF-data normalization

Raw data of the XRF-core scanner, in other words, the element intensities, are obtained in cps and they represent a quantitative approach. However in paleoceanography, it is more adequate the use and comparison of elemental ratios (Tjallingii *et al*., 2007). The element intensities depend on the element concentration, but also on physical properties such as porosity, density or water content, (Richter *et al*., 2006). This last one strongly reduces light element intensities, becoming more susceptible to absorption effects (e.g Al) (Tjallingii *et al*., 2007). In order to reduce these signal artefacts, related to both lithological and water content changes, Al-normalization was performed due to it is considered that aluminium is only present in clays and detrital aluminosilicates (Van der Weijden, 2002). Furthermore, Weltje and Tjallingii (2008) proposed a log-ratio representation for the XRF-core scanner data allowing a convenient way to compare different XRF records (Weltje and Tjallingii 2008). Accordingly, the XRF-core scanning data is presented here as element/Al logarithmic ratio, in order to correct different coefficients of variations between elements and allowing a statistically more robust representation of element ratios (Weltje and Tjallingii 2008).

Currents not only control the grain-size distribution of contourite drifts but also modify the mineralogy of sediments (Mulder *et al.,* 2013). Bahr *et al.* (2014) suggest that Zr/Al ratios represent the relative enrichment of zircon (heavy mineral) versus aluminosilicates (less dense minerals) under current flow, and therefore it can be used for a semi-quantitative assessment of paleocurrent velocity. In order to explore the suitability of this proxy in our sediment core record, a Principle Component Analysis (PCA) was carried out with the Statgrafics software into the standardized XRF data, only considering the elements with a robust signal (i.e. Al, Si, K, Ca, Ti, Fe, Rb, Sr, Zr, and Ba for this statistical treatment.

Chapter III

Results

3.1 Speleothem chronologies

A total of 298 radiometric U/Th dates were performed over 48 speleothems corresponding to 12 different caves, absolute dates with the errors and U contents are given in Annex 6. This intensive dating was required in order to identify those speleothems that covered past interglacial periods and major transitions (glacial terminations or glacial inceptions), target by this thesis (Fig. 3).

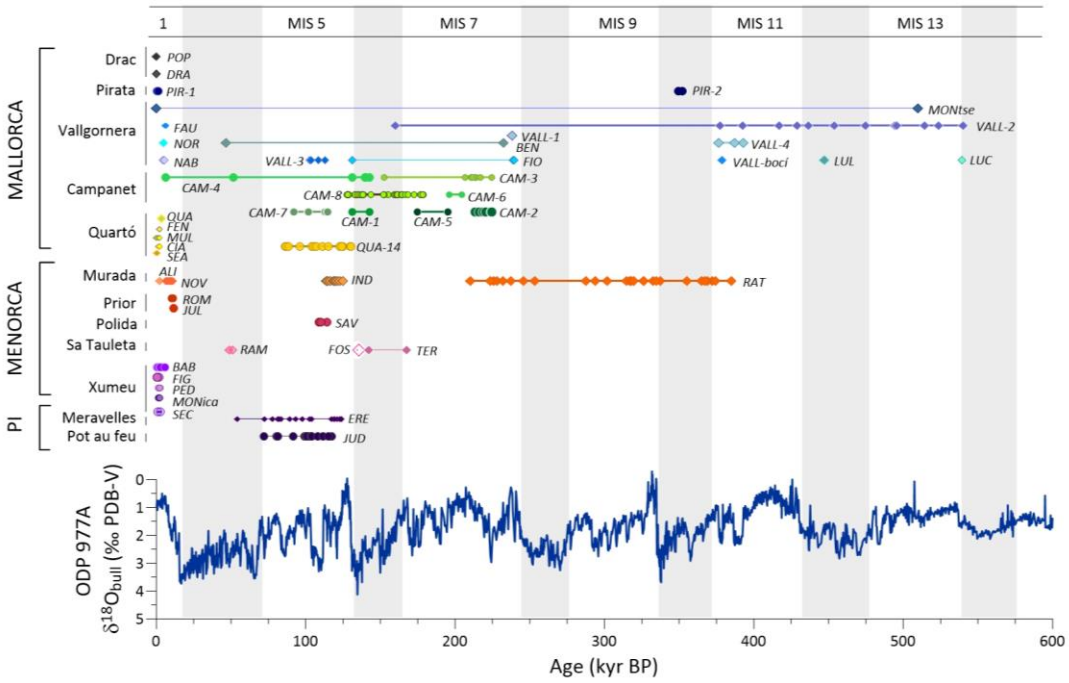

Figure 3. Growth phases of all dated speleothems compared with the $\delta^{18}O$ measured G. bulloides from the marine sediment core ODP 977 from the Alboran Sea (Martrat *et al.*, 2007 and unpublished data). Grey bars indicate glacial periods

Twenty of these speleothem grew in the current interglacial and they were directly discarded for this study with the only exception of NOV that covers the last termination (TI) and the longest section of the MIS 1. Consequently NOV was considered a valuable reference record and thus it was the only Holocene speleothem where the age model and geochemistry analyses were performed. In addition other dated speleothems were also discarded for this study according to several different criteria as: glacial speleothems, those showing visible dissolution structures or high porosity, those covering very long periods but at very low resolution or, on the contrary, those that grew very fast but during very short periods, among others. As a result, the age modelling effort has concentrated in 16 speleothems (Fig. 3.1). Some speleothems were still selected although their records were relatively short in time, but since they provided an overlapping record with others

offering the opportunity to obtain replicates in the geochemical proxy signals allowing further confidence to the climatic interpretations. The selected speleothems provide coverage for the six last interglacial periods (MIS 1, MIS 5, MIS 7, MIS 9, MIS 11, and MIS 13) but MIS 1, 7 and 13 are not completely covered. The MIS 5 is the best represented with at least 6 speleothems that grew during that period, including CAM 8, which, although mostly grew during the glacial period, it was chosen to evaluate its signal during the TII when it overlaps with two other speleothems (FOS and TER).

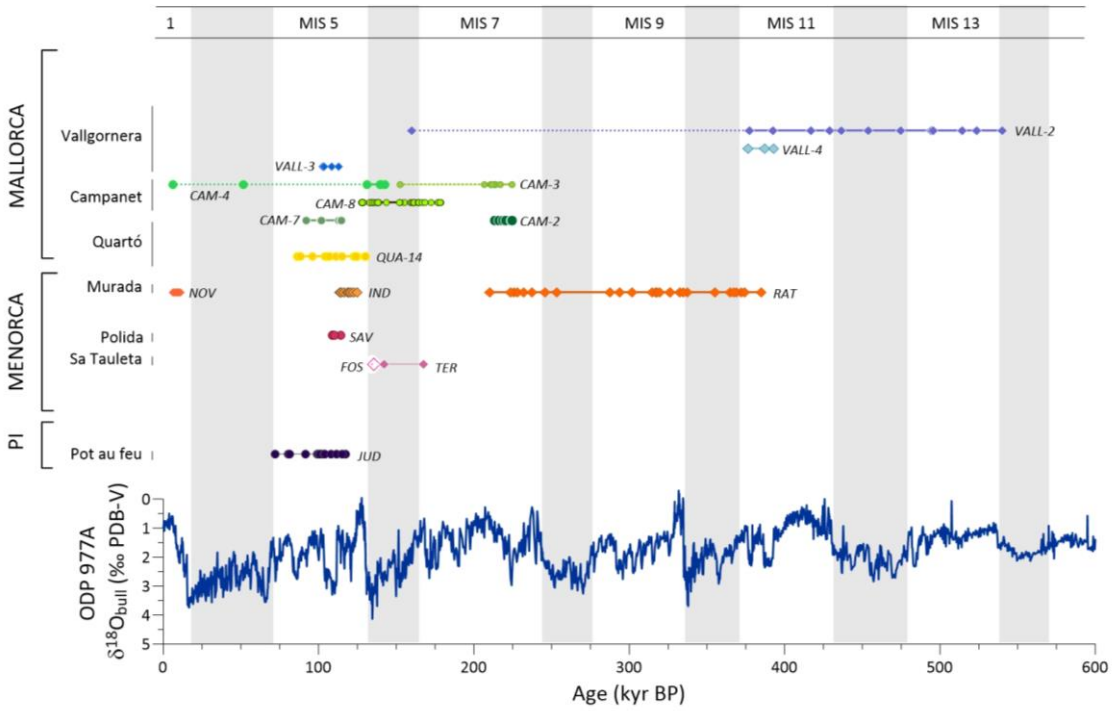

Figure 3.1. Growth phases of the selected speleothems for age modelling compared with the $\delta^{18}O$ measured *G. bulloides* from the marine sediment core ODP 977 from the Alboran Sea (Martrat *et al.*, 2007 and unpublished data). Grey bars indicate glacial periods

3.1.1 Iberian Peninsula speleothem age model

The chronology of JUD speleothem is provided by 14 radiometric dates (Fig 3.2). Several replicates where performed in order to constrain the age model due to the relative large errors usually present in JUD dates. In one case, the error was so large (at 3.6cm) that was invalidated and not included for the age modelling. This sample was located above a visual discontinuity. The presence of detrital material, which could introduce remobilized Th in the calcite, is probably the reason for high age errors (Fig 3.2). This Pyrenean speleothem presents coloured detrital layers and three changes in the growth axis direction at 3.5, 40.6 and 44.8 cm from the top. These visual changes could indicate precipitation/growth breaks but the resolution of the sampling and the errors associated

makes difficult to constrain this short hiatuses only by U-series ages. Moreover, these potential hiatuses have been associated to large positive excursions in the geochemical record (Mg/Ca and $\delta^{13}C$) supporting its relation to events of reduction in effective precipitation. Due to speleothem growth hiatuses are not well detected by statistical methods, the JUD record has been divided in four different data series in order to perform a plausible age modelling. The result of this modelling indicates that JUD speleothem grew from 115 to 68 kyr BP with the 3 growth hiatuses at 108, 104 and 82.5 kyr BP. It presents the slowest growth rate in the top. In contrast, the base present rather fast growth with and intense shift at 101 Kyr through even faster growth period. An extraordinary peak at 100.5 kyr BP is likely a consequence of the modelling software difficulty in managing rapid growths and reversal dates that finally leaves overestimated growth rates in this point. Without considering this peak, the growth rates range between 0.2-16 cm/kyr.

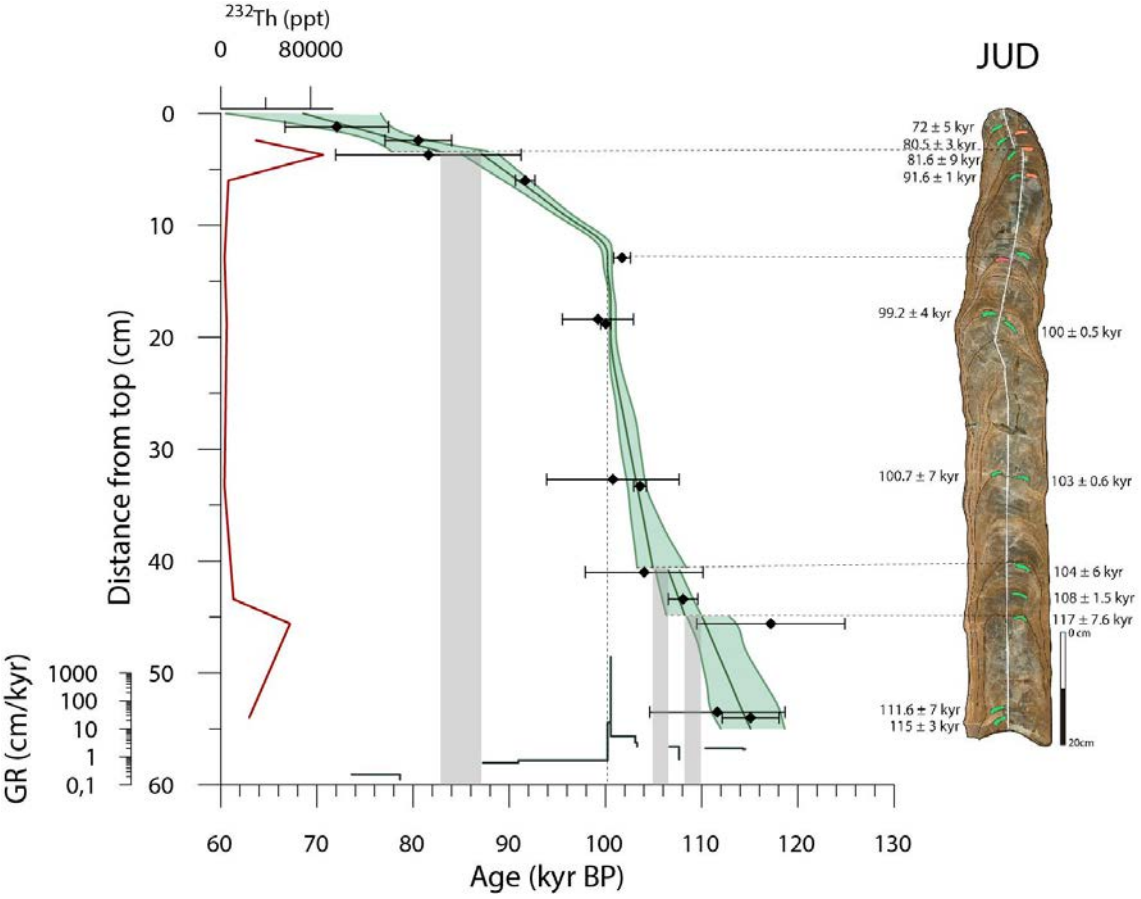

Figure 3.2. JUD age model developed by 14 U/Th radiogenic dates. Center) Modelled chronology with associated age uncertainties (green line and area respectively). The black dots are original U/Th dates used for age modelling. . Dashed lines highlight major layer discontinuities. Grey bars indicate modelled hiatuses in the growth rate. Left) The ^{232}Th content of the dated samples (red line) showing high detrital thorium related to large errors. Bottom) Modelled growth rate in logarithmic scale. Right) Image of JUD speleothem with the position of the sampled radiometric dates and the growth axis used in the geochemical analyses. In green, dates used in the age modelling, in orange, replicated dates and in red, invalid samples.

3.1.2 Minorca speleothem age models

From Murada cave, in Minorca, three speleothems has been modelled. NOV is the youngest one covering from 13 to 6 kyr BP (Fig. 3.3A). The chronology was performed using 9 radiometric dates. The bottom of the speleothem presents three changes in the growth direction with several colour layers. After that the speleothem starts to have a constant colour without visual discontinuities covering almost all the speleothem. The age sampling was performed along that homogeneous coloured region. NOV does not presents any age inversions when taking into account 2σ errors and it have an age-depth model rather linear with fast growth rates, between 5-10 cm/kyr. The second speleothem from the same cave is IND that spans from 125 to 113 kyr BP (Fig. 3.3B). The chronology was performed using 8 radiometric dates. This speleothem shows a homogenous aspect with the absence of important changes in the growth direction or colour layers. That is in line with its extraordinary linear age–depth model with growth rates between 7-8 cm/kyr.

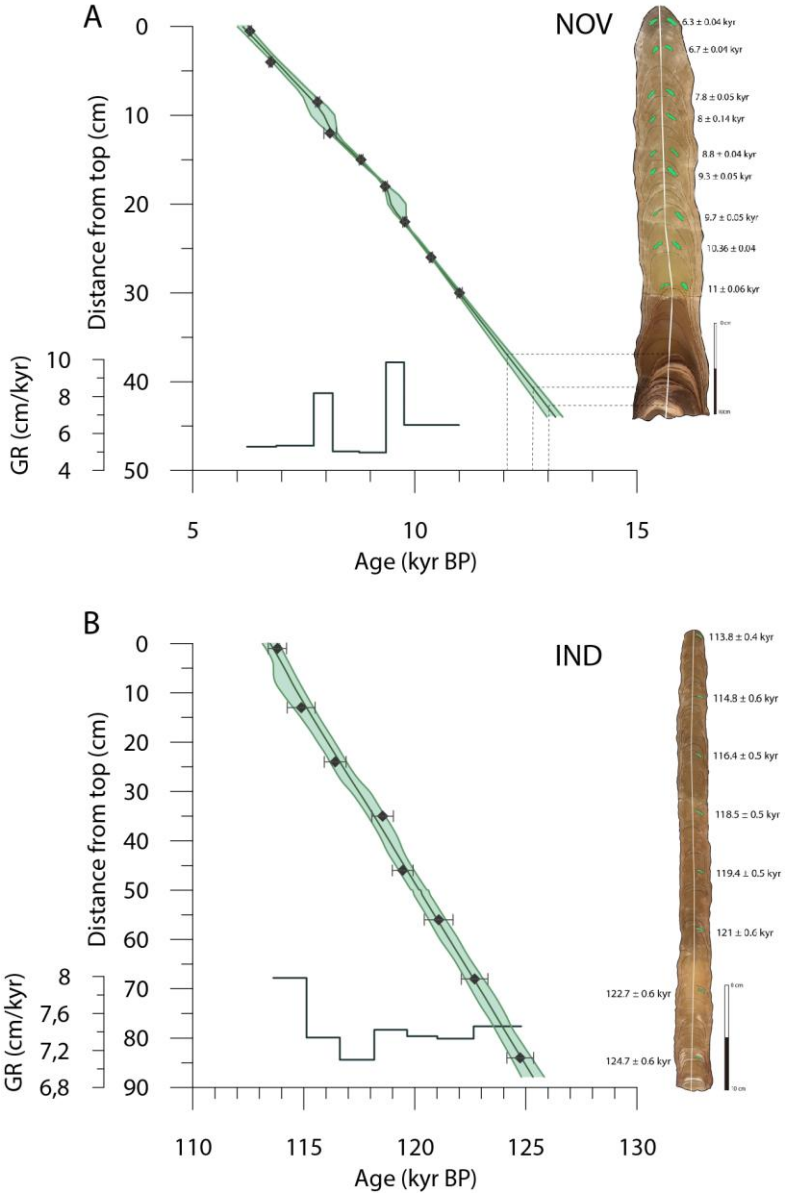

Figure 3.3. Murada cave speleothems age models. A) NOV age model and B) IND age model (green lines). Both plotted with the associated errors (green area), the original U/Th dates (black dots) and the growth rates (dark green). Into the right, the images of each speleothem with the position of the sampled radiometric dates used for the age model (green) and the growth axis used for the geochemical analyses (white line).

Finally, RAT is the oldest speleothem from this cave, spanning from 383 to 210 kyr BP (Fig. 3.4), and also is the speleothem covering the longer time interval (173 kyr). The age model was performed using 27 radiometric dates. Some of these dates are age inversions but in this case they are equally used for the age modelling since they represent short time deviation. Several changes in the growth rate occur along RAT, which fluctuate between 0.07-1.7 cm/kyr (Fig. 3.4). However, two overestimated peaks in the growth rates (24 and 12 cm/kyr) can be observed at 370 and 333 kyr BP respectively due to modelling software incongruences. The absolute age uncertainties of the younger part of the speleothem are shorter and therefore this age model is much robust than the oldest part where errors are larger.

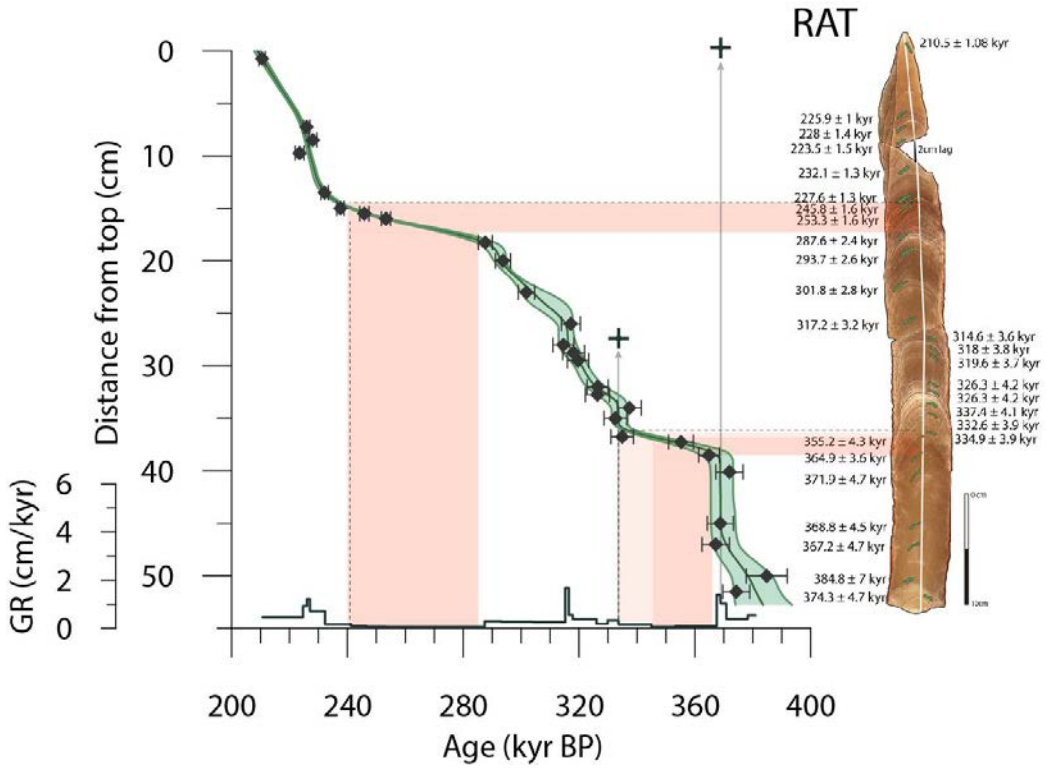

Figure 3.4. RAT speleothem age model from Murada cave (green line), plotted with the associated errors (green area), the original U/Th dates (black dots) and the growth rates (dark green). The black crosses indicate growth rate outliers. The pink grey bars highlight slow growth rate periods and the dashed line points to the major visual layer discontinuity. Into the right, the image of the speleothem with the position of the sampled radiometric dates used for the age model (green) and the growth axis used for the geochemical analyses (white line).

Three more speleothems from Minorca has been modelled from Polida and Sa Tauleta caves. These speleothems were dated at very low resolution using only 4 radiometric dates for SAV and FOS while only 3 for TER age model (Fig. 3.5). This first dating approach indicated some limitations for these speleothems such as: coverage of very short time periods; presence of age inversions or large age uncertainties. In

consequence, any further dating effort was dedicated to them but they were still considered in this age modelling section since they overlap with other selected speleothems and thus they give the opportunity to replicate their geochemical signal. SAV speleothem has two age inversions within its 4 dates but, when taking into account the absolute age uncertainties, only one seems to be an important reversal (Fig. 3.5A). Despite that, all four dates were used for the age model. Although SAV speleothem is relatively long (65cm-long) it only grew from 114 to 108 kyr BP and thus at fast rates (10-13 cm/kyr). FOS speleothem does not present any age inversion when taking into account 2σ errors. This speleothem spans from 136 to 134 kyr BP with variable fast growth rates (4-16 cm/kyr) (Fig. 3.5B). Finally, TER speleothem spans from 168 to 142 kyr BP and its age model was performed using linear interpolation between the three radiometric dates. The TER speleothem present several changes in the growth path and changes in the colour layers and textures. This complexity is not reflected in the used simple age model (Fig. 3.5C).

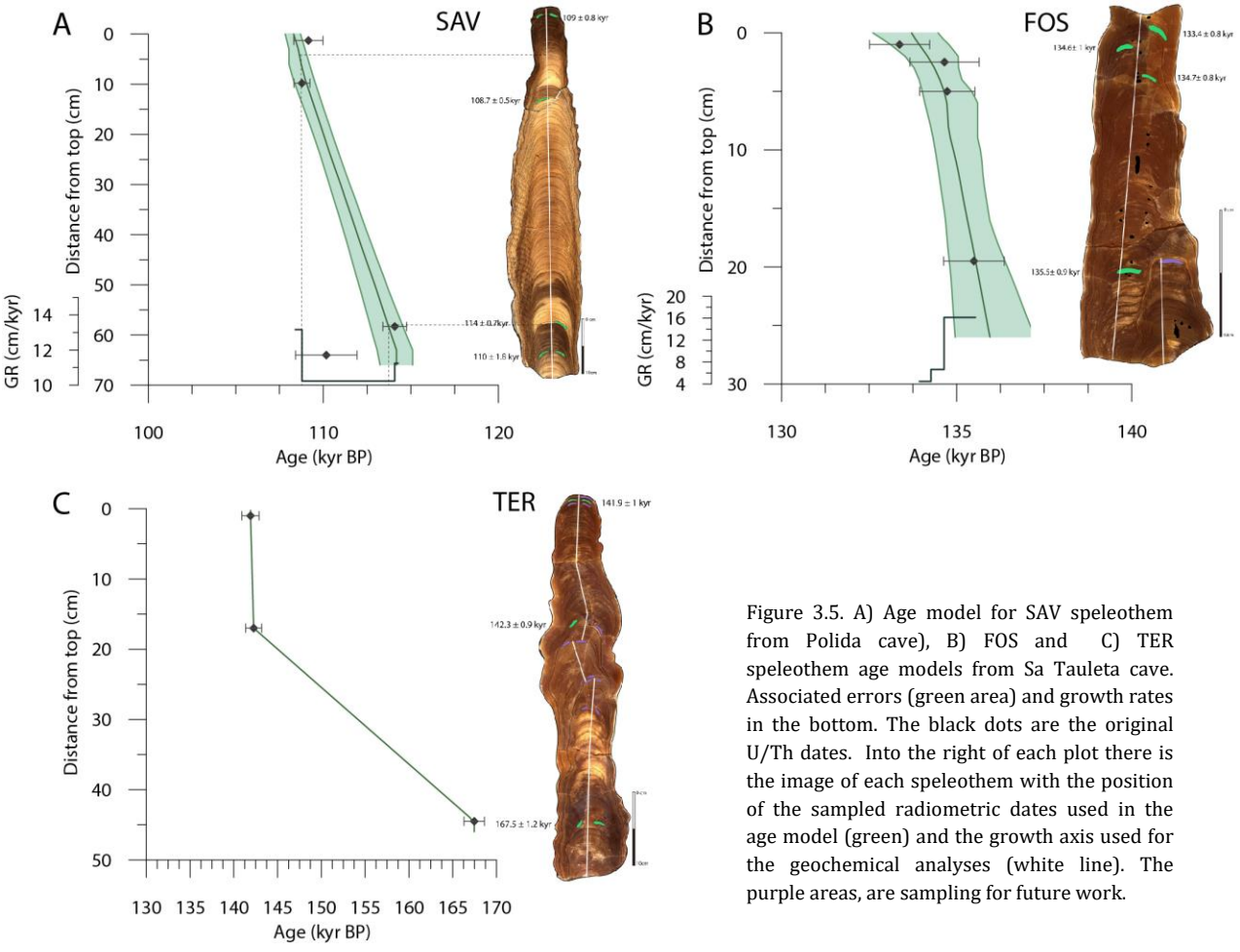

Figure 3.5. A) Age model for SAV speleothem from Polida cave), B) FOS and C) TER speleothem age models from Sa Tauleta cave. Associated errors (green area) and growth rates in the bottom. The black dots are the original U/Th dates. Into the right of each plot there is the image of each speleothem with the position of the sampled radiometric dates used in the age model (green) and the growth axis used for the geochemical analyses (white line). The purple areas, are sampling for future work.

3.1.3 Mallorca speleothem age models

The work in Mallorca has concentrated in 9 speleothems from three different caves, Campanet, Sa Balma des Quartó and Vallgornera. Campanet is the higher represented cave with 5 speleothems. CAM2 chronology was performed using 13 radiometric dates (Fig. 3.6A). Although some of these dates present age inversions, all of them are used in the age modelling. CAM2 speleothem presents a clear layer at 33 cm of depth associated to changes in colour and texture and also in the growth path. This layer also represents a reduction in the growth rate (~0.4 cm/kyr). This visual change could indicate a growth break but the large age uncertainties in this interval difficult to constrain any short hiatuses by U-series ages. After this point, the speleothem presents faster growth (13-19 cm/kyr) with variable textures and colours. This speleothem spans from 225 to 214 kyr BP, overlapping with the CAM3 that spans from 223 to 211 kyr BP.

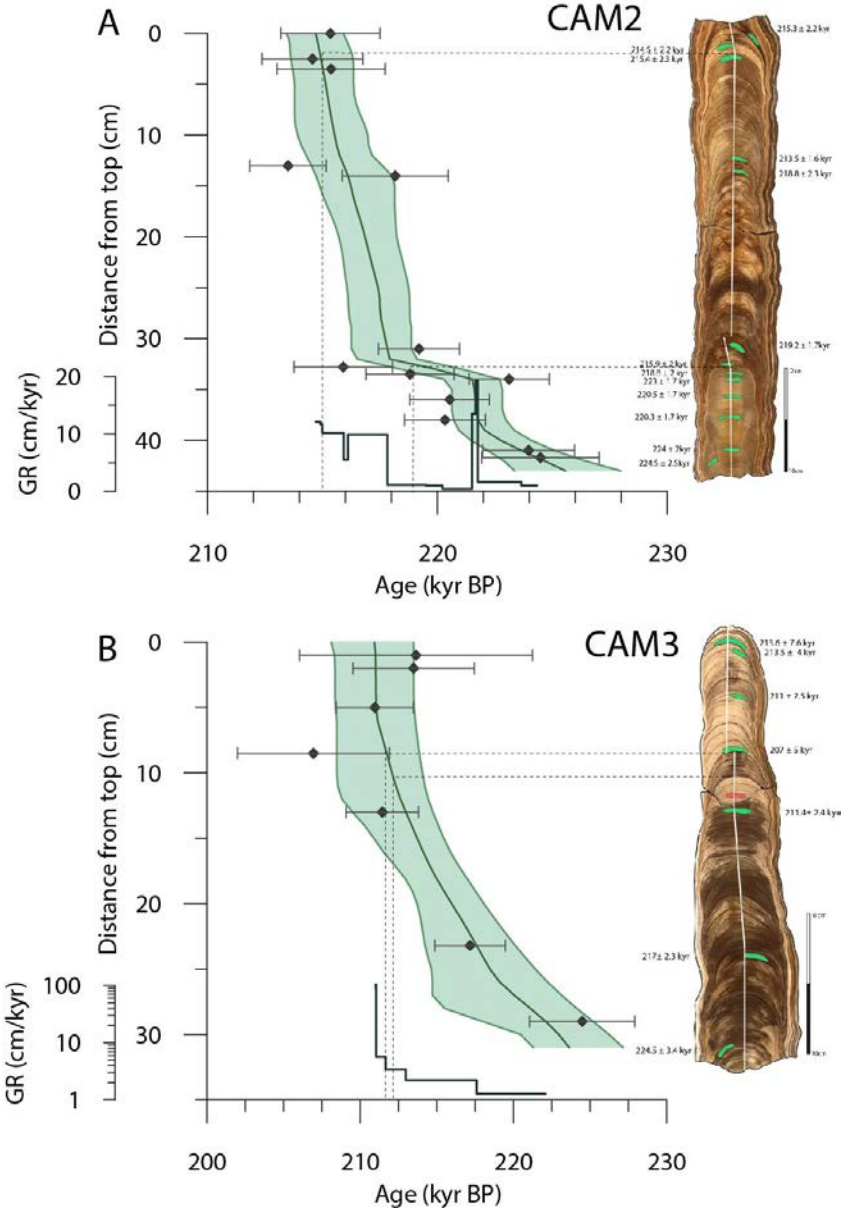

Figure 3.6. A) CAM2 and B) CAM3, speleothem age model for Campanet cave from Mallorca, with associated errors (green line and area respectively) and growth rates in the bottom. The black dots are the original U/Th dates. Into the right of each plot there is the image of each speleothem with the position of the sampled radiometric dates used in the model (green). In red, discarded radiometric dates due to large errors. The growth axis path used for the geochemical analyses is also indicated with a white line. Major layering discontinuities are highlighted with dashed black lines.

The CAM3 age model was provided by 7 radiometric dates however one extra date was analysed and discarded due to its large error (Fig. 3.6B). CAM3 presents several slight changes in the growth path along the axis with growth rates ranging from 1 to 5.6 cm/kyr. However extraordinary high growth rates (104 cm/kyr) are reached in parallel to an abrupt change to white colour in the top of the speleothem with large age uncertainties. The CAM4 speleothem grew much later than the last two, covering from 148 to 143 kyr BP (Fig. 3.7A). The chronology of this speleothem was performed using only 4 of the radiometric dates due to the first two reveals strong hiatus in the top of the speleothem. This growth hiatuses are in line with two prominent white layers. CAM4 presents growth rates of 2-4 cm/kyr with small age uncertainties with the exception of the youngest dates due to the presence of a reversal. The chronology of CAM7 speleothem is provided by 6 radiometric dates and spans from 115 to 92 kyr BP (Fig 3.7B). The speleothem grew during two fast phases. The speleothem present several slight direction changes in the growth axis but one is specially prominent and also associated to a clear change in colour layering and texture (12 cm-depth) when the growth rates decreased substantially (0.2 cm/kyr). This marked layer could represent a growth hiatus but more resolution in the sampling would be required to confirm that. Directly above of this layer, the speleothem present a homogeneous crystalline structure. Throughout of this structure it can be observed the layering of the evolving calcite. Therefore it is probably that dissolution of the youngest calcite with a posterior re-precipitation creates this peculiar structure.

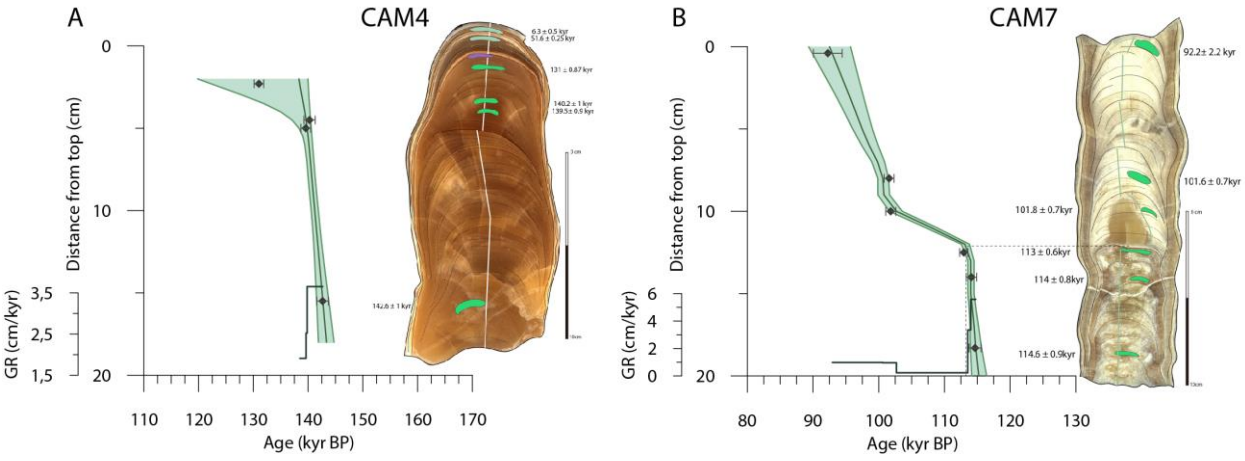

Figure 3.7. A) CAM4 and B) CAM7 age models with associated errors and growth rates in the bottom. The black dots are the original U/Th dates. Into the image of each speleothem it is highlighted the position of the dates used in the model (green). In light green, discarded dates due to high time jumps. The black dashed line highlight an important visual layer discontinuity.

The last speleothem from Campanet cave, CAM8, covers the penultimate glacial period from 178 to 128 kyr BP (Fig. 3.8A). The age model was performed using 28 radiometric dates some of these are age inversions but only one was discarded for the age modelling. This speleothem presents several slight changes in the growth axis direction and well defined multi-colour layering. In the middle of the speleothem there is a notable colour change toward brownish tonality. This colour change coincides with the lowest growth rate phase. Several layers showing visual discontinuities exist but only the most prominent changes in growth axis directions are highlighted in the plot (Fig. 3.8A) as well as the most important colour change. The variability on growth rates in this speleothem is high with ranges between 0.2-7 cm/kyr all over the speleothem but an extraordinary growth rate of 85 cm/kyr is observed at the top of the speleothem. Despite that, two well defined phases of fast growth rate, centred at 160 and 137 kyr, can be observed.

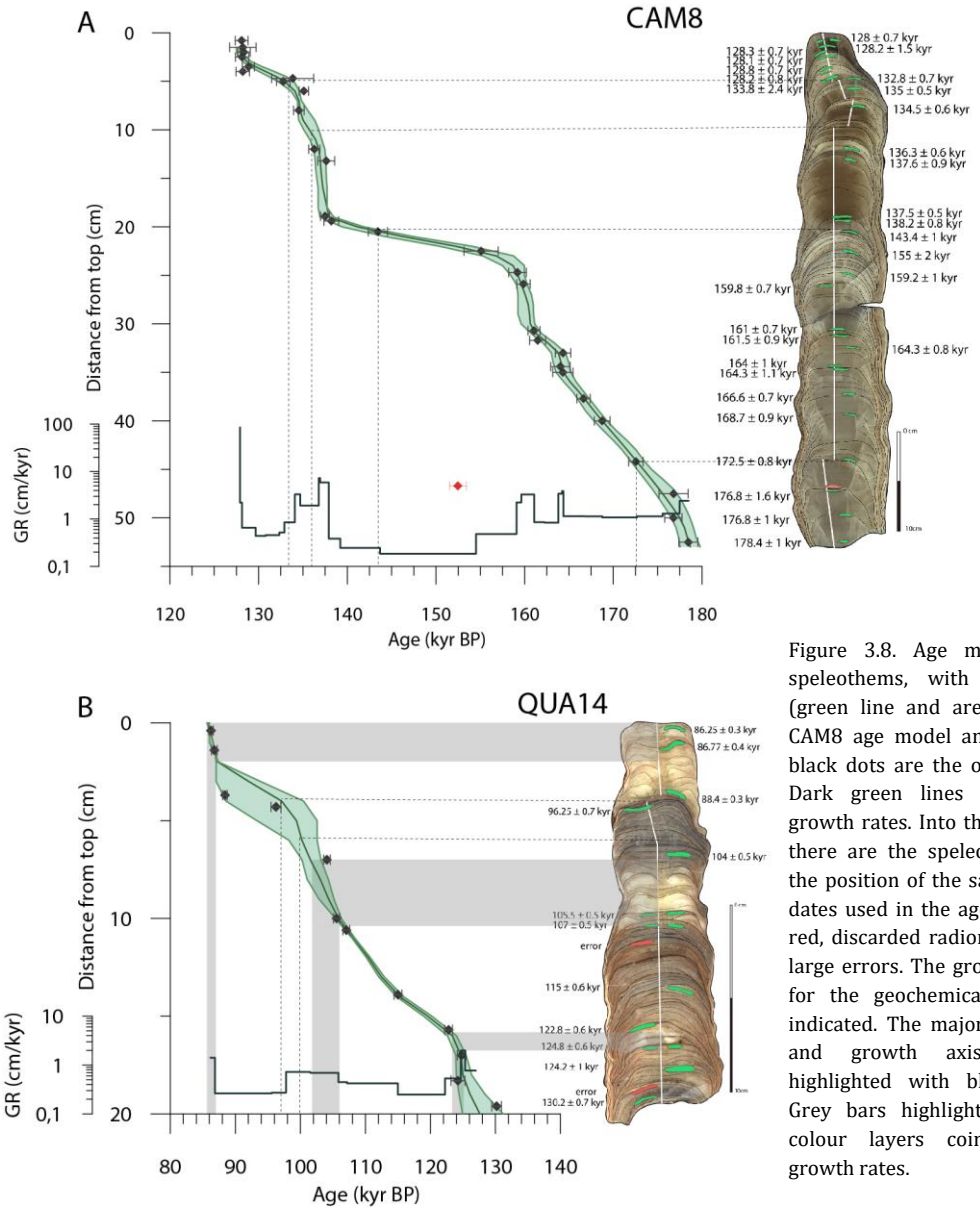

Figure 3.8. Age model for Mallorca speleothems, with associated errors (green line and area respectively). A) CAM8 age model and B) QUA14. The black dots are the original U/Th dates. Dark green lines are the modelled growth rates. Into the right of each plot there are the speleothem images with the position of the sampled radiometric dates used in the age model (green). In red, discarded radiometric dates due to large errors. The growth axis path used for the geochemical analyses is also indicated. The major changes in colour and growth axis directions are highlighted with black dashed lines. Grey bars highlight prominent white colour layers coincident with fast growth rates.

QUA14 is the only speleothem from Sa Balma des Quartó cave. The age model was performed using 12 radiometric dates and spans from 127 to 86 kyr BP (Fig. 3.8B). Although some reversals existed only two dates were discarded for the age modelling. This speleothem is characterised by three very distinctive white areas that correspond to periods of fast growth rates especially at the one that it is located close to the base. The growth rates range between 0.2-2 cm/kyr. Two marked changes in the direction of the growth axis exist in the upper part, where the last one is previously to the youngest withe area.

Three speleothems were selected from the Vallgornera cave. VALL2 is the oldest speleothem among all the selected in this thesis, and spans from 530 to 345 kyr BP (Fig. 3.9), close to the U-series age limit. The chronology is provided by 12 radiometric dates although some of them are reversal. The age uncertainties are higher in the oldest part of the speleothem where the growth rate is higher and coinciding with a light-coloured area. The growth rate ranges between 0.02-1.2 cm/kyr. This speleothem recorded several changes in the direction of the growth axis and coinciding with well-marked colour layers.

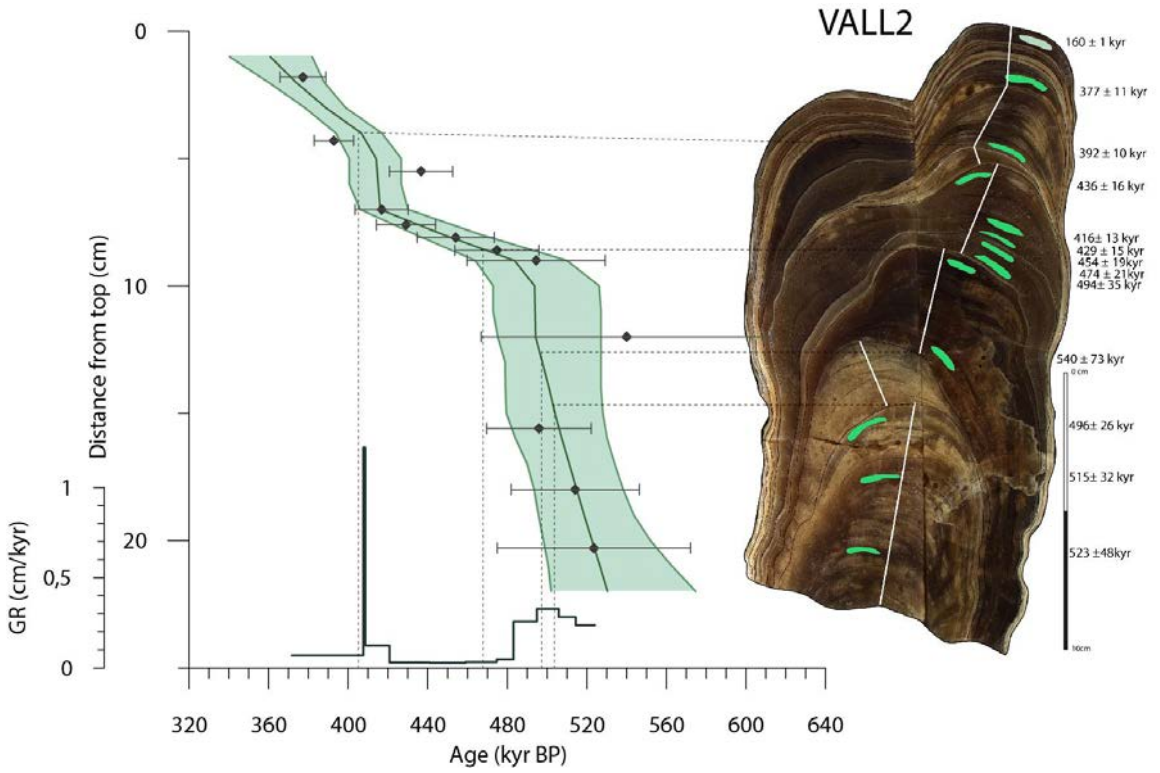

Figure 3.9. VALL 2 speleothem age model from Vallgornera cave with associated errors (green line and area respectively). The black dots are the original U/Th dates. Into the right of the plot there is the image of the speleothem with the position of the sampled radiometric dates used in the age model in green and a discarded date in the top due to a high time jump in light green. The growth axis path used for the geochemical analyses is also indicated with a white line. Major layer discontinuities are highlighted with black dashed lines.

VALL3 chronology was performed using only 4 radiometric dates (Fig. 3.10A). This speleothem spans from 112 to 101 kyr BP and the age-depth model is rather lineal with growth rates around the 2.5 cm/kyr. Due to the centre of the speleothem present clear dissolution marks with holes and even possible re-precipitated calcite, the sampling path selected for geochemical analyses and radiometric ages was displaced towards one lateral. Finally, VALL4 speleothem has the chronology based on only 3 radiometric dates. It is a short speleothem with fast growth rate (~4 cm/kyr), rather lineal, that covers from 387 to 382 kyr BP (Fig. 3.10B).

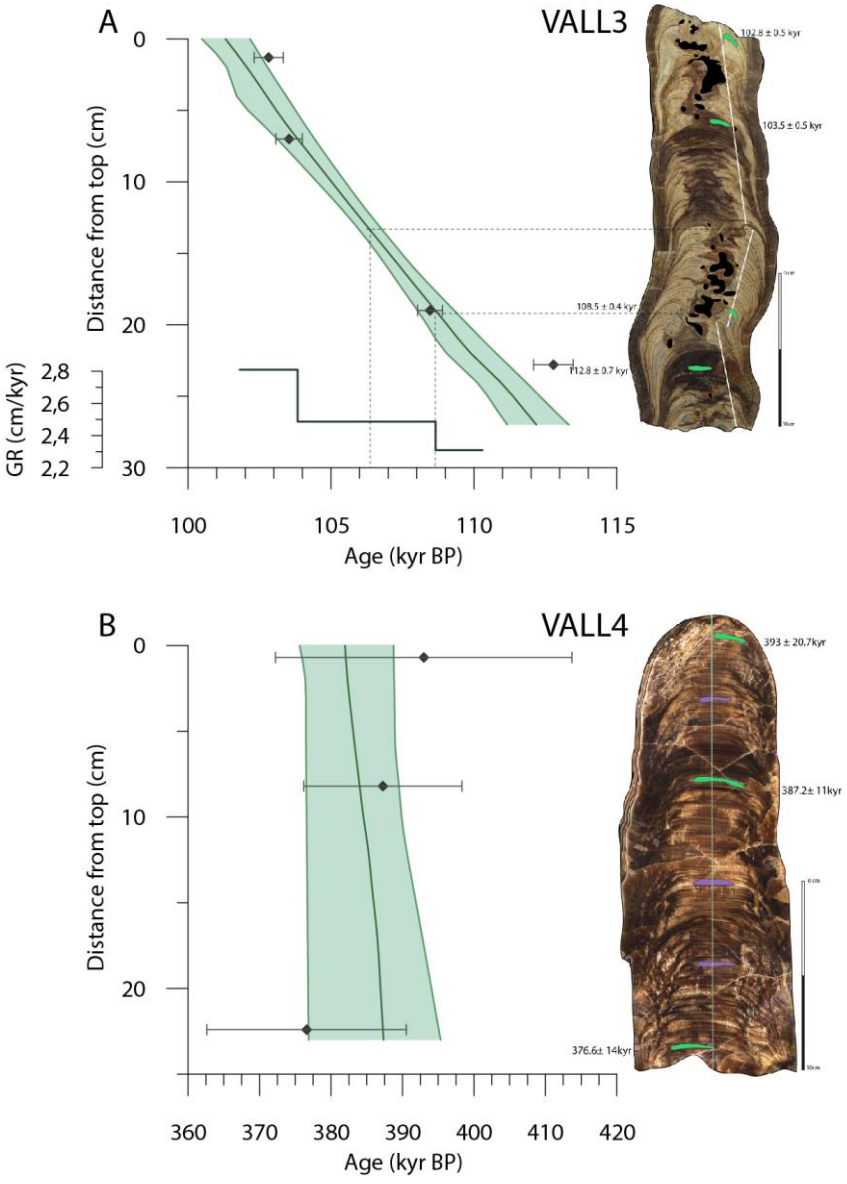

Figure 3.10. Age model for Vallgornera cave speleothems, with associated errors (green line and area respectively). The black dots are the original U/Th dates. A) VALL3 age model and B) VALL4 age model. Into the right of each plot there is the image of each speleothem with the position of the sampled radiometric dates used in the age model (green). In purple sampling for future work in order to improve the age models. The growth axis path used for the geochemical analyses is also indicated with a white line. Major changes in the growth path are highlighted with black dashed lines.

Here below the Table 3 shows a summary of the covered periods and growth rates for the 16 speleothems, which were selected for age modelling and geochemical analysis after the preliminary dating of 48 speleothem considered in this thesis.

Table 3

				U/Th		
Location	Cave	Name	Long. (cm)	Period (kyr)	n. dates	Growth rate range (cm/kyr)
Pyrenees	Pot eu feu	Judit	55	115-68	14	0.2-18
Minorca	Murada	Novena	45	13-6.1	9	5.1-10
	Murada	Indiana	88	125-113	8	7-7.9
	Murada	Ratpenat	50	383-210	27	0.07-24
	Sa Tauleta	Fosca	65	136-134	4	4-16.2
	Sa Tauleta	Teresa	54	168-142	3	1-44.4
	Polida	S'avia	70	114-108	4	10-13.2
Mallorca	Campanet	CAM2	46	225-214	13	0.4-19
	Campanet	CAM3	31	223-211	7	1-104
	Campanet	CAM4	19	148-143	4	2-3.6
	Campanet	CAM7	21	115-92	6	0.2-5.5
	Campanet	CAM8	52	178-128	28	0.7-85
	Vallgornera	VALL2	22	530-345	12	0.02-1.2
	Vallgornera	VALL3	25	112-101	4	2.3-2.8
	Vallgornera	VALL4	23	387-382	3	3.8-4.3
	Es Quartó	QUA14	20	127-86	12	0.2-2

3.2 Speleothem geochemistry

3.2.1 Iberian Peninsula geochemistry results

Geochemical analyses for JUD speleothem involved both stables isotopes and Mg/Ca measurements (Fig. 3.11). The JUD $\delta^{18}O$ values vary from the minimum values (-9 ‰) at about 106 kyr BP to the maximum in the record (–7.9 ‰) at 100 kyr BP, hence with an overall variation of 2.4‰. The $\delta^{18}O$ mean is -7‰ and the $\delta^{13}C$ mean value is -5.42‰.The $\delta^{13}C$ overall variation is 6.33‰ with the minimum value (-8 ‰) at 104 kyr BP and the maximum into the top of the record at 70 kyr BP (-0.5‰). The Mg/Ca mean ratio is 5.5 mmol/mol and the record oscillates between 9.7 mmol/mol and 3.4 mmol/mol in the same time than the $\delta^{13}C$ record. The general patterns among the three records are reasonably similar, although some differences can be observed. For one hand, maximum and minimum values are not coincident in time between the $\delta^{18}O$ and the other two records. On another hand the $\delta^{13}C$ and Mg/Ca present significant enriched values right previous to the hiatus that is not observed in the oxygen record. In general, the $\delta^{13}C$ pattern is coherent with the Mg/Ca ratio along the studied period, although some of the oscillations present a larger expression in the $\delta^{13}C$ record.

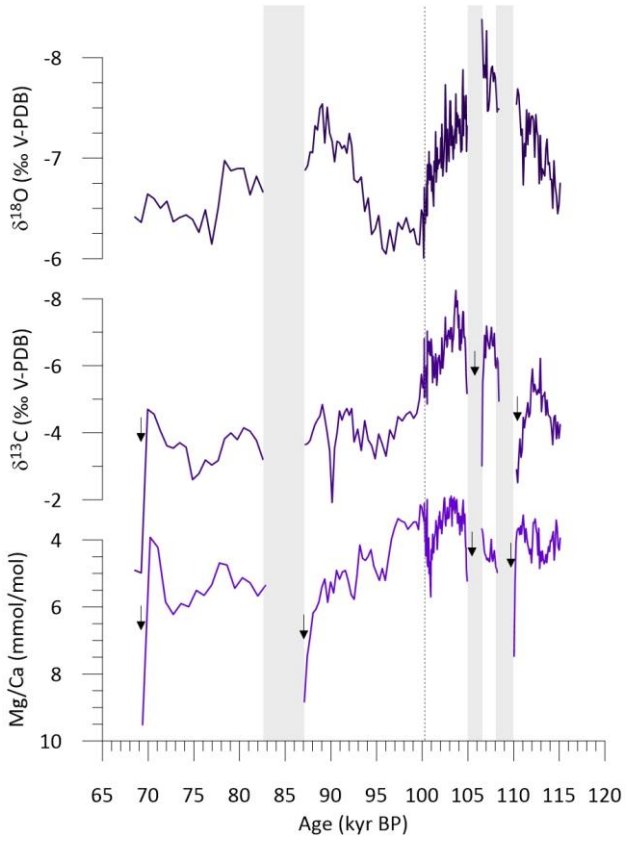

Figure 3.11. $\delta^{18}O$ (top), $\delta^{13}C$ (middle) and Mg/Ca ratios (bottom) from JUD speleothem. Note that the three parameters are plotted with reversal axis. Black arrows show specific trends commented in the main text. The grey bars and the dashed line highlight growth hiatuses and an important visual layer discontinuity as in the JUD age model figure 3.2.

3.2.2 Minorca geochemistry results

The geochemical records acquired from Murada cave speleothems are plotted in figure 3.12. The NOV speleothem presents very parallel evolution in the three studied parameters with a three enrichment picks at the base (13, 12 and 11 ky BP). These events are in line with distinctive coloured layers. These events correspond to the late TI - early Holocene periods although the age model in that part of the speleothem has not a solid constrain. Afterwards, when the chronology is well constrained, all geochemical records stabilise on around the lighter/lower values. The maximum values occurred after 12 kyr BP with values of -4 ‰, 0.2 ‰ and 28.4 mmol/mol for $\delta^{18}O$, $\delta^{13}C$ and Mg/Ca respectively, with an overall variation of 3 ‰, 7.4 ‰ and 23.7 mmol/mol. The IND speleothem is the one analysed at higher resolution. It shows an overall evolution from lower/lighter values at the base toward more enriched/higher values at the top in the three geochemical parameters. However, both the $\delta^{13}C$ and Mg/Ca ratios present a marked inflection point at around 116 kyr BP, when values started to increase more abruptly until the growth was stopped. The Mg/Ca ratios show maximum values of 15.2 mmol/mol and minimum of 5.3 mmol/mol thus with an overall variation around 10 mmol/mol, and a mean value of 8.2 mmol/mol. The $\delta^{13}C$ recorded a mean value of -6.9‰ and the overall variation is 3.66‰. In contrast, the $\delta^{18}O$ record show a progressively enrichment along the whole record with a $\delta^{18}O$ overall variation of 1.45‰ and a $\delta^{18}O$ mean of -5.79‰.

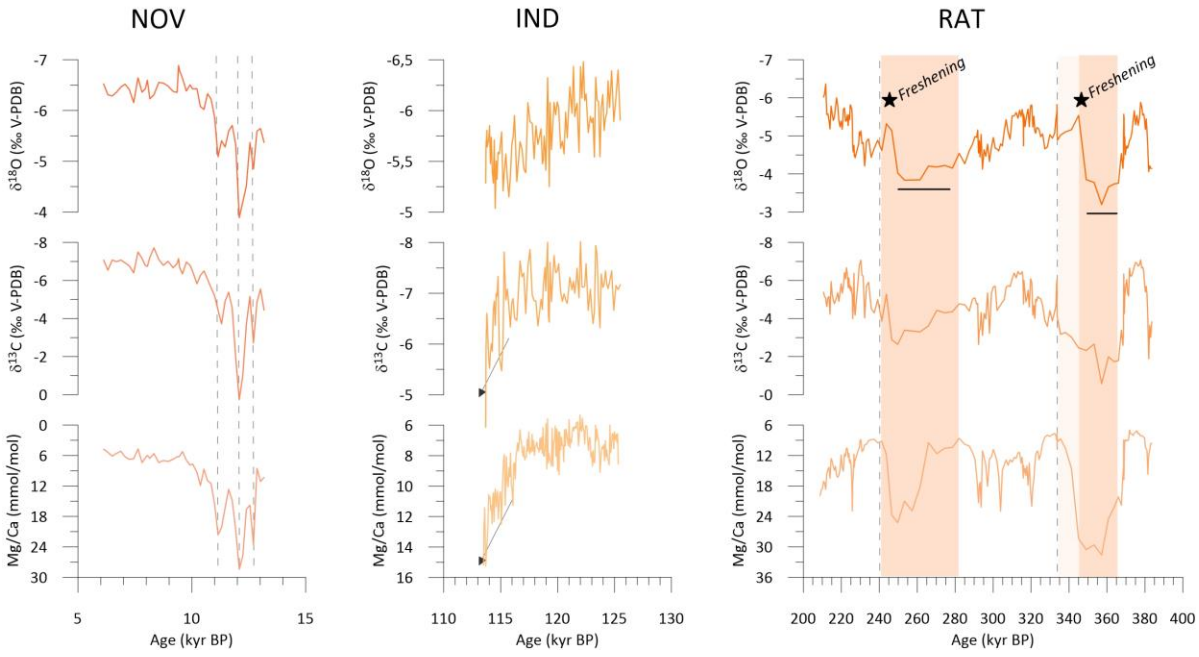

Figure 3.12. $\delta^{18}O$, $\delta^{13}C$ and Mg/Ca records results from Murada cave speleothems. Left) NOV speleothem. Middle) IND speleothem. Right) RAT speleothem. Note that the three parameters are plotted with reversal axis. Grey dashed lines point to layer discontinuities in visual recognition of the speleothem. Black arrows show specific trends commented in the main text. Orange rectangles highlight low growth rate periods. The starts highlight differences among the geochemical parameters commented in the main text.

Finally, RAT speleothem is the one covering a longer time period. In general the three geochemical records present three phases with light isotopes values and low Mg/Ca ratios that are alternated by two phases of heavier isotopes and high Mg/Ca values. The records present an overall variation of 3.2‰, 6.3‰ and 24.6 mmol/mol for $\delta^{18}O$, $\delta^{13}C$ and Mg/Ca respectively. The records corresponding to the two heavier phases (367-347 kyr BP and 263-246 kyr BP) highlighted in figure 3.12 with black horizontal lines, have very low resolution since they correspond to periods of low growth rate (orange rectangles). The end of the low growth rates periods coincides with two layers of visual discontinuities (dashed lines). The three studied geochemical parameters show similarities in the general trend but several differences emerge in the details. Overall, the highest differences occur right after the maximum/heavier values are reached by the three parameters, at the end of the slow growth phases, which always correspond to glacial/interglacial transitions. The minimum Mg/Ca values are always reached well in advance to the lightest values in the $\delta^{13}C$, this is also the case of the $\delta^{18}O$ record although in this case a brief and intense depletion phases appear right before the achievement of minimum Mg/Ca values (black starts).

The geochemical records acquired in speleothems from Polida and Sa Tauleta caves are plotted in Fig. 3.13. Stable isotopes and Mg/Ca ratios were measured in SAV and TER speleothems while only the stable isotopes were analysed for FOS speleothem. SAV stable isotopes records show an overall opposite pattern to that of the Mg/Ca ratio, the lightest isotopic values were reached from 114 to 109.5 kyr BP, when Mg/Ca ratios recorded their highest values. During this time, the $\delta^{18}O$ shows an enrichment tendency while the $\delta^{13}C$ values are rather stable. The overall variability is 2.6 and 7 ‰ for $\delta^{18}O$ and $\delta^{13}C$ respectively. The Mg/Ca ratio shows extreme variability with minimum values of 0.3 mmol/mol and maximum of 60 mmol/mol. Moreover, these Mg/Ca changes occur associated with marked colour discontinuities that may reflect changes in the mineralogy that would involve changes in the element incorporation. The speleothem TER presents very coherent evolution between the $\delta^{13}C$ and Mg/Ca ratios with an initial phase of relative stability (168-152.5 kyr BP) followed by a sudden increase that let a period of relatively high values, which ended at 145 kyr BP when values became suddenly lighter/lower again (Fig. 3.13). The total mean variability for $\delta^{13}C$ is 4.6 ‰ and for the Mg/Ca is 56 mmol/mol. In contrast, the $\delta^{18}O$ show rather opposite trends to those described for $\delta^{13}C$ and Mg/Ca ratios with a clear depleted event between 152.5-145 kyr BP.

Contrary, FOS speleothem shows a parallel evolution in both $\delta^{18}O$ and $\delta^{13}C$ reaching the most depleted values at 134.7 Kyr BP. The total range of variability for $\delta^{18}O$ and $\delta^{13}C$ is 1.2 ‰ and 1.6 ‰ respectively. Mg/Ca ratios are not available in this speleothem.

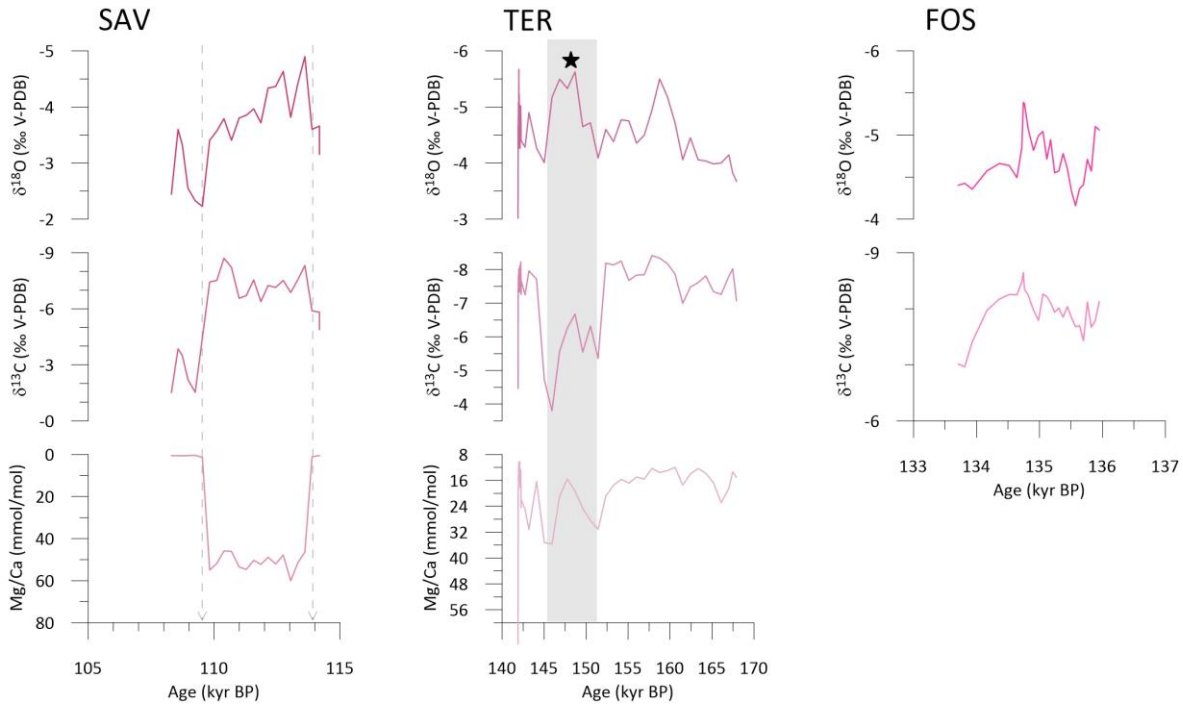

Figure 3.13. $\delta^{18}O$, $\delta^{13}C$ and Mg/Ca records from Left) SAV speleothem, Middle) TER speleothem, Right) FOS speleothem. Note that the three parameters are plotted with reversal axis. Grey dashed lines point to layer discontinuities in visual recognition of the speleothem. The grey area with a black start show the period in which the records are opposites.

3.2.3 Mallorca geochemistry results

The geochemical records acquired from Campanet cave speleothems are plotted in Fig. 3.14 and Fig 3.15. The isotopic records in CAM2 speleothem show noticeable differences in their main patterns while the Mg/Ca ratio record reproduces the $\delta^{18}O$ trends (Fig. 3.14). The $\delta^{18}O$ record shows light values in the oldest period and a progressive transition toward heavier values along the record while the carbon record shows an opposite pattern. The overall variation of CAM2 $\delta^{18}O$, $\delta^{13}C$ and Mg/Ca is 2.5 ‰, 3.5 ‰ and 30 mmol/mol respectively. It is worth to highlight a major change in the growth rate coincident with a visual discontinuity (dashed grey line) at 220 kyr BP that determines the resolution change in the records. The $\delta^{18}O$ and $\delta^{13}C$ records in CAM3 speleothem share the main patterns with a parallel enrichment after 213 kyr BP coincident with a change in both colour and growth axis direction (Fig. 3.14). The overall variation of $\delta^{18}O$ and $\delta^{13}C$ is 2 ‰ and 5 ‰ respectively. Similarly the $\delta^{18}O$ and $\delta^{13}C$

records of CAM4 speleothem show the same with a general trend to lighters values along the speleothem. The growth axis direction change is in line with minimum $\delta^{18}O$ values however this peak is not recorded in the $\delta^{13}C$ signal. The overall variation for this speleothem is 1.3 ‰ and 3.5 ‰ for $\delta^{18}O$ and $\delta^{13}C$ respectively (Fig. 3.14).

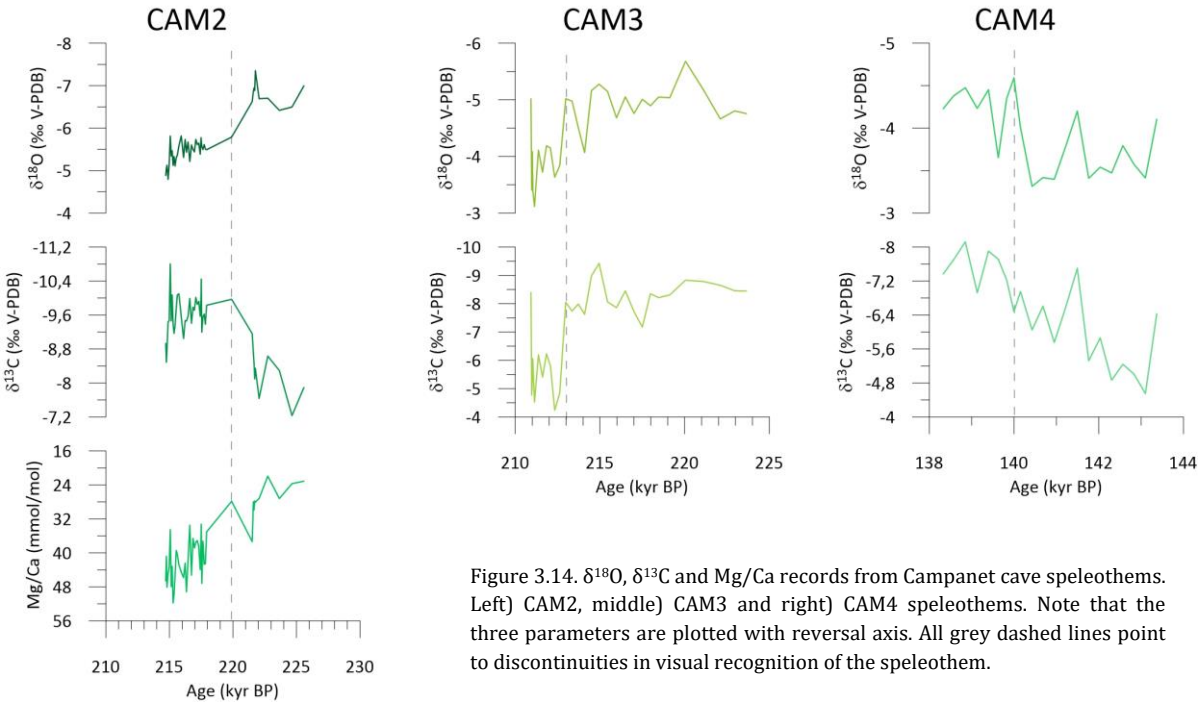

Figure 3.14. $\delta^{18}O$, $\delta^{13}C$ and Mg/Ca records from Campanet cave speleothems. Left) CAM2, middle) CAM3 and right) CAM4 speleothems. Note that the three parameters are plotted with reversal axis. All grey dashed lines point to discontinuities in visual recognition of the speleothem.

The CAM7 speleothem presents major changes in the crystalline structure associated to a very distinct geochemical signal (Fig. 3.15). Before and after the discontinuity, the isotope values change from light to heavy values, but the change is particularly large in the Mg/Ca record likely reflecting mineralogical changes. The $\delta^{18}O$ and $\delta^{13}C$ records from CAM8 show similar general patterns and highlight the occurrence of two major structures with enriched values at ~167 and ~133 kyr BP. Although these second structure is in line with a relevant growth axis direction discontinuity, not all the discontinuities are synchronous with remarkable changes in the geochemical signal. The overall variation is 5.6 ‰ and 10 ‰ for $\delta^{18}O$ and $\delta^{13}C$ respectively (Fig. 3.15).

The only speleothem from Es Quartó cave, QUA14, present very similar general trends on its geochemical records (Fig. 3.15). This speleothem presents major changes in the crystalline fabric that have been characterized by analyses of luminescence that provide high resolution record of changes in colour along the speleothem (Fig. 3.15).

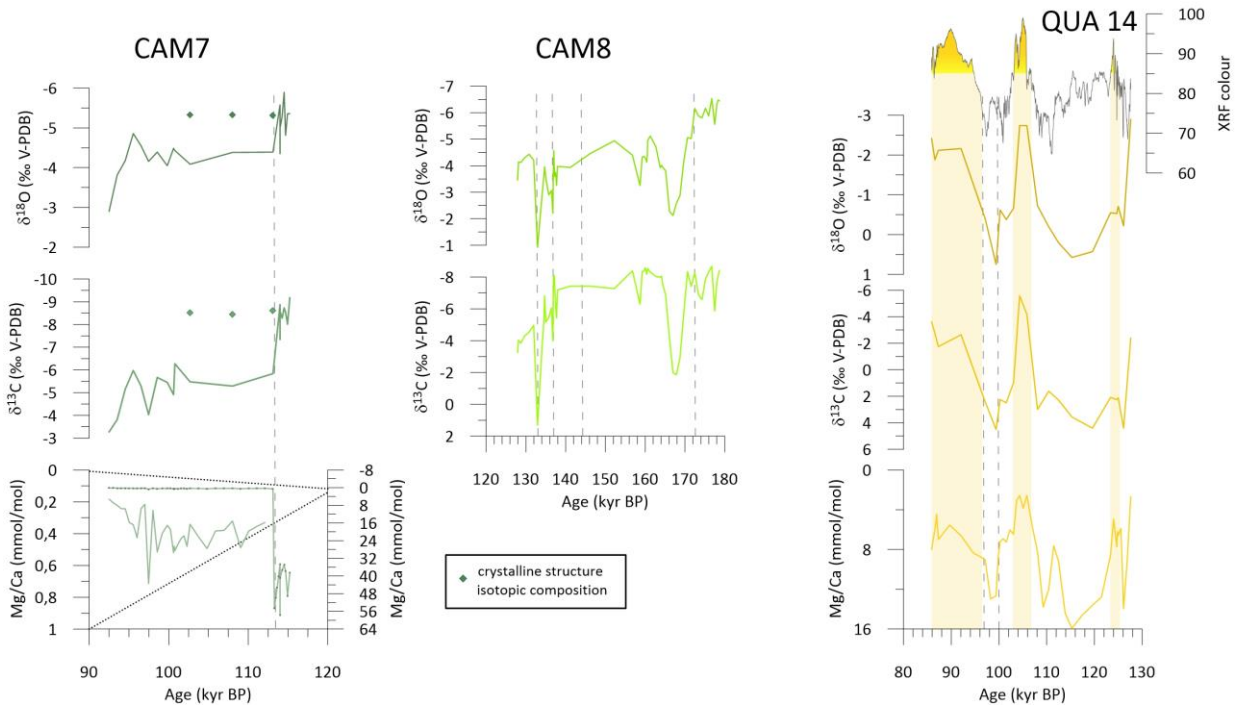

Figure 3.15. $\delta^{18}O$, $\delta^{13}C$ and Mg/Ca records of left) CAM7 and middle) CAM8 speleothems from Campanet cave. Into the right) QUA14 speleothem from es Quartó cave, where the geochemical records are compared with the luminescence results. Yellow-orange rectangles highlight white-coloured areas of fast growth rates. All grey dashed lines point to discontinuities in visual recognition of the speleothem. Note that the three geochemical parameters are plotted with reversal axis.

The QUA14 speleothem present three well defined areas of high luminescence reflecting white colour areas and which are in line with fast growth rates. Coinciding with these white-coloured fast growth rate areas the geochemical records shows light isotopes and low Mg/Ca ratios, although at the oldest white-coloured period the isotopic light anomaly is not so well represented. These structures are alternated by two periods (124-107 and 103-96 kyr BP) of high values in all three geochemical parameters and these periods correspond with changes in the growth axis direction. The Mg/Ca ratio record has been analysed at higher resolution providing a better characterization of the oldest white-coloured interval. The overall variation of QUA14 for $\delta^{18}O$, $\delta^{13}C$ and Mg/Ca is 3.6 ‰, 10 ‰ and 13.3 mmol/mol respectively.

The geochemical records acquired in Vallgornera cave speleothem are plotted in Fig. 3.16. The three geochemical parameters of the VALL2 (the oldest among all the studied speleothems) present a very consistent evolution with a remarkable structure of heavier $\delta^{18}O$, $\delta^{13}C$ and higher Mg/Ca ratios between 510 and 455 kyr BP. This interval is also coincident with three major changes in the growth axis direction and colour laminations. After that, all three records show relatively light/low values until the end of the record. The overall variation is 3.4 ‰, 3.8 ‰ and 15.7 mmol/mol for $\delta^{18}O$, $\delta^{13}C$ and Mg/Ca ratio

respectively. Isotopic records in the VALL3 speleothem present some significant differences in the oldest part of the records, when $\delta^{13}C$ reach the heaviest values peaking at 110.4 ky BP while the $\delta^{18}O$ record is rather flat. Changes in the growth axis direction at the base of the speleothem are in line with the termination of this $\delta^{13}C$ structure. The overall variation for the $\delta^{18}O$ and $\delta^{13}C$ is 1 ‰, 4.2 ‰ respectively. Finally, VALL4 speleothem has only been analysed for the Mg/Ca ratio, presenting a major change around 384 ky BP when the ratio shifted from higher to lower values with an overall variation of 6 mmol/mol.

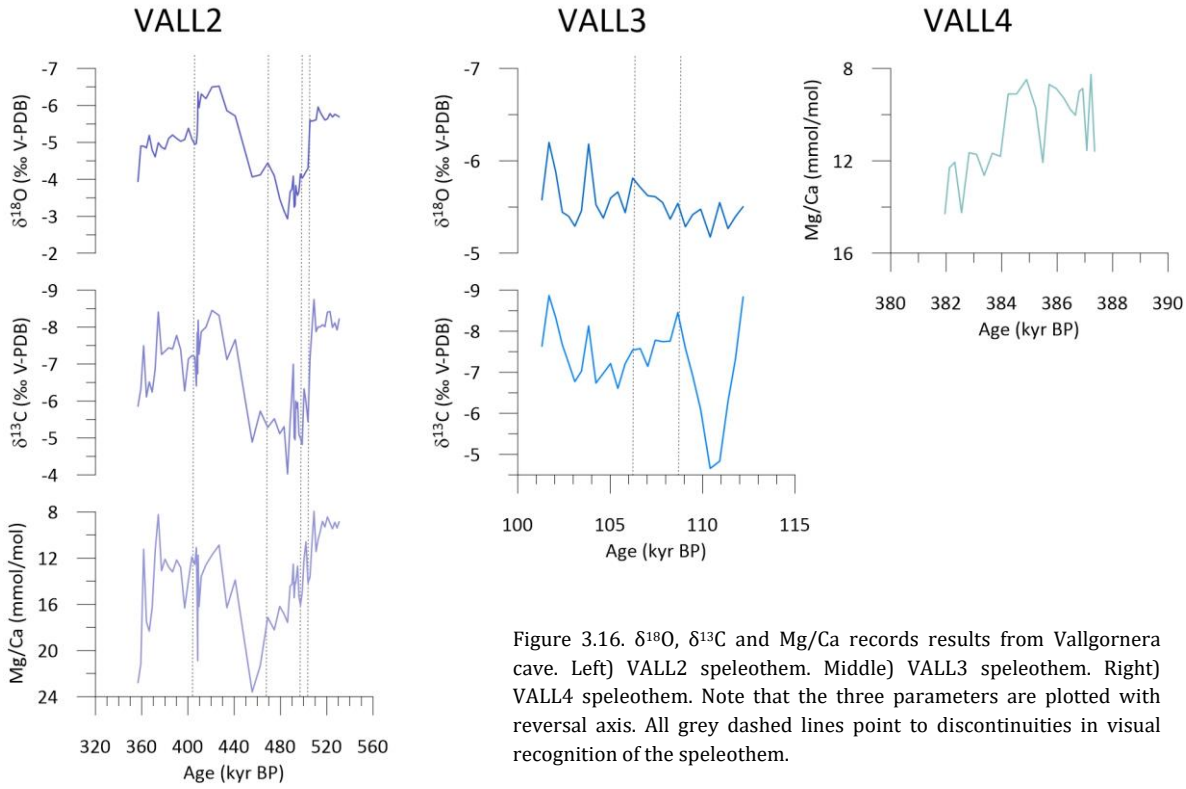

Figure 3.16. $\delta^{18}O$, $\delta^{13}C$ and Mg/Ca records results from Vallgornera cave. Left) VALL2 speleothem. Middle) VALL3 speleothem. Right) VALL4 speleothem. Note that the three parameters are plotted with reversal axis. All grey dashed lines point to discontinuities in visual recognition of the speleothem.

3.3 The assemblage signal of the studied speleothems

Several factors can control the speleothem isotopic composition and also the trace element incorporation (see section 2.4.3 and 2.5.4), and they can vary according to the region or to the cave. But even in close locations inside the same cave chamber, speleothems can provide different absolute values due to for example different percolation features or chamber conditions. Hence multiproxy approaches are necessary in order to better understand proxy signals and connect it with climate. Moreover, the evaluation of independent speleothems overlapped on time can bring a light on the suitability of their chemical records for paleoclimate interpretations. Several temporal overlaps exist for the speleothems here studied, but in order to better compare the intensity of the changes between the different geochemical records, the records have been normalized. This has been done in base to the mean value of each speleothem record. In the figure 3.17 can be seen the difference between absolute and normalized data for all the analysed speleothems.

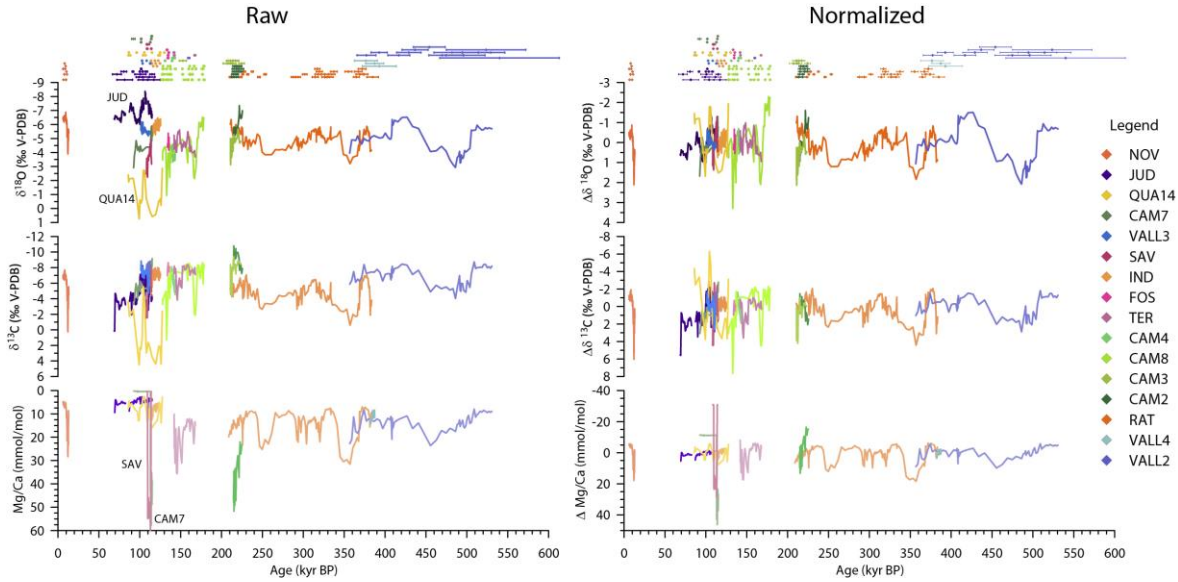

Figure 3.17. $\delta^{18}O$, $\delta^{13}C$ and Mg/Ca records from all speleothems indicating the control age points and associated errors. Left) Raw data, Right) normalized data.

The isotopic oxygen records are the most variable in absolute values but once they are normalized the amplitude changes are very comparable for most of the speleothems. Among all the speleothems, JUD is the one with lighter $\delta^{18}O$ values while the QUA14 presents the heaviest values (fig. 3.17). Taking the consideration that JUD is the only speleothem from a Pyrenees cave, and thus the one form a higher altitude, these observations are indeed in line with the spatial gradient observed by European

speleothems. The altitude factor generates a shift to lower $\delta^{18}O$, as such in JUD speleothem, while those speleothems from caves close to the Mediterranean coast have enriched $\delta^{18}O$ values, likely reflecting a more dominant source effect over the signal (Mc Dermott *et al.,* 2011). Regarding to the $\delta^{13}C$ records, the absolute values are not as variable such as of the $\delta^{18}O$ and when comparing the normalized values the variability is consistent among speleothems. The amplitude changes in the Mg/Ca records are also quite comparable among the different speleothems with the only exception of SAV and CAM7 speleothems which grew during very short periods within the MIS 5 period. These speleothems present extremely large Mg/Ca variations, which are in line with texture and colour changes that designates visual discontinuities likely related to changes in the mineralogy that could be the cause for the large chemical changes. In the view of these circumstances, these two speleothems were discarded for further discussions.

Overall, the geochemical record acquired in this thesis cover almost continuously the last 5 interglacial periods and the glacial intervals between them. In general, cold stadial periods present the heavier isotopic values with high Mg/Ca ratios in contrast to low values during interstadials (Fig. 3.18). This data comparison allows evaluating the suitability of individual speleothems as climate archives.

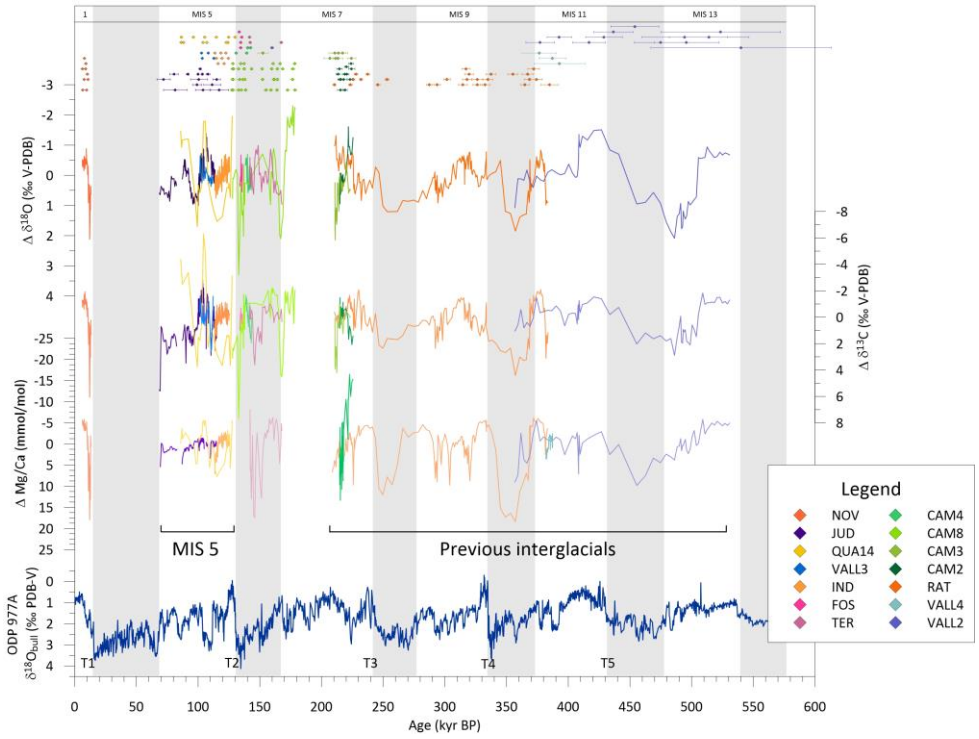

Figure 3.18. Normalized $\delta^{18}O$, $\delta^{13}C$ and Mg/Ca records from several speleothems indicating the control age points and associated errors and compared with the $\delta^{18}O$ measured *G. bulloides* from the marine sediment core ODP 977 from the Alboran Sea (Martrat *et al*., 2007 and unpublished data). Grey bars indicate glacial periods. The horizontal black lines covers the time intervals discussed in sections 4.3 and 4.4

The MIS 5 is the better represented period with several overlapped speleothems and two of them with high resolution (JUD and IND). This period has also been the one studied in detail by the marine records and, in consequence, it will be the object of specific attention in a dedicated section where both speleothem and marine records will be integrated (Section 4.4). On the other hand, the MIS 5 previous interglacial periods will be discussed in a separate section (4.3) where RAT and VALL2 speleothems will concentrate the most attention due to their long time coverage. Additionally, several terminations are also covered by the speleothem records and recognized in their geochemical signals, usually as intense depletions in the isotope records and rapid transitions toward low Mg/Ca ratios. However, the TII is not well recorded in any of the studied speleothems since none of them grew continuously along this transition. Interestingly, six of the studied speleothems grew close to the TII but all of them stopped or started to grew close to this transition, just before and after, avoiding its whole coverage. Since the focus of attention of the study is on the interglacial periods and associated transitions those speleothems that completely grew during the glacial period MIS 6 (CAM8, TER and FOS) has not been included in the discussion.

Here below in table 3.1 is provided a summary of the geochemistry results for all the 16 selected speleothems.

Table 3.1

				Isotopes						Mg/ Ca			
Location	Cave	Name	Long. (cm)	num. samples	resolution (cm)	$\delta^{18}O$ mean (‰)	$\delta^{18}O$ range (‰)	$\delta^{13}C$ mean (‰)	$\delta^{13}C$ range (‰)	num. samples	resolution (cm)	mean (mmol/mol)	range (mmol/mol)
Pyrenees	Pot eu feu	Judit	55	233	0,25	-7	2,4	-5,40	6,3	233	0,25	5,5	6,3
Minorca	Murada	Novena	45	45	1,0	-6	3	-5,8	7,4	45	1	10,5	23,7
	Murada	Indiana	88	93	1,0	-5,8	1,4	-6,9	3,6	180	0,5	8,2	10
	Murada	Ratpenat	50	197	0,25	-5	3,2	-5	6,3	204	0,25	13,2	24,6
	Sa Tauleta	Fosca	65	28	1,0	-4,7	1,2	-8	1,6	n	n	n	n
	Sa Tauleta	Teresa	54	65	0.5/1	-4,6	2,4	-7,4	4,6	65	0,5/1	18,2	56
	Polida	S'avia	70	23	3,0	-3,6	2,8	-6	7	23	3	31,4	59,7
Mallorca	Campanet	CAM2	46	45	1,0	-5,7	2,5	-9,3	3,5	45	1	38,4	30
	Campanet	CAM3	31	28	1,0	-5,3	2	-8,4	5	n	n	n	n
	Campanet	CAM4	19	21	0.5/1	-3,9	1,3	-6,5	3,5	n	n	n	n
	Campanet	CAM7	21	21	1,0	-4,6	3	-6,4	5,5	47	0,50	11,6	56,8
	Campanet	CAM8	52	56	0.5/1	-4,2	5,6	-6,4	10	n	n	n	n
	Vallgornera	VALL2	22	70	0,2	-5	3,4	-7	3,8	70	0,2	13,8	15,7
	Vallgornera	VALL3	25	28	1,0	-5,5	1	-7,2	4,2	n	n	n	n
	Vallgornera	VALL4	23	n	n	n	n	n	n	24	1	10,7	6
	Es Quartó	QUA14	20	21	1,0	-0,9	3,6	-0,7	10	41	0,5	8,2	13,3

3.3.1 The speleothem records for old interglacial periods

The old interglacial periods refer to those interglacial previous to the last interglacial (MIS 5) which are covered by the studied speleothems, and thus correspond to MIS 7, 9, 11 and 13, although the MIS 7 and 13 are not totally represented (Fig. 3.19). In absolute time this period corresponds to 540 to 210 kyr BP and is mostly covered by VALL2 and RAT speleothems, from Mallorca and Minorca respectively. VALL 2, the oldest one, started to grow at the end of the MIS 13 and recorded the onset of the MIS 12 glacial period with a rapid isotopic enrichment in line with the first change in growth axis direction (Fig. 3.19). After the glacial maximum around 455 kyr BP the three geochemical records agree in a transition toward low/light values that correspond to the Termination V (TV). During the Interglacial MIS 11 values maintained relatively stable but with some internal variability as an enriched event at 408 kyr better represented in the Mg/Ca record and also coincident with other change in growth axis direction.

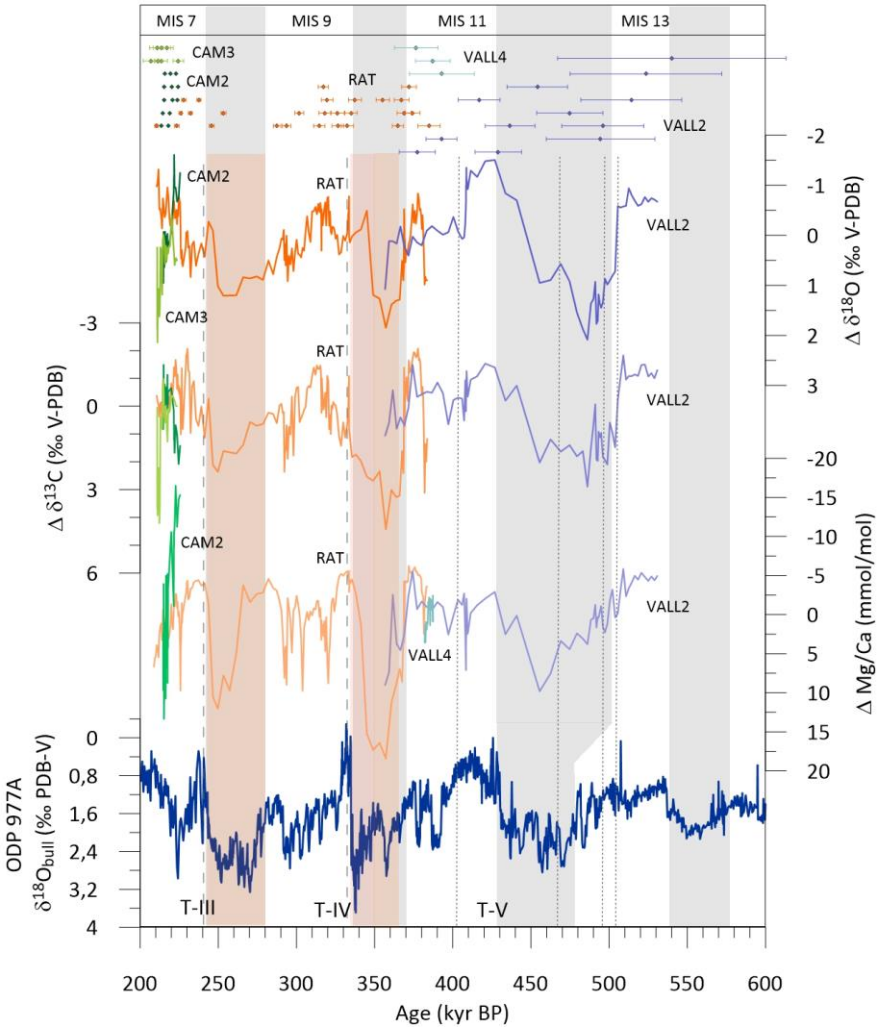

Figure 3.19. Normalized $\delta^{18}O$, $\delta^{13}C$ and Mg/Ca records from several speleothems covering old interglacial periods indicating the control age points and associated errors and compared with the $\delta^{18}O$ measured *G. bulloides* from the marine sediment core ODP 977 from the Alboran Sea (Martrat *et al.,* 2007 and unpublished data). Grey bars indicate glacial periods. Grey lines highlight visual discontinuities in speleothems. The orange rectangles highlight RAT low growth rate periods.

The VALL4 speleothem grew very shortly by the end of the MIS 11 but its Mg/Ca record is coherent with the VALL2 speleothem and also RAT speleothem that started to growth by the time that VALL 4 was forming (390 kyr BP) (Fig. 3.19). Both VALL4 and RAT speleothems agree recording a drop phase in Mg/Ca ratios at 380 kyr BP that precedes to the full transition at ~370 kyr BP toward MIS 10 glacial conditions which is well represented in both isotopic and Mg/Ca ratios from RAT and also VALL2, although with a less robust chronology. The RAT speleothem fully covers two glacial terminations (TIV and TIII) well represented by a rapid transition toward light isotopes and low Mg/Ca ratios although the precise time of the major changes are not coincident between the different proxies. The $\delta^{18}O$ record is the first to present a transition toward lighter values while Mg/Ca ratios drop abruptly later with an even later depletion phase in the $\delta^{13}C$ record. The interglacial MIS 9 is represented in the Mg/Ca record by three structures of relatively low values separated by brief and abrupt drops, structures that are not well represented in the isotopic records. Finally, the interglacial MIS 7 is covered by the RAT speleothem but the second half also overlaps with the CAM2 and CAM3 speleothem (Fig. 3.19). The three records show coherent trend although with variable magnitude. It is worth to highlight that the RAT speleothem presents a very accurate chronology and continuity in its growth patterns. It also needs to be recognized that this speleothem was collected from the same chamber and from a near location to IND and NOV speleothems, which also present exceptional accurate chronologies and records for the MIS 5 and MIS 1. This feature supports the dominance of stable cave conditions for speleothem growth during interglacial climate conditions, providing to these speleothem a good value as paleoclimate archives.

3.3.2 The speleothem records for the Last Interglacial

A total of 4 speleothems grew during the last interglacial (MIS 5) but none of them cover entirely the whole interglacial period. These speleothems come from different sites, the IND speleothem from Minorca, the JUD speleothem from the Pyrenees and VALL3 and QUA14 from Mallorca. IND and JUD speleothems have been studied in more detail and at higher resolution than the VALL3 and QUA14 speleothems (Fig. 3.20). In general, the four speleothems show the same general trend in the $\delta^{18}O$ signal with two enriched periods, one at the end of the MIS 5e and other one in the middle of the MIS 5c. During these enriched periods the speleothems present several changes in the growth axis direction, in the case of the ~100 kyr BP event both QUA14 and JUD speleothem changed

synchronously their growth axis direction. Between these events the $\delta^{18}O$ record was dominated by relatively light values in JUD but also in QUA14 speleothem where they coincided with white-coloured phases of fast growth rate. The lightest $\delta^{18}O$ values occurred at 120-110 kyr BP at the beginning of the warm sub-stage MIS 5c. The $\delta^{13}C$ and Mg/Ca ratio records agree with same of the features described for the $\delta^{18}O$ records but overall present several differences. For instance, during the MIS 5e the IND speleothem shows a shift to higher values at 116kyr BP in both Mg/Ca and $\delta^{13}C$ that is not observed in the $\delta^{18}O$ record. JUD speleothem presents some growth hiatus coincident with cold stadial periods always preceded by large enrichments in the $\delta^{13}C$ and Mg/Ca ratio and not observed in the $\delta^{18}O$ signal. The $\delta^{13}C$ and Mg/Ca enrichment associated to the JUD hiatus during the MIS 5d is also detected in the QUA14 and the VALL3 records although it does not occur for the second JUD hiatus at ~105kyr BP. The VALL3 speleothem detected two changes in its growth axis directions in line with these JUD hiatuses.

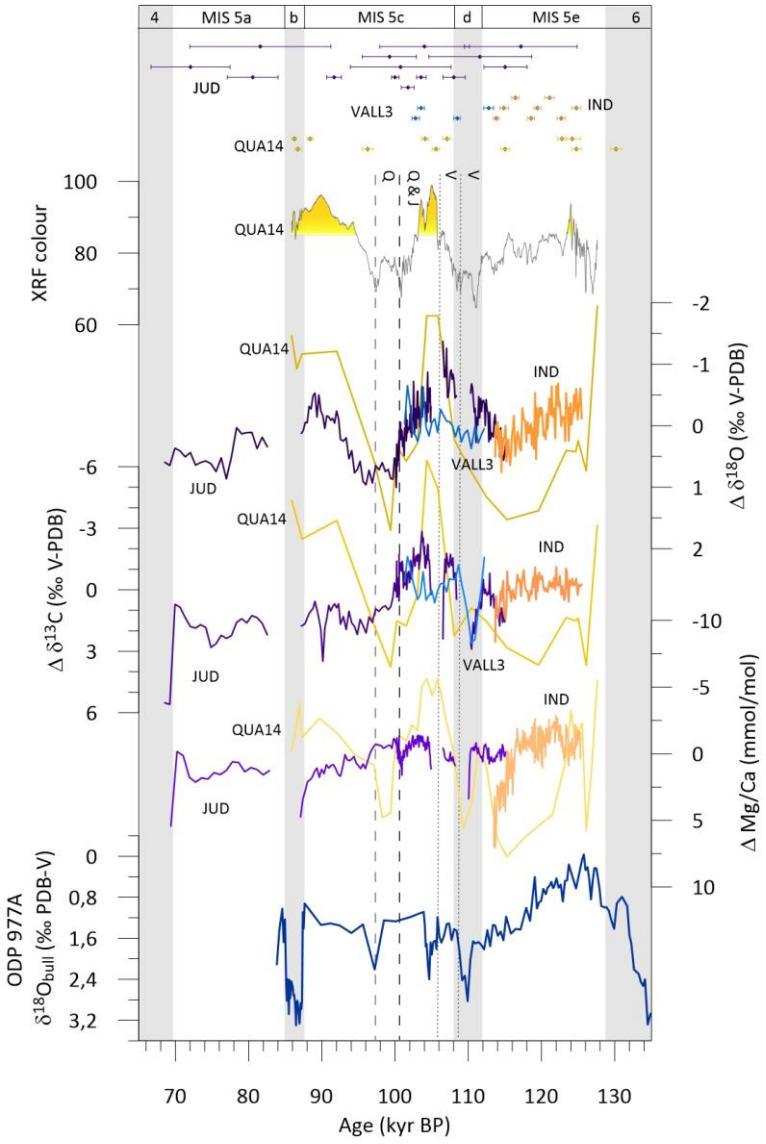

Figure 3.20. Normalized $\delta^{18}O$, $\delta^{13}C$ and Mg/Ca records from several speleothem covering the MIS 5 indicating the control age points and associated errors and compared with the $\delta^{18}O$ measured *G. bulloides* from the marine sediment core ODP 977 from the Alboran Sea (Martrat *et al.*, 2007). The luminescence record of QUA14 is also represented with grey and yellow colours. Vertical grey lines highlight visual discontinuities in speleothems V) VALL3, J) JUD and Q) QUA14. Grey bars indicate stadial periods.

3.4 Marine chronological framework

The sequence of marine isotope stages/sub-stages (MISs) and also Greenland Stadials can be well identified in the $\delta^{18}O_{G.bulloides}$ records of the three studied cores, which in addition show an extraordinary resemblance among them (Fig. 3.21). The age model of ODP Site 977A and PP10-17 are mostly based on previous published chronologies (Martrat *et al.,* 2007; Brocheray *et al.,* 2014 and Rodriguez-Lazaro *et al*., 2017) with the addition of some tie points for coherence between the three studied records. These additional tie points were assessed on the basis of the alignment of the $\delta^{18}O_{G.bulloides}$ records with: 1) the Greenland ice core record for the MIS 5 and 4 period using the $\delta^{18}O$ of NGRIP2 50 yrs means on the GICC05modelext timescale record (Rasmussen *et al.,* 2014; Seierstad *et al.,* 2014) (Fig. 3.21 A); 2) the $\delta^{18}O_{G.bulloides}$ record from ODP Site 975 to constrain the penultimate deglaciation and the MIS 5e (Marino *et al.*, 2015) (Fig. 3.21 B); and 3) the $\delta^{18}O_{G.bulloides}$ record from ODP Site 976 to anchor the oldest part of the age model (Jiménez-Amat and Zahn, 2015) (Fig. 3.21 C). The ODP Site 975 chronology is based in the alignment with an eastern Mediterranean core previously tuned to the radiometrically chronology of the Soreq record, while the ODP 976 site age model was also correlated with speleothem records from European caves (Drysdale *et al*., 2009; Couchoud *et al*., 2009), thus both marine records are independent to orbital tuning. Furthermore, the age model of core MD99-2343 was produced in this study by alignment of its $\delta^{18}O_{G.bulloides}$ record with the NGRIP2 record (Rasmussen *et al.,* 2014; Seierstad *et al.,* 2014). Although the potential uncertainties associated with the correlation of SST and $\delta^{18}O_{G.bulloides}$ with the NGRIP2 record due to the effect of light melt water into the surface waters, the alignment was performed since several studies have shown the suitability of the use of the $\delta^{18}O$ ice cores record from Greenland as an isotopic chronostratigraphic reference for age modelling for both Mediterranean (Cacho *et al.,* 1999; Martrat *et al.,* 2007; Rohling *et al*., 1998; Sierro *et al.,* 2005; Sprovieri *et al.,* 2006) and N Atlantic cores (Cayre *et al.,* 1999; Govin *et al.,* 2015). Moreover, cold stadial events were well characterized by the presence of *N. pachyderma sin*. in the PP10-17 core by Rodriguez-Lazaro *et al.,* (2017), increasing the confidence of the alignment of the Cantabrian core with the Greenland record. In summary, 54 tie points have been used for the tuning of all three sediment cores in base of the most relevant structures, particularly those corresponding to the penultimate deglaciation and the Greenland Stadials (GS) (Table Annex 7).

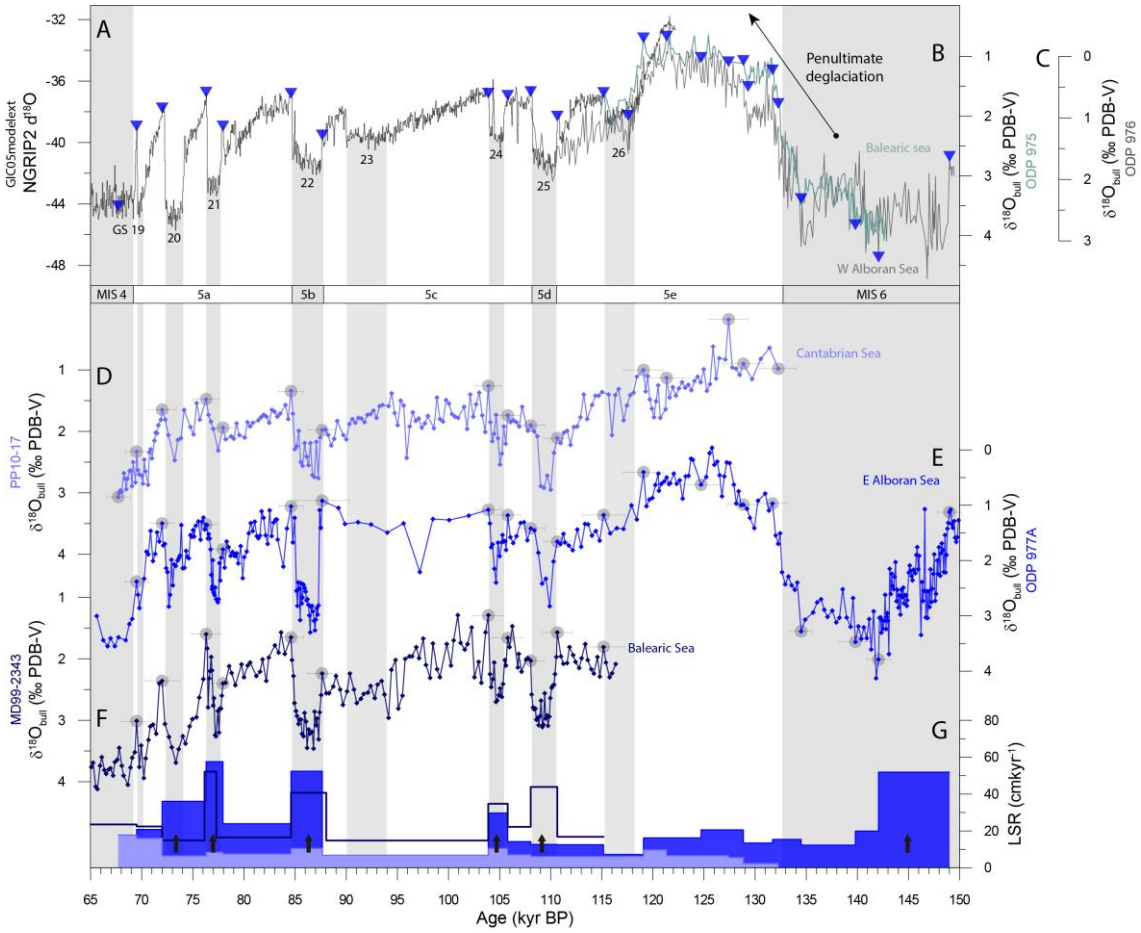

Figure 3.21. Records used for the age model construction of the studied marine cores A) $\delta^{18}O$ NGRIP2 GICC05modelext timescale record use as a reference record (Rasmussen *et al.,* 2014; Seierstad *et al.,* 2014). B) The $\delta^{18}O_{G.bulloides}$ ODP Site 975 record from the Balearic Sea used as a reference record (Marino *et al.*, 2015). C) The $\delta^{18}O_{G.bulloides}$ ODP Site 976 record from the West Alboran Sea also used as a reference record (Jiménez-Amat and Zahn, 2015). D) $\delta^{18}O_{G.bulloides}$ for PP10-17 core E) $\delta^{18}O_{G.bulloides}$ for ODP Site 977 modified from Martrat *et al.,* 2007 and F) $\delta^{18}O_{G.bulloides}$ for MD99-2343 core. G) Linear sedimentation rates (LSR) for the three studied marine cores. The blue triangles indicate the tie points used in this study. Gray circles indicate the tie points over each tuned record indicating the uncertainties of the used alignment. Vertical grey bars show Marine Isotopic Stages and sub-stages (MIS 4-6) and/or Greenland stadials (GS19-26).

Correlations among the marine records were estimated by linear interpolation using the Analyseries Software package (Paillard *et al*., 1996**)**. The relative age uncertainties were estimated for every performed alignment following the approach used by Grant *et al.,* (2012) and consisting in the propagation of involved uncertainties by means of the mean squared estimate (MSE) (Table Annex 7). These chronological uncertainties include the reference record age uncertainties (only provided in the case of the ODP 975), the sample spacing from the aligned and reference records and, an extra-imposed uncertainty. The extra uncertainty depends of the level of the alignments confidence, and consists in this study in the addition of ±0.5 kyr for those alignments whose reference age uncertainty is provided (ODP 975) and ±1 kyr for those where the reference age uncertainties are not

provided (NGRIP and ODP976). The obtained age models indicate that PP10-17 samples used in this study spans from 132 to 68 kyr BP, therefore it starts recording the middle of the penultimate deglaciation (Fig. 3.21D), whereas ODP Site 977A samples exceeds the MIS5 interglacial period, from the end of the MIS 6 until the beginning of the MIS 4 (Fig. 3.21 E). MD99-2343 samples spans from 116 to 64 kyr BP, leaving thus the MIS 5e poorly represented in the Balearic Sea (Fig. 3.21 F). The temporal resolution achieved within those three records reach centennial scale, allowing identifying changes and fluctuations that occurred within multi-centennial/millennial time scales. Average sedimentation rates range from 10.6 cm/kyr, 22.8 cm/kyr to 30.2 cm/kyr for cores PP10-17 (Cantabrian), ODP Site 977A (Alboran) and MD99-2343 (Balearic), respectively (Fig. 3.21 G). In the context of the Mediterranean Basin, both Mediterranean sediment cores present high sedimentation rates, which are coherent with other studies from this region (Frigola *et al.,* 2008, 2007; Jiménez-Amat and Zahn, 2015). Note that the highest sedimentation rates occurred during intervals with heavy $\delta^{18}O$ values, corresponding to cold stadials periods.

3.5 Marine core results

3.5.1 Cantabrian sediment core

The Mg/Ca ratios of the sediment core PP10-17 ranges between 3.92 and 1.8 mmol/mol, with a ratio mean of 2.7 mmol/mol. This oscillation corresponds to an amplitude of 7.3°C for the SST in the Cantabrian Sea during the studied period. The measured SST and the associated errors are plotted in Fig. 3.22. The MIS 5e and c sub-stages show warm SST while MIS 5a was generally cooler. At 101.5 kyr BP the record shows an abrupt cold event. Although in general, the core show moderate $\delta^{18}O_{sw}$ values during stadials, it is worth to highlight two extreme freshening events. The first one at the end of the MIS 6, and the other at 101.5 kyr BP, coinciding with this cold Cantabrian event during the MIS 5c.

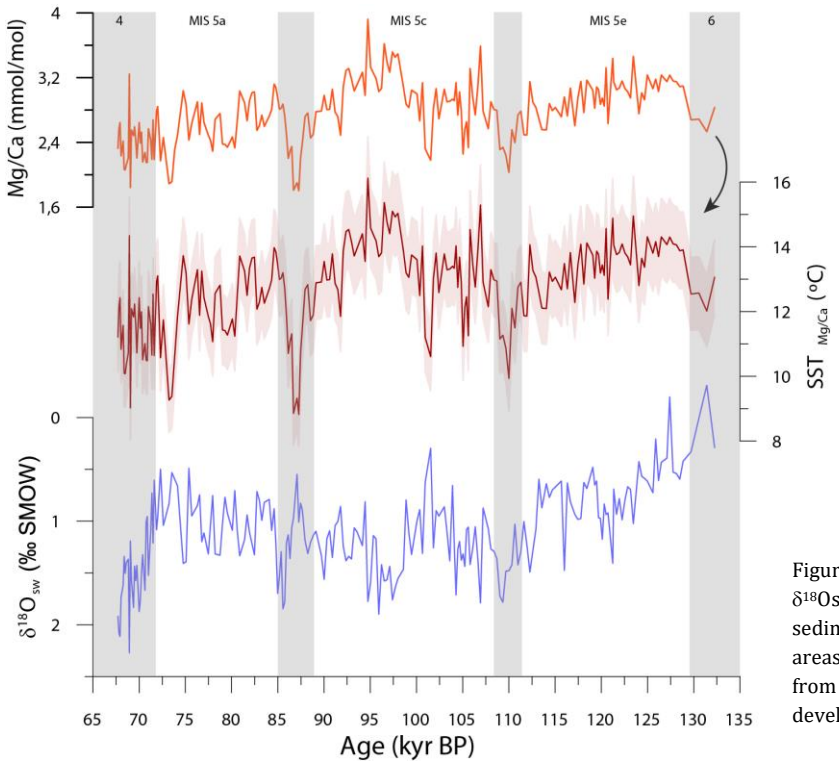

Figure 3.22. Mg/Ca, SST and the δ^{18}Osw results for the PP10-17 sediment core. The pink shaded areas integrate uncertainties derived from the SST *G. bulloides*-calibration developed in Cisneros et al. (2016).

3.5.2 Alboran sediment core

ODP Site *977A* Mg/Ca ratios mean is 3.4 mmol/mol and the record oscillates between 4.9 mmol/mol and 2 mmol/mol that correspond to SST amplitude of 7.5°C for the Alboran Sea (Fig. 3.23). Mg/Ca-derived SST record show three cold intervals alternated with two warm periods coherent with the cold and warm marine sub-stages. The

minimum SST values were reached around 130 kyr BP during the MIS 6 while warmer temperatures were reached at 120 kyr BP (MIS 5e). Regarding to the $\delta^{18}O_{sw}$ record the most prominent structure is the rapid freshening event with a ~3‰ lightening around 133 kyr BP at the end of the MIS 6. In general, the core shows high or moderate values during stadials and full glacial while fresher values during warm sub-stages.

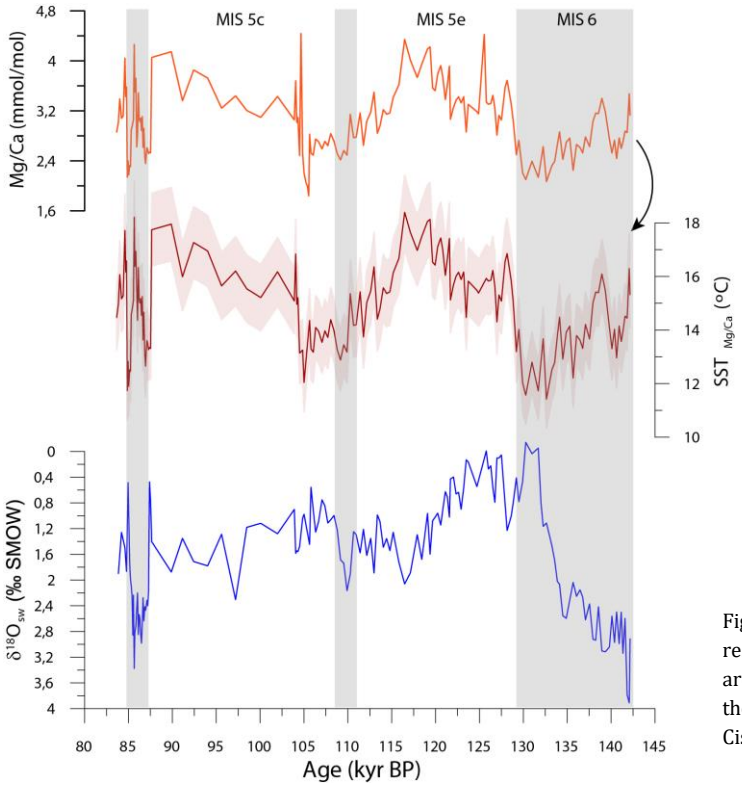

Figure 3.23. Mg/Ca, SST and the δ^{18}Osw results for the ODP 977 site. The pink shaded areas integrate uncertainties derived from the SST *G. bulloides*-calibration developed in Cisneros et al. (2016).

3.5.3 Balearic sediment core

The mean Mg/Ca ratio in *MD99-2343* core is 3.9 mmol/mol and oscillates between 6 and 2.5 mmol/mol corresponding to an overall SST amplitude of 8°C in the Balearic Sea during the studied period. The Mg/Ca ratios and the inferred SST with associated errors are shown in Fig 3.24. Maximum SST values were recorded at the oldest interval of the record at the end of the MIS 5e and reached almost 20°C while minimum temperature, around 12°C, is recorded at 105.5 kyr BP and coinciding with a cold stadial. Although the record shows three warm sub-stages, the observed general trend is a slightly cooling. The core show relatively high-moderate values of $\delta^{18}O_{sw}$ during stadial periods and the MIS 4 (>3‰) and light values at the beginning of the warm-sub stages (MIS 5a and b).

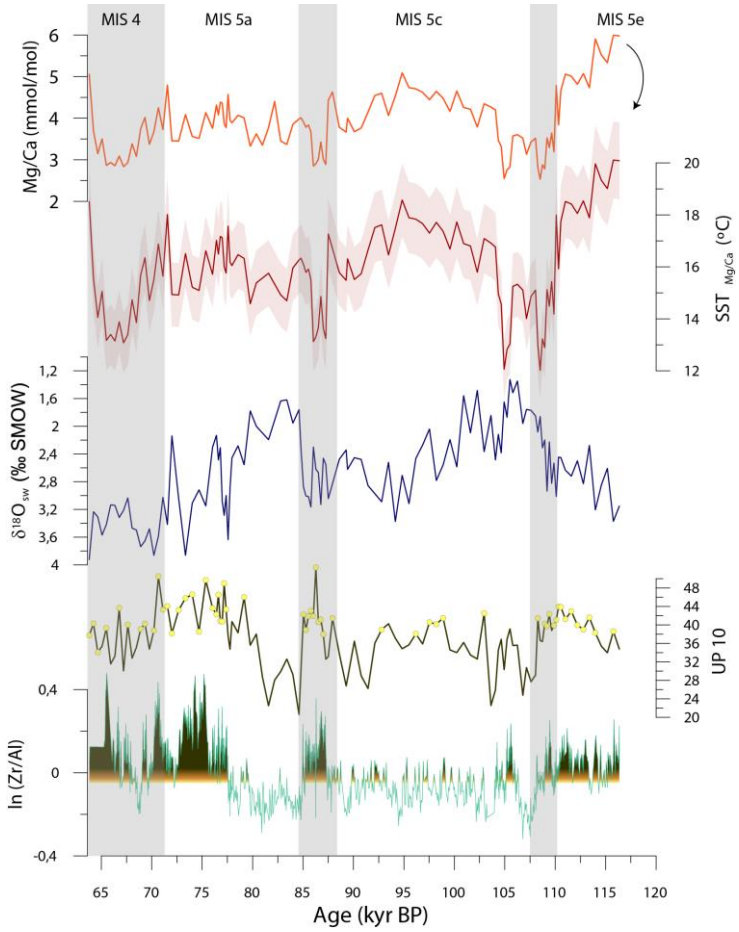

Figure 3.24. Mg/Ca, SST, $\delta^{18}O_{sw}$ UP10 and Zr/Al results for the MD99-2343 core. The pink shaded areas integrate uncertainties derived from the SST *G. bulloides*-calibration developed in Cisneros et al.,(2016)

The UP10 index and Zr/Al record have been analysed in order to elucidate the sedimentological changes in the Minorca Drift associated to deep current intensity (Fig. 3.24). The UP10 record has not obvious long-term trend. It presents high values in line with cold stages but also at the end of the warm sub-stages MIS 5 e and c, while low UP10 is always present within the warm intervals. The clustering analysis of grain size modal distribution results are shown in fig 3.25, and are classified from cluster 1 to 4 according to their frequency within samples. All samples show a low mode around 0.25 μm whereas the principal mode is slightly different among clusters. The Cluster 1 that comprises the 49% of all the samples has the main mode around 10 μm while the Cluster 2 (38% of samples) has the main mode around 8 μm and it is better classified. The cluster 1 corresponds to the coarser samples and it is associated to high UP10 index values (Fig. 3.24: yellow dots) whereas cluster 2 is associated to low UP10. The other two less abundant clusters present a bimodal peak with the major mode around 20 μm with a sharp decrease of coarse grains and are not interpreted due to its poor abundance.

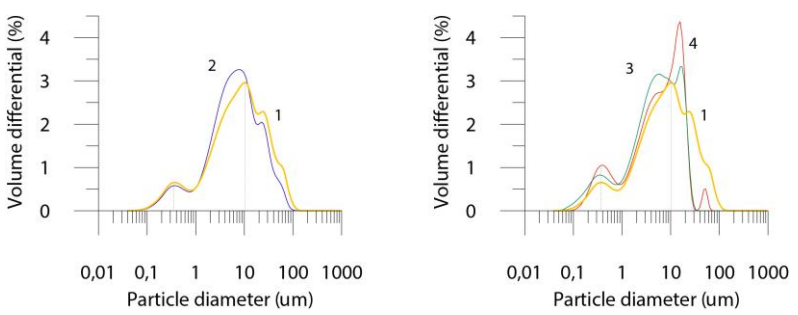

Figure 3.25. MD99-2343 core modal distribution classified in four groups (Clusters 1-4). In left, comparison between the Cluster 1 which has the coarsely modal distribution compared with the Cluster 2. In the right comparision of Cluster 1 with less abundant clusters 3 and 4.

The principal component analysis results of the elemental XRF-data shows that the PC-1, explaining the 77% of the total variance, can be interpreted as carbonate versus detrital siliciclastic supplies (Ca and Sr opposed to all the other elements) (Fig. 3.26). The PC-2 explains 9.49% of the variance and opposes the aluminosilicates elements to barium, which can be related to productivity. Although explaining only a 5.6% of the total variance, the PC-3 is clearly dominated by Zr, reinforcing the Zr/Al as a proxy of accumulated heavy minerals due to current intensity sorting. The measured Zr/Al ratio results are plotted using logarithm values in order to amplify its variability in figure 3.24 with brown coloured areas highlighting the higher intervals. The variability of this record is in line with the UP10 index record and also coincides with the appearance of cluster1 samples. The record shows low values during all the warm sub-stage MIS c whereas the MIS 5a present low but also high values and until the end of the record.

PC	Variance (%)	Cumulative Variance (%)
1	77,14	77,14
2	9,49	86,63
3	5,63	92,26
4	3,40	95,66
5	2,39	98,05
6	0,85	98,90
7	0,39	99,29
8	0,30	99,59
9	0,24	99,83
10	0,17	100,00

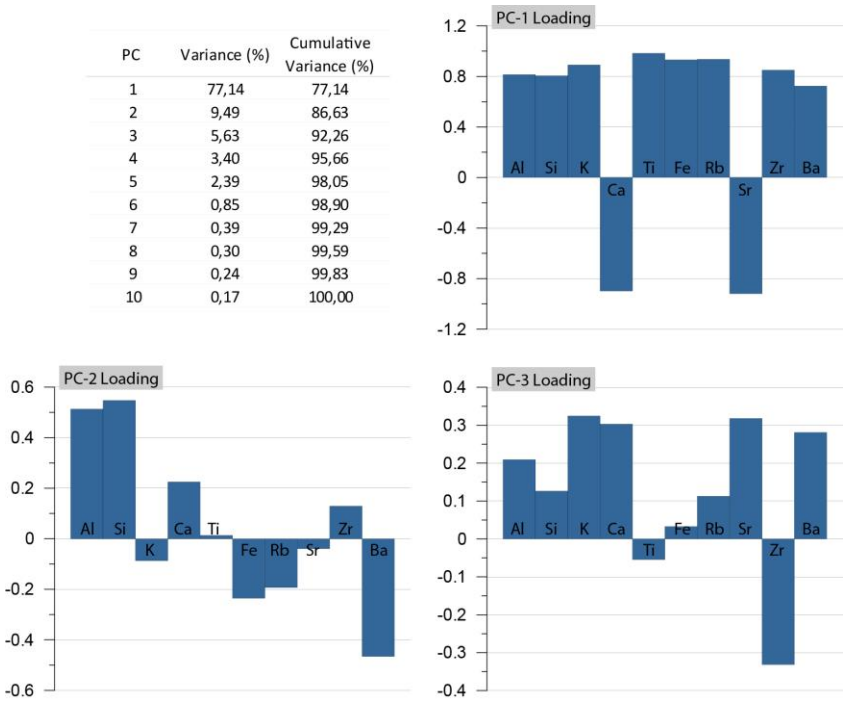

Figure 3.26. Principal Component Analysis (PCA) of MD99-2343 XRF-elemental data with loadings of PC-1, PC-2 and PC-3.

3.6 Evaluating the overlapped cores

The Balearic record shows the widest range of variability even though it does not cover the last deglaciation, which is only fully represented in the Alboran record (>5°C warming) (Fig. 3.27). In general, the Cantabrian SST record was about 2-3°C colder than the western Mediterranean Sea records, which is consistent with the current SST pattern, where spring SST mean are 14°C, 17.6°C and 16.7°C for Cantabrian, Alboran and Balearic seas respectively (Picciolo, 2006). The three SST records show strong similarities in the general trend during the overlapped periods despite the warmest temperatures did not occur synchronously among the three studied areas (Fig. 3.28 C, D and E). The cooling phase that ended MIS 5e was more progressive and smoothed in the Cantabrian region than in the western Mediterranean, where the Balearic record presents the largest SST change (Fig. 3.28 C, D and E: dashed red arrows). In fact, during the warm sub-stages and especially at the end of the MIS 5e the temperature gradient between the Cantabrian basin and the W Mediterranean sub-basins was relatively high and even higher to those of today (Fig. 3.27). In contrast to the regional heterogeneities of the warm periods, the stadial periods show very distinctive and homogeneous cold conditions among all SST records, except during the GS26 and GS23. These synchronic cold conditions among the three basins achieve similar SST between the Cantabrian and the Alboran or even the Balearic Sea during stadials, especially at GS25 and 24 (Fig. 3.28). Moreover, during the MIS 5c at 101.5 kyr BP occurred an intense cold event in the Cantabrian record that is not reflected in the W Mediterranean records (Fig. 3.28 C: grey dashed vertical line).

The $\delta^{18}O_{sw}$ evolution is also very heterogeneous among the three studied areas. The Cantabrian and Alboran Sea $\delta^{18}O_{sw}$ show more comparable values and significantly lighter than those from the Balearic Sea, reflecting the evaporation character of the Mediterranean basin (Pierre, 1999). A very remarkable rapid freshening event with a ~3‰ lightening in the Alboran-$\delta^{18}O_{sw}$ signal is shown at ~132.5 kyr BP, likely reflecting the sea ice melting associated to the HS11 that marks the onset of the penultimate deglaciation (Fig. 3.28). Regarding the intensity of the changes, the Alboran Sea $\delta^{18}O_{sw}$ show larger enrichments than the Cantabrian record in relation to the stadial periods. The GS26, 23 and 20 stadials periods show a strong regional contrast, with significant isotopic enrichments in the Balearic core that are not detected in the Cantabrian site, while during the GS25, 24 and 22 the isotopic composition of the sea water was very similar among the basins (Fig. 3.28).

Moreover, periods of relatively heavier isotopes in surface sea water and cold SST, are characterized by high UP10 values in the Balearic region (Fig. 3.28). This fact indicates an increment in the deep current intensity during cold stadial periods and the beginning of the MIS 4. In contrast, interstadial periods present both high and low UP10 values with relatively high internal oscillations. Particularly, the end of MIS 5e and especially the end of MIS 5a present high UP10 values and almost all samples belongs to the cluster 1. The lowest UP10 percentages indicating weaker deep current intensity are also found during these warm intervals. As currents not only control the grain-size distribution of contourite drifts but also modify the mineralogy of sediments, the extraordinary fit between the UP10 and the Zr/Al ratio corroborate the use of these proxies as deep-water paleocurrent intensity proxies in the Balearic Sea (Fig. 3.28).

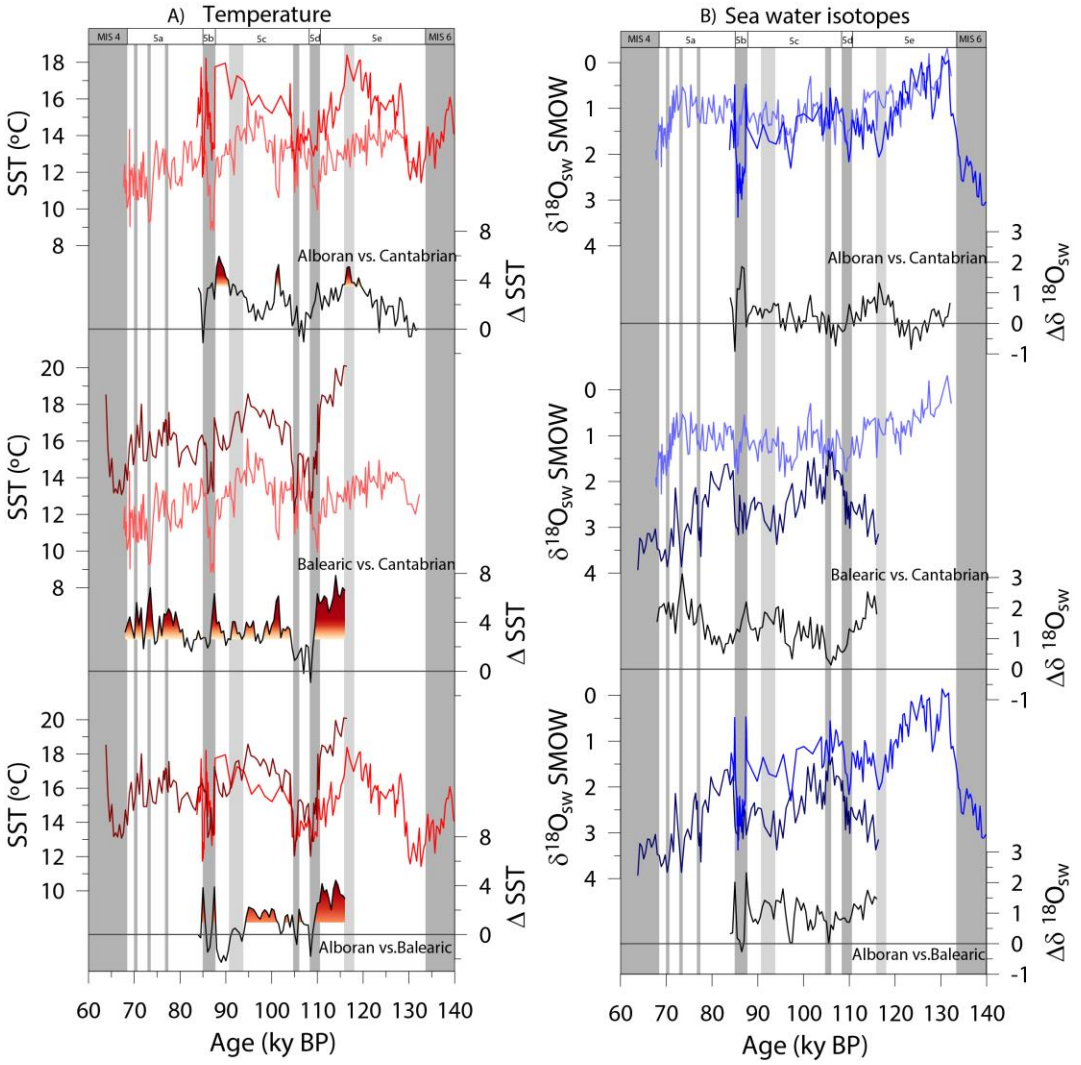

Figure 3.27. A) Marine core SST records (left axis) with calculated gradient among basins (right axis). Actual SST differences between basins are used as colour gradient threshold in plotted curves. B) Marine $\delta^{18}O_{sw}$ records (left axis) with calculated gradient among basins. Horizontal lines at zero shows moments were SST or $\delta^{18}O_{sw}$ are the same in both sites. Vertical grey bars: MIS 4-5 and/or GS18-25.

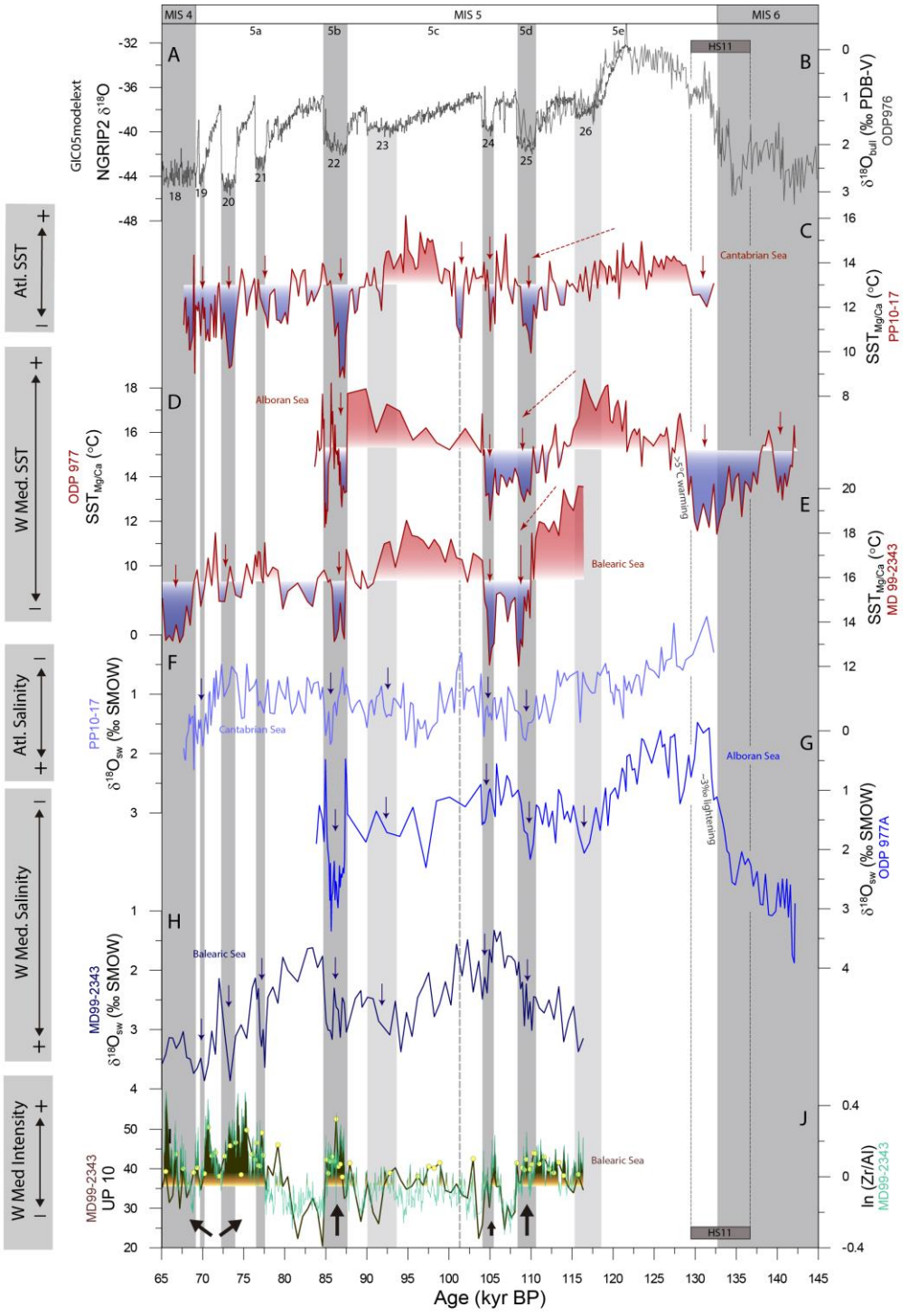

Figure 3.28. Comparison of the studied marine records with some reference records. A) reference record $\delta^{18}O$ NGRIP2 (Rasmussen *et al.,* 2014; Seierstad *et al.,* 2014), B) The $\delta^{18}O_{G.bulloides}$ ODP Site 976 record from the West Alboran Sea (Jiménez-Amat and Zahn, 2015). C) Mg/Ca-SST record from PP10-17 core of the Cantabrian Sea, D) Mg/Ca-SST record from ODP Site 977A of the East Alboran Sea and E) Mg/Ca-SST record from MD99-2343 core of the Balearic Sea. Mean sea surface temperature, 12.7°C, 14.8°C and 15.9°C for Cantabrian, Alboran and Balearic records respectively, are used as colour gradient threshold in plotted curves. The red arrows highlight cooling trends and the vertical grey dashed line points to the Cantabrian cold event. F) $\delta^{18}O_{sw}$ record from PP10-17 core, G) $\delta^{18}O_{sw}$ record from ODP Site 977A and H) $\delta^{18}O_{sw}$ record from MD99-2343 core. The blue arrows highlight heavy $\delta^{18}O_{sw}$ events. I) Non-carbonate UP10 index from core MD99-2343 with samples corresponding to cluster-1 indicated by yellow dots. J) Zirconium geochemical record normalized to aluminum and plotted in logarithmic scale (Zr/Al) from MD99-2343 core. The black arrows point to high deep current intensities. The grey dashed rectangle shows the Heinrich Stadial 11 (HS11). Vertical grey bars: MIS 4-6 and/or Greenland stadials (GS18-26).

Everything is correlated to everything

Laurent Labeyrie

Chapter IV

Discussion

4.1 Interpretation of speleothem proxies

Several processes can control the $\delta^{18}O$, $\delta^{13}C$ and Mg/Ca signal in speleothems and a strategy to elucidate its potential climatic signal is to produce multi-proxy records from several speleothems, when possible. These three studied geochemical parameters show distinctive relationships depending of the speleothem records and the studied periods (Annex 8). In particular, the speleothems IND (Menorca) and JUD (Pyrenees) that correspond to the MIS 5, show higher positive correlation between the Mg/Ca and $\delta^{13}C$ records than with the $\delta^{18}O$ record, pointing to a different processes controlling these signals (Table 4 and Fig. 4). In contrast, RAT (Menorca) and VALL2 (Mallorca) that cover MIS 7e-MIS 12 present significant positive correlation between $\delta^{18}O$ and the $\delta^{13}C$ while a weaker one between the Mg/Ca and $\delta^{13}C$ records. These significant differences observed depending on the speleothem highlight the strong complexity when confronting climatic interpretations and prevent a general interpretation.

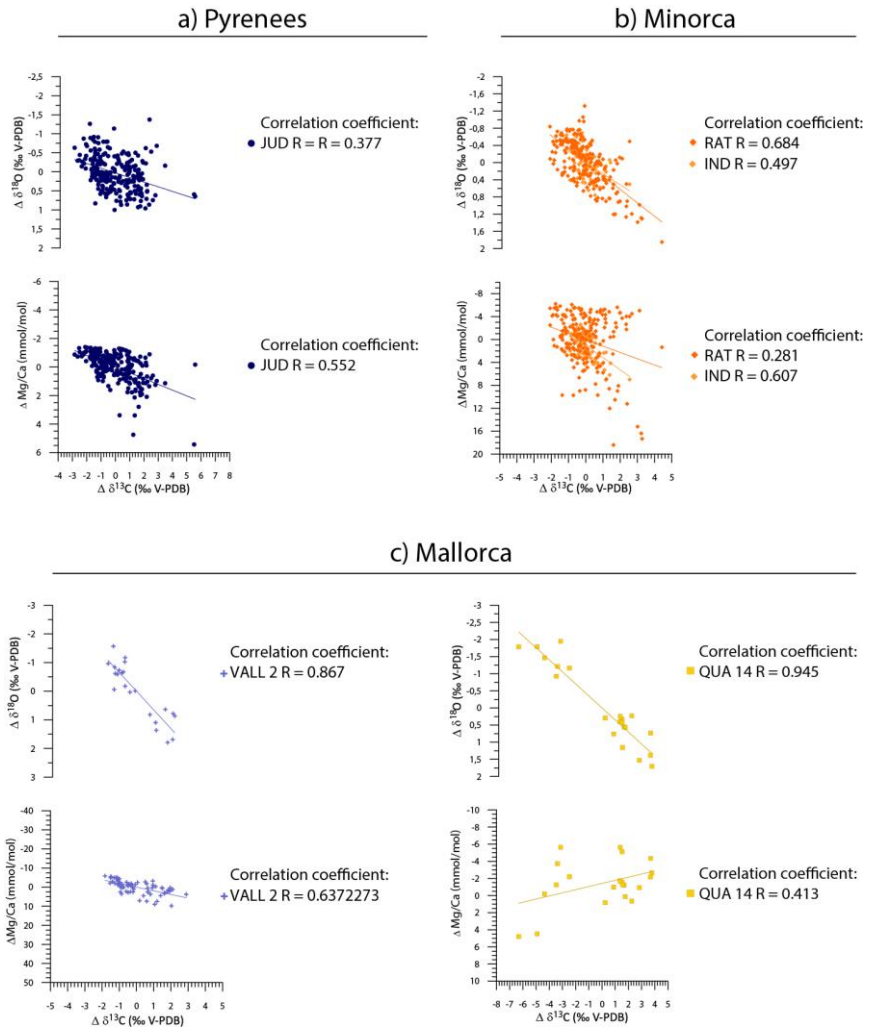

Figure 4. This study speleothem geochemistry records plotted as $\delta^{18}O$ vs. $\delta^{13}C$ and Mg/Ca vs. $\delta^{13}C$ for with the correlation coefficients for each speleothem.

Table 4. Summary of the geochemical correlation coefficients.

Correlation coefficients		
Speleothem	$\delta^{18}O$ vs $\delta^{13}C$	Mg/Ca vs δ13C
JUD	0.377	**0.552**
IND	0.497	**0.607**
RAT	**0.684**	0.281
VALL 2	**0.867**	0.637
QUA 14	**0.945**	0.413

At the temporal scale of this study, changes in the marine $\delta^{18}O_{sw}$ can play an important role in the $\delta^{18}O_{speleo}$ imprint since glacial-interglacial cycles involved major changes in the ice sheets extent and in precipitation/evaporation changes, which are the major controllers of $\delta^{18}O_{sw}$ at global and regional scale respectively (Drysdale *et al*., 2009; Marino *et al*., 2015). However the $\delta^{18}O$ speleothem signal could depend also of changes in rainfall patterns, atmospheric air temperature, amount effect, PCP, growth rates or kinetic effects among others (Fairchild *et al.,* 2007, 2006; Lachniet 2009; McDermott, 2004; Stoll *et al*., 2015). Therefore, despite the interpretation of the $\delta^{18}O_{espeleo}$ recording $\delta^{18}O_{sw}$ changes at large-scale, other processes could be superimposed into this signal. For example in several European speleothems the $\delta^{18}O_{speleo}$ has been interpreted as a combination between temperature and amount effect (Bartolomé *et al.,* 2015; Vansteenberge *et al.,* 2016). Although $\delta^{18}O$-$\delta^{13}C$ covariations have been suggested a consequence of kinetic effects which are independent of environmental and climatic signals several publications argued that processes leading changes in $\delta^{18}O$ can be associated with hydroclimatic changes causing parallel shifts in the $\delta^{13}C$ (Baldini et al., 2005; Dorale et al., 1998; Dorale and Liu, 2009, Fairchild and Baker 2012; Hellstrom et al., 1998). The enhanced precipitation that leave lighter $\delta^{18}O_{speleo}$ and $\delta^{18}O_{sw}$ over the Mediterranean could induce vegetation expansion and increments in soil CO_2 activity in the Balearic Islands, assuming that this region is moisture-limited. Several mid-latitude speleothem studies interpreted $\delta^{13}C$ shifts in terms of changes in vegetation/soil activity, like for example in the Mallorca Island (Hodge *et al.,* 2008b), in the northeast IP (Bartolomé *et al.,* 2015; Perez-Mejias *et al*., 2017; Moreno *et al.,* 2010) or in the southwest France (Genty *et al.,* 2003). Higher water availability due to an enhanced rainfall amount and ultimately, more atmospheric moisture is related to lowest $\delta^{13}C$ values in speleothems due to enhanced soil activity (Fairchild and Treble, 2009). By contrast, highest $\delta^{13}C$ values

are often attributed to aridity or less atmospheric moisture. However vegetation/soil activity is also controlled by optimum temperature for vegetation (Fairchild and Treble, 2009). Therefore we argue that when covariations are found, both proxies recorded mostly regional precipitation but also temperature changes, both closely related to NH summer insolation that induce both $\delta^{18}O_{sw}$ changes and vegetation/soil activity changes. Moreover, when close observations of the $\delta^{18}O$-$\delta^{13}C$ covariation are made some slight differences arise. For example in the case of the RAT speleothem at 350-330 kyr where a relevant decoupling of both signals occur and the $\delta^{13}C$ is more in line with the Mg/Ca evolution (Fig. 4.3). In these cases, $\delta^{13}C$ may record vegetal response while the $\delta^{18}O$ signal rather records the $\delta^{18}O_{sw}$ signature associated with major changes in the accumulation/melting rates of large ice sheets rather than regional precipitation changes. This interpretation is in the same line than previous stalagmites studies from the western mediterranean region (Pérez-Mejías *et al.*, 2017). Other short-term differences between the $\delta^{18}O$ and $\delta^{13}C$ may also reflect inside-cave environment variables such as ventilation (changes in the pCO_2) or the growth rate that can alter the isotopic composition (Baldini *et al*., 2008, 2010; Day and Henderson 2011; Stoll *et al*., 2015). Fast growth rates (>50μm/yr) has been associated with 1‰ decreases of the $\delta^{18}O$ signal in north Iberian Peninsula speleothems (Stoll *et al*., 2015). Furthermore, growth rates can vary along speleothem axis at different timescales, consequently complicating the interpretation of stalagmite proxy records (Baldini *et al*., 2008). In that way, abrupt changes in the growth rate in line with isotopic decreases, as is the case of QUA14, could alter the climatic signals.

The explanation for the Mg/Ca and $\delta^{13}C$ covariations in JUD and IND speleothems could be in part associated to the enhanced degassing and thus PCP within the karst system which strongly influences both proxies. The principal controlling factors of the Mg/Ca ratio variability seems to be derived from the bedrock composition and the groundwater residence time, ultimately related to PCP (Fairchild *et al.,* 2000). Assuming that the bedrock composition did not change over time, variations in the precipitation/evaporation balance in the region should be related to the amount of water infiltrating into the karst system. Consequently, high residence time favours PCP and slows both growth and drip rates, increasing the Mg/Ca ratio in the speleothem calcite due to the preferential calcium lost. In consequence, higher Mg/Ca ratios in speleothems suggest drier conditions and vice versa (Fairchild *et al.,* 2000; Moreno *et al.,* 2010). Hence when co-variation between Mg/Ca and $\delta^{13}C$ exist they can be interpreted as water availability proxies indicating arid or wet periods.

4.2 Precession signal in $\delta^{18}O$ records

The studied $\delta^{18}O_{speleo}$ records provide for the very first time the possibility to analyse the hydroclimate variability in the western Mediterranean region during several glacial/interglacial cycles. These records reveal an overall dominance of lighter values during interglacial marine isotope stages (MIS 13, 11, 9, 7 and 5), in contrast to the glacial periods that are characterized by heavier $\delta^{18}O_{speleo}$ (Fig. 4.1 A and B). However, these interglacial marine isotope stages present remarkable internal variability overprinted to the overall light values. This variability presents a dominant precession cycle, with lighter $\delta^{18}O_{speleo}$ in line with precession minima and thus high NHSI (Fig. 4.1 F). The $\delta^{18}O_{speleo}$ variability associated to these precession cycles is particularly large in those speleothems covering the MIS 5. In contrast, the precession cycles are less obvious in the $\delta^{18}O_{speleo}$ covering the previous marine isotopic stages MIS 11 and 9, probably also reflecting the lower amplitude of the precession cycles during these isotopic stages as a consequence of the eccentricity minimum. Glacial periods are represented by rather constant heavy $\delta^{18}O_{speleo}$ values although this little variability can be an artefact of the slow growth rate associated to these periods and the consequent reduced resolution of the corresponding records.

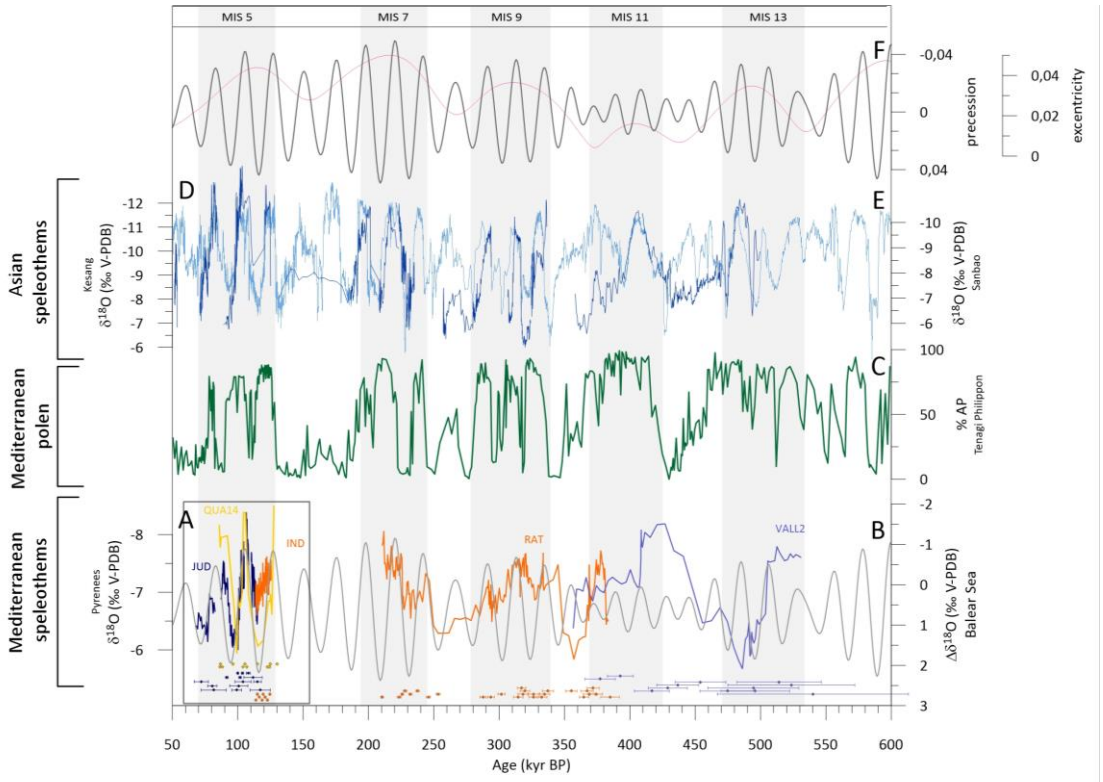

Figure 4.1 A) Judit $\delta^{18}O_{speleo}$ record from Pyrenees. B) Normalized $\delta^{18}O_{speleo}$ from several Balearic speleothems (QUA14, IND, RAT and VALL2) (Both plotted over the precession curve and with the U/Th ages of this with the 2σ error bars. C) The Tenaghi Philippon arboreal pollen record from Greece (Tzedakis *et al*., 2006) D and E) $\delta^{18}O_{speleo}$ records from Kesang and Sanbao caves in China (Cheng *et al*., 2012, 2016). F) Precession and excentricity curves (Laskar, 2004).

A precessional dominance in $\delta^{18}O_{speleo}$ has previously been founded in Asian speleothem records dominated by monsoon dynamics (Fig. 4.1 D and E) (Wang, *et al.,* 2001; Cai *et al.,* 2015; Cheng *et al.,* 2016). These records reveal that, during the past 600kyr BP, low precession conditions (enhanced north hemisphere summer insolation - NHSI) generated a northward displacement of the ITCZ, increasing summer monsoon precipitation. Thus these periods of minimum precession are represented in the Asian $\delta^{18}O_{speleo}$ signal by light values, reflecting the enhanced precipitation over China and India. Summer monsoon variability inferred from this Asian speleothem records show similar precession oscillations among the MIS 13, 11, 9, 7 and 5.

Moreover, the Tenaghi Philippon pollen record, which indicates changes in the arboreal vegetation in the eastern Mediterranean region, also recorded clear precession oscillations (Tzedakis *et al*., 2006) (Fig. 4.1 C). The Mediterranean Sea also receives a strong precession influence through the African monsoon which control major changes in river runoff along the North African coast (Rohling *et al.,* 2014; Bosman *et al*., 2015; Grant *et al*., 2016). These conditions had a major effect in the Mediterranean oceanography, drastically changing its evaporation-precipitation balance and leading to the precessional-cyclic formation of the so-called sapropel layers in the Eastern Mediterranean Sea and overall changes in the Mediterranean $\delta^{18}O_{sw}$ composition (Bar-Matthews *et al*., 2000; Toucane et al., 2015; Bosman *et al*., 2015; Rohling *et al*., 2015). Furthermore, precession minima (high NHSI) also cause higher seasonality and air-sea temperature gradients that derive in enhanced evaporation from the Mediterranean basin itself and therefore higher locally convective precipitation. Overall, these studies point that precesional driven increases in both summer monsoon but also in winter precipitation were major factors enhancing the freshwater supply of the Mediterranean Sea (Bosman *et al*., 2015; Grant *et al*., 2016; Rohling *et al*., 2014, 2015). In addition, precipitation is also related to more storm tracks reaching the south Western Europe and western Mediterranean at times of enhanced insolation seasonality (Sierro *et al*., 2000; Stoll *et al*., 2015). These conditions are supported by some western Mediterranean cores that recorded precession paced rhythm in the $\delta^{18}O_{sw}$ signal by planktonic foraminifera in the Tyrrhenian Sea or in the sedimentological record from the Balearic Sea (Toucanne *et al*., 2012; Frigola *et al*., 2008).

The precessional signal identified in the $\delta^{18}O_{speleo}$ records from this study could reflect changes in the Mediterranean $\delta^{18}O_{sw}$ derived from the evaporation/precipitation patterns of the whole basin. This impact of the $\delta^{18}O_{sw}$ over the $\delta^{18}O_{speleo}$ was previously tested after comparing $\delta^{18}O_{speleo}$ records from different European and Mediterranean caves, and demonstrated that heaviest $\delta^{18}O_{speleo}$ concentred in Mediterranean speleothems

likely capturing the enriched signal of the Mediterranean Sea waters (McDermott *et al.,* 2011). One of the novelties of the current thesis is the parallel reconstruction of both $\delta^{18}O_{speleo}$ and $\delta^{18}O_{sw}$ records that can explore further the potential link between these two signals. This speleothem-marine comparison is focused on the MIS 5 since this is the period when both the studied marine and cave records overlap (Fig. 4.2).

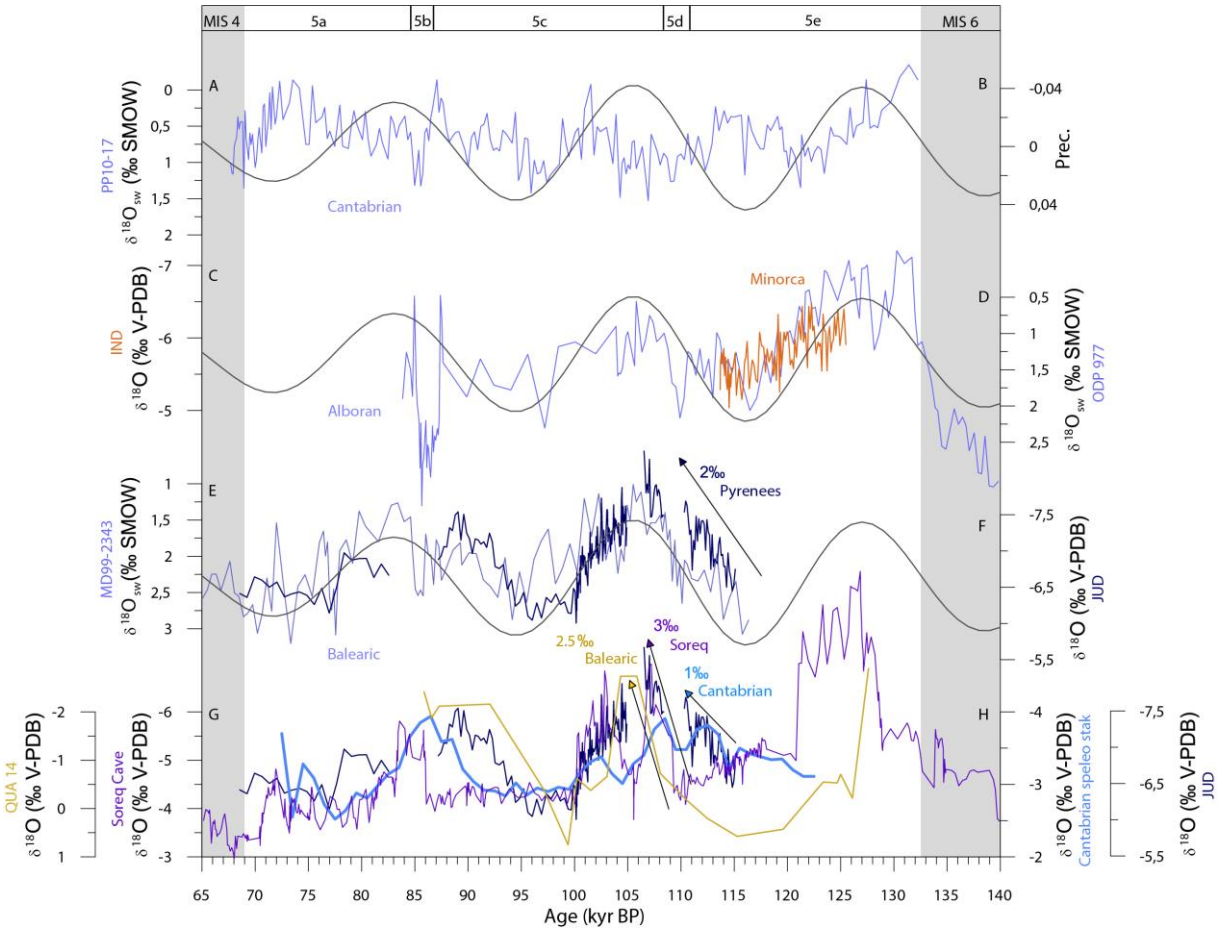

Figure 4.2. Precession index compared with marine and speleothem oxygen isotope records. A) PP10-17 core $\delta^{18}O_{sw}$, B) Precession curve (Laskar, 2004), C) IND $\delta^{18}O_{speleo}$ D) ODP Site 977 $\delta^{18}O_{sw}$, E) MD99-2343 core $\delta^{18}O_{sw}$ F) JUD $\delta^{18}O_{speleo}$, G) Soreq cave $\delta^{18}O_{speleo}$ (Bar-Matthews *et al.,* 2000, 2003). H) Cantabrian $\delta^{18}O_{speleo}$ stack (Stoll *et al*., 2015). Arrows show the $\delta^{18}O_{speleo}$ change in ‰ during a half precession cycle. Vertical grey bars: MIS 4 and MIS 6 glacial periods.

A precessional rhythm in speleothem $\delta^{18}O_{speleo}$ records have already been found in a stacked record from the Cantabrian Margin, in the north-west IP, and in records from the Soreq Cave from Israel, in the easternmost Mediterranean region (Grant *et al*., 2012; Bar-Matthews *et al*., 2003, 2000; Stoll *et al.,* 2015). But the magnitude of the $\delta^{18}O_{speleo}$ oscillations is far larger in the Mediterranean records, likely reflecting the enhanced $\delta^{18}O_{sw}$ variability in its rain source area in contrast to those from the Cantabrian sector, where rain is fuelled from the Atlantic region (Fig. 4.2). The studied $\delta^{18}O_{speleo}$ records (IND, JUD and QUA14) show higher amplitude than the Cantabrian stack record but shorter than

those form the Soreq cave record. In particular, focussing in the precession minimum at 115-95 kyr BP (the central cycle of the MIS 5), the Cantabrian speleothem stack shows a $\delta^{18}O_{speleo}$ depletion of about 1.2‰ while in the Pyrenean speleothem JUD is of 2‰ and in the Balearic speleothem QUA14 is of 2.5‰, but in this last case, an amplification in the chemical signal due to textural changes, cannot be discarded (See Section 3.2.3). This $\delta^{18}O_{speleo}$ depletion is of 3‰ in the signal from Soreq Cave (Grant *et al*., 2012; Bar-Matthews *et al*., 2003, 2000). This intensification of the precession amplitude signal toward the most Mediterranean caves likely reflects the precession driven intensification of the African summer monsoon that through enhanced Nile river runoff introduced strong changes in the hydrological balance of the Mediterranean basin and those in its $\delta^{18}O_{sw}$ composition (Rohling *et al.,* 2014).

In the marine realm, the largest oscillation within the studied records occurred in the Balearic $\delta^{18}O_{sw}$, with a depletion of almost 2‰ while in the Alboran $\delta^{18}O_{sw}$ it was of 1.5‰ and any evident $\delta^{18}O_{sw}$–precession depletion occurred in the Cantabrian $\delta^{18}O_{sw}$ record (Fig. 4.2 A,D and E). These marine records support a stronger $\delta^{18}O_{sw}$–precession signal into the Mediterranean region than the Cantabrian Sea likely related to regional precipitation/evaporation ratio.

In consequence, the described precession signal in the studied speleothem records is interpreted here to reflect mostly changes in $\delta^{18}O_{sw}$ from the humidity source area. Therefore, the enhanced $\delta^{18}O_{speleo}$ intensity in the Pyrenees (JUD) in contrast to the speleothem stack from the Cantabrian support a significance contribution of the western Mediterranean as humidity source to this mountain region. Studies dedicated to present day precipitation sources reveal the IP itself and its proximal marine areas, such as the western Mediterranean Sea, as the principal contributors of moisture to precipitation (Krklec and Domínguez-Villar 2014; Nieto *et al*., 2010; Gimeno *et al*., 2010). The subtropical North Atlantic is also identified as an important contributor, particularly during autumn and winter through storm tracks, when precipitation is mainly as snow in the Pyrenees, while during the thaw season, Mediterranean source areas became dominant. Our results supports that western Mediterranean source rainwater would account for the enhanced intensity of the precession signal detected in the Balearic speleothems and even the central southern Pyrenees during the MIS 5.

4.3 Previous Interglacials

This section focuses in those interglacial Marine Isotopic Stages previous to the MIS 5, which are represented by the speleothems RAT and VALL2 from the Balearic Islands. The geochemical records from both speleothems record well the Glacial/interglacial sequence with a clear contrast between heavy and light $\delta^{18}O$ values corresponding to glacial and interglacial periods respectively (Fig. 4.3). Furthermore, these interglacial periods can also be characterized by light $\delta^{13}C$ and low Mg/Ca ratios pointing to enhanced precipitation conditions that led a larger vegetation extent and higher soil activity in contrast to the glacial periods represented by high values that represent dry conditions with poorer vegetation cover and soil activity (Fig. 4.3). Both RAT and VALL2 speleothems cover continuously more than 300 kry corresponding to three full glacial/interglacial cycles. Thus, this is an unprecedented record to analyse the hydroclimate variability in the western Mediterranean. U/Th dates for RAT speleothem present very short errors providing an exceptional accurate absolute chronology for MIS 11 to 7. Conversely, the high errors provided by the absolute VALL2 ages introduce large uncertainties in the chronology of the observed structures. In particular, a large discrepancy can be observed for the timing of the glacial structure corresponding to the MIS 12 between the VALL2 and the Tenaghi Philippon pollen record in the eastern Mediterranean Sea (Tzedakis *et al.,* 2003), where maximum glacial conditions developed about 25 kyr later than in VALL2. This asynchrony points to a misadjusted in the age model in VALL2 although the chronology of this pollen record is not based in absolute dates and relays on orbital tuning. Despite that, an extraordinary resemblance of the large-scale oscillations can be observed between both VALL2 and RAT records and the Tenaghi Philippon pollen record (Fig. 4.3). This pollen record and also the RAT and VALL2 speleothem records have resolution enough to analyse suborbital oscillations produced during MIS 13, 11, 9, and 7, being the MIS 9 the best resolved and accurately dated stage (Fig. 4.3).

At the moment any continuous European speleothem record cover several glacial-interglacial cycles as is the case of the here presented Balearic RAT and VALL2 records. However, some shorter speleothem records provide a partial overlap with them and allow discussing the obtained results in a broader regional context. This is the case of the iconic speleothem record of the Antro del Corchia cave in the Apennine karst in Italy (Drysdale *et al.,* 2004). Despite the CC1 speleothem from this cave present several growth hiatuses, it present continuous growth over the MIS 9. Another record is from Spannagel cave in the Austrian Alps, which grew without interruptions during the penultimate interglacial (MIS

7) (Spötl *et al.,* 2008). Finally, other speleothem that slightly overlap the MIS 7 is one from the IP, covering also the T-III (Perez-Mejias *et al.,* 2017) (Fig. 4.3).

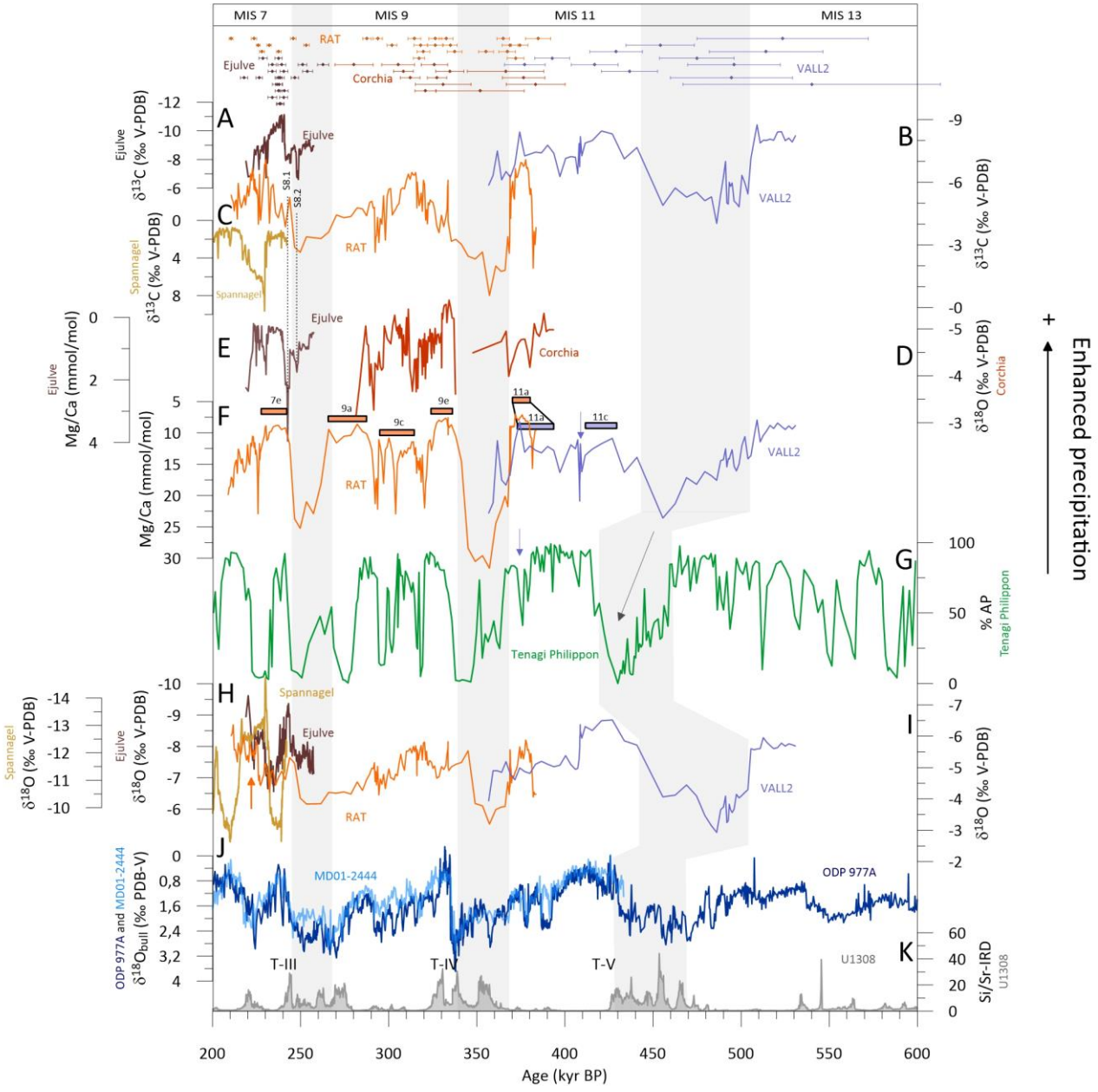

Figure 4.3. Comparison of RAT and VALL2 speleothem records with other paleoclimate records. A) $\delta^{13}C$ speleothem record from Ejulve cave record located in the eastern Iberian Peninsula with the U/Th ages plotted with 2σ error bars on the top (Pérez-Mejías *et al*., 2017). B) $\delta^{13}C$ RAT and VALL2 speleothem records with the U/Th ages plotted with 2σ error bars on the top. C) $\delta^{13}C$ speleothem record from Spannagel Cave in Austria (Spötl *et al*., 2008). D) $\delta^{18}O$ speleothem record from Chorchia cave in Italy with the U/Th ages plotted with the 95% error bars on the top (Drysdale *et al*., 2004). E) Mg/Ca ratio record from Ejulve speleothem (Pérez-Mejías *et al*., 2017). F) Mg/Ca ratios from RAT and VALL2 speleothem records. G) The Tenaghi Philippon arboreal pollen record from Greece (Tzedakis *et al*., 2006). H) $\delta^{18}O$ speleothem records from Ejulve and spannagel caves. I) RAT and VALL2 $\delta^{18}O$ records. J) $\delta^{18}O$ marine records from sediment cores MD21-2444 from the Portuguese Iberian margin and ODP 977 site from the Alboran Sea (Hodell *et al*., 2013; Martrat *et al*., 2007 and unpublished data). K) Si/Sr-IRD record of U1308 core (Hodell *et al.,* 2008). Black arrow pointing possible age model inconsistency between VALL2 and the Pollen record. Blue arrows highlighting the dry event that divided the MIS 11 in substages. Vertical grey bars indicate glacial periods.

4.3.1 The MIS 11

Interestingly, the MIS 11 has been suggested as a good analogue for the Holocene period due to its similitudes in terms of orbital configuration and the consequent insolation distribution, but also due to atmospheric CO_2 concentrations comparable to the pre-industrials ones (Loutre and Berger 2003; Tzedakis 2010). The MIS 11 is particularly anomalous because its long-duration in front to most of the Quaternary interglacial periods. However the characterization of this period within the western Mediterranean has not been possible due to the lack of available terrestrial records in the region. The geochemical records from VALL2 provide the opportunity to elucidate this information. Low oscillations in the Mg/Ca ratio and $\delta^{13}C$ records points to rather stable climate conditions along the MIS 11 with mainly constant water availability over the Balearic Islands and in line with the eastern Mediterranean vegetation stability inferred from the Tenaghi Philippon pollen record (Tzedakis *et al.,* 2003) (Fig. 4.3). However, a rapid dry event could be identify at 408 kyr BP that could be the same vegetation depression at ~377 kyr BP in the pollen record, assuming that there is a ~25 kyr deviations among both chronologies. The interglacial acme is difficult to characterize in the VALL2 records since Mg/Ca and $\delta^{13}C$ values are comparable before and after this short dry event suggesting equal wet and/or vegetation activity conditions. Therefore, the interstadials MIS 11c and 11a can be identified in these records (Fig. 4.3). Assuming that the interglacial acme occurs well after the deglaciation and until the described dry event, the MIS 11c interglacial acme duration would be of ~20 kyr, although large uncertainties exist in the age model. Furthermore, the Mg/Ca ratio and $\delta^{13}C$ records of RAT speleothem suggest that the MIS 11a starts at ~ 380 kry BP which is almost in line with the vegetation recuperation after the depression in the pollen record.

The $\delta^{18}O$ record of the VALL2 shows lighter values during the MIS 11c probably reflecting lighter western Mediterranean surface waters for this substage. The marine $\delta^{18}O$ records also record lighter values for this substage according to the N Atlantic core U1308 and the Alboran core 977. Nevertheless, since any $\delta^{18}O_{sw}$ reconstruction for this time period is available, these light values could reflect the warm SST interpreted for this period (Martrat *et al*. 2007). The Si/Sr record from core U1308 indicates that IRD discharges concentrated during the glacial MIS 12 period but they were almost absence during the MIS 11 (Fig. 4.3) (Hodell *et al*., 2008). Even though the limited resolution of the VALL2 record, it agrees with the marine records in suggesting relatively climate stability along the MIS 11. This relative MIS 11 stability is also supported by the larger millennial scale variability observed for younger interglacial stages by the RAT speleothem (Fig. 4.3).

4.3.2 The MIS 9

Contrary to the stable conditions over the MIS 11, the RAT speleothem clearly recorded intersatial-stadial variability along the MIS 9 period. The actual timing and duration of this period is very solid due to the well resolved RAT age model and resolution. In base to the Mg/Ca record, the MIS 9 shows three wet periods alternated with abrupt and shorter dry events. These dry events correspond to the stadial periods MIS 9d and MIS 9b and they are centred at 320 kyr BP and 293 kyr BP respectively. Conversely, the three wet periods has been identified as the substages MIS 9e, 9c and 9a, being the MIS 9e the shortest one lasting about 15 kyr (Fig. 4.3). According to the Mg/Ca record, the MIS 9c was slightly less humid than the other two warm substages but this record also reveals several internal abrupt dry events. These brief dry events contrast with the rather stable hydrological conditions interpreted for MIS 9e and 9a. The RAT Mg/Ca record also indicates that the humid conditions during the considered pure interglacial (MIS 9e) were comparable to those of the MIS 9a. In addition, the MIS 9e was not a remarkable stage in the $\delta^{13}C$ record, which shows the lightest values for the MIS 9. Overall, the Mg/Ca record appears to have a more coherent signal reporting wetter interstadial and dryer stadial periods, a variability comparable to that previously documented by the eastern Mediterranea pollen sequence from Tenaghi Philippon (Fig. 4.3). While the $\delta^{13}C$ signal seems to have a more complex pattern although the main enrichments/depletions are also represented.

The MIS 9 speleothem $\delta^{18}O$ record is also available from Corchia cave in Italy, where the substages MIS 9e, 9c and 9a are also clearly identified. These warm substages are represented by light values in the Corchia $\delta^{18}O$ record and interpreted as periods of greater moisture availability due to the enhanced evaporation led by regional warm SST (Drysdale *et al.,* 2004). The Corchia $\delta^{18}O$ record shows an extraordinary resemblance with the RAT Mg/Ca record variability although some of the apparent time offsets may result from the chronology uncertainties which are higher in the Corchia speleothem. Nevertheless, both speleothems reinforce the interpretation of enhanced precipitation over the Western Mediterranean during interstadial periods alternating with abrupt dry stadial periods (Fig. 4.3). These millennial-scale abrupt dry events can also be recognized as intervals of reduced tree population in the Tenaghi Philippon pollen record from the eastern Meditarranean region (Fig. 4.3). These vegetation reductions have been interpreted to reflect cold and arid conditions associated to overall ice volume variations (Tzedakis *et al.,* 2003).

4.3.3 The MIS 7

The MIS 7 is an anomalous stage since the overall maximum interglacial conditions were weaker than those achieved during other late Quaternary interglacials but, surprisingly, two of the MIS 7 interstadial (MIS 7c and d) achieve the threshold defined for interglacial conditions (PAGES, 2016). However, the RAT speleothem stopped its growth at 210 kyr BP recording partially the MIS 7. The Mg/Ca record show a clear structure that indicates an increment in the water availability associated to the onset of the MIS 7e. An abrupt dry event can be recognized at 229 ky BP likely indicating the occurrence of a stadial period that punctuated this interglacial sub-stage, which lasted ~15kyr. The enhanced precipitation structure is also observed in new $\delta^{13}C$ and Mg/Ca high resolution records from MIS 7e from the Ejulve cave in the eastern IP, where has been interpreted as indicator of vegetation productivity (Fig. 4.3) (Pérez- Mejías *et al.,* 2017). This structure and interpretation is also coherent with the $\delta^{13}C$ record from the Spannagel cave in the Austrian Alps (Fig. 4.3) (Spötl *et al.,* 2008). However, the stadial dry condition duration is longer in the Alpine speleothem likely due to its northern and higher position were the N Atlantic climate influence could exert a stronger impact. The climate amelioration of the MIS 7e was also recorded eastward in the Tenaghi Philippon pollen record with a rapid increment of the arboreal pollen at the same time than our record (Fig. 4.3) (Tzedakis *et al.,* 2003).

The $\delta^{18}O$ record of the RAT speleothem presents lighter values during the MIS 7c than during the MIS 7e. This feature it can be also observed not only in the speleothem records (Ejulve and Spannagel) but also in the MD01-2444 and the ODP 977 marine records from the Portuguese margin and the Alboran Sea respectively (Fig. 4.3) (Hodell *et al*., 2013; Martrat *et al*., 2007). Furthermore the N Atlantic core U1308 recorded high IRD discharge over this interglacial marine isotopic stage (Hodell *et al*., 2008) fact that could induce climate variability in the system.

4.4 The MIS 5: Marine and speleothem signals

The MIS 5 stage is studied by means of a detailed comparison of the studied marine and terrestrial records covering several rapid and/or large climatic changes. The MIS 5 discussion is divided in three sections that allow high resolution climate reconstruction of: the penultimate deglaciation (T-II), the MIS 5e (LIG-acme and the glacial inception), and the early glacial period (MIS 5d- MIS 4). The speleothem records have been compared against two different locations of sediment core records; the Cantabrian Sea, represented by the marine core PP10-17 and the W. Mediterranean, analysed with the core ODP Site 977 from the Alboran Sea and the MD99-2343 from the Balearic Sea.

4.4.1 The penultimate deglaciation and the last interglacial onset

This interval is only represented in the Cantabrian Sea and the Alboran Sea marine records (Fig. 4.4). One of the most remarkable features during this period is the intense water-surface freshening detected in the two $\delta^{18}O_{SW}$ records (Fig. 4.4 H and I). In the case of the Alboran record, this intense freshening (~132-130 kyr BP) occurred after two small initial pulses (Fig. 4.4 I: Dark blue arrows). This sequence of several pulses has been identified in previous studies from the W-Iberian margin and the westernmost Alboran Sea (Fig. 4.4 H and I) (Jiménez-Amat and Zahn 2015; Tzedakis *et al*., 2018). Further west, into the Balearic Sea, the core ODP Site 975 discussed by Rodríguez-Sanz *et al.* (2017) also recorded this intense late MIS 6 freshening. The Alboran record also shows extreme cold SST contemporary to this freshening event (Fig. 4.4 F). Although this extreme cold SST event is not well recorded in the Cantabrian record (Fig. 4.4 E), the presence of the benthic foraminifer *Cibicides wuellestorfi* found in the same samples of this core by Rodríguez-Lazaro *et al*. (2017), also indicates glacial conditions. According to N Atlantic records, this freshening was associated to the HE-11, as such shown by an increase in the Si/Sr ratio, a proxy for IRD discharge, from the N Atlantic core U1308 (Fig. 4.4 M) (Hodell *et al*., 2008). Large ice-sheet meltwater fluxes spreading into the N Atlantic Ocean reduced high latitude sea surface salinity and increased vertical stratification allowing an AMOC weakening (Hodell *et al*., 2008; Marino *et al.*, 2015; Oppo *et al*., 2006; Seidenkratz *et al*., 1996). This freshwater anomaly entered via the Strait of Gibraltar into the western Mediterranean basin, reaching comparable light isotopic values in the Alboran and the Cantabrian basins (Fig. 3.27), while it was progressively vanished along its path toward the eastern Mediterranean basin (Rodríguez-Sanz *et al.,* 2017).

Therefore, the present study allows detecting the HE-11 impact on surface water properties confirming previous recent studies (Jiménez-Amat and Zahn 2015; Rodríguez-Lazaro *et al*., 2017; Rodríguez-Sanz *et al.,* 2017) not only in the western Mediterranean Sea but also in the Cantabrian Sea.

Coinciding with the end of the HE-11, a rapid and intense warming occurred in both studied records related to the penultimate deglaciation as previously documented in W-Iberian and Alboran records (Jiménez-Amat and Zahn, 2015; Martrat *et al*., 2007, 2014; Tzedakis *et al*., 2018) (Fig. 4.4 E and F: red arrows). It is also highly remarkable the comparable SST and $\delta^{18}O_{SW}$ values in both the eastern (977 site) and the western (976 site) Alboran cores during the HE-11 and the penultimate deglaciation (Fig. 4.4 F and I). These homogenous surface water properties likely reflect a strong surface stratification in the eastern and western Alboran sub-basins, which contrast with the habitual strong mixing that led to a regional gradient in surface properties during other periods (Català *et al.*, 2019). AMOC reinforcement after the HE-11 allowed climate amelioration with an increase in precipitation and the consequent development of the Mediterranean forest, as detected through pollen records at the onset of the LIG (Sánchez-Goñi *et al.,* 2012; Tzedakis *et al*., 2018) (Fig. 4.4 G: red arrow).

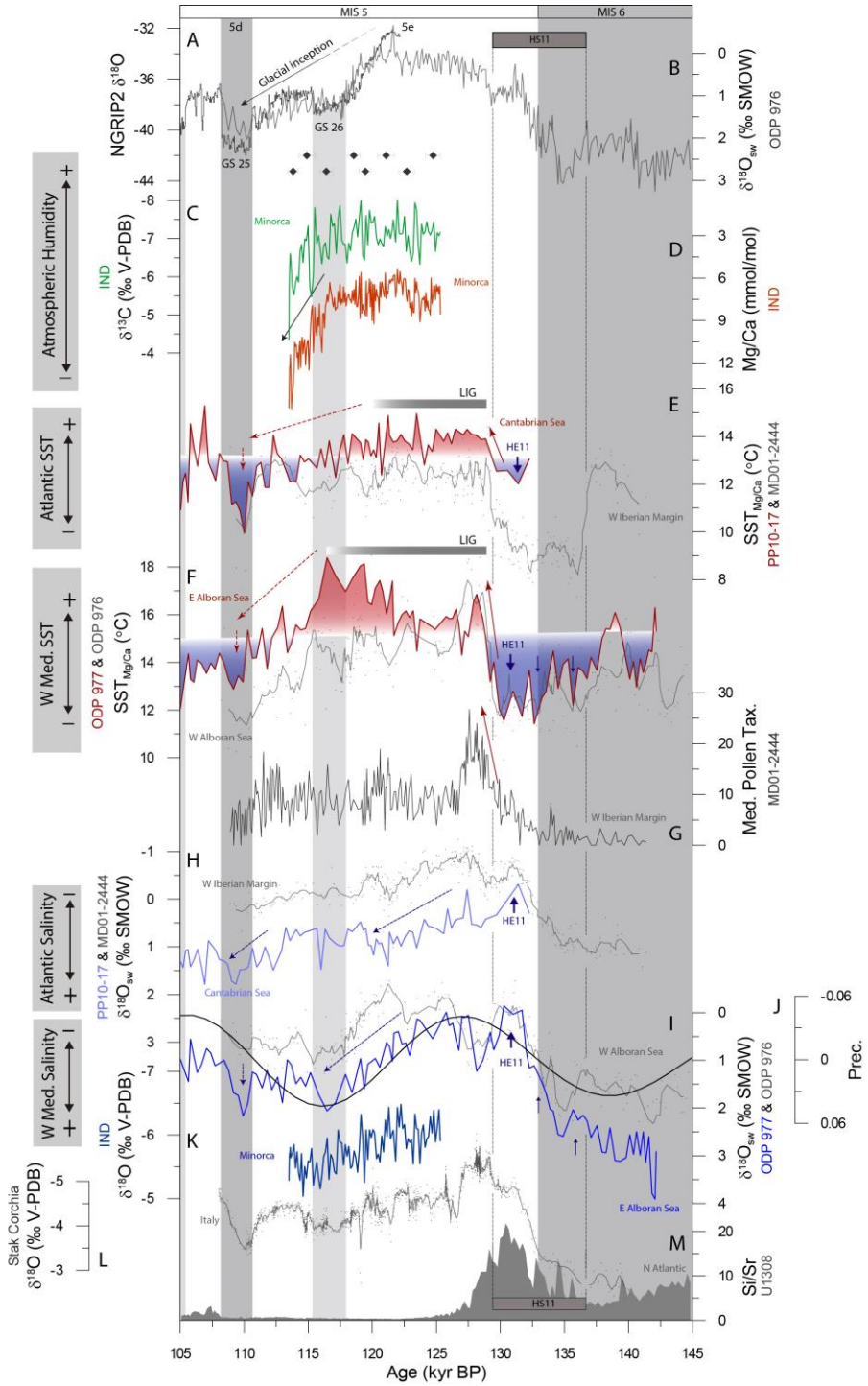

Figure 4.4 A comparison of this study records to several published records from 145 to 105 kyr BP. Reference records: A) $\delta^{18}O$ NGRIP2 GICC05modelext timescale record (Rasmussen *et al.,* 2014; Seierstad *et al.,* 2014) and B) $\delta^{18}O_{G.bulloides}$ ODP Site 976 record (Marino *et al.*, 2015). C) IND $\delta^{13}C$ and D) IND Mg/Ca ratios with the U/Th ages plotted with 2σ error bars on the top. E) Mg/Ca-SST of PP10-17 core in red and MD01-2444 core in grey (Tzedakis *et al.*, 2018). F) Mg/Ca-SST of ODP Site 977A in red and ODP Site 976 in grey (Jiménez-Amat and Zahn, 2015). G) Mediterranean pollen taxa record of core MD01-2444 (Tzedakis *et al.*, 2018). H) $\delta^{18}O_{sw}$ of PP10-17 core in blue and MD01-2444 core in grey (Tzedakis *et al.*, 2018). I) $\delta^{18}O_{sw}$ of ODP Site 977A in blue and ODP Site 976 in grey (Jiménez-Amat and Zahn, 2015). J) Precession curve (Laskar, 2004). K) IND $\delta^{18}O_{speleo}$. L) Corchia stack $\delta^{18}O_{speleo}$ (Tzedakis *et al.*, 2018). M) Si/Sr-IRD record of U1308 core (Hodell *et al.*, 2008). Grey dashed rectangle: Henrich stadial 11 (HS11). Blue arrows: Penultimate deglaciation cold SST and light $\delta^{18}O_{sw}$ surface waters events related to HS11. Red arrows: Penultimate deglaciation climatic amelioration. Horizontal grey bars: Warm SST plateau or LIG-acme. Black arrow: Glacial inception speleothem aridity tendency. Dashed red arrows: Glacial inception SST falls. Dashed blue arrows: $\delta^{18}O_{sw}$ enrichments trends during the LIG-acme and the glacial inception. Vertical grey bars: MIS 5-6 and/or GS25-26.

4.4.2 The LIG-acme and the glacial inception

The LIG-acme is defined as the interval within the MIS 5e containing peak values or a plateau in a given record (Govin *et al*., 2015). Accordingly, here it has been established the LIG-acme in base to the plateau of maximum SST (Fig. 4.4 E and F: horizontal grey bars), although the records show significant differences between the Cantabrian and the Alboran Sea. The Cantabrian record present a shorter LIG-acme with more stable SST than the Alboran Sea, which show a prominent SST maximum at the end of its LIG-acme. Stability of warm benthic foraminifera and ostracod assemblages was also found in the Cantabrian Sea during this period (Rodriguez-Lazaro *et al*., 2017). In spite of this, several short-term oscillations can be observed in both seas, being particularly acute in the Alboran record. The LIG-acme variability has been previously described in records from the North Atlantic, W-Iberian Margin and even in the central Mediterranean (Oppo *et al.,* 2001, 2006; Sprovieri *et al*., 2006; Tzedakis *et al*., 2018). The studied resolution prevents any detailed correlation with these events but the main patterns in the Cantabrian LIG-acme SST record are very comparable to those from the W-Iberian margin (Tzedakis *et al*., 2018) (Fig. 4.4 E). The largest LIG-acme SST variability occurred in the Alboran Sea where significant differences occurred between the W and E-Alboran sub-basins (977 vs. 976 sites), with a large decoupling by the end of the LIG-acme, when the eastern site recorded the warmest SST. Such warm end of the LIG-acme is also confirmed in Balearic Sea SST record (Fig. 3.27 and 3.28) although it does not fully cover the LIG. The Minorca speleothem $\delta^{13}C$ and Mg/Ca records (Fig. 4.4 C and D) indicate the dominance of stable humid conditions during the whole LIG-acme defined by warm SST, although with several short millennial scale oscillations, and in agreement with a general increase in water availability in the Mediterranean region and southern Europe during the LIG (Bar-Matthews *et al*., 2000; Couchoud *et al*., 2009; Genty *et al.,* 2013; Meyer *et al.,* 2008; Moseley *et al*., 2015; Sánchez-Goñi *et al.,* 1999, 2005).

Both Alboran SST and Minorca speleothem $\delta^{13}C$ and Mg/Ca records locate the glacial inception at the end of GS26 (116.5 kyr BP) with a clear intense cooling and aridification phase (Fig. 4.4 C and D: black arrow, note the reverse axis). Thus, the onset of the glacial inception in the western Mediterranean occurred later than in other northern regions, where earlier changes have been associated to the growing ice sheets and changes in the N Atlantic circulation during the GS26 (Fig. 4.5) (Demeney *et al*., 2017; Genty *et al.,* 2003; Moseley *et al*., 2015; Sirocko *et al.,* 2005; Tzedakis *et al*., 2018; Vansteenberge *et al*., 2016).

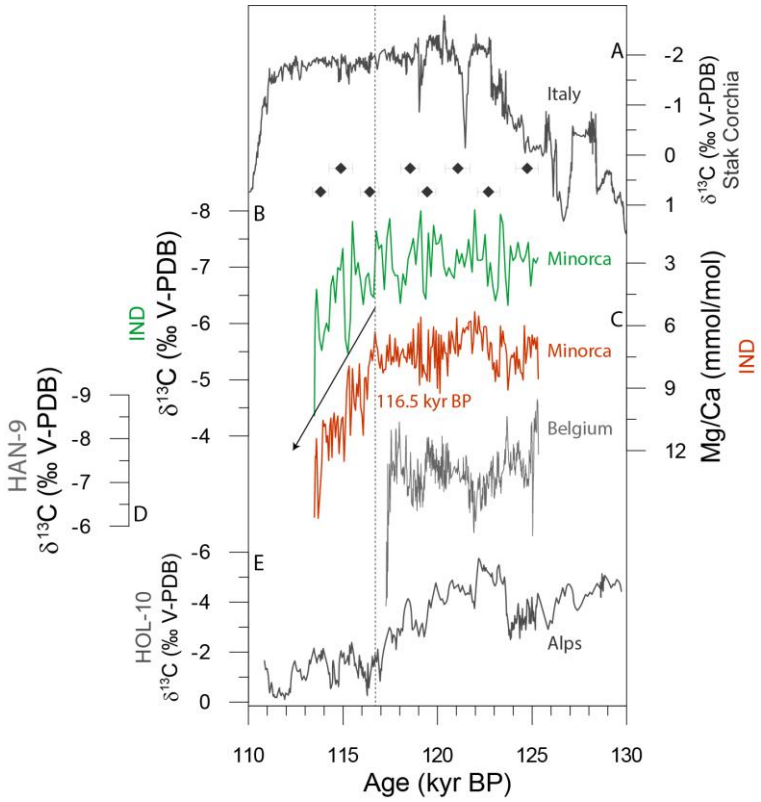

Figure 4.5: Comparison of the *Indiana* aridity trend during the glacial inception with other european terrestrial records. A) stacked $\delta^{13}C$ record of Corchia cave (Tzedakis *et al.*, 2018) witch not show a clear aridity trend during the glacial inception. B) IND $\delta^{13}C$ and C) IND Mg/Ca ratios with the U/Th ages from IND speleothem plotted with 2σ error bars on the top. D) $\delta^{13}C$ record of Han-sur-Lesse cave (Vansteenberge *et al.*, 2016) that show an abrupt shift toward dyers conditions that marks the onset of the glacial inception at 117.5 Kyr and culminate with a hiatuses in the speleothem growth and E) $\delta^{13}C$ record of Hölloch cave (Moseley *et al.*, 2015) that show an earlier and more progressive glacial inception.

Moreover, the Cantabrian SST record show a smoothed cooling during the glacial inception, that starts previous to GS26, and therefore also in agreement with the heterogeneous LIG-acme duration discussed in other studies (Bakker *et al.,* 2012, 2014; Hoffman *et al.,* 2017). But in any case, none of the studied SST records support an intense cooling event around the IP associated to the GS26. This is in line with other N Atlantic records that suggest a subtle stadial cooling in the eastern Atlantic but a significant cooling event C25 (GS26 equivalent) in the northern and western subpolar locations (McManus *et al*., 2002). In contrast, the GS26 is well marked in the Alboran Sea $\delta^{18}O_{sw}$ as an enrichment event also presented in the Corchia stack speleothem record (Tzedakis *et al*., 2018) and to some extend in the Minorca $\delta^{18}O$ record but it is not detected in the Cantabrian $\delta^{18}O_{sw}$ (Fig. 4.4 H, I and L).

According to all the studied SST records, the glacial inception culminated at MIS 5d (GS25) with an intense cooling phase (Fig. 4.4 E and F: red dashed arrows). The global glacial inception should be related to a weakening of the AMOC that caused climate deterioration, changing the strength and position of westerly winds and also the migration of rain belts (Bardají *et al.,* 2009; PAGES, 2016). But, the variable timing of the glacial inception may reflect the operation of climate feedbacks with diachronous responses across Europe (Govin *et al.,* 2015).

4.4.3 The early glacial

During the early glacial period the SST evolution among the three studied areas is dominated by the occurrence of a series of cooling events from 111 to 65 kyr BP in agreement with the GS sequence (Fig. 3.28 A, C, D and E). Furthermore, a weak stadial expression is shown in the SST records from the three regions during GS23, comparable to previously discussed weak GS26. For most of the GS, SST dropped to 13-12°C in western Mediterranean cores and to 10-9°C in the Cantabrian Sea, reducing the inter-basin gradients bellow 3°C and in some extreme cases, as the GS25 and 24, this gradient almost disappeared (Fig. 3.27). Regarding to the Alboran and Balearic Sea, SST values for each GS were identical, indicating strong homogeneous surface properties. In contrast to the overall homogeneous stadial inter-regional response, the Cantabrian record shows the occurrence of an extreme cold and freshening event at 101.5 kyr BP (beginning of the MIS 5c), which is not expressed in the Mediterranean SST records (Fig. 3.28 C: dashed grey vertical line) and it is likely recording a regional feature.

In the continent, the Pyrenean speleothem also supports a rapid atmospheric reorganization associated with stadials. Growth hiatus and intense enrichments in the $\delta^{13}C$ and Mg/Ca signal occurred synchronous to cold stadials supporting the establishment of drier conditions in the Southern Central Pyrenees (Fig. 4.6 black arrows). The aridity during stadials had a broad extent due to they are also recognized in some Balearic speleothems (VALL3, QUA14) (Fig. 4.6). This is consistent with another Iberian Peninsula speleothem (Pérez-Mejías *et al.,* 2019) and even European speleothem records indicating a robust relation between AMOC changes and European precipitation variability during the early glacial (Drysdale *et al.,* 2005, 2007; Genty et al., 2003; Vansteenberge et al., 2016). These Mediterranean dry stadial conditions are consistent with the heavy δ18Osw events (Fig. 4.7 G and H, blue arrows) overprinted on the large-scale precession signal of the Mediterranean δ18Osw records previously discussed (Section 4.2). These heavy stadial δ18Osw events, much intense in the Mediterranean records, should reflect conditions of enhanced evaporation-precipitation balance over the whole basin (Rohling *et al*., 1999) that were further strengthened eastward as shown in the δ18Ospeleo Soreq record (Fig. 4.7 G, I and J) (Bar-Matthews *et al*., 2000).

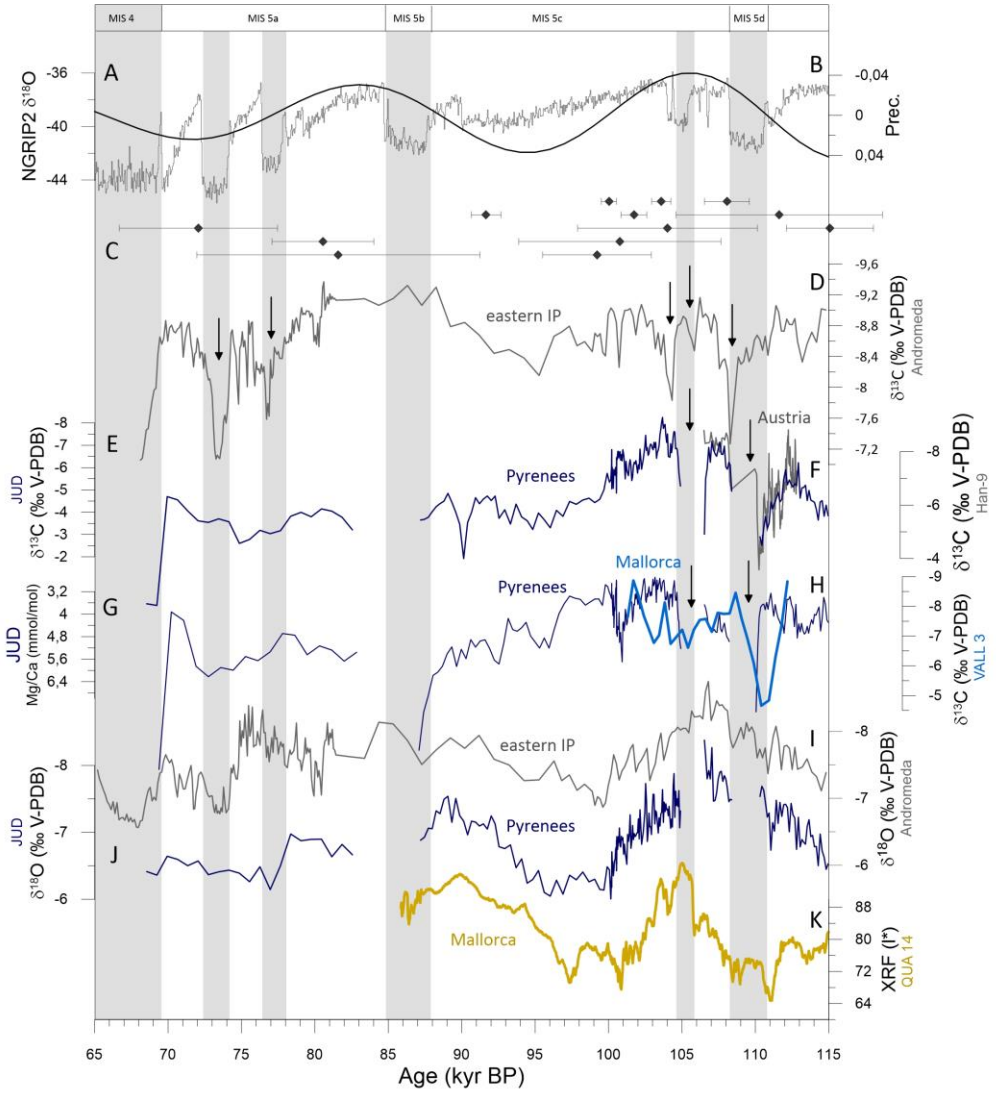

Figure 4.6: Comparison of the *Judit* general trends during the early glacial with Balearic and other european speleothem records. A) Reference record $\delta^{18}O$ NGRIP2 (Rasmussen *et al.,* 2014; Seierstad *et al.,* 2014). B) Precession curve (Laskar, 2004). C) U/Th ages from Judit speleothem plotted with 2σ error bars. D) $\delta^{13}C$ record of Ejulve cave (Pérez-Mejías *et al*., 2019). E) JUD $\delta^{13}C$ record. F) The $\delta^{13}C$ record of Han-sur-Lesse cave (Vansteenberge *et al*., 2016). G) JUD Mg/Ca record. H) VALL3. I) $\delta^{18}O$ record of Ejulve cave (Pérez-Mejías *et al*., 2019). J) QUA14 brightness data. Black arrows highligthing dry events.

The proxy record for deep-water current intensities in the Balearic core (UP 10 and Zr/Al ratio records in Fig. 4.7 E and F) also show a distinctive signal with relative high values for most of the stadial periods. The Balearic core location corresponds to a contournitic drift shaped by deep water currents associated with the formation of WMDW in the Gulf of Lion, were westerly winds acts (Frigola *et al.* 2007; Cisneros *et al*., 2019). Consistently with the previously described changes for MIS 3 in the same location (Frigola *et al.,* 2008), the overall set of data supports enhanced stadial formation of WMDW in the Gulf of Lion while cold SST and dry conditions dominated over the whole basin.

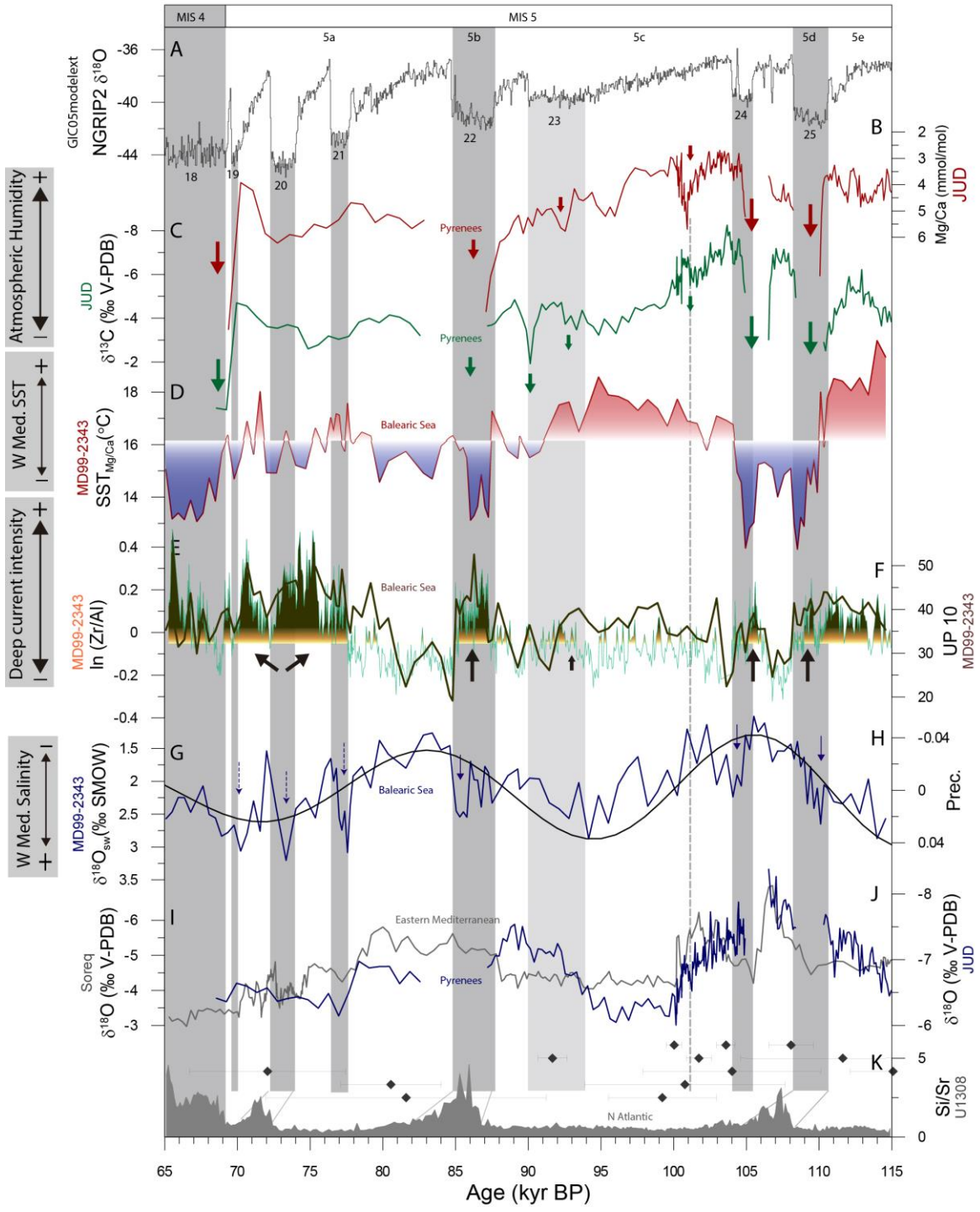

Figure 4.7 Comparison of this study records to some published data during the Early glacial. A) reference record $\delta^{18}O$ NGRIP2 (Rasmussen *et al.,* 2014; Seierstad *et al.,* 2014), B) JUD Mg/Ca ratios C) JUD $\delta^{13}C$ record, D) Mg/Ca-SST of MD99-2343 core, E) Zr/Al ratio plotted in logarithmic scale of MD99-2343 core, F) MD99-2343 non-carbonate UP10 fraction, G) $\delta^{18}O_{sw}$ of MD99-2343 core, H) Precession curve (Laskar, 2004), I) Stacked Soreq $\delta^{18}O_{speleo}$ record (Bar-Matthews *et al.,* 2000, 2003), J) JUD $\delta^{18}O_{speleo}$ record with the U/Th ages plotted with 2σ error bars on the bottom and K) Si/Sr-IRD record of U1308 core (Hodell *et al*., 2008). Red and green arrows: dry events discussed in the text. Black arrows: High deep current intensities. Blue arrows: heavy $\delta^{18}O_{sw}$ events. Vertical grey dashed line: Cantabrian cold event. Vertical grey dashed line: Cantabrian cold event. Vertical grey bars: MIS 4-5 and/or GS18-25.

These observations highlight an overall rapid interregional coupling in the ocean and atmosphere response during the stadial intervals. Our results are coherent with the oceanic-atmosphere re-adjustments observed in model studies after fresh water impose weakening of the AMOC (Ivanovic *et al*., 2018; Kageyama *et al*., 2010; Van Meerbeeck *et al*., 2011). The AMOC weakening reported in these studies support strong westerlies transport of cold and drier air masses due to its path over extended sea ice rather than ocean waters into W Europe and also reducing air temperature in the IP. The Intertropical Convergence Zone (ITCZ) and the atmospheric convection cells were displaced southward, decreasing consequently the moisture availability in mid-latitudes. Moreover extremely cold temperatures surrounding the IP reduced the evaporation on proximal areas, including the western Mediterranean Sea and enhancing the aridity in the region during the cold stadials.

In contrast to the stadial conditions, the SST evolution during the warm interstadials is more heterogeneous among the studied records, showing a diachronic establishment of maximum SST conditions (Fig. 3.28 C, D and E) and reaching large gradients among basins (Fig. 3.27). This regional heterogeneity suggest more complex feedback connections during warm intervals of full AMOC operation, which could probably cause displacements of the polar/subtropical gyres and therefore changes in the surface water properties arriving to the studied areas (Mary *et al*., 2017). The speleothem record support relatively humid conditions during warm interstadials, consistent with an active AMOC that would bring mild and humid westerly winds over Europe (Ivanovic *et al*., 2018; Kageyama *et al*., 2010; Van Meerbeeck *et al*., 2011). Nevertheless some variability occurred within the interstadial periods, the Pyrenean record shows a transition in the mid MIS 5c towards less humid conditions. This is consistent with previous observations in a Mallorca speleothem record (Dumitru *et al*., 2018), and a change from more developed Mediterranean vegetation to steppic pollen taxa detected in southern European pollen records and interpreted as a transition from warm-humid to warm-dry conditions during the MIS 5c (Sánchez-Goñi *et al*., 2005, 1999; Tzedakis *et al*., 2003; Wulf *et al.,* 2018).

Overall, climatic conditions were slightly different during MIS 5a stadial and interstadials periods. SST records during MIS 5a reflect dominant cold conditions in both the Cantabrian and the Mediterranean sectors, even for the interstadial periods (Fig. 3.28 C, D). Acute stadial $\delta^{18}O_{sw}$ enrichments occurred during stadials (GS21, 20 and 19) (Fig. 4.7 G: blue dashed arrows), while relatively fresh $\delta^{18}O_{sw}$ dominated in the Cantabrian record (Fig. 3.28 F). Those climatic conditions maintained an overall intense deep-water convection in the Western Mediterranean Sea (Fig. 4.7 E and F). Nevertheless, dry

conditions may have not been as extreme as previous stadials since the Pyrenean speleothem maintained its growth, although at low rate and Mg/Ca and $\delta^{13}C$ record only moderate high values. Moreover, major development of Pyrenean glaciers occurred during this period (Lewis *et al.,* 2009; Peña *et al*., 2003), also supporting some degree of humidity supply. Therefore, the last hiatus at the MIS 5b and the end of the Pyrenean speleothem growth at the beginning of the MIS 4 could reflect this maximum extension of Pyrenean ice, preventing water seepage into the karst and suggesting the establishment of full glacial conditions.

4.5 Interglacial transitions: Terminations

According to the collected speleothems, glacial terminations involved difficulties in the speleothem growth in the studied region. This situation could have been extreme during the penultimate deglaciation (T-II), a transition which is not fully covered by any of the sampled speleothems and it involved the end or marked the onset of their growth. The previous three terminations are fully represented by two of the studied speleothems (VALL2 and RAT) but involved a significant decrease in their growth rate. Therefore four Terminations (T-II-V) suggest that these periods of rapid ice melting represented major distortions in the hydrological conditions of the studied area. Among these terminations, T-III and T-IV are those recovered with higher resolution and solid chronologies and are the discussed with more attention (Fig. 4.8).

The T-III is well covered by the accurately dated RAT speleothem from Menorca and is characterized by a rapid change from dry to humid conditions that culminated at ~243 kyr BP accordingly to both Mg/Ca and $\delta^{13}C$ records. But this rapid climatic change was preceded by a $\delta^{18}O_{speleo}$ depletion in the RAT record that it can be observed also in the $\delta^{18}O$ of both Ejulve and Spannagel speleothem records at higher resolution (Fig. 4.8). Besides their different locations these three speleothems show similar trends of their geochemical records along the T-III pointing their connection to broadly regional processes (Pérez-Mejías *et al.,* 2017; Spötl *et al.,* 2008). During the T-IV also occurs an early light $\delta^{18}O_{speleo}$ event but in this case it precedes climatic amelioration inferred from the Mg/Ca and $\delta^{13}C$ records by about 10 kyr. Moreover, the described light $\delta^{18}O$ speleothem structures occur, within the chronological uncertainties, when the Si/Sr ratio from core U1308 indicates the development of an IRD discharge in the N Atlantic (Fig. 4.8) (Hodell *et al*., 2008). These IRD events would be analogous to the HE11 that initiated the T-II and produced a large light $\delta^{18}O_{sw}$ anomaly in surface waters from the N Atlantic and Western Mediterranean Sea as was discussed in section 4.4.1. So far, any $\delta^{18}O_{sw}$ is available for T-III and T-IV but this early light $\delta^{18}O_{speleo}$ anomaly could reflect a major $\delta^{18}O_{sw}$ freshening in the rain source region. These observations are supported by the light *G. bulloides* $\delta^{18}O$ anomalies recorded at the onset of both T-III and T-IV in the North Atlantic and also Alboran cores (Fig. 4.8) (Hodell *et al*., 2008, 2013; Martrat *et al*., 2007 and unpublished data) which are comparable to that recorded for the T-II and, according to the marine results from this thesis, corresponds to an intense $\delta^{18}O_{sw}$ depletion. Thus, these new speleothem records would indicate an imprint of these early deglacial large ice-sheet meltwater fluxes spreading into the N Atlantic Ocean that led to a major event of AMOC weakening. This situation is consistent with the two stadial events (stadial 8.1 and 8.2) defined in the

Ejulve speleothem record and associated to cold and arid conditions in the north western IP just at the onset of the T-III (Fig. 4.3) (Pérez-Mejías *et al.,* 2017). Regarding to the T-V, a similar light $\delta^{18}O_{speleo}$ structure can be recognized although is difficult to achieve a confident conclusion due to the VALL2 speleothem present lower growth rates and also age uncertainties. In consequence, these new speleothem records supports that the glacial terminations systematically initiated with a major ocean freshening event in the North Atlantic associated to extreme arid conditions in the IP. But these records also suggest that the actual chronology of these terminations in the marine record may need a further revision and thus also the orbital conditions that led the system into the deglacial mode.

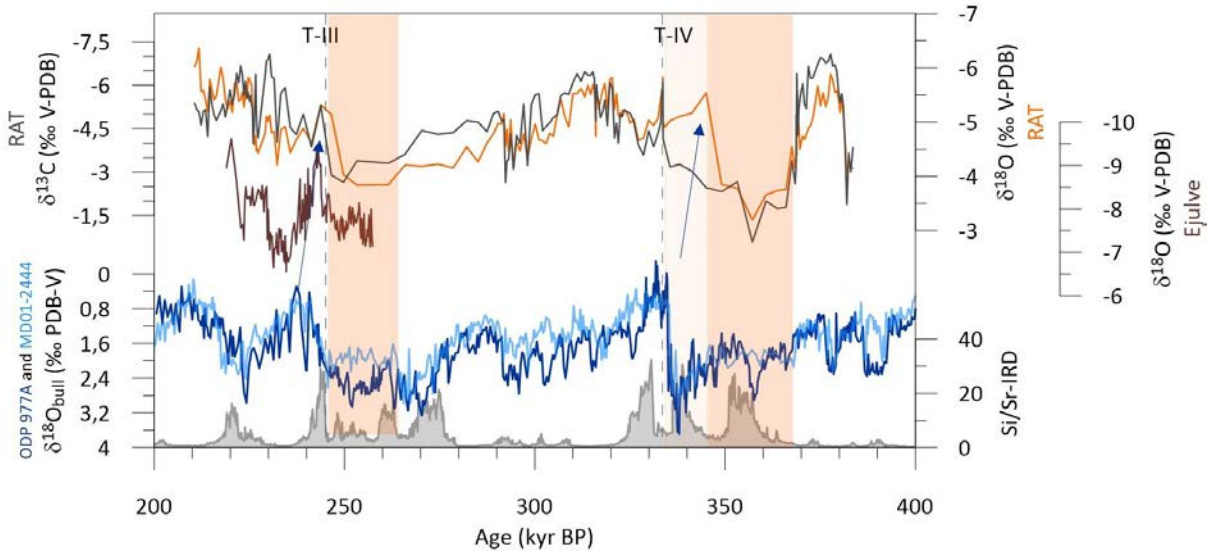

Fig 4.8: Comparison of RAT and Ejulve speleothems geochemical response with the $\delta^{18}O$ and IRD discharge in marine cores during terminations (T-III and T-IV) (Hodell *et al*., 2008, 2013; Martrat *et al*., 2007 and unpublished data; Pérez-Mejías *et al.*, 2017).

Just a perfect day
You made me forget myself
I thought I was
Someone else, someone good

Oh, it's such a perfect day
I'm glad I spent it with you
Oh, such a perfect day
You just keep me hanging on

You're going to reap just what you sow

Lou Reed

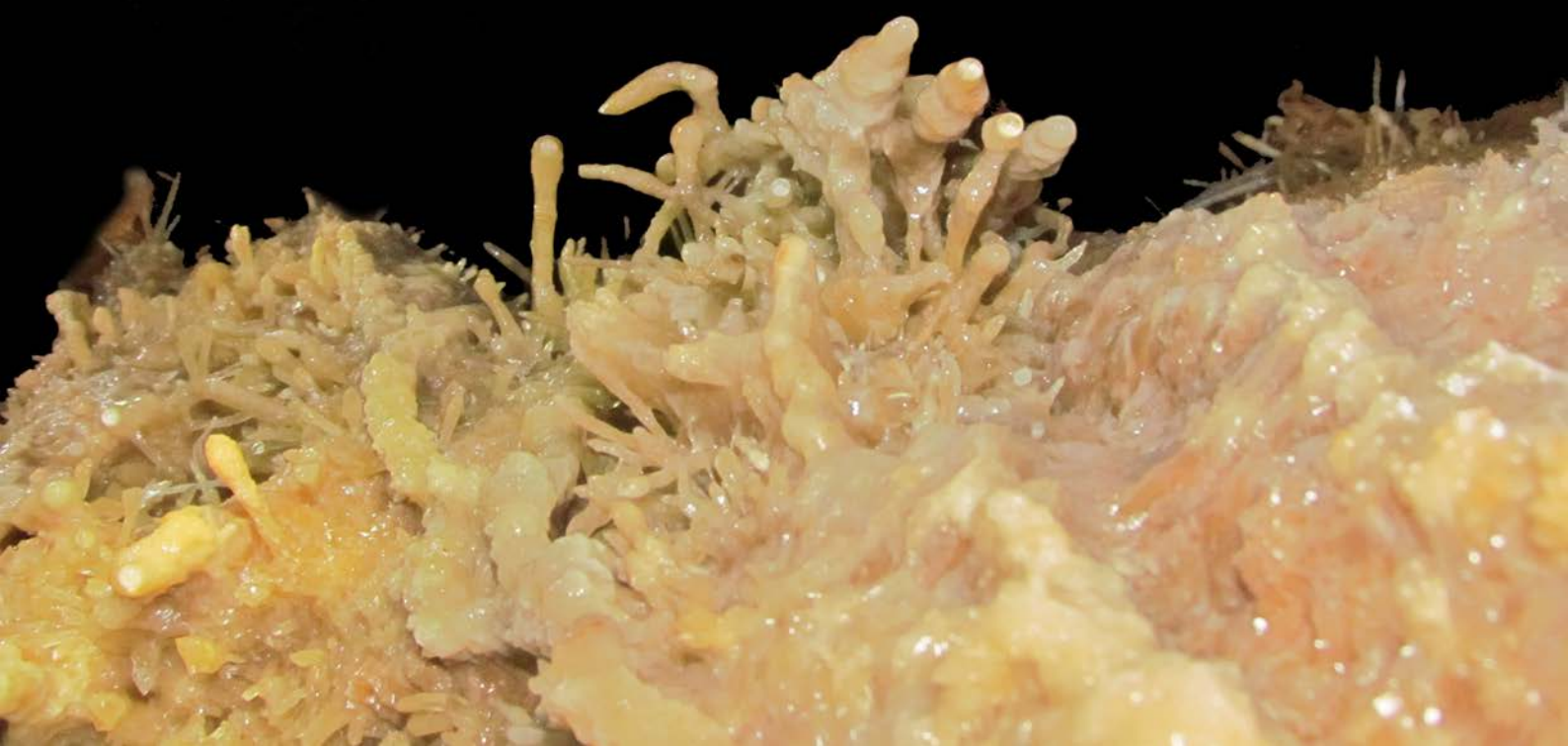

Chapter V

Conclusions

Conclusions

The collected speleothems in this study have revealed an heterogeneity in their geochemical signal as a consequence of different growing conditions, underlining the not suitability of every speleothems for reliable paleoclimate reconstructions and the need of a careful selection. In this regard, changes in the crystalline textures often are related to changes in the applied chemical ratios that enhance or mask the overall dominant climatic signal.

One of the innovative aspects of this research has been the parallel acquisition of $\delta^{18}O_{sw}$ and $\delta^{18}O_{speleo}$ records that provide the basis to directly test the potential influence of the marine signal in the cave precipitates. This exercise has allowed identifying a strong $\delta^{18}O$ precessional-scale signal that dominates both marine and cave records. The combined study of marine records from the Cantabrian realm, the westernmost Mediterranean Sea (Alboran Sea), and the central W Mediterranean (Balearic Sea), shows that this $\delta^{18}O_{sw}$ precession signal becomes amplified towards the Mediterranean region, consistent with the precesional control on the evaporation-precipitation balance of the whole Mediterranean basin. The recorded intensity of the $\delta^{18}O$ signal in speleothems from the Balearic Islands and the south central Pyrenees is larger than that detected in other more Atlantic influenced cave carbonates. These observations led to argue a relevant contribution of the Western Mediterranean Sea as humidity source to precipitation over the two studied locations.

A big novelty of this Ph.D. thesis is the completion of speleothem records for the last four interglacial periods which cover almost continuously a period of about 300 kyr and constitutes a pioneer achievement for the Mediterranean region. These interglacial periods correspond to the MIS 5, 7, 9, and 11 and the corresponding geochemical records indicate that they were periods of enhanced precipitation and climate amelioration with a well-developed vegetation cover. The MIS 11c denotes a long stable interglacial climate plateau with mainly constant water availability over the Balearic Islands. The geochemical speleothem signals reveal that the MIS 9e had comparable humid conditions to MIS 9a while MIS 9c was highly instable with several short-term dry events. The MIS 7 was not entirely recorded, but it records the interglacial sub-stage corresponding to the MIS 7e, supporting the increment in water availability in the Balearic region during this period.

Glacial Terminations represented periods of slow growth or even interruptions within the studied speleothem collection. In particular, the penultimate termination (TII)

should have involved extreme conditions since it is only represented by growth interruptions within the studied speleothems. Previous Terminations (T-III, IV and V) are recorded, but with significant decreases in the growth rates, supporting their association to major climate distortions that should have seriously altered the hydrological climatology in the region.

In consequence, the T-II study in here is based only on marine records. The new produced $\delta^{18}O_{sw}$ records show that the penultimate glaciation ended with an intense light anomaly that reached comparable values in both the Cantabrian and Western Mediterranean regions. This situation is interpreted to reflect a major North Atlantic surface freshening likely related to the HE11 melting. The intensity of the anomaly and the regional coverage of the freshening point out this as a major melting episode. These extreme ocean conditions may be the cause of a reduced evaporation that potentially led to the hydrological disruption in the Balearic area that prevented any speleothem growth. The end of this episode was linked to an AMOC reinforcement with an intense SST warming, larger in the Mediterranean region than in the Atlantic one, which marked the onset of the LIG period.

Previous glacial Terminations (T-III, IV and V) are represented in the studied records as rapid transitions toward more humid conditions and by an earlier intense $\delta^{18}O$ depletion likely reflecting ocean freshening phases comparable to that recorded for HE11 in T-II. The potential correspondence of these light episodes with the marine record opens the possibility to improve the accuracy of the marine chronologies but would involve a significant change in the timing of T-IV and the interglacial MIS 9e.

The integrated study of both speleothem and marine records for the last interglacial (MIS 5e) indicates a regional decoupling of SST and $\delta^{18}O_{sw}$ records among the three studied marine areas. This regional heterogeneity suggests high complexity in the climate response around the IP during warm periods. The studied Minorca speleothem record for this MIS 5e shows the dominance of relatively humid conditions. In addition, the achieved high resolution in this record, allows the identification of several centennial-scale minor oscillations in the humidity conditions from Minorca.

The onset of the last glaciation or the so-called glacial inception was not synchronous around the IP. SST in the Cantabrian Sea started to cold earlier than the stadial GS26 while the western Mediterranean started to cold later, by the end of the GS26, and at the same time than an aridification phase started in Minorca. After the GS26 a sequence of stadials occurred leading the Earth into a glaciation, these stadials are well

represented in the studied SST records by extreme cold conditions with homogeneous values around the Iberian Peninsula confirming the wide regional impact of these events of reduced AMOC. The speleothem records suggest the installation of drier conditions during these intervals in the south central Pyrenees and the Balearic Islands, which in some cases caused short hiatus in the speleothem growth. These conditions probably were a consequence of the diminished evaporation by the extreme cold conditions in both the N Atlantic Ocean and western Mediterranean Sea. The marine studied records from the Minorca drift indicate a stadial enhancement of deep convection in the Gulf of Lions likely responding to the overall cold and dry climatic conditions in the basin. In contrast, the interstadial intervals from this early glacial period show an overall regional heterogeneity, as it was also the case of the interglacial MIS 5e, pointing again to a much complex regional response to the ocean-atmosphere interconnections during warm episodes. Finally, the Pyrenean speleothem growth ended at the end of the MIS 5a likely due to the development of full glacial conditions in the region that led into the maximum extension of Pyrenean glaciers.

References

AEMET-IM., 2011. Atlas Climàtico Ibèrico. Temperatura del aire y precipitación 1971-2000. Agencia Estatal de Meteorología. ISBN: 978-84-7837-079-5.

Alley R. B., Marotzke J., Nordhaus W. D., Overpeck J. T., Peteet D. M., Pielke R. A., Pierrehumbert R. T., Rhines P. B., Stocker T. F., Talley L. D. and Wallace J. M., 2003. Abrupt Climate Change. Science, 299, 2005–2010.

Araguás-Araguás L., Froehlich K. and Rozanski K., 2000. Deuterium and oxygen-18 isotope composition of precipitation and atmospheric moisture. Hydrol. Process. 14, 1341–1355.

Ayalon A., Bar-Matthews M. and Sass E., 1998. Rainfall-recharge relationships within a karstic terrain in the Eastern Mediterranean semi-arid region, Israel: $\delta^{18}O$ and δD characteristics. J. Hydrol. 207, 18–31.

Bahr, A., Jimenez-Espejo, F.J., Kolasinac, N., Grunert, P., Hernandez-Molina, F.J., Rohl, U., Voelker, A.H.L., Escutia, C., Stow, D.A. V., Hodell, D., Alvarez-Zarikian, C.A., 2014. Deciphering bottomcurrent velocity and paleoclimate signals fromcontourite deposits in the Gulf of Cadiz during the last 140 kyr: An inorganic geochemical approach. Geochemistry Geophys. 15, 1–16. doi:10.1002/2014GC005356.

Baker, A., Smart, P.L. , Edwards, R.L. and Richards, D.A., 1993. Annual banding in a cave stalagmite. Nature, 364, 518–520.

Baker, A., Barnes W. L. and Smart P. L., 1997. Variations in the discharge and organic matter content of stalagmite drip waters in Lower Cave, Bristol. Hydrol. Process. 11, 1541–1555.

Bakker, P., Renssen, H., 2014. Last interglacial model-data mismatch of thermal maximum temperatures partially explained. Clim. Past, 10, 1633–1644. doi:10.5194/cp-10-1633-2014.

Bakker, P., Van Meerbeeck, C.J., Renssen, H., 2012. Sensitivity of the North Atlantic climate to Greenland Ice Sheet melting during the Last Interglacial. Clim. Past 8, 995–1009. doi:10.5194/cp-8-995-2012.

Baldini J. U. L., McDermott F. and Fairchild I. J., 2006. Spatial variability in cave drip water hydrochemistry: Implications for stalagmite paleoclimate records. Chem. Geol. 235, 390–404.

Bar -Matthews, M., Ayalon , A. and Kaufman, A., 1997. Late Quaternary paleoclimate in the Eastern Mediterranean region from stable isotope analysis of speleothems at Soreq Cave, Israel . Quaternary Research, 47, 155–168.

Bar-Matthews, M., Ayalon, A., Kaufman, A., and Wasserburg, G., 1999. The Eastern Mediterranean paleoclimate as a reflection of region events: Soreq Cave, Israel. Earth and Planetary Science Letters, 166, 85–95. https://doi.org/10.1016/S0012-

821X98.00275-1.

Bar-Matthews, M., Ayalon, A., Gilmour, M., Matthews, A., Hawkesworth, C.J., 2003. Sea – land oxygen isotopic relationships from planktonic foraminifera and speleothems in the Eastern Mediterranean region and their implication for paleorainfall during interglacial intervals. Geoch. et Cosmoch. Acta, 67, 3181–3199.

Bar-Matthews, M., Ayalon, A., Kaufman, A., 2000. Timing and hydrological conditions of Sapropel events in the Eastern Mediterranean, as evident from speleothems, Soreq cave, Israel. Chem. Geol. 169, 145–156. doi:10.1016/S0009-254199.00232-6.

Bárcena, M.A., Flores, J.A., Sierro, F.J., Pérez-Folgado, M., Fabres, J., Calafat, A., Canals, M., 2004. Planktonic response to main oceanographic changes in the Alboran Sea, Western Mediterranean, as documented in sediment traps and surface sediments. Mar. Micropaleontol. 53, 423–445. doi:10.1016/j.marmicro.2004.09.009.

Bardají, T., Goy, J.L., Zazo, C., Hillaire-Marcel, C., Dabrio, C.J., Cabero, A., Ghaleb, B., Silva, P.G., Lario, J., 2009. Sea level and climate changes during OIS 5e in the Western Mediterranean. Geomorphology 104, 22–37. doi:10.1016/j.geomorph.2008.05.027.

Barker, S., Cacho, I., Benway, H., Tachikawa, K., 2005. Planktonic foraminiferal Mg/Ca as a proxy for past oceanic temperatures: A methodological overview and data compilation for the Last Glacial Maximum. Quat. Sci. Rev. 24, 821–834. doi:10.1016/j.quascirev.2004.07.016.

Barker, S., Greaves, M., Elderfield, H., 2003. A study of cleaning procedures used for foraminiferal Mg/Ca paleothermometry. Geochemistry, Geophys. Geosystems 4, 1–20. doi:10.1029/2003GC000559.

Barker, S., Knorr, G., Edwards, R. L., Parrenin, F., Putnam, A. E., Skinner, L. C., Wolff, E., & Ziegler, M., 2011. 800,000 Years of abrupt climate variability. Science, 3346054, 347–351. https://doi.org/10.1126/science.1203580.

Bartolomé, M., Moreno, A., Sancho, C., Stoll, H.M., Cacho, I., Spötl, C., Belmonte, Á., Edwards, R.L., Cheng, H., Hellstrom, J.C., 2015. Hydrological change in Southern Europe responding to increasing North Atlantic overturning during Greenland Stadial 1. Proc. Natl. Acad. Sci. 112, 6568–6572. doi:10.1073/pnas.1503990112.

Berger, A., 1988. The peak at 3-7 days 3. Extensive swampg at the origin of coal the " Little Ice Age" which began seventeenth century with rapid expansion of the radiation. Geophysique , 264, 624–657.

Berger, A., and Loutre, M. F., 2002. An exceptionally long interglacial ahead? Science, 2975585, 1287–1288. https://doi.org/10.1126/science.1076120.

Bianchi, G.G., Hall, A., McCave, I.N. and Joseph, L., 1999. Measurement of the sortable silt current speed proxy using the Sedigraph 5100 and Coulter Multisizer IIe: precesion

and accuracy. Sedimentology, 46, 1001-1014.

Bigg, G. R., Jickells, T. D., Liss, P. S., and Osborn, T. J., 2003. The role of the oceans in climate. International Journal of Climatology. 2310, 1127–1159. https://doi.org/10.1002/joc.926.

Boch R., Cheng H., Spötl C., Edwards R. L., Wang X. and Häuselmann P., 2011. NALPS: a precisely dated European climate record 120–60 ka. Clim. Past, 7, 1247–1259.

Bond, G., Heinrich, H., Broecker, W.S., Labeyrie, L., MCmanus, J., Andrews, J.T., Huon, S., Jantschik, R., Clasen, S., Simet, C., Tedesco, K., Klas, M., Bonani, G. and Ivy, S., 1992. Evidence for masive discharges of icebergs inthe the North Atlantic ocean during the last glacial period. Nature, 360, 245-249.

Bond, G., Broecker, W.S., Johnsen, S.J., McManus, J., Labeyrie, L., Jouzel, J. i Bonani, G., 1993. Correlations between climate records from North Atlantic sediments and Greenland ice; Nature, 365: 143-147.

Borsato, A., Frisia, S., Fairchild, I.J., 2007. Trace element distribution in annual stalagmite laminae mapped by micrometer-resolution X-ray fluorescence: implications for incorporation of environmentally significant species. Geochimica et Cosmochimica Acta, 71, 1494–1512.

Bradley, R.S., 1999. Paleoclimatology: Reconstructing Climates of the Quaternary. International Geopgysics series, Vol. 68. ISBN-13: 978-0-12-124010-3.

Breecker, D. O., Payne, A. E., Quade, J., Banner, J. L., Ball, C. E., Meyer, K. W., & Cowan, B. D., 2012. The sources and sinks of CO_2 in caves under mixed woodland and grassland vegetation. Geochimica et Cosmochimica Acta, 96, 230-246.

Breitenbach, S. F. M., Rehfeld, K., Goswami, B., Baldini, J. U. L., Ridley, H. E., Kennett, D. J., Marwan, N., 2012. Constructing proxy records from age models COPRA. Climate of the Past, 8, 1765-1779.

Brocheray, S., Cremer, M., Zaragosi, S., Schmidt, S., Eynaud, F., Rossignol, L., Gillet, H., 2014. 2000 years of frequent turbidite activity in the Capbreton Canyon Bay of Biscay. Mar. Geol. 347, 136–152. doi:10.1016/j.margeo.2013.11.009.

Cacho, I., Grimalt, J.O., Canals, M., Sbaffi, L., Shackleton, N.J., Schönfeld, J., Zahn, R., 2001. Variability of the Western Mediterranean sea surface temperature during the last 25,000 years and its connection with the Northern Hemisphere climatic changes. Paleoceanography, 16, 40–52. doi:10.1029/2000PA000502.

Cacho, I., Grimalt, J.O., Pelejero, C., Canals, M., Sierro, F.J., Flores, J.A., Shackleton, N., 1999. Dansgaard-Oeschger and Heinrich event imprints in Alboran Sea paleotemperatures. Paleoceanography, 14, 698–705. doi:10.1029/1999PA900044.

Cacho, I., Shackleton, N., Elderfield, H., Sierro, F.J., Grimalt, J.O., 2006. Glacial rapid

variability in deep-water temperature and $\delta^{18}O$ from the Western Mediterranean Sea. Quat. Sci. Rev. 25, 3294–3311. doi:10.1016/j.quascirev.2006.10.004.

Cai, Y., Zhang, H., Cheng, H., An, Z., Edwards, L.R., Wang, X., Tan, L., Liang, F., Wang, J., Kelly, M., 2012. The Holocene Indian monsoon variability over the southern Tibetan Plateau and its teleconnections. Earth and Planetary Science Letters, 335–360, 135-144. https://doi.org/10.1016/j.epsl.2012.04.035.

Cai, Y., Fung, I. Y., Edwards, R. L., An, Z., Cheng, H., Lee, J. E., Tan, L., Shen, C. C., Wang, X., Day, J. A., Zhou, W., Kelly, M. J., and Chiang, J. C. H., 2015. Variability of stalagmite-inferred Indian monsoon precipitation over the past 252,000 y. Proceedings of the National Academy of Sciences of the United States of America, 11210, 2954–2959. https://doi.org/10.1073/pnas.1424035112.

Català, A., Cacho, I., Frigola, J., Pena, L.D, Lierer, F., 2019. Holocene hydrography evolution in the Alboran Sea: a multi-record and multy-proxy comparison. Clim. Past, 15, 1-15.

Cayre, O., Lancelot, Y., Vincent, E., Hall, M.A., 1999. Paleoceanographic reconstructions from planktic formaninfera off the Iberian Margin: Temperature, salinity, and Heinrich events. Paleoceanography, 14, 384–396.

Chave, K. E., 1954. Aspects of the Biogeochemistry of magnesium: Calcareous marine organisms. Journal of Geology, 62, 266-283.

Cheng, H, Edwards, R. ., Hoff, J., Gallup, C. ., Richards, D. ., & Asmerom, Y., 2000. The half-lives of uranium-234 and thorium-230. Chemical Geology, 1691., 17–33. https://doi.org/10.1016/S0009-254199.00157-6.

Cheng H., Edwards R. L., Wang Y., Kong X., Ming Y., Kelly M. J., Wang X. and Gallup C. D., 2006. A penultimate glacial monsoon record from Hulu Cave and two-phase glacial terminations. Geology 34, 217–220.

Cheng, H., Edwards, R.L., Broecker, W.S., Denton, G.H., Kong, X., Wang, Y., Zhang, R., Wang, X., 2009. Ice Age Terminations. Science, 326, 248-252. doi: 10.1126/science.1177840

Cheng, H., Sinha, A., Wang, X., Cruz, F. W., and Edwards, R. L., 2012. The Global Paleomonsoon as seen through speleothem records from Asia and the Americas. Climate dynamics, 395., 1045-1062.

Cheng, Hai, Lawrence Edwards, R., Shen, C. C., Polyak, V. J., Asmerom, Y., Woodhead, J., Hellstrom, J., Wang, Y., Kong, X., Spötl, C., Wang, X., & Calvin Alexander, E., 2013. Improvements in ^{230}Th dating, ^{230}Th and ^{234}U half-life values, and U-Th isotopic measurements by multi-collector inductively coupled plasma mass spectrometry. Earth and Planetary Science Letters, 371–372, 82–91. https://doi.org/10.1016/j.epsl.2013.04.006.

Cheng, Hai, Spötl, C., Breitenbach, S. F. M., Sinha, A., Wassenburg, J. A., Jochum, K. P., Scholz,

D., Li, X., Yi, L., Peng, Y., Lv, Y., Zhang, P., Votintseva, A., Loginov, V., Ning, Y., Kathayat, G., & Edwards, R. L., 2016. Climate variations of Central Asia on orbital to millennial timescales. Scientific Reports, 5, 1–11. https://doi.org/10.1038/srep36975.

Cisneros, M., Cacho, I., Frigola, J., Canals, M., Masqué, P., Martrat, B., Casado, M., Grimalt, J.O., Pena, L.D., Margaritelli, G., Lirer, F., 2016. Sea surface temperature variability in the central-western Mediterranean Sea during the last 2700 years: A multi-proxy and multi-record approach. Clim. Past, 12, 849–869. doi:10.5194/cp-12-849-2016.

Cisneros, M., Cacho, I., Frigola, J., Sanchez-Vidal, A., Calafat, A., Pedrosa-Pàmies, R., Rumín-Caparrós, A., Canals, M., 2019. Deep-water formation variability in the north-western Mediterranean Sea during the last 2500 yr: A proxy validation with present-day data. Glob. and Planetary Change, 177, 56-68 https://doi.org/10.1016/j.gloplacha.2019.03.012.

Clark and Fritz, 1997. Environmental Isotopes in Hydrogeology. Lewis Publishers, New York.

Cobb K. M., Adkins J. F., Partin J. W. and Clark B., 2007. Regional-scale climate influences on temporal variations of rainwater and cave dripwater oxygen isotopes in northern Borneo. Earth Planet. Sci. Lett. 263, 207–220.

Comas, M.C., Zahn, R., Klaus, A., 1996. Shipboard Scientific Party 2 HOLE 816A. Proc. ODP, Ink. Repts 161, 299–353. doi:10.2973/odp.proc.ir.147.104.1993.

Coplen, T.B., 1996. New guidelines for reporting stable hydrogen, carbon, and oxygen isotope-ratio data. Geochim. Cosmochim. Acta 60, 3359–3360. doi:10.1016/0016-703796.00263-3.

Couchoud, I., Genty, D., Hoffmann, D., Drysdale, R., Blamart, D., 2009. Millennial-scale climate variability during the Last Interglacial recorded in a speleothem from south-western France. Quat. Sci. Rev. 28, 3263–3274. doi:10.1016/j.quascirev.2009.08.014.

Craig, H., Gordon, L., 1965. Deuterium and oxygen 18 variations in the ocean and the marine atmosphere. Stable Isotopes in Oceanographic Studies and Paleotemperatures , 9-130.

Cruz F. W., Burns S. J., Karmann I., Sharp W. D., Vuille M., Cardoso A. O., Ferrari J. A., Silva Dias P. L. and Viana O., 2005. Insolation-driven changes in atmospheric circulation over the past 116,000 years in subtropical Brazil. Nature, 434, 63–66.

Cruz F. W., Vuille M., Burns S. J., Wang X., Cheng H., Werner M., Lawrence Edwards R., Karmann I., Auler A. S. and Nguyen H., 2009. Orbitally driven east–west antiphasing of South American precipitation. Nat. Geosci. 2, 210– 214.

Davis, J.C., 2002. Statistics and data analysis in Geology. 3er ed. John Wiley & Sons.

Day, C. C., and Henderson, G. M., 2013. Controls on trace-element partitioning in cave-

analogue calcite. *Geochimica et Cosmochimica Acta*, *120*, 612-627.

Demény, A., Kern, Z., Czuppon, G., Németh, A., Leél-Őssy, S., Siklósy, Z., Lin, K., Hu, H.M., Shen, C.C., Vennemann, T.W., Haszpra, L., 2017. Stable isotope compositions of speleothems from the last interglacial – Spatial patterns of climate fluctuations in Europe. Quat. Sci. Rev. 161, 68–80. doi:10.1016/j.quascirev.2017.02.012.

Dorale, J .A., González, L. A., Reagan, M. K., Pickett, D. A., Murrell, M. T., Baker, R. G., 1992. A high-resolution record of holocene climate change in speleothem calcite from Cold Water Cave, Northeast Iowa. Science. 258, 1626–1630. doi:10.1126/science.258.5088.1626.

Dorale, J. A., Onac, B. P., Fornós, J. J., Ginés, J., Ginés, A., Tuccimei, P., Peate, D. W., 2010. Sea-level highstand 81,000 years ago in Mallorca. Science. 327, 860–863. doi:10.1126/science.1181725.

Drysdale, R. N., Zanchetta, G., Hellstrom, J. C., Fallick, A. E., Zhao, J. X., Isola, I., & Bruschi, G., 2004. Palaeoclimatic implications of the growth history and stable isotope $\delta^{18}O$ and $\delta^{13}C$. Geochemistry of a Middle to Late Pleistocene stalagmite from central-western Italy. Earth and Planetary Science Letters, 2273–4, 215–229. https://doi.org/10.1016/j.epsl.2004.09.010.

Drysdale, R. N., Zanchetta, G., Hellstrom, J. C., Fallick, A. E., Zhao, J. X., 2005. Stalagmite evidence for the onset of the Last Interglacial in southern Europe at 129 ± 1 ka. Geophys. Res. Lett. 32, 1–4. doi:10.1029/2005GL024658.

Drysdale, R., Zanchetta, G. & Hellstrom, J., 2006. Late Holocene drought responsible for the collapse of old world civilizations is recorded in an Italian flowstone. Geology, 34, 101–104.

Drysdale, R. N., Zanchetta, G., Hellstrom, J. C., Fallick, A. E., McDonald, J., Cartwright, I., 2007. Stalagmite evidence for the precise timing of North Atlantic cold events during the early last glacial. Geology, 35, 77–80. doi:10.1130/G23161A.1.

Drysdale, R. N. Hellstrom, J. C., Zanchetta, G., Fallick, A. E., Sánchez-Goñi, M. F., Couchoud, I., 2009. Evidence for obliquity forcing of glacial termination II. Science, 3255947., pp.1527–1531. doi: 10.1126/science.1170371.

Dulinski, M. and Rozanski, K., 1990. Formation of 13C/12C isotope ratios in speleothems: a semi-dynamic model . Radiocarbon, 32, 7–16.

Dumitru, O. A., Forray, F. L., Fornós, J. J., Ersek, V., Onac, B. P., 2017. Water isotopic variability in Mallorca: a path to understanding past changes in hydroclimate. Hydrol. Process. 31, 104–116. doi:10.1002/hyp.10978.

Dumitru, O. A., Onac, B. P., Polyak, V. J., Wynn, J. G., Asmerom, Y., Fornós, J. J., 2018. Climate variability in the western Mediterranean between 121 and 67 ka derived from a

Mallorcan speleothem record. Palaeogeogr. Palaeoclimatol. Palaeoecol. 506, 128–138. doi:10.1016/j.palaeo.2018.06.028.

Dutton, A., and Lambeck, K., 2012. Ice volume and sea level during the last interglacial. Science, 337, 216–219. doi:10.1126/science.1205749.

Edwards, R. L., Chen, J. H., & Wasserburg, G. J., 1987. ^{238}U-^{234}U ^{230}Th-^{232}Th systematics and the precise measurement of time over the past 500,000 years. Earth and Planetary Science Letters, 812–3., 175–192. https://doi.org/10.1016/0012-821X87.90154-3.

Edwards R., Gallup C. and Cheng H., 2003. Uranium-series dating of marine and lacustrine carbonates. Uranium-series geochemistry Reviews in mineralogy and geochemistry. Geochemical society and mineralogical society of America, 363–405.

Elderfield, H., and Granssen, G., 2000. Past temperatures and $d^{18}O$ of surface ocean waters inferred from foraminiferal Mg/Ca ratios. Nature, 405, 442–445.

Elderfield, H., J. Yu, P. Arnand, T. Kiefer, and B. Nyland., 2006. Calibrations for benthic foraminiferal Mg/Ca paleothermometry and the carbonate ion hypothesis. Earth and Planetary Science letters, 250, 633-649.

Elderfield, H., Ferretti, P., Greaves, M., Crowhurst, S., McCave, I. N., Hodell, D., & Piotrowski, A. M., 2012.. Evolution of ocean temperature and ice volume through the mid-Pleistocene climate transition. Science, 3376095, 704-709.

Emiliani, C., 1955. Pleistocene temperatures. Journal of Geology, 63, 538-578.

Epstein, S. and Mayeda, T., 1953. Variation of O^{18} content of waters from natural sources. Geochimica et Cosmochimica Acta, 45, 213-224.

Fairchild, I. J., Tooth, A. F., Huang, Y., Borsato, A., Frisia, S., McDermott, F., 1996. Spatial and temporal variations in waterand stalactite chemistry in currently active caves: a precursor to interpretations of past climate. Pro-ceedings of the fourth International Symposium on the Geochemistry of the Earth's Surface. University of Leeds, 229–233.

Fairchild, I.J. and Baker, A., 2012. Speleothem science: from process to past environments. John Wiley & Sons. Oxford, UK. http://dx.doi.org/10.1002/9781444361094.

Fairchild, I.J., Borsato, A., Tooth, A.F., Frisia, S., Hawkesworth, C.J., Huang, Y., McDermott, F., Spiro, B., 2000. Controls on trace element Sr-Mg. compositions of carbonate cave waters: Implications for speleothem climatic records. Chem. Geol. 166, 255–269. doi:10.1016/S0009-254199.00216-8.

Fairchild, I.J., McMillan, E.A., 2007. Speleothems as indicators of wet and dry periods. Int. J. Speleol. 36, 69–74. doi:10.5038/1827-806X.36.2.2.

Fairchild, I.J., Smith, C.L., Baker, A., Fuller, L., Spötl, C., Mattey, D., McDermott, F., 2006. Modification and preservation of environmental signals in speleothems. Earth-Science Rev. 75, 105–153. doi:10.1016/j.earscirev.2005.08.003.

Fairchild, I.J., Treble, P.C., 2009. Trace elements in speleothems as recorders of environmental change. Quat. Sci. Rev. 28, 449–468. doi:10.1016/j.quascirev.2008.11.007.

Feng, W., Banner, J. L., Guilfoyle, A. L., Musgrove, M. L., & James, E. W., 2012.. Oxygen isotopic fractionation between drip water and speleothem calcite: A 10-year monitoring study, central Texas, USA. Chemical Geology, 304–305, 53–67. https://doi.org/10.1016/j.chemgeo.2012.02.004.

Ferguson, J. E., Henderson, G. M., Kucera, M., and Rickaby, R. E. M., 2008. Systematic change of foraminiferal Mg/ Ca ratios across a strong salinity gradient. Earth Planet. Sc. Lett., 265, 153–166, https://doi.org/10.1016/j.epsl.2007.10.011.

Ferrer, L., Fontán, A., Mader, J., Chust, G., González, M., Valencia, V., Uriarte, A., Collins, M.B., 2009. Low-salinity plumes in the oceanic region of the Basque Country. Cont. Shelf Res. 29, 970–984. doi:10.1016/j.csr.2008.12.014.

Fletcher, W. J. and Sánchez-Goñi, M.F., 2008. Orbital and sub-orbital scale climate impacts on vegetation of the western Mediterranean basin over the last 48,000yr. Quat. Res. 70, 451–464. doi:10.1016/j.yqres.2008.07.002.

Frigola, J., Moreno, A., Cacho, I., Canals, M., Sierro, F.J., Flores, J.A., Grimalt, J.O., 2008. Evidence of abrupt changes in Western Mediterranean Deep Water circulation during the last 50 kyr: A high-resolution marine record from the Balearic Sea. Quat. Int. 181, 88–104. doi:10.1016/j.quaint.2007.06.016.

Frigola, J., Moreno, A., Cacho, I., Canals, M., Sierro, F.J., Flores, J.A., Grimalt, J.O., Hodell, D.A., Curtis, J.H., 2007. Holocene climate variability in the western Mediterranean region from a deepwater sediment record. Paleoceanography 22, 1–16. doi:10.1029/2006PA001307.

Ganopolski, A., Winkelmann, R. and Schellnhuber, H.J., 2016. Critical insolation-Co2 relation for diagnosing past and future glacial inception. Nature, 529, 200-203. doi:10.1028/nature16494.

Gascoyne, M., 1983. Trace element partition coefficients in the calcite water system and their palaeoclimatic significance in cave studies. Journal of Hydrology, 61, 213–222

Gazis, C., and Feng, X. 2004. A stable isotope study of soil water: Evidence for mixing and preferential flow paths. Geoderma, 1191–2, 97–111. https://doi.org/10.1016/S0016-706103.00243-X.

Genty, D., Baker, A., Vokal, B., 2001. Instra and inter-annual growth rate of modern stalagmites. Chem. Geol. 176, 191–212. doi:10.1016/S0009-254100.00399-5.

Genty, D., Blamart, D., Ouahdi, R., Gilmour, M., Baker, A., Jouzel, J., Van-Exter, S., 2003. Precise dating of Dansgaard-Oeschger climate oscillations in western Europe from

stalagmite data. Nature, 421, 833–837. doi:10.1038/nature01391.

Genty D., Blamart D., Ghaleb B., Plagnes V., Causse C., Bakalowicz M., Zouari K., Chkir N., Hellstrom J. and Wainer K., 2006. Timing and dynamics of the last deglaciation from European and North African $\delta^{13}C$ stalagmite profiles comparison with Chinese and South Hemisphere stalagmites. Quat. Sci. Rev. 25, 2118–2142.

Genty, D., Verheyden, S., Wainer, K., 2013. Speleothem records over the last interglacial. Investigating Past Interglacials, PAGES news, 21, 1–2.

Gimeno, L., Nieto, R., Trigo, R.M., Vicente-Serrano, S.M., López-Moreno, J.I., 2010. Where does the Iberian Peninsula moisture come from? An answer based on a lagrangian approach. J. Hydrometeorol. 11, 421–436. doi:10.1175/2009JHM1182.1.

Gibbard, P. L., & West, R. G., 2000. Quaternary chronostratigraphy: the nomenclature of terrestrial sequences. Boreas, 2*9*4, 329-336.

Gines, J., Joan, J., Gines, A., Vesica, P., and Eis, P. L. n.d... espeleotemes de Mallorca : canvis del nivell de la Mediterrania i paleoclima Pleistoce Superior.

Govin, A., Capron, E., Tzedakis, P.C., Verheyden, S., Ghaleb, B., Hillaire-Marcel, C., St-Onge, G., Stoner, J.S., Bassinot, F., Bazin, L., Blunier, T., Combourieu-Nebout, N., El Ouahabi, A., Genty, D., Gersonde, R., Jimenez-Amat, P., Landais, A., Martrat, B., Masson-Delmotte, V., Parrenin, F., Seidenkrantz, M.S., Veres, D., Waelbroeck, C., Zahn, R., 2015. Sequence of events from the onset to the demise of the Last Interglacial: Evaluating strengths and limitations of chronologies used in climatic archives. Quat. Sci. Rev. 129, 1–36. doi:10.1016/j.quascirev.2015.09.018.

Grant, K.M., Rohling, E.J., Bar-Matthews, M., Ayalon, A., Medina-Elizalde, M., Bronk Ramsey, C., Satow, C., Roberts, A.P., 2012. Rapid coupling between ice volume and polar temperature over the past 150 kyr. Nature, 491, 744-747. doi: 10.1038/nature11593

Grant, K. M., Grimm, R., Mikolajewicz, U., Marino, G., Ziegler, M., & Rohling, E. J., 2016. The timing of Mediterranean sapropel deposition relative to insolation, sea-level and African monsoon changes. Quaternary Science Reviews, 140, 125–141. https://doi.org/10.1016/j.quascirev.2016.03.026.

Guijarro, J. A., 1986. Contribución a la bioclimatología de Baleares.

Gunn, J., 2004. Encyclopedia of Caves and Karst Science. Fitzroy Dean , New York.

Hall, I. R., & McCave, I. N., 2000. Palaeocurrent reconstruction, sediment and thorium focussing on the Iberian margin over the last 140 ka. Earth and Planetary Science Letters, 1781–2, 151–164. https://doi.org/10.1016/S0012-821X00.00068-6.

Hellstrom, J.C., McCulloch, M.T. and Stone J., 1998. A 31,000 year high resolution record of southern hemisphere maritime climate changes, from the stable isotope geochemistry of New Zealand speleothems. Quaternary Research, 50, 167–178.

Hellstrom, J., 2003. Rapid and accurate U/Th dating using parallel ion-counting multi-collector ICP-MS. J. Anal. At. Spectrom. 18, 1346–1351. doi:10.1039/b308781f.

Hellstrom, J., 2006. U–Th dating of speleothems with high initial ^{230}Th using stratigraphical constraint. Quaternary Geochronology, 14, 289-295.

Hembleden, C., 1989. Modern Planktonic Foraminifera, Springer, 363.

Hendy, C. H., & Wilson, A. T., 1968. Palaeoclimatic data from speleothems. Nature. 2195149, 48–51. https://doi.org/10.1038/219048a0.

Hendy, C.H., 1971. The isotopic geochemistry of speleothems. The calculation of the effects of different modes of formation on the isotopic composition of speleothems and their applicability as palaeoclimatic indicators. Geochimica et Cosmochimica Acta, 358, 801-824.

Hodell, D.A., Channell, J.E.T., Curtis, J.H., Romero, O.E., 2008. Onset of ‘“ Hudson Strait ”’ Heinrich events in the eastern North Atlantic at the end of the middle Pleistocene transition 640ka. Paleoceanography, 23, 1–16. doi:10.1029/2008PA001591.

Hodell, D.A., Minth, E.K., Curtis, J.H., McCave, I.N., Hall, I.R., Channell, J.E.T., Xuan, C., 2009. Surface and deep-water hydrography on Gardar Drift Iceland Basin. during the last interglacial period. Earth Planet. Sci. Lett. 288, 10–19. doi:10.1016/j.epsl.2009.08.040.

Hodge, E.J., Richards, D.A., Smart, P.L., Andreo, B., Hoffmann, D.L., Mattey, D.P., González-ramón, A., 2008a. Effective precipitation in southern Spain ~ 266 to 46 ka. based on a speleothem stable carbon isotope record 69, 447–457. doi:10.1016/j.yqres.2008.02.013.

Hodge, E.J., Richards, D.., Smart, P.., Ginés, A., Mattey, D., 2008b. Sub-millennial climate shifts in the western Mediterranean during the last glacial period recorded in a speleothem from Mallorca, Spain. J. Quat. Sci. 23, 713–718. doi:10.1002/jqs.1198.

Hodkinson, J.R., 1966. Particle sizing by means of the forward scattering lobe, Applied optics, 5 5., 839-844.

Hoffmann, D. L., Prytulak, J., Richards, D. A., Elliott, T., Coath, C. D., Smart, P. L., and Scholz, D., 2007. Procedures for accurate U and Th isotope measurements by high precision MC-ICPMS. 264, 97–109. https://doi.org/10.1016/j.ijms.2007.03.020.

Hoffman, J.S., Clark, P.U., Parnell, A.C., He, F., 2017. Regional and global sea-surface temperatures during the last interglaciation. Science. 355, 276–279. doi:10.1126/science.aai8464.

Hoogakker, B. A. A., Klinkhammer, G. P., Elderfield, H., Rohling, E. J., and Hayward, C., 2009. Mg/Ca paleothermometry in high salinity environments, Earth Planet. Sc. Lett., 284, 583–589, doi:10.1016/j.epsl.2009.05.027.

Hönisch, B., Allen, K. A., Lea, D. W., Spero, H. J., Eggins, S. M., Arbuszewski, J., DeMenocal, P., Rosenthal, Y., Russell, A. D., and Elderfield, H., 2013. The influence of salinity on Mg/Ca in planktic foraminifers evidence from cultures, core-top sediments and complementary $d^{18}O$. Geochim. Cosmochim. Ac., 121, 196–213.

Huang, Y. , Fairchild, I.J., Borsato, A., 2001. Seasonal variations in Sr, Mg and P in modern speleothems Grotta di Ernesto, Italy.

Imbrie,J. and Imbrie, K., 1979. Ice Ages: Solving the Mystery, short Hills, NJ, Enslow

Imbrie, J., Hays, J.D., Martinson, D.G., McIntyre, A., Mix, A.C., Morley, J.J., Pisias, N.G., Prell, W.i Shackleton, N., 1984. The orbital theory of Pleistocene climate: support from a revised chronology of the marine $d^{18}O$ record. Proceedings of the NATO Advanced Research Workshop on Milankovitch and Climate. D. Reidel Publishing Company, Palisades, Nova York, 269-305.

Imbrie, J., Boyle, E., Clemens, C., Duffy, A., Howard, W., Kukla, G., Kutzbach, J.E., Martinson, D.G., McIntyre, A., Mix, A.C., Molfi no, B., Morley, J.J., Peterson, L.C., Pisias, N.G., Prell, W., Raymo, M.E., Shackleton, N.J. i Toggweiler, J.R., 1992. On the structure and origin of major glaciation cycles. Linear responses to Milankovitch forcing. Paleoceanography, 7: 701-738.

IPCC-2013, Climate Change 2013. The Physical Science Basis: Working Group I Contribution to the IPCC Fifth Assessment Report, Cambridge Univ. Press.

Ivanovic, R. F., Gregoire, L J., Burke, A., Wickert, A. D., Valdes, P. J., Ng, H.C., Robinson, L.F., McManus, J.F., Mitrovica, J.X., Dentith, J.E., 2018. Acceleration of Northern Ice Sheet Melt Induces AMOC Slowdown and Northern Cooling in Simulations of the Early Last Deglaciation. Paleoceanography and Paleoclimatology, 33, 807-824. https:// doi.org/10.1029/2017PA003308.

Jansà, A., 2014. El clima de les illes Balears. Lleonard Muntaner. ISBN:978-84-16116-05-8.

Jansen, J.H.F., Van der Gaast, S.J., Koster, B. i Vaars, A.J., 1998. CORTEX, a shipboard XRF-scanner for element analyses in split sediment cores; Marine Geology, 151: 143153.

Jiménez-Amat, P., Zahn, R., 2015. Offset timing of climate oscillations during the last two glacial-interglacial transitions connected with large-scale freshwater perturbation. Paleoceanography, 30, 768–788. doi:10.1002/2014PA002710.

Johnson, K. R., Hu, C., Belshaw, N. S., & Henderson, G. M., 2006. Seasonal trace-element and stable-isotope variations in a Chinese speleothem: The potential for high-resolution paleomonsoon reconstruction. Earth and Planetary Science Letters, 2441–2, 394–407. https://doi.org/10.1016/j.epsl.2006.01.064.

Kageyama, M., Paul, A., Roche, D. M., Van Meerbeeck, C. J., 2010. Modelling glacial climatic millennial-scale variability related to changes in the Atlantic meridional overturning

circulation: a review. Quat. Sci. Rev. 29, 2931-2956. doi: 10.1016/j.quascirev.2010.05.029.

Kaufman, A., and Broecker, W., 1965. Comparison of Th^{230} and C^{14} ages for carbonate materials from Lakes Lahontan and Bonneville. Journal of geophysical Research, 7016., 4039-4054.

Koster R. D., Valpine D. P. de and Jouzel J., 1993. Continental water recycling and $H_2{}^{18}O$ concentrations. Geophys. Res. Lett. 20, 2215–2218.

Kowalczk A. J. and Froelich P. N., 2010. Cave air ventilation and CO_2 outgassing by radon 222 modeling: How fast do caves breathe? Earth Planet. Sci. Lett. 289, 209–219.

Koutavas, A., and J. Lynch-Stieglitz, 2004. Variability of the marine ITCZ over the eastern Pacific during the past 30,000 years. The Hadley Circulation: Present, Past and Future, 347–369.

Krklec, K. and Domínguez-Villar, D., 2014. Quantification of the impact of moisture source regions on the oxygen isotope composition of precipitation over Eagle Cave, central Spain. Geoch. Cosm. Acta 134, 39-54. doi: 10.1016/j.gca.2014.03.011.

Lachniet, M.S., 2009. Climatic and environmental controls on speleothem oxygen-isotope values. Quat. Sci. Rev. 28, 412–432. doi:10.1016/j.quascirev.2008.10.021.

Lea, D., 1999. Trace elements in foraminiferal calcite in Modern foraminifera. Luer Academic Press, UK. pp.259-277.

Lea D.W., 2003. Elemental and isotopic proxies of marine temperatures, in the Oceans and Marine Geochemistry. Elsevier-Pergamon, Oxford.

Lea, D.W., Pak, D.K., Paradis, G., 2005. Influence of volcanic shards on foraminiferal Mg/Ca in a core from the Galápagos region. Geochemistry, Geophys. Geosystems 6, 1–13. doi:10.1029/2005GC000970.

Lewis, C.J., McDonald, E. V., Sancho, C., Peña, J.L., Rhodes, E.J., 2009. Climatic implications of correlated Upper Pleistocene glacial and fluvial deposits on the Cinca and Gállego Rivers NE Spain. based on OSL dating and soil stratigraphy. Glob. Planet. Change 67, 141–152. doi:10.1016/j.gloplacha.2009.01.001.

Lionello, P., 2012. The Climate of the Mediterranean Region: From the Past to the Future, 1st ed. Elsevier Inc. doi:10.1016/B978-0-12-416042-2.00009-4.

Lisiecki, L. E., and Raymo, M. E., 2005.. A Pliocene-Pleistocene stack of 57 globally distributed benthic $\delta^{18}O$ records. Paleoceanography, 201, 1–17. https://doi.org/10.1029/2004PA001071.

López-Mir, B., 2013. Extensional salt tectonics in the Cotiella post-rift basin south-central Pyrenees: 3D structure and evolution. PhD of Department of Geodinamics and Geophysics, University of Barcelona.

Loutre, M.F. and Berger, A., 2000. Future climatic changes: are we entering an exceptionally long interglacial. Climatic Change 46, 61-90.

Loutre, M. F., and Berger, A., 2003. Marine Isotope Stage 11 as an analogue for the present interglacial. Global and Planetary Change, 363, 209–217. https://doi.org/10.1016/S0921-818102.00186-8.

Ludwig, K.R., Simmons, K.R., Szabo, B.J., 1992. Massspectrometric ^{230}Th-^{234}U-^{238}U dating of the Devils Hole calcite vein. Science, 258, 284-287.

Maldonado, A. and Canals, M., 1982. El margen continental sur-balear: un modelo deposicional reciente sobre un margen de tipo pasivo. Acta Geologica Hispanica, 17, 241-254.

Marino, G., Rohling, E.J., Rodríguez-Sanz, L., Grant, K.M., Heslop, D., Roberts, A.P., Stanford, J.D., Yu, J., 2015. Bipolar seesaw control on last interglacial sea level. Nature, 522, 197–201. doi:10.1038/nature14499.

Martin, J.M., Elbaz-Poulichet, F., Guieu, C., Loÿe-Pilot, M.D., Han, G., 1989. River versus atmospheric input of material to the mediterranean sea: an overview. Mar. Chem. 28, 159–182. doi:10.1016/0304-420389.90193-X.

Martinson, D. G., Pisias, N. G., Hays, J. D., Imbrie, J., Moore, T. C., and Shackleton, N. J., 1987. Age dating and the orbital theory of the ice ages: Development of a high-resolution 0 to 300,000-year chronostratigraphy. Quaternary research, 27(1), 1-29.

Martrat, B., Grimalt, J.O., Lopez-Martínez, C., Cacho, I., Sierro, F.J., Flores, J.A., Zahn, R., Canals, M., Curtis, J.H., Hodell, D.A., 2004. Abrupt Temperature Changes in the Western Mediterranean over the Past 250,000 Years. Science, 306, 1762–1765. doi:10.1126/science.1101706.

Martrat, B., Grimalt, J.O., Shackleton, N.J., De Abreu, L., Hutterli, M.A., Stocker, T.F., 2007. Four climate cycles of recurring deep and surface water destabilizations on the Iberian margin. Science, 317, 502–507. doi:10.1126/science.1139994.

Martrat, B., Jimenez-Amat, P., Zahn, R., Grimalt, J.O., 2014. Similarities and dissimilarities between the last two deglaciations and interglaciations in the North Atlantic region. Quat. Sci. Rev. 99, 122–134. doi:10.1016/j.quascirev.2014.06.016.

Martrat, B., Tzedakis, P.C., Margari, V., Skinner, L., Hodell, D.A., Grimalt, J.O., 2015. Oceanic processes as potential trigger and amplifying mechanisms for Heinrich events. PAGES Mag. 23, 1–2.

Mary, Y., Eynaud, F., Colin, C., Rossignol, L., Brocheray, S., Mojtahid, M., Garcia, J., Peral, M., Howa, H., Zaragosi, S., Cremer, M., 2017. Changes in Holocene meridional circulation and poleward Atlantic flow: The Bay of Biscay as a nodal point. Clim. Past 13, 201–216. doi:10.5194/cp-13-201-2017.

Mashiotta, T.A., Lea, D.W. and Spero, H.J., 1999. Glacial-interglacial changes in Subantarctic sea surface temperature and $\delta^{18}O$-water using foraminiferal Mg. Earth Planet. Sc. Lett. 170, 417432.

Mattey, D., Lowry, D., Duffet, J., Fisher, R., Hodge, E., and Frisia, S., 2008. A 53 year seasonally resolved oxygen and carbon isotope record from a modern Gibraltar speleothem: reconstructed drip water and relationship to local precipitation. Earth and Planetary Science Letters, 269(1-2), 80-95.

McCartney, M.S., Mauritzen, C., 2001. On the origin of the warm inflow to the Nordic Seas. Prog. Oceanogr. 51, 125–214. doi:10.1016/S0079-661101.00084-2.

McCave, I.N. and Hall, I.R., 2006. Size sorting in marine muds: Processes, pitfalls, and prospects for paleoflow-speed proxies. Geochemistry, Geophys. Geosystems, 7. doi:10.1029/2006GC001284.

McCave, I.N., Manighetti, B., Robinson, S.G., 1995. Sortable Silt and Fine Sediment Size Composition Slicing - Parameters for Paleocurrent Speed and Paleoceanography. Paleoceanography, 10, 593–610. doi:10.1029/94PA03039.

McDermott, F., Frisia, S., Huang, Y., Longinelli, A., Spiro, B., Heaton, T.H.E., Hawkesworth, C.J., Borsato, A., Keppens, E. i Fairchild, I.J., 1999. Holocene climate variability in Europe: Evidence from $d^{18}O$, textural and extension-rate variations in three speleothems. Quaternary Science Reviews, 18: 1021-1038.

McDermott F., Mattey D. P. and Hawkesworth C. J., 2001. Centennial-scale Holocene climate variability revealed by a high-resolution speleothem $d^{18}O$ record from SW Ireland. Science, 294, 1328–1331.

McDermott, F., 2004. Palaeo-climate reconstruction from stable isotope variations in speleothems: A review. Quat. Sci. Rev. 23, 901–918. doi:10.1016/j.quascirev.2003.06.021.

McDermott F., Schwarcz, H. and Rowe, P.J., 2006. Isotopes in Speleothems. In Isotopes in Palaeoenvironmental Research Springer. 185–226.

McDermott, F., Atkinson, T., Fairchild, I,J., Baldini, L., Mattey, D.P., 2011. A first evaluation of the spatial gradients in $d^{18}O$ recorded speleothems. Global and Planetari change, 79, 275-287.

McDonald, J., Drysdale, R., Hill, D., Chisari, R., and Wong, H., 2007. The hydrochemical response of cave drip waters to sub-annual and inter-annual climate variability, Wombeyan Caves, SE Australia. Chemical Geology, 244, 605-623.

McManus, J.F., Oppo, D.W., Keigwin, L.D., Cullen, J.L., Bond, G.C., 2002. Thermohaline Circulation and Prolonged Interglacial Warmth in the North Atlantic. Quat. Res. 58, 17–21. doi:10.1006/qres.2002.2367.

McQueen, J. B., 1967. Some methods for classification and analysis of multivariate observations, statistics and probability. Univ. of California. Press. Proc. Fifth Berkeley Symp. on Math. Statist. and Prob., Vol. 1, 281-297.

Meyer, M.C., Spötl, C., Mangini, A., 2008. The demise of the Last Interglacial recorded in isotopically dated speleothems from the Alps. Quat. Sci. Rev. 27, 476–496. doi:10.1016/j.quascirev.2007.11.005.

Mickler, P. J., Stern, L. A., and Banner, J. L., 2006. Large kinetic isotope effects in modern speleothems. Bulletin of the Geological Society of America, 1181–2, 65–81. https://doi.org/10.1130/B25698.1

Milankovitch, M., 1941. Canon of Insolation and the Ice Age Problem. Royal Academy of Serbia 133, 633.

Millot, C., 1999. Circulation in the Western Mediterranean Sea. J. Mar. Syst. 20, 423–442. doi:10.1016/S0924-796398.00078-5.

Moreno, A., Cacho, I., Canals, M., Prins, M. A., Sánchez-Goni, M. F., Grimalt, J. O., & Weltje, G. J., 2002. Saharan dust transport and high-latitude glacial climatic variability: The Alboran Sea record. Quaternary Research, 583, 318–328. https://doi.org/10.1006/qres.2002.2383.

Moreno, A., Cacho, I., Canals, M., Grimalt, J.O., Sánchez-Goñi, M.F., Shackleton, N., Sierro, F.J., 2005. Links between marine and atmospheric processes oscillating on a millennial time-scale. A multi-proxy study of the last 50,000 yr from the Alboran Sea Western Mediterranean Sea. Quat. Sci. Rev. 24, 1623–1636. doi:10.1016/j.quascirev.2004.06.018.

Moreno, A., Stoll, H., Jiménez-Sánchez, M., Cacho, I., Valero-Garcés, B., Ito, E., Edwards, R.L., 2010. A speleothem record of glacial 25-11.6 kyr BP. rapid climatic changes from northern Iberian Peninsula. Glob. Planet. Change, 71, 218–231. doi:10.1016/j.gloplacha.2009.10.002.

Morse, J. and Bender, M.L., 1990. Partition coefficients in calcite: Examination of factors influencing the validity of experimental results and their application to natural systems. Chemical Geology, 82, 265-277.

Mortyn, P. G., and Charles, C. D., 2003. Planktonic foraminiferal depth habitat and $\delta^{18}O$ calibrations: Plankton tow results from the Atlantic sector of the Southern Ocean. Paleoceanography, 182.

Moseley, G. E., Spötl, C., Svensson, A., Cheng, H., Brandstätter, S., and Edwards, R. L., 2014. Multi-speleothem record reveals tightly coupled climate between central europe and greenland during marine isotope stage 3. Geology, 4212, 1043–1046. https://doi.org/10.1130/G36063.1.

Moseley, G.E., Spötl, C., Cheng, H., Boch, R., Min, A., Edwards, R.L., 2015. Termination-II interstadial/stadial climate change recorded in two stalagmites from the north European Alps. Quat. Sci. Rev. 127, 229–239. doi:10.1016/j.quascirev.2015.07.012.

Moseley, G. E., Edwards, R. L., Wendt, K. A., Cheng, H., Dublyansky, Y., Lu, Y., ... & Spötl, C. 2016. Reconciliation of the Devils Hole climate record with orbital forcing. Science, *351*6269, 165-168.

Mulder, T., Hassan, R., Ducassou, E., Zaragosi, S., Gonthier, E., Hanquiez, V., Marchès, E., Toucanne, S., 2013. Contourites in the Gulf of Cadiz: A cautionary note on potentially ambiguous indicators of bottom current velocity. Geo-Marine Lett. 33, 357–367. doi:10.1007/s00367-013-0332-4.

Nieto, R., Gimeno, L., Drumond, A., Hernandez, E., 2010. A Lagrangian identification of the main moisture sources and sinks affecting the Mediterranean area. WSEAS Trans. Env. and Dev. 6, 365-374.

Nürnberg, D., 1995. Magnesium in tests of Neogloboquadrina pachyderma sinistral from high northern and southern latitudes. Journal of Foraminiferal Research. 25, 350-368.

Nürnberg, D., Bijma, J., Hembleben, c., 1996. Assessing the realiability of magnesium in foraminiferal calcite as a proxy for wáter mass temperaturas. Geochimica et Cosmochimica Acta, 60, 803-814.

Oppo, D.W., Keigwin, L.D., Mcmanus, J.F., Cullen, J.L., 2001. Persistent suborbital climate variability in marine isotopestage 5 and Termination II. Paleoceanography, 16, 280–292.

Oppo, D.W., Mcmanus, J.F., Cullen, J.L., 2006. Evolution and demise of the Last Interglacial warmth in the subpolar North Atlantic. Quat. Sci. Rev. 25, 3268–3277. doi:10.1016/j.quascirev.2006.07.006.

Otvos, E. G., 2015. The last interglacial stage: Definitions and marine highstand, North America and Eurasia. Quaternary International, 383, 158-173.

Paillard, D., Labeyric, L. & Yiou, P., 1996. Machintosh program performs time-series analysis. Eos Transactions, AGU 77,376.

PAGES, P.I.W.G. of P., 2016. Interglacials of the last 800,000years. Rev. Geophys. 54, 162–219. doi:10.1002/2015RG000482.Received.

Pastor, F., Valiente, J.A., Palau, J.L., 2017. Sea Surface Temperature in the Mediterranean: Trends and Spatial Patterns 1982–2016. Pure Appl. Geophys. doi:10.1007/s00024-017-1739-z.

Pena, L.D., Cacho, I., Calvo, E., Pelejero, C., Eggins, S., Sadekov, A., 2008. Characterization of contaminant phases in foraminifera carbonates by electron microprobe mapping.

Geochemistry, Geophys. Geosystems 9. doi:10.1029/2008GC002018.

Pena, L.D., Calvo, E., Cacho, I., Eggins, S., Pelejero, C., 2005. Identification and removal of Mn-Mg-rich contaminant phases on foraminiferal tests: Implications for Mg/Ca past temperature reconstructions. Geochemistry, Geophys. Geosystems 6. doi:10.1029/2005GC000930.

Peña, J.L., Sancho, C., Lewis, C., Mcdonald, E.E., 2004. Datos cronológicos de las morrenas terminales del glaciar del Gállego y su relación con las terrazas fluvioglaciares Pirineo de Huesca.. Geogr. Física Aragón. Asp. Gen. y temáticos Univ. Zaragoza e Inst. Fernando el Católico 71–84. ISBN: 849621429X.

Pérez-Brunius, P., Rossby, T., Watts, D.R., 2004. Absolute Transports of Mass and Temperature for the North Atlantic Current– Subpolar Front System. J. Phys. Oceanogr. 34, 1870–1883. doi:10.1175/1520-04852004.034<1870:ATOMAT>2.0.CO;2.

Pérez-Mejías, C., Moreno, A., Sancho, C., Bartolomé, M., Stoll, H., Cacho, I., Cheng, H., & Edwards, R. L., 2017. Abrupt climate changes during Termination III in Southern Europe. Proceedings of the National Academy of Sciences of the United States of America, 11438, 10047–10052. https://doi.org/10.1073/pnas.1619615114.

Pérez-Mejías, C., Moreno, A., Sancho, C., Martín-García, R., Spötl, C., Cacho, I., Cheng, H., & Edwards, R. L., 2019. Orbital-to-millennial scale climate variability during Marine Isotope Stages 5 to 3 in northeast Iberia. Quaternary Science Reviews, 224. https://doi.org/10.1016/j.quascirev.2019.105946.

Picciolo, A.R., 2006. National Oceanographic Data Center. AIBS Bull. 13, 38. doi:10.2307/1292958.

Pierre, C., 1999. The oxygen and carbon isotope distribution in the Mediterranean water masses. Mar. Geol. 153, 41–55. doi:10.1016/S0025-322798.00090-5.

Pinardi, N., Masetti, E., 2000. Variability of the large scale general circulation of the Mediterranean Sea from observations and modelling: a review. Palaeogeography, Palaeoclima. Palaeoeco., 158, 153–173.

Pingree, R.D. and B. Le Cann, 1990. Structure, strength and seasonality of the slope currents in the Bay of Biscay region. J. mar. biol. Ass. U.K., 70: 857-885.

Pollard, R.T., Griffiths, M.J., Cunningham, S.A. Read, J.F., Pérez, F.f., Rios, A.F., 1996. Vivaldi 1991 a study of the formation, circulation and ventilation of Eastren North Atlantic Central Water. Progress in Oceanography, 37, 167-192.

Potts, P.J. and Webb, P.C., 1992. X-ray fl uorescence spectrometry; Journal of Geochemical Exploration, 44: 251-296.

Povea, P., Cacho, I., Moreno, A., Men, M., Fernando, J.M., 2015. A new procedure for the

lithic fraction characterization in marine sediments from high productivity areas : Optimization of analytical and statistical procedures. Limnol. Oceanogr. Methods 13, 127–137. doi:10.1002/lom3.10013.

Railsback, L. B., Gibbard, P. L., Head, M. J., Voarintsoa, N. R. G., & Toucanne, S., 2015. An optimized scheme of lettered marine isotope substages for the last 1.0 million years, and the climatostratigraphic nature of isotope stages and substages. Quaternary Science Reviews, 111, 94–106. https://doi.org/10.1016/j.quascirev.2015.01.012.

Ramsey , B. C., 2008. Deposition models for chronological records . Quaternary Science Reviews, 27, 42–60.

Rasmussen, S.O., Bigler, M., Blockley, S.P., Blunier, T., Buchardt, S.L., Clausen, H.B., Cvijanovic, I., Dahl-Jensen, D., Johnsen, S.J., Fischer, H., Gkinis, V., Guillevic, M., Hoek, W.Z., Lowe, J.J., Pedro, J.B., Popp, T., Seierstad, I.K., Steffensen, J.P., Svensson, A.M., Vallelonga, P., Vinther, B.M., Walker, M.J.C., Wheatley, J.J., Winstrup, M., 2014. A stratigraphic framework for abrupt climatic changes during the Last Glacial period based on three synchronized Greenland ice-core records: Refining and extending the INTIMATE event stratigraphy. Quat. Sci. Rev. 106, 14–28. doi:10.1016/j.quascirev.2014.09.007.

Rebesco, M., Hernández-Molina, F.J., Van Rooij, D., Wåhlin, A., 2014. Contourites and associated sediments controlled by deep-water circulation processes: State-of-the-art and future considerations. Mar. Geol. 352, 111–154. doi:10.1016/j.margeo.2014.03.011.

Richards and Dorale, 2003. Uranium-series Chronology and Environmental Applications of Speleothems. School of Geograph. Sci., Univ. of Bristol. 1529-6466/00/0052-0010$10.00.

Richter, T.O., van der Gaast, S., Koster, B., Vaars, A., Gieles, R., de Stigter, H.C., De Haas, H., van Weering, T.C.E., 2006. The Avaatech XRF Core Scanner: technical description and applications to NE Atlantic sediments. Geol. Soc. London, Spec. Publ. 267, 39–50. doi:10.1144/GSL.SP.2006.267.01.03.

Rigual-Hernández, A.S., Sierro, F.J., Bárcena, M.A., Flores, J.A., Heussner, S., 2012. Seasonal and interannual changes of planktic foraminiferal fluxes in the Gulf of Lions NW Mediterranean. and their implications for paleoceanographic studies: Two 12-year sediment trap records. Deep. Res. Part I Oceanogr. Res. Pap. 66, 26–40. doi:10.1016/j.dsr.2012.03.011.

Robinson, Simon G. and McCave, I.N., 1994. Orbital forcing of bottom-current enhanced sedimentation on Feni Drift, NE Atlantic, during the mid-Pleistocene. Paleoceanography 9, 943–972.

Rodriguez-Lazaro, J., Pascual, A., Cacho, I., Varela, Z., Pena, L.D., 2017. Deep-sea benthic response to rapid climatic oscillations of the last glacial cycle in the SE Bay of Biscay. J. Sea Res. 130, 49–72. doi:10.1016/j.seares.2017.06.002.

Rodríguez-Sanz, L., Bernasconi, S.M., Marino, G., Heslop, D., Müller, I.A., Fernandez, A., Grant, K.M., Rohling, E.J., 2017. Penultimate deglacial warming across the Mediterranean Sea revealed by clumped isotopes in foraminifera. Sci. Rep. 7, 1–11. doi:10.1038/s41598-017-16528-6.

Rohling, E. J., Marino, G., and Grant, K. M., 2015. Mediterranean climate and oceanography, and the periodic development of anoxic events sapropels. Earth-Science Reviews, 143, 62–97. https://doi.org/10.1016/j.earscirev.2015.01.008.

Rohling, E.J., Foster, G.L., Grant, K.M., Marino, G., Roberts, A.P., Tamisiea, M.E., Williams, F., 2014. Sea-level and deep-sea-temperature variability over the past 5.3 million years. Nature 508, 477-482. doi: 10.1038/nature13230.

Rohling, E.J., Abu-Zied, R.H., Casford, J.S.L., Hayes, A., Hoogakker, B., 2009. The marine environment: present and past, The physical geography of the Mediterranean. Oxford University Press, Oxford, 33–67.

Rohling, E.J., 1999. Environmental control on Mediterranean salinity and $d^{18}0$. Paleoceanography, vol. 14, n 6, 706-715.

Rohling, E.J., Hayes, A., De Rijk, S., Kroon, D., Zachariasse, W.J., Eisma, D., 1998. Abrupt cold spells in the northwest Mediterranean. Paleoceanography 13, 316–322. doi:10.1029/98PA00671.

Rothwell, G.R., Rack, F.R., 2006. New techniques in sediment core analysis: an introduction. Geol. Soc. London, Spec. Publ. 267, 1–29. doi:10.1144/GSL.SP.2006.267.01.01.

Rosenthal, Y., Boyle, E.A., Slowey, N., 1997. Temperature control on the incorporation of magnesium, strontium, fluorite and cadmium into benthic foraminiferal shells from Little Bahama Bank : Prospects for thermocline paleoceanography. Geochemica et Cosmochimica Acta, 61, 3633-3643.

Rozanski, K., Sonntag, C., and Munnich, K. O., 1982. Factors controlling stable isotope composition of European precipitation. Tellus, 342, 142–150. https://doi.org/10.3402/tellusa.v34i2.10796.

Rozanski K., Araguás-Araguás L. and Gonfiantini R., 1993. Isotopic patterns in modern global precipitation. Geophys. Monogr. Ser. 78, PP. 1-36.

Rudiman, W.F. 2001. Earth's Climate. Past and Future. Freeman and Comapany, NY, 465pp.

Ruddiman, W. F., 2005. Plows, plagues, and petroleum: how humans took control of climate. Princeton University Press. Vol. 46. ISBN: 0691133980.

Ruddiman, W. F., 2006. Ice-driven CO_2 feedback on ice volume. Climate of the Past, 21, 43–55. https://doi.org/10.5194/cp-2-43-2006.

Sánchez-Goñi, M.F., Eynaud, F., Turon, J.L., Shackleton, N.J., 1999. High resolution palynological record off the Iberian margin: Direct land-sea correlation for the Last Interglacial complex. Earth Planet. Sci. Lett. 171, 123–137. doi:10.1016/S0012-821X99.00141-7.

Sánchez-Goñi, M.F., Loutre, M.F., Crucifix, M., Peyron, O., Santos, L., Duprat, J., Malaizé, B., Turon, J.L., Peypouquet, J.P., 2005. Increasing vegetation and climate gradient in Western Europe over the Last Glacial Inception 122-110 ka.: Data-model comparison. Earth Planet. Sci. Lett. 231, 111–130. doi:10.1016/j.epsl.2004.12.010.

Sánchez-Goñi, M.F., Bakker, P., Desprat, S., Carlson, A.E., Van Meerbeeck, C.J., Peyron, O., Naughton, F., Fletcher, W.J., Eynaud, F., Rossignol, L., Renssen, H., 2012. European climate optimum and enhanced Greenland melt during the last interglacial. Geology 40, 627–630. doi:10.1130/G32908.1.

Scholz, D., Hoffmann, D.L., 2011. StalAge: An algorithm designed for construction of speleothem age models. Quat. Geoch. 6, 369–382. doi:10.1016/j.quageo.2011.02.002.

Scholz, D., Hoffmann, D. L., Hellstrom, J., Ramsey, C.B., 2012. A comparison of different methods for speleothem age modelling. Quaternary geochronology, 14, 94-104.

Schubert, B. A., and Jahren, A. H., 2012.. The effect of atmospheric CO_2 concentration on carbon isotope fractionation in C3 land plants. Geochimica et Cosmochimica Acta, 96, 29–43. https://doi.org/10.1016/j.gca.2012.08.003.

Seidenkrantz, M., Bornmalm, L., Johnsen, S.J., Knudsen, K.L., Kuijpers, A., Lauritzen, S., Leroy, S.A.G., Mergeai, I., Schweger, C., Vliet-lanoe, B.V.A.N., Alberta, T., 1996. Two-step deglaciation at the oxygen isotope stage 6/5e transition: The zeifen-kattegat climate oscillation. Quat. Sci. Rev. 15, 63–75.

Seierstad, I.K., Abbott, P.M., Bigler, M., Blunier, T., Bourne, A.J., Brook, E., Buchardt, S.L., Buizert, C., Clausen, H.B., Cook, E., Dahl-Jensen, D., Davies, S.M., Guillevic, M., Johnsen, S.J., Pedersen, D.S., Popp, T.J., Rasmussen, S.O., Severinghaus, J.P., Svensson, A., Vinther, B.M., 2014. Consistently dated records from the Greenland GRIP, GISP2 and NGRIP ice cores for the past 104ka reveal regional millennial-scale δ18O gradients with possible Heinrich event imprint. Quat. Sci. Rev. 106, 29–46. doi:10.1016/j.quascirev.2014.10.032.

Sen Gupta, B.K., 1999. Introduction to modern Foraminifera. In: Sen Gupta, B.K., Eds... Modern Foraminifera, Great Britain, Kluwer Academic Publishers, pp. 3-6.

Shackleton, N.J., 1967. Oxygen isotope analyses and Pleistocene temperatures re-assessd. Nature, 215, 15-17.

Shackleton, N. J., 1969. The last interglacial in the marine and terrestrial records. Proceedings of the Royal Society of London. Series B. Biological Sciences, 1741034, 135-154.

Shackleton, N.J., 1974. Attainment of isotopic equilibrium between ocean water and the benthonic foraminifera genus Uvigerina: Isotopic changes in the ocean during the last glacial. Colloq. Int. du C.N.R.S 203–209.

Shackleton, N.J., and Hall, M.A., 1984. Oxygen and carbon isotope Stratigraphy of Deep-Sea Drilling Project Hole-552a-Plio-Pleistocene Glacial History. Initial Reports of the Deep Sea Drilling Project, 81 DEC., 599-609.

Shakun, J. D., Lea, D. W., Lisiecki, L. E., and Raymo, M. E., 2015. An 800-kyr record of global surface ocean $\delta^{18}O$ and implications for ice volume-temperature coupling. Earth and Planetary Science Letters, 426, 58-68.

Sharp, 2007. Principles of Stable Isotope Geochemistry., Pearson Prentice Hall, Upper Saddle River, NJ.

Shen, C., Edwards, R.L., Cheng, H., Dorale, J.A., Thomas, R.B., Moran, S.B., Weinstein, S.E., Edmonds, H.N., 2002. Uranium and thorium isotopic and concentration measurements by magnetic sector inductively coupled plasma mass spectrometry. Chem. Geo. 185, 165–178.

Sierro, F.J., Hodell, D.A., Curtis, J.H., Flores, J.A., Reguera, I., Colmenero-Hidalgo, E., Barcena, M.A., Grimalt, J.O., Cacho, I., Frigola, J., Canals, M., 2005. Impact of iceberg melting on Mediterranean thermohaline circulation during Heinrich events. Paleoceanography 20, 1–13. doi:10.1029/2004PA001051.

Sirocko, F., Seelos, K., Schaber, K., Rein, B., Dreher, F., Diehl, M., Lehne, R., Jäger, K., Krbetschek, M., Degering, D., 2005. A late Eemian aridity pulse in central Europe during the last glacial inception. Nature 436, 833–836. doi:10.1038/nature03905.

Spötl, C., Fairchild, I. J., & Tooth, A. F., 2005. Cave air control on dripwater geochemistry, Obir Caves Austria: Implications for speleothem deposition in dynamically ventilated caves. Geochimica et Cosmochimica Acta, 6910, 2451–2468. https://doi.org/10.1016/j.gca.2004.12.009.

Spötl, C., Scholz, D., and Mangini, A., 2008. A terrestrial U/Th-dated stable isotope record of the Penultimate Interglacial. Earth and Planetary Science Letters, 2763–4., 283–292. https://doi.org/10.1016/j.epsl.2008.09.029.

Sprovieri, R., Di Stefano, E., Incarbona, A., Oppo, D.W., 2006. Suborbital climate variability during Marine Isotopic Stage 5 in the central Mediterranean basin: evidence from calcareous plankton record. Quat. Sci. Rev. 25, 2332–2342. doi:10.1016/j.quascirev.2006.01.035.

Stoll, H., Mendez-Vicente, A., Gonzalez-Lemos, S., Moreno, A., Cacho, I., Cheng, H., Edwards, R.L., 2015. Interpretation of orbital scale variability in mid-latitude speleothem d 18 O : Significance of growth rate controlled kinetic fractionation effects. Quat. Sci. Rev. 127, 215–228. doi:10.1016/j.quascirev.2015.08.025.

Tang, K., and Feng, X., 2001. The effect of soil hydrology on the oxygen and hydrologen isotopic compositions of plants' source water. Earth and Planetary Science Letters, 1853–4, 355–367. https://doi.org/10.1016/S0012-821X00.00385-X.

Thompson, P., Schwarcz, H.P. and Ford, D.C., 1974. Continental Pleistocene Climatic Variations from Speleothem Age and Isotopic Data. Science, 1844139, pp. 893895.

Tjallingii, R., Röhl, U., Kölling, M., Bickert, T., 2007. Influence of the water content on X-ray fluorescence corescanning measurements in soft marine sediments. Geochemistry, Geophys. Geosystems 8, 1–12. doi:10.1029/2006GC001393.

Toucanne, S., Angue Minto'o, C. M., Fontanier, C., Bassetti, M. A., Jorry, S. J., and Jouet, G., 2015. Tracking rainfall in the northern Mediterranean borderlands during sapropel deposition. Quaternary Science Reviews, 129, 178–195. https://doi.org/10.1016/j.quascirev.2015.10.016.

Toucanne, S., Jouet, G., Ducassou, E., Bassetti, M. A., Dennielou, B., Angue Minto'o, C. M., Lahmi, M., Touyet, N., Charlier, K., Lericolais, G., and Mulder, T., 2012. A 130,000-year record of Levantine Intermediate Water flow variability in the Corsica Trough, western Mediterranean Sea. Quaternary Science Reviews, 33, 55–73. https://doi.org/10.1016/j.quascirev.2011.11.020.

Toyofuku, T., Kitazato, H., Kawahata, H., Tsuchiya, M., Nohara, M., 2000. Evaluation of Mg/Ca thermometry in foraminifera: Comparison of experimental results and measurements in nature. Paleoceaography, 15, 456-464.

Treble, P., Shelley, J. M. G., and Chappell, J., 2003. Comparison of high resolution sub-annual records of trace elements in a modern speleothem with instrumental climate data from southwest Australia. Earth and Planetary Science Letters, 2161–2., 141–153. https://doi.org/10.1016/S0012-821X03.00504-1.

Tremaine D. M., Froelich P. N. and Wang Y., 2011. Speleothem calcite farmed in situ: Modern calibration of $\delta^{18}O$ and $\delta^{13}C$ paleoclimate proxies in a continuously-monitored natural cave system. Geochim. Cosmochim. Acta 75, 4929–4950.

Tzedakis, C., 2003. Timing and duration of Last Interglacial conditions in Europe: A chronicle of a changing chronology. Quat. Sci. Rev. 22, 763–768. doi:10.1016/S0277-379103.00004-0.

Tzedakis, P. C., Frogley, M. R., Lawson, I. T., Preece, R. C., Cacho, I., and De Abreu, L., 2004. Ecological thresholds and patterns of millennial-scale climate variability: the

response of vegetation in Greece during the last glacial period. Geology, 322., 109-112.

Tzedakis, P. C., Hooghiemstra, H., and Pälike, H., 2006. The last 1.35 million years at Tenaghi Philippon: revised chronostratigraphy and long-term vegetation trends. Quaternary Science Reviews, 2523–24, 3416–3430. https://doi.org/10.1016/j.quascirev.2006.09.002.

Tzedakis, P.C., Raynaud, D., McManus, J.F., Berger, A., Brovkin, V., Kiefer, T., 2009. Interglacial diversity. Nat. Geosci. 2, 751.

Tzedakis, P. C., 2010. The MIS11-MIS1 analogy, southern European vegetation, atmospheric methane and the "early anthropogenic hypothesis. Climate of the Past, 62., 131–144. https://doi.org/10.5194/cp-6-131-2010.

Tzedakis, P.C., Wolff, E.W., Skinner, L.C., Brovkin, V., Hodell, D.A., McManus, J.F., Raynaud, D., 2012. Can we predict the duration of an interglacial? Clim. Past 8, 1473–1485. doi:10.5194/cp-8-1473-2012.

Tzedakis, P.C., Drysdale, R.N., Margari, V., Skinner, L.C., Menviel, L., Rhodes, R.H., Taschetto, A.S., Hodell, D.A., Crowhurst, S.J., Hellstrom, J.C., Fallick, A.E., Grimalt, J.O., McManus, J.F., Martrat, B., Mokeddem, Z., Parrenin, F., Regattieri, E., Roe, K., Zanchetta, G., 2018. Enhanced climate instability in the North Atlantic and southern Europe during the Last Interglacial. Nat. Commun. 9, 4235. doi:10.1038/s41467-018-06683-3.

Urey, H.C., 1947. The thermodynamics of isotopic substances, Journal of the Chemical Society of London, 562-581.

Van Der Weijden, C. H., 2002. Pitfalls of normalization of marine geochemical data using a common divisor. Marine Geology, 1843–4, 167–187. https://doi.org/10.1016/S0025-322701.00297-3.

Van Meerbeeck, C. J., Renssen, H., Roche, D. M., Wohlfarth, B., Bohncke, S. J. P., Bos, J. A. A., Engels, S., Helmens, K. F., Sánchez-goñi, M. F., Svensson, A., Vandenberghe, J., 2011. The nature of MIS 3 stadial e interstadial transitions in Europe : New insights from model and data comparisons. Quat. Sci. Rev. 30, 3618-3637. doi: 10.1016/j.quascirev.2011.08.002.

van Raden, U. J., Groeneveld, J., Raitzsch, M., and Kucera, M., 2011. Mg/ Ca in the planktonic foraminifera Globorotalia inflata and Globigerinoides bulloides from Western Mediterranean plankton tow and core top samples. Mar. Micropaleontol., 78, 101–112, doi:10.1016/j.marmicro.2010.11.002.

Vansteenberge, S., Verheyden, S., Cheng, H., Edwards, R.L., Keppens, E., Claeys, P., 2016. Paleoclimate in continental northwestern Europe during the Eemian and early Weichselian 125-97 ka.: Insights from a Belgian speleothem. Clim. Past 12, 1445–

1458. doi:10.5194/cp-12-1445-2016.

Vargas-Yáñez, M., García-Martínez, M.C., Moya, F., Balbín, R., López-Jurado, J.L., Serra, M., Zunino, P., Pascual, J., Salat, J., 2017. Updating temperature and salinity mean values and trends in the Western Mediterranean: The RADMED project. Prog. Oceanogr. 157, 27–46. doi:10.1016/j.pocean.2017.09.004.

Velasco, J.P.B., Baraza, J., Canals, M., Balón, J., 1996. La depresión periférica y el lomo contourítico de Menorca: evidencias de la actividad de corrientes de fondo al N del talud Balear. Geogaceta 20, 359–362.

Waelbroeck, C., Labeyrie, L., Michel, E., Duplessy, J.C., McManus, J.F., Lambeck, K., Balbon, E., Labracherie, M., 2002. Sea-level and deep water temperature changes derived from benthic foraminifera isotopic records. Quat. Sci. Rev. 21, 295–305. doi:10.1016/S0277-379101.00101-9.

Wang, C., 2001. A unified oscillator model for the El Niño-Southern Oscillation. Journal of Climate, 14, 98-115.

Weltje, G.J. and Tjallingii, R., 2008. Calibration of XRF core scanners for quantitative geochemical logging of sediment cores: Theory and application. Earth Planet. Sci. Lett. 274, 423–438. doi:10.1016/j.epsl.2008.07.054.

West, R. G., 1984. Interglacial, interstadial and oxygen isotope stages. Dissertationes Botaniceae, 72, 345–357.

Wong, C., and Banner, J. L., 2010. Response of cave air CO_2 and drip water to brush clearing in central Texas: Implications for recharge and soil CO_2 dynamics. Journal of Geophysical Research: Biogeosciences, 115G4.

Wong, C.I. and Breecker, D.O., 2015. Advancements in the use of speleothems as climate archives. Quat. Sci. Rev. 127, 1–18. doi:10.1016/j.quascirev.2015.07.019.

Wulf, S., Hardiman, M.J., Staff, R.A., Koutsodendris, A., Appelt, O., Blockley, S.P.E., Lowe, J.J., Manning, C.J., Ottolini, L., Schmitt, A.K., Smith, V.C., Tomlinson, E.L., Vakhrameeva, P., Knipping, M., Kotthoff, U., Milner, A.M., Müller, U.C., Christanis, K., Kalaitzidis, S., Tzedakis, P.C., Schmiedl, G., Pross, J., 2018. The marine isotope stage 1–5 cryptotephra record of Tenaghi Philippon, Greece: Towards a detailed tephrostratigraphic framework for the Eastern Mediterranean region. Quat. Sci. Rev. 186, 236–262. doi:10.1016/j.quascirev.2018.03.011.

Yin, Q. Z., and Berger, A., 2010. Insolation and CO_2 contribution to the interglacial climate before and after the Mid-Brunhes Event. Nature Geoscience, 34, 243-246.

Yu, J., Elderfield, H., Greaves, M., Day, J., 2007. Preferential dissolution of benthic foraminiferal calcite during laboratory reductive cleaning. Geochemistry, Geophys. Geosystems 8. doi:10.1029/2006GC001571.

Yuan D., Cheng H., Edwards R. L., Dykoski C. A., Kelly M. J., Zhang M., Qing J., Lin Y., Wang Y., Wu J., Dorale J. A., An Z. and Cai Y., 2004. Timing, Duration, and Transitions of the Last Interglacial Asian Monsoon. Science 304, 575–578.

Zachos, J. C., Dickens, G. R., and Zeebe, R. E. 2008. An early Cenozoic perspective on greenhouse warming and carbon-cycle dynamics. Nature, 4517176, 279–283. https://doi.org/10.1038/nature06588.

Annex

Annex 1

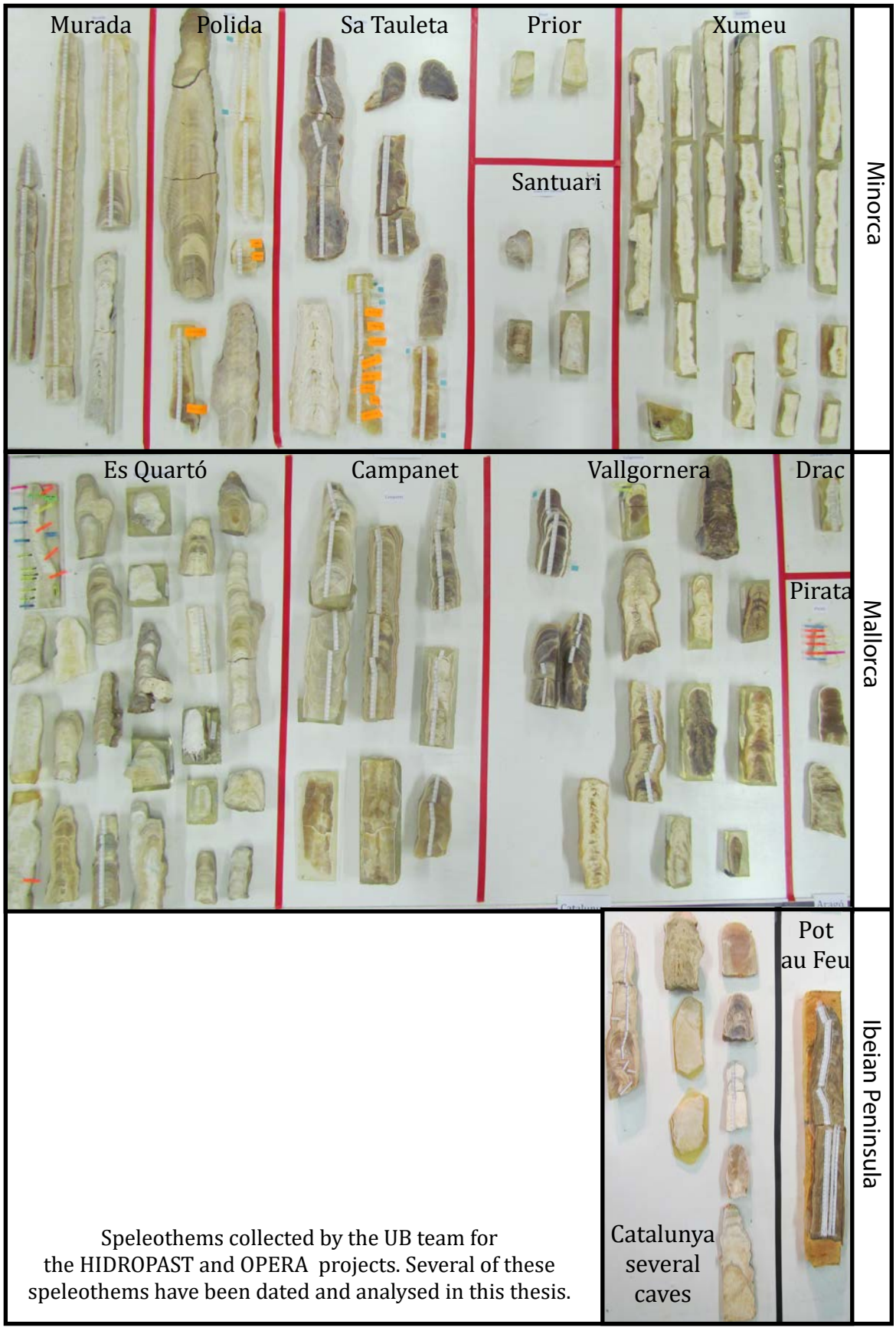

Speleothems collected by the UB team for the HIDROPAST and OPERA projects. Several of these speleothems have been dated and analysed in this thesis.

Annex 2

UNIVERSITY OF MINNESOTA
Driven to Discover℠

Processing Carbonate Samples for U/Th Isotope Analysis

General Preparation (Day 1)

1. Select samples for analyses (13 samples fit in centrifuge). Order them from youngest to oldest (or best guess for this order). Write sample IDs on a post-it and tape it outside of the clean lab window for reference inside the cleanroom. Place samples in a Ziploc bag. *(Note that if you are transferring bulk sample to a smaller vial, it is best to use GLASS vials to minimize static effects in the lab).*

2. Wash the outside of each sample vial and the Ziploc bag with super clean H_2O sprayed onto a kimwipe. Once all are dry, place the samples back in the bag and then into the transfer box.

3. Create a new page in your Cleanroom Lab book. Enter the sample IDs and create "Chemistry ID's" (shorter labels) for each one. *(The labeling convention that I used was "LC-A1" (LC=Lost City, A= batch, 1=sample number (youngest to oldest))*. If you haven't created a new page in a while, it is helpful to look at past entries as an example. In the left-hand column, enter the procedure notes (shorthand) – these remain the same for all carbonate chemistry samples.

4. Using the chemistry ID, label 30 ml Teflon beakers for each sample and include 1 blank. Label the cap and also 2x on the sides of each beaker. Place these in order in a clean green block holder.

Weighing Procedure (Day 1)

Even though you may already have weights of each sample, it is a good idea to re-weigh each sample prior to chemistry.

1. In the balance room, clean the bench space with superclean H_2O on a kimwipe (wiping from top to bottom, left to right (not back and forth). Also gently wipe down the balance.
2. Put down clean crew wipes.
3. Carefully remove samples from transfer box- put them in order of their chemistry IDs. Put the block(s) of Teflon beakers in front of the sample vials. All should be in the same alphanumeric order of the chemistry IDs.
4. For each sample:
    a) tare the Teflon beaker with the cap on
    b) *Carefully* pour the sample from the glass vial to the beaker. Do not touch the glass vial to the Teflon beaker. Approximately 0.1-0.2g works well for high U samples (2-5ppm). Put the cap back on the beaker.

c) Weigh and record sample weight.
d) Using a squirt bottle filled with superclean H_2O, wash down the sides of the beaker 2x. Remember not to squirt the water directly into the sample!
e) Replace the cap and gently swirl. Place the beaker back in the green block holder.

5. Place sample vials back in the plastic Ziploc and put back in the transfer box.
6. Clean bench area and balance again with kimwipe and superclean H_2O. Dispose of all used kimwipes in the balance room garbage can. Make sure the lid is tightly secured on the garbage can.

Digestion Procedure (Day 1)

Bring all samples (in the green block holder) into a clean fume hood (if you are in doubt of its cleanliness, wipe down with superclean H_2O). Put down 2-3 crew wipes.

1. Open each sample and put them in order with the cap down.
2. Add 7N HNO_3 (or 14N HNO_3) dropwise to each beaker until samples are completely dissolved****.** For carbonates, this can take a while. Be careful to not add too much acid too quickly as many samples can be overly effervescent.

   ****** If the sample ***does not completely dissolve*** during digestion in 7HNO3:
   (This happened with several of the older samples. River recommended the following):
   1. Pour the sample into a clean centrifuge tube.
   2. Centrifuge for ~7 min at 2600 rpm
   3. Pour supernate into NEW Teflon beaker, label, and set aside.
   4. Re-suspend un-dissolved particles in 7N HNO_3
   5. Pour into the *original* Teflon beaker.
   6. Add ~10 drops concentrated HF
   7. Heat the sample on the hotplate.
   8. Add 1 drop $HClO_4$
   9. Dry down completely.
   10. Add 0.5-1ml 7N HNO_3
   11. Add 1-2 drops H_3BO_3 (this gets rid of the HF)
   12. Dry down completely.
   13. Add ~0.5ml 7N HNO_3
   14. Pour this back in with the rest of the sample.

3. Replace caps and put beakers back into green block holder.

Spiking Procedure (Day 1)

Samples must be COMPLETELY dissolved before spiking!!!!

The lab spikes contain the following concentrations of isotopes:

Spike	Coral-D2B	Speleoth-1H
^{233}U (pmol/g)	7.9602 ± 0.0001	0.78997 ± 0.0002
^{229}Th (pmol/g)	0.3848 ± 0.0001	0.22815 ± 0.0001

Only Hai and River are authorized to issue spike stock solution- (*plan ahead for this!*). The amount you add to each sample is roughly determined by the U concentration of each sample- knowing this value will help so that the sample is neither over-spiked nor under-spiked. **To prepare for spiking samples:**

1. Calculate the <u>total</u> amt of spike you will need for all samples and blanks that you are processing on a given day. *In general, you want the $^{235}U/^{233}U$ ratio to be ~10. Remember that*

^{238}U~^{235}U. See table below for a guide.(If you have **no idea** what the ^{238}U concentration of your sample is, you should spike your sample with a mass equal to your sample size.) **REMEMBER:** It is better to under-spike than it is to over-spike.

2. Tare the weight of a clean 7 ml Teflon beaker. Pour approximately the total amount of spike from your stock bottle into the beaker. Do **NOT** pipet your spike from the bottle into the beaker! Record the total mass in the lab book.
3. Use a calculator to adjust the amounts for each sample according to if you have slightly more or less spike than you intended. *Use percentages to do this!! (For example, a flat 0.05g more spike added to each sample will not be proportional).*
4. Pipet the spike into each sample (see procedure below). Note that River's pipet is off by about +0.04g.

General spike approximations for sample size ~0.2g (coral-B spike):

^{238}U (ppm)	Sample Size (g)	Coral-B Spike (g)
2	0.2	0.15
3	0.2	0.2
5	0.2	0.3
10	0.2	0.6

General spike approximations for sample size ~0.2g (speleo-1H spike):

^{238}U (ppm)	Sample Size (g)	Speleo-1H Spike (g)
.2	0.2	0.12
.5	0.2	0.30
1	0.2	0.60
1.5	0.2	0.91

To spike the samples:
Bring all samples (with cap on), spike, and 100µl adjustable pipette into the balance room. Clean pipette tip with superclean H_2O before using. If available, bring a 0.5-5µL or 2-20µL micro-pipette to use for spiking your chemistry blank.
For each sample:

1. Tare Teflon beaker containing sample.
2. Remove cap, pipette in appropriate amount of spike to each sample, and replace cap. For spiking your chemistry blank, do not use over 4µL of spike. If micro-pipette's are not available, dilute spike with 1.5 N nitric until spike concentration is equivalent. Ideally, chemistry blanks should be spiked with 2 µL of spike.
3. Record mass of spike in cleanroom lab book.
4. Put beaker back in green block holder (it's ok not to swirl- the reflux step will take care of mixing).
5. After all samples are spiked, bring samples back to fume hood. Clean bench space in the balance room when done with superclean H_2O.
6. Place the pipet tip that came in direct contact with the spike in the solid radioactive waste ziplock bag under the hood sink. If you spilled any spike on the counters or floor of the balance room, dispose of all wipes in the solid radioactive waste ziplock bag and notify our radiation safety officer. Make sure the solid radioactive waste ziplock bag is closed at all times!

7. Remove cap and add ~3-6 drops concentrated $HClO_4$ to each sample: this is to get rid of organics (Th likes to stick to organics!). Add more drops of $HClO_4$ if you suspect there is a lot of organics in your sample.
8. Swirl and replace cap.
9. Put all samples on a clean hotplate at 400°F for **REFLUX**ing (setting at MAX on the new hotplates). Samples should be on hotplate for 1-2 hrs. After this time, turn off the hotplate.
10. Before removing cap, tap all moisture from cap and beaker sides down to the base.
11. If the solution looks sticky, add more drops $HClO_4$.
12. Dry down completely.

Iron Co-Precipitation Procedure (Day 2)

1. Add enough 2N HCl to re-dissolve each sample. Do not add too much HCl to avoid $CaCl_2$ saturation problem. Place samples back on hotplate to help re-dissolve the sample.
2. While samples are warming, prepare centrifuge tubes:
    a) rinse centrifuge parts with superclean H_2O, shake to dry
    b) cut parafilm, rinse both sides of each piece with superclean H_2O
    c) label sides of tubes, cap loosely with parafilm and place in order in rack
3. Transfer each sample by pouring into centrifuge tube.
4. Add 1 drop of $FeCl_2$ to each sample. Shake to mix.
5. Add ~2 drops or more concentrated NH_4OH to neutralize solution. The amount of NH_4OH used will depends on the acidic condition. Shake to mix – you will see the Fe ppt at the bottom of the tube.
6. Place tubes in centrifuge holders (use 2 holders)
    a) place 1 empty tube in middle of a holder
    b) tare holder that does not have an empty tube
    c) Weigh other holder- add water to empty tube (or to a sample if necessary) to balance weight to < 0.1g difference.
7. Centrifuge all samples and blanks 3x for 7 min at 2500 rpm:
    a) between each round of centrifuging, pour off the supernate into the sink
    b) add superclean H_2O to the halfway up the tube, mix, balance, and centrifuge again
    c) after the last centrifuge, only pour off the supernate and place in rack.
8. Check all Teflon beakers. If the inner of Teflon beaker is sticky, wipe it out with a piece of clean Crew wipe and rinse it with superclean water. Dry on hotplate.

Prepare Samples for Columns (Day 2)

1. Add 10-15 drops 14N HNO_3 to centrifuge tube to dissolve sample
2. Pour back into Teflon beaker.
3. Add some superclean H_2O to centrifuge tube; pour back into Teflon beaker.
4. Dry down on hot plate
5. Add 1 drop $HClO_4$. Dry down.
6. Add 1-2 drops 14 HNO_3 to beaker. Dry down. (If you sample doesn't completely redissolve, you can try adding one drop HF, but likely your sample is dirty.)
7. Add 1-2 drops 14 HNO_3 to beaker. Dry to *nearly complete* (small dot left).
8. Dissolve sample in ~0.5cc 7N HNO_3 (heat if necessary, (MAKE SURE TO NOT HEAT TOO MUCH, OTHERWISE YOU WILL DRY DOWN THE SAMPLE- USUALLY A COUPLE MINUTES MAX ON THE HOTPLATE WORKS)).
    a. If the sample sticks to the bottom or sides (organics present), add one to two drop(s) $HClO_4$ to remove the organics and dry down on hotplate.

b. Remove from hotplate, put cap on and let cool. Re-dissolve in ~0.5 cc HNO_3 and make sure it is no longer sticking to the bottom/sides (if so repeat step a. If still sticking after two iterations, talk to Hai/River

Making Columns (Day 2 or 3)

Note that you can do steps 1-4 the day before starting column chemistry.

1. On column bench, lay out clean crew wipes.
2. Take out one 5 cm acid-cleaned columns for each sample and blank.
3. Carefully insert frits evenly into each column.
4. Round out the top of each column with the white insertion stick.
5. Place 1 small (~5 ml) Pyrex beaker under each column to collect chemical waste. Use a sharpie to label the plastic column holder with each chemical ID.
6. Fill each column with superclean H_2O and lay on its side- the column must be totally full of water (NO air bubbles!!!).
7. Place each column in column holder.
8. With a clean pipet (use Hai's with River's dedicated resin pipet tip) set at ~865ml, and pipet clean resin into each column so that it is filled.
9. Remove any excess water and resin with pipet (ok to squirt back into clean resin stock)
10. Place whole rack on your bench.

Column Conditioning (Day 3)

1. Add 3 CVs SC H_2O + 1 drop of 14N HNO_3 to get rid of U, Th and other trace metals.
2. Add 2 CV 7N HNO_3 to each column.
3. Add 1 CV 7N HNO_3 to each column.

Column Chemistry (Day 3)

1. Add dissolved sample (in ~0.5cc 7N HNO_3) to column by *carefully* pouring in. Clean beaker afterwards by rinsing with superclean H_2O and pour into acid waste bottle.
2. Let this run thru the column and into the waste beaker.
3. To remove **Fe***:
    a) add 1 CV 7N HNO_3 to each column
    b) add 1 CV 7N HNO_3 to each column
    c) once all the acid has passed through the column, removed the waste beaker and dispose of all the waste into the waste acid bottle. (Rinse beakers before storing them on your bench)

    * This should be (still) collected into the waste beaker – the liquid should turn pale yellow to Mountain Dew color

4. To collect **Thorium:**
    a) place a clean, labeled 7 ml or 15ml Teflon beaker[1] under each column
    b) add 2 CV 6N HCl to each column
    c) add 1 CV 6N HCl to each column
    d) remove Teflon beaker when collection is done
    e) add 1-2 drops $HClO_4$ to beaker
    f) dry down at 450°F

[1] River suggests cleaning the beaker before use by adding superclean water and 1-2 drop(s) 14N HNO_3. Heat on the hot plate for ~5 minutes with cap on, and pour out water. If it looks sticky, wipe with a clean Crew wipe and check again with water for stickiness.

5. To collect **Uranium:**
    a) place original 30 ml Teflon beaker under each column
    b) add 2 CV superclean H_2O to each column
    c) add 2 CV superclean H_2O to each column
    d) remove beaker when collection is done
    e) add 1-2 drops $HClO_4$ to beaker
    f) dry down at 450°F

Second Column Collection for Th (Day 3 or 4) (optional, for samples going to be run on cups)

1. Add 1-2 drops 14N HNO_3 to each Th sample then dry down.
2. Repeat
3. Add 1 drop HClO4 and dry down
4. Bring sample up in ~0.3cc 7N HNO_3
5. Make new 4cm columns- make and condition same as before
6. Add sample to each column
7. Remove Fe (same as before, using 7N HNO_3)
8. Clean beaker with superclean H_2O, wipe inside with crew wipe if there is any organic material.
9. Collect Th into same Teflon beakers, same method as before (using HCl)
10. Add 1-2 drops $HClO_4$, dry down at 450°F

Preparing Samples for Storage (Day 4)

1. Label 1 ml ICP vials (top and side) for each sample
    a) create 2 vials for each sample – label one "U" and the other "Th"
    b) place in order in holder
2. Add 1 drop 14N HNO_3 to each sample, dissolve sample on hot plate.
3. If any sticky spots found in the beaker, dry down completely and add 1-2 drops $HClO_4$, and dry it completely on hot plate.
4. Add 1 drop 14N HNO_3 to each sample, dissolve sample on hot plate, dry down. *(If sticky spot is always there, you better transfer solution to a new beaker, add 2 drops $HClO_4$ to decompose organic material. If the organic problem cannot be solved, go through one more column to separate the organics.)* [**NOTE: this is not very likely. If you need to go through the column again, prepare and condition as before]**
5. Add 1 drop 14N HNO_3 to each sample. Dry to <u>*nearly complete*</u> (small dot left) *(this happens quickly so watch it carefully- it is wise to do only one or max. two samples at a time for this step – if it dries completely, add a drop again and dry to nearly complete.)*
6. Quickly add ~0.2ml 1% HNO_3 to the beaker- swirl to mix*
   ** Note –if the sample appears to be sticking to the walls, there are still organics left in the sample. Add 1-2 drops $HClO_4$, dry down and restart this process again at step 2.*
7. Let sample cool down on glass plate. *(If any sticky spots found, it probably means that a certain level of organic material is still left; more $HClO_4$ should be treated to solve the problem.)*
8. Transfer to correct vial. Add 1% HNO_3 to the ~0.3ml mark, cap, shake, and store for future analysis on the mass spec.

Method from River Shen, adapted from Minnesota Isotope Lab: K. Ludwig 8/12/04 (revised by J. Retrum and H. Chen; revised 9/21/15 by J. Nissen

Beakers pre-cleaning

1. Clean outside of beakers with alcohol to erase the pen mark.
2. Rinse with dilute HCl (~1N). Full one beaker and transfer the acid between beakers. When finish put the acid waste into the radioactive waste.
3. Fill beakers with dilute reagent grade HCl 5-10% (by volume)
4. Beakers should be completely full and refluxed with taps for ~2 hours.
5. Empty the beakers and wipe inside with clean wipes

Beakers cleaning steps

Aqua regia

1. Place the beakers in a large glass beaker (with teflon discs)
2. Fill it with 50% Aqua Regia (1/2 SC water + 3/8 HCl + 1/8 HNO_3)
3. Boil it on a hot plate for 6-8 hours
4. Empty the glass beaker into the waste acid bottle.
5. Rinse the glass beaker 2-3 times with super clean water

Nitric acid

6. Fill the glass beaker with (1/2 way) super clean water
7. Top off with reagent grade HNO_3
8. Boil it for 6 hours
9. Empty the beaker into waste acid bottle
10. Rinse the glass beaker 2-3 times with super clean water

Perclorich acid

11. Fill the glass beaker (1/2 way) with super clean water
12. Top off with reagent grade HCl
13. Boil it for 6 hours
14. Empty the beaker into waste acid bottle
15. Rinse the glass beaker 2-3 times with super clean water

Final rinse

16. Fill the glass beaker with super clean water
17. Add 1% GFS HNO_3 (by volume)
18. Boil it for 2 hours
19. Empty the glass beaker into the sink and rinse it 3 times
20. Move the glass beaker to the clean sink
21. Change your gloves
22. Rinse individually each beaker and cap 3 times
23. Set out to dry overnight

Beakers can be kept overnight in the next step solution. If beakers are kept in the previous step solution overnight, they will need to be brought to a boil before solution can be changed

Annex 3

UNIVERSITAT DE BARCELONA

Foraminifera isotopes cleaning procedure

Necessary material:

- Micropipette (100-1000 µl)
- Pipette tips (100 – 1000 µl)
- Vial rack
- Ultrasonic bath

Chemical reagents

- Methanol

Procedure

1. Introduce samples for isotopic measurements into clean vials.
2. Add few drops of methanol to the vials containing the samples.
3. Place the vial rack in the ultrasonic bath during 30seconds.
4. Remove the excess of methanol with the pipette leaving a small drop at the bottom.
5. Dry the samples under the laminar flux fume hood at the cleaning laboratory.
6. Once samples are dry putt caps and store it until the analysis in the mass spectrometer.

Revised by J.Torner (04-2016)

DEPGM Laboratori de Sedimentologia

Annex 4

UNIVERSITAT DE BARCELONA

Foraminifera Mg/Ca cleaning procedure

Material:

- Micropipette (100-1000 µl)
- Micropipette (10-100 µl)
- Pipette tips (100 – 1000 µl)
- Pipette tips (50- 1000 µl)

Chemical reagents

- Citric acid + NH_3
- 0.1 M NaOH
- 0.001 M HNO_3

Procedure

Remember to prepare routinely a procedure blank

Clay Removal

1. Clean the work space before start.
2. Clean the micropipette (10-100 µl).
3. Add 20-30µl of MilliQ water with the micropipette to the eppendorf vials containing sample already crashed.
4. Sonicate briefly (20-30s) in the ultrasounds bath.
5. Add 300-400µl of MilliQ water with the water dispenser. Each vial must be treated individually at this stage (slightly bang the vial with the spatula).
6. Allow sample to settle (30s) and remove the overlying solution with the 1000µl-pipette at 650 µl. Leave about 20-30µl of MilliQ water in the vials.
7. Clean the pipette between samples (2x HNO3 + 3x MilliQ water).
8. Repeat steps 4-7 two more times. Clay rich samples should be repeated as many times as necessary
9. Add few drops of Methanol (200 µl) into each vial.
10. Sonicate briefly (20-30s) in the ultrasounds bath.

11. Allow sample to settle for a few seconds, slightly tap the vial with the spatula in order to remove bubbles)
12. Remove the supernatant solution with the 1000µl-pipette at 650 µl.
13. Repeat steps 9-12 one more time.
14. Fill the Eppendorf with MilliQ water.
15. Allow sample to settle for a few seconds and remove the supernatant solution with a 1000µl- pipette at 650 µl.

Reductive cleaning

This is the more time-consuming step of the whole procedure. Safety glasses, lab coats must be worn all the time at this step. Work ALWAYS ***UNDER THE GAS HOODS.***

The ultrasonic bath must be heated (over 90ºC) before starting with this step (about 2 hours).

Turn on the heater for the MilliQ water used in step 6 (about 15 min).

1. Prepare a mixture of 500µl of hydrazine hydroxide and 2000µl of the Citric acid + NH_3 (stored in the special hydroxide container)
2. Add 100µl of the final mixture to each vial and secure caps in order to prevent sample to pop up while reacting.
3. Place the sample rack into the thermal ultrasonic bath for 30 minutes (bath has to be at 90ºC), sonicating briefly (5-10s) every 2 minutes (Use the timer and prepare a table to mark each sonication step).
4. Immediately after the bath, place again the sample rack into the gas hood and CAREFULLY open vials (at this stage, some vials could tend to pop up) and squirt MilliQ water into the vials (including lids) as soon as possible in order to slow down the reaction.
5. Tap the vials with the spatula in order to remove bubbles and remove the overlying solution with the 1000µl-pipette at 650 µl.
6. Repeat steps 4-5 two more times.
7. Add 400µl of MilliQ water (aprox 80ºC) into the vials and wait for 5 minutes.
8. Remove the overlying solution with the 1000µl-pipette at 650 µl (after light tapping to remove bubbles)
9. Repeat steps 7-8 one more time.
10. Squirt cold MilliQ water into the vials.
11. Remove the overlying solution with a 1000µl-pipette at 650 µl (after light tapping to remove bubbles).

It is VERY IMPORTANT to remove any reagent that could remain into the samples to prevent further dissolution.

Switch off the temperature control in the ultrasonic bath

Oxidative cleaning

Heat the water bath before starting this step (about 1 hour).

1. Prepare the Alkali buffered 1% H_2O_2 solution: Add 100 µl of Hydrogen peroxide (stored in the fridge) to 10 ml 0.1M NaOH.
2. Add 250µl of alkali buffered 1% H_2O_2 to each vial and secure the caps of the vials to prevent popping open.
3. Place the rack of samples into the hot bath for 5 minutes. At 2.5 minutes remove the rack momentarily and rap on the bench top in order to remove the bubbles.
4. After the 5 minutes, remove the rack and rap again on the bench top, and then place it into the ultrasonic bath, sonicating briefly (10-15s).
5. Repeat steps 3-4 one more time.
6. Immediately after fill vials with MilliQ water in order to slow down the reaction. Add water also to the vials caps.
7. Remove the overlying water with a 1000µl-pipette at 650 µl. At this step foraminifera fragments tend to be attached to the vial walls, shake vials to let fragments to settle down (sample lost can be critical at this step).
8. Repeat steps 6-7 two more times.

Weak acid leaching

1. Add 250µl of 0.001M HNO_3 to each sample.
2. Ultrasonicate samples for 30s.
3. Add MilliQ water into each sample in order to slow down reaction.
4. Tap the vials with the spatula in order to remove bubbles and remove the overlying water with a 1000µl-pipette at 650 µl .
8. Repeat steps 3-4 one more times.
9. Pipette out water as much as possible with a 10-100µl micropipette

Revised by J.Torner (03-2020)

DEPGM Laboratori de Sedimentologia

Reagents preparation

Reductive reagent (Citric acid+NH_4)

Work under the gas hood

1. Weight 5,25g of Citric Acid in a precipitates glass
2. Add 100 ml of NH_4 (30%)
3. Place precipitates glass in a hot plate (40-50ºC) with a magnetic spinner to promote mixing.
4. Transfer to a pre-cleaned plastic bottle and store in the fridge

Oxidizing reagent (to remove organic matter)

1. Hydrogen peroxide 30% w/v. (stored in fridge).
2. 0.1M sodium hydroxide (Aristar grade) in MilliQ water

0.1M NaOH = 4g / litre. (NaOH = 40.00g g mol^{-1})

Weak acid leach

0.001 M HNO_3

- 0.5 litre bottle: 34.7µl HNO_3 (65%) + MilliQ water
- 1 litre bottle: 69.4 µl HNO_3 (65%) + MilliQ water

UNIVERSITAT DE BARCELONA

Foraminifera Mg/Ca dissolution procedure

Necessary material:

- Micropipette (100-1000 µl)
- Micropipette (10-100 µl)
- Pipette tips (100 – 1000 µl)
- Pipette tips (50- 1000 µl)

Chemical reagents

- 1% ultrapure HNO3

Procedure

Dissolution

Dissolution should be done the day before of measurements with the ICP-MS

Make sure that you already have a list with the sample code and dissolution order.

1. Add 400µl of 1% HNO_3 (ultrapure) to each sample (make it in groups of 6).
2. Individually place samples into the ultrasonic bath (about 15 seg) to promote dissolution.
3. Be sure that all the samples are correctly dissolved. Repeat the step 2 as times as necessary
4. Shake the vials to homogenize solution.
5. Place samples (groups of 6) into the micro centrifuge device, place them in the rotor symmetrically. Centrifuge samples for 5 minutes at 6000 rpm.
6. Transfer **370**µl of sample into clean eppendorf using a clean tip.
7. Transfer an aliquot into other vial.

Reagents preparation

1% ultrapure HNO_3 Aristar grade

- 1/5 dilution from 5% ultrapure HNO_3 Aristar grade with MilliQ water

Revised by J.Torner (03-2020)

DEPGM Laboratori de Sedimentologia

Annex 5

UNIVERSITAT DE BARCELONA

Grain size distribution procedure

This procedure has been designed for clay/silty sediment samples with low sand content. Indicated for samples with 15-50% in carbonate contents and a low opal content (<2%).

Remember to prepare routinely the standard samples from Menorca (MR3.5) and Alborán (T1) cores.

Use 0.25 g of lyophilized samples for each kind of analysis (bulk sample and/or non-carbonate sample)

Procedure

Organic matter attack

1. Put the sample in a glass beaker correctly named
2. Add 50 mL of 10% H_2O_2 in order to attack the o.m.
3. Led the sample into the fume hood during 24h
4. Shake beakers every 2-3h
5. Put the beaker into the oven at 60°C until it is completely dry.
6. Repeat steps 1-5.

Carbonate attack

1. Add 50 mL of HCl 1M in the glass beaker
2. Led the sample into the fume hood during 3h
3. Transfer the sample in a "coulter" vial. Recover the remains with distilled water
4. Centrifuge samples and remove the supernatant solution.

Disaggregation of samples

1. Add 30-40 mL of sodium polyphosphate
2. Unltrasonicate the "coulter" vials 1 minute
3. Put vials in the orbital shaker during 2-3h
4. Pull samples in the coulter

Revised by J.Torner (03-2020)

DEPGM Laboratori de Sedimentologia

Annex 6

^{230}Th dating results. The error is 2σ error.

	Cave Name	Sample Name	Sample depth (cm)	^{238}U (ppb)	^{232}Th (ppt)	^{230}Th / ^{232}Th (atomic x10^{-6})	δ^{234}U* (measured)	^{230}Th / ^{238}U (activity)	^{230}Th Age (yr) (uncorrected)	^{230}Th Age (yr) (corrected)	$\delta^{234}U_{initial}$** (corrected)	^{230}Th Age (yr BP)*** (corrected)
1	Meravelles	**ERE**	50	61 ±0	4546 ±91	269 ±5	671.6 ±1.8	1.2142 ±0.0021	125091 ±453	**123979 ±906**	953 ±4	**123913 ±906**
2	Meravelles	**ERE**	60	104.5 ±0.1	5721 ±115	372 ±7	708.7 ±2.2	1.2346 ±0.0023	123565 ±488	**122767 ±743**	1002 ±4	**122701 ±743**
3	Meravelles	**ERE**	70	95.4 ±0.1	881 ±18	2116 ±43	676.3 ±1.9	1.1857 ±0.0022	119575 ±448	**119437 ±458**	947 ±3	**119371 ±458**
4	Meravelles	**ERE**	95	90.4 ±0.1	1547 ±31	1128 ±23	644.0 ±1.9	1.1715 ±0.0029	121413 ±559	**121151 ±588**	907 ±3	**121085 ±588**
5	Meravelles	**ERE**	100	173.3 ±0.2	3330 ±67	1040 ±21	676.3 ±1.8	1.2117 ±0.0025	124034 ±492	**123748 ±530**	959 ±3	**123682 ±530**
6	Meravelles	**ERE**	105	232.4 ±0.3	3745 ±75	1207 ±24	669.0 ±1.8	1.1797 ±0.0026	119517 error	**119275 error**	937 error	**119209 error**
7	Meravelles	**ERE**	125	489.9 ±0.9	2755 ±55	4479 ±90	1142.5 ±2.6	1.5272 ±0.0036	117502 ±506	**117438 ±508**	1591 ±4	**117372 ±508**
8	Meravelles	**ERE**	160	77 ±0	4077 ±82	364.0 ±7.3	789.6 ±1.8	1.1622 ±0.0019	103480 ±309	**102733 ±611**	1055 ±3	**102667 ±611**
9	Meravelles	**ERE**	165	62.3 ±0.1	1485 ±30	762 ±15	694.3 ±2.4	1.1027 ±0.0030	104490 ±504	**104130 ±563**	931 ±4	**104064 ±563**
10	Meravelles	**ERE**	190	62.6 ±0.1	144 ±3	8387 ±172	865.3 ±2.3	1.1701 ±0.0031	97786 ±428	**97754 ±428**	1140 ±3	**97688 ±428**
11	Meravelles	**ERE**	215	76.0 ±0.1	454 ±9	3294 ±66	956.3 ±2.2	1.1930 ±0.0025	93373 ±326	**93295 ±330**	1244 ±3	**93229 ±330**
12	Meravelles	**ERE**	230	62.1 ±0.1	293 ±6	4057 ±82	955.8 ±2.7	1.1597 ±0.0031	89647 ±394	**89585 ±397**	1231 ±4	**89519 ±397**
13	Meravelles	**ERE**	265	75.3 ±0.1	314 ±6	3640 ±74	645.4 ±2.0	0.9196 ±0.0024	83631 ±344	**83564 ±347**	817 ±3	**83498 ±347**
14	Meravelles	**ERE**	280	95.8 ±0.1	394 ±8	3835 ±77	737.4 ±2.5	0.9570 ±0.0019	81537 ±281	**81475 ±284**	928 ±3	**81409 ±284**
15	Meravelles	**ERE**	290	69.8 ±0.1	432 ±9	2746 ±55	848.9 ±1.9	1.0300 ±0.0022	82430 ±279	**82343 ±286**	1071 ±3	**82277 ±286**
16	Meravelles	**ERE**	315	87.8 ±0.1	269 ±5	5779 ±118	1005.1 ±2.4	1.0755 ±0.0029	77755 ±314	**77715 ±315**	1252 ±3	**77649 ±315**
17	Meravelles	**ERE**	345	80.1 ±0.1	372 ±7	3514 ±71	939.1 ±2.2	0.9893 ±0.0025	72823 ±273	**72760 ±277**	1153 ±3	**72694 ±277**
18	Meravelles	**ERE**	375	303 ±0	1249 ±25	2795.4 ±56.4	721.0 ±1.8	0.6980 ±0.0017	54504 ±182	**54439 ±188**	841 ±2	**54373 ±188**

U decay constants: l_{238} = 1.55125x10^{-10} (Jaffey et al., 1971) and l_{234} = 2.82206x10^{-6} (Cheng et al., 2013). Th decay constant: l_{230} = 9.1705x10^{-6} (Cheng et al., 2013).

*$\delta^{234}U = ([^{234}U/^{238}U]_{activity} - 1)$x1000. ** $\delta^{234}U_{initial}$ was calculated based on ^{230}Th age (T), i.e., $\delta^{234}U_{initial} = \delta^{234}U_{measured} \times e^{l_{234}T}$.

Corrected ^{230}Th ages assume the initial ^{230}Th/^{232}Th atomic ratio of 4.4 ±2.2 x10^{-6}. Those are the values for a material at secular equilibrium, with the bulk earth ^{232}Th/^{238}U value of 3.8. The errors are arbitrarily assumed to be 50%.

***B.P. stands for "Before Present" where the "Present" is defined as the year 1950 A.D.

^{230}Th dating results. The error is 2σ error.

Sample depth (cm)	^{238}U (ppb)	^{232}Th (ppt)	^{230}Th / ^{232}Th (atomic x10^{-6})	δ^{234}U* (measured)	^{230}Th / ^{238}U (activity)	^{230}Th Age (yr) (uncorrected)	^{230}Th Age (yr) (corrected)	$\delta^{234}U_{Initial}$** (corrected)	^{230}Th Age (yr BP)*** (corrected)
JUD_2.5	89.0 ±0.1	31331 ±627	51 ±1	915.8 ±2.1	1.0973 ±0.0032	85468 ±378	80613 ±3469	1150 ±12	**80551 ±3469**
JUD_3.5	102.5 ±0.1	91270 ±1827	21 ±0	823.5 ±2.1	1.1207 ±0.0028	95055 ±398	81660 ±9640	1037 ±28	**81598 ±9640**
JUD_6.2	74.8 ±0.1	6868 ±138	215 ±4	968.6 ±2.3	1.1969 ±0.0048	92915 ±564	91725 ±1011	1255 ±5	**91663 ±1011**
JUD_13	80.0 ±0.1	3470 ±69	443 ±9	804.0 ±2.1	1.1642 ±0.0055	102405 ±768	101794 ±878	1072 ±4	**101732 ±878**
JUD_19	132.7 ±0.1	5381 ±108	466 ±9	795.5 ±1.9	1.1454 ±0.0021	100668 ±328	100092 ±521	1055 ±3	**100030 ±521**
JUD_32.5	77.7 ±0.1	3385 ±68	432 ±9	750.7 ±2.0	1.1408 ±0.0031	104288 ±479	103654 ±654	1006 ±3	**103592 ±654**
JUD_42.5	78.2 ±0.1	11393 ±228	137 ±3	785.3 ±1.8	1.2069 ±0.0028	110197 ±446	108129 ±1530	1066 ±5	**108067 ±1530**
JUD_44.5	84.4 ±0.1	61745 ±1236	29 ±1	767.9 ±2.0	1.3076 ±0.0037	127959 ±676	117242 ±7699	1069 ±23	**117180 ±7699**
JUD_53	88.0 ±0.1	25390 ±508	72 ±1	776.5 ±1.9	1.2606 ±0.0030	119259 ±517	115147 ±2961	1075 ±9	**115085 ±2961**
IND_12.5	129.0 ±0	44 ±1	65347 ±1439.9	945.2 ±4.0	1.3587 ±0.0035	114953 ±626	114949 ±626	1307 ±6	**114887 ±626**
IND_23.5	139.0 ±0	60 ±1	52332 ±1127.8	961.1 ±2.7	1.3820 ±0.0030	116484 ±491	116478 ±491	1335 ±4	**116416 ±491**
IND_34.5	133.9 ±0.2	31 ±1	100774 ±2445	991.5 ±2.6	1.4208 ±0.0030	118618 ±484	118615 ±484	1386 ±4	**118553 ±484**
IND_45.5	121.7 ±0.2	43 ±1	67972 ±1597	1025.0 ±2.5	1.4532 ±0.0029	119519 ±468	119515 ±469	1436 ±4	**119453 ±469**
IND_56.0	120.1 ±0.3	22 ±1	134581 ±3636	1057.6 ±3.5	1.4905 ±0.0040	121139 ±647	121137 ±647	1489 ±6	**121075 ±647**
IND_67.5	109.0 ±0.2	40 ±1	68042 ±1567	1084.3 ±3.6	1.5234 ±0.0035	122758 ±597	122754 ±597	1533 ±6	**122692 ±597**
IND_83.5	94.3 ±0.2	187 ±4	13112 ±267	1131.1 ±3.1	1.5759 ±0.0039	124828 ±601	124805 ±601	1609 ±5	**124743 ±601**

U decay constants: l_{238} = 1.55125x10^{-10} (Jaffey et al., 1971) and l_{234} = 2.82206x10^{-6} (Cheng et al., 2013). Th decay constant: l_{230} = 9.1705x10^{-6} (Cheng et al., 2013).

*$\delta^{234}U = ([^{234}U/^{238}U]_{activity} - 1)$x1000. ** $\delta^{234}U_{initial}$ was calculated based on ^{230}Th age (T), i.e., $\delta^{234}U_{initial} = \delta^{234}U_{measured} \times e^{l_{234}xT}$.

Corrected ^{230}Th ages assume the initial ^{230}Th/^{232}Th atomic ratio of 4.4 ±2.2 x10^{-6}. Those are the values for a material at secular equilibrium, with the bulk earth ^{232}Th/^{238}U value of 3.8. The errors are arbitrarily assumed to be 50%.

***B.P. stands for “Before Present” where the “Present” is defined as the year 1950 A.D.

^{230}Th dating results. The error is 2σ error.

Sample depth (mm)	^{238}U (ppb)	^{230}Th/^{238}U (activity)	^{234}U/^{238}U (activity)	^{232}Th/^{238}U (activity)	^{230}Th/^{232}Th	^{234}U/^{238}U (initial)	Age (Kyr BP)	**230Th Age (corrected) (Kyr BP)**
JUD_15	NR	1.2723 ±0.0087	1.7973 ±0.0059	0.0824 ±0.0052		2.0943 ±0.0226	118.262	**111.629 ± 7.027**
JUD_140	41	1.2138 ±0.0074	1.7852 ±0.0035	0.0728 ±0.0019	16.660	2.0575 ±0.0189	110.906	**105.348 ± 6.212**
JUD_225	50	1.1552 ±0.078	1.7351 ±0.0023	0.0766 ±0.0017	15.075	1.9794 ±0.0188	107.647	**101.507 ± 6.759**
JUD_365	NR	1.1634 ±0.0054	1.7963 ±0.0069	0.0432 ±0.0012		2.0549 ±0.0130	102.733	**99.2173 ± 3.700**
JUD_414	42	1.0694 ±0.0304	1.7581 ±0.0025	0.1413 ±0.0048	7.568	1.9542 ±0.0374	93.685	**81.3252 ± 13.885**
JUD_487	63	1.1725 ±0.0058	1.9531 ±0.0053	0.0250 ±0.0001	46.860	2.2275 ±0.0087	91.027	**89.5258 ± 2.019**
JUD_525	58	1.0585±0.0097	1.8911 ±0.005	0.0661 ±0.0016	16.004	2.1096 ±0.0181	82.596	**77.6122 ± 5.573**
JUD_538	NR	1.0482 ±0.0077	1.9597 ±0.0045	0.0694 ±0.0021		2.1773 ±0.0186	77.369	**72.0687 ± 5.387**

Activity ratios were determined by MC-ICP-MS following Hellstrom (2003). Ages in ka before present are corrected for initial 230Th using eqn. 1 of Hellstrom (2006). (230Th/232Th)i of 0.9 ± 0.6 and the decay constants of Cheng et al (2013). Uncertainties were propagated using Monte-Carlo simulation of each of the input activity ratios and initial (234U/238U) is calculated using the corrected age of each sample. U content is marked n.r. where sample weights were not recorded.

^{230}Th dating results. The error is 2σ error.

	Cave Name	Sample Name	Sample depth (cm)	^{238}U (ppb)	^{232}Th (ppt)	^{230}Th / ^{232}Th (atomic x10^{-6})	δ^{234}U* (measured)	^{230}Th / ^{238}U (activity)	^{230}Th Age (yr) (uncorrected)	^{230}Th Age (yr) (corrected)	$\delta^{234}U_{initial}$** (corrected)	^{230}Th Age (yr BP)*** (corrected)
1	Murada	**RAT_A**	0.75	186.0 ±0.2	1697 ±34	3951 ±79	1249.1 ±2.5	2.1858 ±0.0039	210673 ±1087	**210591 ±1088**	2263 ±8	**210525 ±1088**
2	Murada	**RAT_A.1**	7.25	125.6 ±0.1	1179 ±24	3947 ±79	1246.2 ±2.2	2.2458 ±0.0033	226066 ±1054	**225984 ±1055**	2358 ±8	**225918 ±1055**
3	Murada	**RAT_B**	8.5	118.7 ±0.1	645 ±13	6804 ±137	1235.1 ±2.7	2.2415 ±0.0044	228149 ±1397	**228102 ±1397**	2351 ±11	**228036 ±1397**
4	Murada	**RAT_B.1**	9.75	83.8 ±0.1	1188 ±24	2542 ±51	1200.3 ±2.3	2.1862 ±0.0052	223677 ±1510	**223550 ±1511**	2256 ±11	**223484 ±1511**
5	Murada	**RAT_B.2**	13.5	85.7 ±0.1	1269 ±25	2389 ±48	1135.8 ±2.1	2.1465 ±0.0037	232313 ±1265	**232178 ±1267**	2187 ±9	**232112 ±1267**
6	Murada	**RAT c**	15	54.6 ±0.1	584 ±12	3312.0 ±66.6	1120.2 ±2.1	2.1475 ±0.00353	237779 ±1277	**237680 ±1278**	2190.8 ±8.9	**237616 ±1278**
7	Murada	**RAT_C.1**	15.5	76.1 ±0.1	4946 ±99	519 ±10	1009.5 ±2.0	2.0490 ±0.0038	246517 ±1518	**245888 ±1574**	2021 ±10	**245822 ±1574**
8	Murada	**RAT_D**	16	75.3 ±0.1	2113 ±42	1159 ±23	925.9 ±2.0	1.9725 ±0.0033	253671 ±1568	**253388 ±1578**	1893 ±9	**253326 ±1578**
9	Murada	**RAT_E**	18.25	78.5 ±0.1	654 ±13	3843 ±77	834.4 ±2.0	1.9399 ±0.0038	287767 ±2405	**287682 ±2404**	1879 ±14	**287620 ±2404**
10	Murada	**RAT_E.1**	20	90.0 ±0.1	445 ±9	6121 ±124	738.5 ±2.2	1.8340 ±0.0036	293865 ±2657	**293810 ±2656**	1692 ±14	**293744 ±2656**
11	Murada	**RAT_F**	23	94.2 ±0.1	657 ±13	4069 ±82	636.2 ±1.8	1.7211 ±0.0034	301956 ±2809	**301874 ±2808**	1491 ±13	**301812 ±2808**
12	Murada	**RAT_F.1**	26	80.5 ±0.1	55 ±2	38662 ±1081	528.9 ±1.9	1.6075 ±0.0028	317242 ±3246	**317232 ±3246**	1295 ±13	**317166 ±3246**
13	Murada	**RAT_G**	28	96.1 ±0.1	230 ±5	10923 ±221	515.8 ±1.9	1.5882 ±0.0034	314689 ±3633	**314657 ±3632**	1253 ±14	**314595 ±3632**
14	Murada	**RAT_H**	28.75	87.6 ±0.1	686 ±14	3275 ±66	486.5 ±1.7	1.5556 ±0.0035	318254 ±3778	**318148 ±3776**	1194 ±13	**318086 ±3776**
15	Murada	**RAT_H.1**	29.5	103.9 ±0.1	172 ±4	15358 ±318	476.0 ±2.0	1.5440 ±0.0030	319752 ±3689	**319729 ±3689**	1173 ±13	**319663 ±3689**
16	Murada	**RAT_H.2**	32	63.9 ±0.1	144 ±3	11459 ±245	485.3 ±1.7	1.5627 ±0.0030	326523 ±3661	**326492 ±3661**	1219 ±13	**326426 ±3661**
17	Murada	**RAT_I**	32.75	89.9 ±0.1	153 ±3	15552 ±315	520.6 ±1.8	1.6073 ±0.0039	326426 ±4204	**326404 ±4203**	1308 ±16	**326342 ±4203**
18	Murada	**RAT_I.1**	34	72.7 ±0.1	217 ±4	9021 ±186	535.3 ±1.9	1.6372 ±0.0033	337484 ±4138	**337446 ±4137**	1387 ±17	**337380 ±4137**
19	Murada	**RAT_J**	35	81.5 ±0.1	162 ±3	13893 ±281	573.2 ±1.8	1.6805 ±0.0036	332647 ±3944	**332622 ±3943**	1465 ±17	**332560 ±3943**
20	Murada	**RAT_J.1**	36.75	80.7 ±0.1	195 ±4	11499 ±240	573.5 ±1.8	1.6833 ±0.0034	334990 ±3912	**334960 ±3911**	1476 ±17	**334894 ±3911**
21	Murada	**RAT_J.2**	37.25	85.1 ±0.1	572 ±12	5019 ±102	838.0 ±2.2	2.0452 ±0.0041	355336 ±4289	**355275 ±4288**	2284 ±28	**355209 ±4288**
22	Murada	**RAT_J.3**	38.5	122.2 ±0.1	113 ±2	35121 ±759	768.4 ±1.8	1.9654 ±0.0028	365001 ±3564	**364990 ±3564**	2152 ±22	**364924 ±3564**
23	Murada	**RAT_J.4**	40.1	151.9 ±0.2	59 ±2	80965 ±2468	716.0 ±1.9	1.9038 ±0.0036	372020 ±4716	**372014 ±4716**	2046 ±28	**371948 ±4716**
24	Murada	**RAT_J.5**	45	146.9 ±0.2	53 ±2	86817 ±2581	723.2 ±2.0	1.9102 ±0.0033	368865 ±4477	**368860 ±4477**	2048 ±27	**368794 ±4477**
25	Murada	**RAT_J.6**	47	118.5 ±0.1	45 ±1	81924 ±2460	716.5 ±2.1	1.9001 ±0.0035	367292 ±4708	**367287 ±4708**	2020 ±28	**367221 ±4708**
26	Murada	**RAT_J.7**	50	92.8 ±0.1	52 ±2	55752 ±1711	709.6 ±2.5	1.9067 ±0.0049	384890 ±7090	**384883 ±7090**	2103 ±43	**384817 ±7090**
27	Murada	**RAT k**	51.5	86.0 ±0.1	258 ±5	10410 ±211	707.5 ±2.0	1.8948 ±0.0033	374408 ±4678	**374378 ±4677**	2035 ±27	**374314 ±4677**
28	Murada	IND-0.5	1	162 ±0	284 ±6	13043.8 ±262.9	994.5 ±2.6	1.3876 ±0.0025	113896 ±413	**113874 ±413**	1371 ±4	**113812 ±413**
29	Murada	IND-12.5	13	129 ±0	44 ±1	65347.3 ±1439.9	945.2 ±4.0	1.3587 ±0.0035	114953 ±626	**114949 ±626**	1307 ±6	**114887 ±626**
30	Murada	IND-23.5	24	139 ±0	60 ±1	52332.2 ±1127.8	961.1 ±2.7	1.3820 ±0.0030	116484 ±491	**116478 ±491**	1335 ±4	**116416 ±491**
31	Murada	IND-34.5	35	133.9 ±0.2	31 ±1	100774 ±2445	991.5 ±2.6	1.4208 ±0.0030	118618 ±484	**118615 ±484**	1386 ±4	**118553 ±484**
32	Murada	IND-45.5	46	121.7 ±0.2	43 ±1	67972 ±1597	1025.0 ±2.5	1.4532 ±0.0029	119519 ±468	**119515 ±469**	1436 ±4	**119453 ±469**
33	Murada	IND-56.0	56	120.1 ±0.3	22 ±1	134581 ±3636	1057.6 ±3.5	1.4905 ±0.0040	121139 ±647	**121137 ±647**	1489 ±6	**121075 ±647**
34	Murada	IND-67.5	68	109.0 ±0.2	40 ±1	68042 ±1567	1084.3 ±3.6	1.5234 ±0.0035	122758 ±597	**122754 ±597**	1533 ±6	**122692 ±597**
35	Murada	IND-83.5	84	94.3 ±0.2	187 ±4	13112 ±267	1131.1 ±3.1	1.5759 ±0.0039	124828 ±601	**124805 ±601**	1609 ±5	**124743 ±601**
36	Murada	NOV-0.5	0.5	107.4 ±0.2	140 ±3	1298.8 ±27.0	799.4 ±2.5	0.1025 ±0.0005	6372 ±33	**6351 ±36**	814 ±3	**6289 ±36**
37	Murada	NOV-4.0	4	118 ±0	26 ±1	8529.6 ±235.5	867.1 ±2.6	0.1137 ±0.0006	6820 ±39	**6816 ±39**	884 ±3	**6754 ±39**
38	Murada	NOV-8.5	8.5	112.0 ±0.2	43 ±1	5311 ±132	772.2 ±2.8	0.1241 ±0.0007	7880 ±47	**7873 ±48**	790 ±3	**7811 ±48**
39	Murada	NOV-12.0	12	159 ±0	1910 ±38	187.2 ±3.8	840.7 ±2.8	0.1363 ±0.0005	8341 ±35	**8153 ±137**	860 ±3	**8091 ±137**
40	Murada	NOV-15.0	15	129.2 ±0.3	30 ±1	10083 ±268	798.9 ±2.9	0.1411 ±0.0006	8856 ±43	**8853 ±43**	819 ±3	**8791 ±43**
41	Murada	NOV-18.0	18	131.4 ±0.2	238 ±5	1394 ±29	837.7 ±3.9	0.1530 ±0.0006	9423 ±42	**9395 ±47**	860 ±4	**9333 ±47**
42	Murada	NOV-22.0	22	121.6 ±0.3	28 ±1	11244 ±296	822.4 ±3.3	0.1582 ±0.0007	9840 ±46	**9837 ±46**	846 ±3	**9775 ±46**
43	Murada	NOV-26.0	26	122.5 ±0.2	57 ±1	6011 ±128	837.4 ±3.2	0.1688 ±0.0005	10434 ±38	**10426 ±39**	862 ±3	**10364 ±39**
44	Murada	NOV-30.0	30	123.1 ±0.1	280 ±6	1291 ±26	827.0 ±2.7	0.1781 ±0.0008	11104 ±53	**11068 ±59**	853 ±3	**11006 ±59**
45	Murada	ALI 1.2	1.2	282.9 ±0.4	4638 ±93	39 ±1	733.6 ±2.2	0.0391 ±0.0002	2486 ±13	**2211 ±195**	738 ±2	**2147 ±195**

U decay constants: $l_{238} = 1.55125 \times 10^{-10}$ (Jaffey et al., 1971) and $l_{234} = 2.82206 \times 10^{-6}$ (Cheng et al., 2013). Th decay constant: $l_{230} = 9.1705 \times 10^{-6}$ (Cheng et al., 2013).

*$\delta^{234}U = ([^{234}U/^{238}U]_{activity} - 1) \times 1000$. ** $\delta^{234}U_{initial}$ was calculated based on ^{230}Th age (T), i.e., $\delta^{234}U_{initial} = \delta^{234}U_{measured} \times e^{l_{234}T}$.

Corrected ^{230}Th ages assume the initial $^{230}Th/^{232}Th$ atomic ratio of 4.4 ±2.2 x10^{-6}. Those are the values for a material at secular equilibrium, with the bulk earth $^{232}Th/^{238}U$ value of 3.8. The errors are arbitrarily assumed to be 50%.

***B.P. stands for "Before Present" where the "Present" is defined as the year 1950 A.D.

^{230}Th dating results. The error is 2σ error.

	Cave Name	Sample Name	Sample depth (cm)	^{238}U (ppb)	^{232}Th (ppt)	^{230}Th / ^{232}Th (atomic x10^{-6})	δ^{234}U* (measured)	^{230}Th / ^{238}U (activity)	^{230}Th Age (yr) (uncorrected)	^{230}Th Age (yr) (corrected)	$\delta^{234}U_{Initial}$** (corrected)	^{230}Th Age (yr BP)*** (corrected)
1	Na Polida	SAV-1.3	1.3	2957.2 ±10.3	275 ±6	118711 ±2422	52.6 ±2.2	0.6707 ±0.0026	109216 ±839	**109213 ±838**	72 ±3	**109151 ±838**
2	Na Polida	**SAV 9.8**	9.8	303.5 ±0.4	513 ±10	6928 ±140	108.7 ±1.5	0.7099 ±0.0014	108887 ±456	**108844 ±457**	148 ±2	**108780 ±457**
3	Na Polida	**SAV_58.3**	58.3	294 ±1	409 ±8	8391.9 ±171.0	78.9 ±1.7	0.7078 ±0.0021	114180 ±682	**114143 ±682**	109 ±2	**114081 ±682**
4	Na Polida	SAV-64.0	64	4055.6 ±24.9	215 ±5	220625 ±4663	98.6 ±6.6	0.7078 ±0.0046	110236 ±1759	**110234 ±1759**	135 ±9	**110172 ±1759**
5	Prior	**JUL Bottom**		164.4 ±0.3	709 ±14	452 ±9	170.3 ±2.2	0.1182 ±0.0005	11582 ±60	**11475 ±96**	176 ±2	**11411 ±96**
6	Prior	**ROM Top**		264.0 ±0.6	213 ±4	2265 ±47	199.0 ±2.0	0.1108 ±0.0004	10550 ±47	**10530 ±49**	205 ±2	**10466 ±49**
7	Prior	**ROM Bottom**		236.2 ±0.6	177 ±4	2445 ±51	118.0 ±2.6	0.1110 ±0.0005	11380 ±61	**11361 ±63**	122 ±3	**11297 ±63**
8	SaTauleta	**FOS 1**	1	600 ±1	157 ±3	49790.4 ±1059.1	101.3 ±1.7	0.7895 ±0.0023	133440 ±860	**133433 ±860**	148 ±2	**133369 ±860**
9	SaTauleta	**FOS_2.5**	2.5	569.9 ±1.2	293 ±6	25377 ±524	98.7 ±2.0	0.7913 ±0.0025	134731 ±988	**134718 ±988**	144 ±3	**134652 ±988**
10	SaTauleta	**FOS_5**	5	559.0 ±1.0	167 ±4	43752 ±939	100.2 ±1.7	0.7928 ±0.0020	134804 ±790	**134796 ±790**	147 ±2	**134730 ±790**
11	SaTauleta	**FOS 19.5**	19.5	798 ±2	155 ±3	67093.2 ±1427.6	94.4 ±1.7	0.7902 ±0.0022	135562 ±865	**135556 ±865**	138 ±2	**135492 ±865**
12	SaTauleta	**RAM 7.6**	7.6	478.1 ±0.7	81 ±2	40840 ±919	144.9 ±1.6	0.4179 ±0.0010	49002 ±166	**48998 ±166**	166 ±2	**48934 ±166**
13	SaTauleta	**RAM 19.9 OK**	19.9	400.3 ±0.5	465 ±9	5991 ±121	118.8 ±1.5	0.4217 ±0.0008	51110 ±159	**51081 ±160**	137 ±2	**51017 ±160**
14	SaTauleta	TER-1.0	1	567.4 ±1.1	57 ±1	129928 ±2791	74.4 ±2.3	0.7919 ±0.0019	141971 ±988	**141968 ±988**	111 ±4	**141906 ±988**
15	SaTauleta	TER-17.0	17	802.5 ±1.7	78 ±2	135998 ±2880	79.9 ±1.9	0.7976 ±0.0020	142337 ±924	**142334 ±924**	119 ±3	**142272 ±924**
16	SaTauleta	TER-44.5	44.5	424.1 ±0.7	401 ±8	15032 ±303	82.3 ±2.0	0.8627 ±0.0018	167550 ±1168	**167526 ±1168**	132 ±3	**167464 ±1168**
17	Xuemeu	**BAB Top**		259.0 ±0.5	92 ±2	230 ±24	60.5 ±1.7	0.0050 ±0.0005	511 ±52	**501 ±52**	61 ±2	**437 ±52**
18	Xuemeu	**BAB_13.2**	13.2	296 ±0	26 ±1	2403.3 ±59.2	39.4 ±1.5	0.0129 ±0.0002	1365 ±17	**1362 ±17**	40 ±2	**1300 ±17**
19	Xuemeu	**BAB_20.3**	20.3	209 ±0	58 ±1	353.0 ±12.1	35.4 ±1.3	0.0059 ±0.0001	627 ±15	**619 ±16**	35 ±1	**557 ±16**
20	Xuemeu	**BAB_22.3**	22.3	214 ±0	687 ±14	113.2 ±2.4	37.4 ±1.5	0.0221 ±0.0002	2346 ±19	**2255 ±67**	38 ±2	**2193 ±67**
21	Xuemeu	**BAB_31**	31	218 ±0	34 ±1	780.7 ±27.0	35.9 ±1.4	0.0074 ±0.0001	783 ±14	**779 ±14**	36 ±1	**717 ±14**
22	Xuemeu	**BAB_32**	32	199 ±0	124 ±3	328.5 ±7.9	34.3 ±1.4	0.0123 ±0.0002	1309 ±17	**1292 ±21**	34 ±1	**1230 ±21**
23	Xuemeu	**BAB_43,7**	43.7	207 ±0	22 ±1	1501.5 ±63.1	42.3 ±1.9	0.0096 ±0.0001	1011 ±15	**1008 ±15**	42 ±2	**946 ±15**
24	Xuemeu	**BAB_67**	67	233 ±0	257 ±5	216.9 ±4.9	33.7 ±1.7	0.0145 ±0.0002	1545 ±16	**1514 ±27**	34 ±2	**1452 ±27**
25	Xuemeu	**BAB_67.5**	67.5	204 ±0	17 ±1	2094.9 ±104.2	29.3 ±1.4	0.0105 ±0.0001	1122 ±16	**1120 ±16**	29 ±1	**1058 ±16**
26	Xuemeu	**BAB_71**	71	265 ±0	35 ±1	4768.7 ±104.1	20.3 ±1.6	0.0387 ±0.0002	4211 ±28	**4207 ±28**	21 ±2	**4145 ±28**
27	Xuemeu	**BAB_72**	72	364 ±1	4 ±1	36375.2 ±9930.0	25.5 ±1.7	0.0232 ±0.0002	2497 ±23	**2497 ±23**	26 ±2	**2435 ±23**
28	Xuemeu	**BAB_89.5**	89.5	266.5 ±0.4	23 ±1	5110 ±125	33.4 ±1.5	0.0263 ±0.0002	2815 ±27	**2813 ±27**	34 ±2	**2751 ±27**
29	Xuemeu	**BAB Bottom**		324.1 ±0.7	137 ±3	2228 ±47	110.3 ±2.3	0.0571 ±0.0003	5755 ±31	**5744 ±32**	112 ±2	**5680 ±32**
30	Xuemeu	**FIG_0.5**	0.5	229.5 ±0.4	52 ±1	232 ±6	64.1 ±1.5	0.0032 ±0.0001	326 ±6	**320 ±7**	64 ±1	**258 ±7**
31	Xuemeu	**FIG_23.5**	23.5	271 ±1	17 ±1	1481.2 ±91.2	56.6 ±1.6	0.0058 ±0.0003	599 ±28	**597 ±28**	57 ±2	**535 ±28**
32	Xuemeu	**FIG_25**	25	167 ±0	383 ±8	119.3 ±2.7	67.0 ±1.4	0.0166 ±0.0002	1708 ±19	**1645 ±48**	67 ±1	**1583 ±48**
33	Xuemeu	**FIG_41.5**	41.5	251 ±0	47 ±1	773.1 ±35.5	55.2 ±1.6	0.0088 ±0.0003	909 ±35	**904 ±35**	55 ±2	**842 ±35**
34	Xuemeu	**FIG_54**	54	256.6 ±0.4	32 ±1	1236 ±30	60.6 ±1.6	0.0095 ±0.0001	979 ±12	**976 ±13**	61 ±2	**914 ±13**
35	Xuemeu	**FIG_7**	7	294 ±1	111 ±2	775.7 ±23.3	67.6 ±1.6	0.0178 ±0.0004	1833 ±39	**1823 ±40**	68 ±2	**1761 ±40**
36	Xuemeu	**FIG_8**	8	246 ±0	53 ±1	538.9 ±13.3	55.5 ±1.5	0.0070 ±0.0001	726 ±10	**720 ±11**	56 ±1	**658 ±11**
37	Xuemeu	**MONica_1.2**	1.2	257.0 ±0.4	14 ±0	4040 ±103	54.5 ±1.5	0.0131 ±0.0001	1359 ±15	**1358 ±15**	55 ±2	**1296 ±15**
38	Xuemeu	**MONica_12.5**	12.5	229 ±0	4 ±1	15593.9 ±3818.9	50.8 ±1.7	0.0153 ±0.0005	1596 ±50	**1595 ±50**	51 ±2	**1533 ±50**
39	Xuemeu	**MONica_20**	20	255 ±0	10 ±0	8789.1 ±215.6	46.3 ±1.4	0.0211 ±0.0002	2224 ±20	**2223 ±20**	47 ±1	**2161 ±20**
40	Xuemeu	**MONica_21**	21	268 ±0	9 ±1	8777.5 ±673.7	49.4 ±1.5	0.0189 ±0.0003	1977 ±36	**1976 ±36**	50 ±2	**1914 ±36**
41	Xuemeu	**MONica_47.5**	47.5	184.4 ±0.2	18 ±0	3594 ±91	22.4 ±1.4	0.0218 ±0.0002	2347 ±24	**2344 ±24**	23 ±1	**2282 ±24**
42	Xuemeu	**PED Top**		185 ±0	82 ±2	489.0 ±16.6	52.7 ±1.7	0.0132 ±0.0004	1380 ±37	**1367 ±38**	53 ±2	**1303 ±38**
43	Xuemeu	**PED_19**	19	218 ±0	9 ±1	7047.1 ±551.7	39.5 ±1.8	0.0172 ±0.0002	1823 ±22	**1821 ±22**	40 ±2	**1759 ±22**
44	Xuemeu	**PED_2.5**	2.5	253 ±0	15 ±1	4025.8 ±216.6	55.1 ±1.5	0.0140 ±0.0002	1461 ±20	**1460 ±20**	55 ±2	**1398 ±20**
45	Xuemeu	**PED_4.2**	4.2	280 ±0	30 ±1	3952.5 ±86.7	40.4 ±1.5	0.0259 ±0.0002	2748 ±20	**2745 ±20**	41 ±2	**2683 ±20**
46	Xuemeu	**PED_46.5**	46.5	189.4 ±0.2	16 ±0	3985 ±100	19.9 ±1.5	0.0208 ±0.0002	2251 ±24	**2248 ±24**	20 ±2	**2186 ±24**
47	Xuemeu	**SEC_2**	2	126 ±0	368 ±7	82.9 ±2.1	312.8 ±2.0	0.0147 ±0.0002	1231 ±20	**1166 ±50**	314 ±2	**1104 ±50**
48	Xuemeu	**SEC_50.2**	50.2	269 ±0	12 ±0	11878.0 ±259.4	345.6 ±1.8	0.0330 ±0.0002	2707 ±16	**2706 ±16**	348 ±2	**2644 ±16**

U decay constants: $l_{238} = 1.55125 \times 10^{-10}$ (Jaffey et al., 1971) and $l_{234} = 2.82206 \times 10^{-6}$ (Cheng et al., 2013). Th decay constant: $l_{230} = 9.1705 \times 10^{-6}$ (Cheng et al., 2013).

*$\delta^{234}U = ([^{234}U/^{238}U]_{activity} - 1) \times 1000$. ** $\delta^{234}U_{initial}$ was calculated based on ^{230}Th age (T), i.e., $\delta^{234}U_{initial} = \delta^{234}U_{measured} \times e^{l_{234}T}$.

Corrected ^{230}Th ages assume the initial ^{230}Th/^{232}Th atomic ratio of 4.4 ±2.2 x10^{-6}. Those are the values for a material at secular equilibrium, with the bulk earth ^{232}Th/^{238}U value of 3.8. The errors are arbitrarily assumed to be 50%.

***B.P. stands for "Before Present" where the "Present" is defined as the year 1950 A.D.

^{230}Th dating results. The error is 2σ error.

	Cave Name	Sample Name	Sample depth (cm)	^{238}U (ppb)	^{232}Th (ppt)	^{230}Th / ^{232}Th (atomic x10^{-6})	δ^{234}U* (measured)	^{230}Th / ^{238}U (activity)	^{230}Th Age (yr) (uncorrected)	^{230}Th Age (yr) (corrected)	$\delta^{234}U_{initial}$** (corrected)	^{230}Th Age (yr BP)*** (corrected)
1	Pirata	**PIR2_top**		653.0 ±1.7	24 ±1	475064 ±14442	91.2 ±2.0	1.0770 ±0.0031	349715 ±8631	**349712 ±8631**	245 ±8	**349646 ±8631**
2	Pirata	**PIR2_bottom**		755.3 ±2.9	121 ±3	110850 ±2340	87.7 ±2.7	1.0736 ±0.0045	352269 ±12677	**352263 ±12676**	237 ±11	**352197 ±12676**
3	Pirata	**PIR1_Top**		118.0 ±0.2	2002 ±40	11 ±0	116.2 ±1.7	0.0113 ±0.0004	1114 ±37	**671 ±316**	116 ±2	**605 ±316**
4	Pirata	**PIR1_Bottom**		115.6 ±0.1	198 ±4	127 ±7	137.2 ±1.9	0.0132 ±0.0006	1272 ±60	**1228 ±67**	138 ±2	**1162 ±67**
5	Drac	**POP 1.2**	1.2	379.5 ±0.7	135 ±3	54 ±4	55.5 ±1.7	0.0012 ±0.0001	120 ±9	**111 ±11**	56 ±2	**47 ±11**
6	Drac	**POP 8**	8	278.2 ±0.4	1636 ±33	4 ±0	58.5 ±1.4	0.0016 ±0.0001	162 ±13	**0 ±115**	59 ±1	**-64 ±115**
7	Drac	**POP 7.2**	7.2	319.3 ±0.5	405 ±8	24 ±2	50.7 ±1.8	0.0018 ±0.0002	189 ±16	**154 ±30**	51 ±2	**90 ±30**
8	Drac	**POP 0.4**	0.4	382.3 ±0.5	144 ±3	115 ±9	54.8 ±1.6	0.0026 ±0.0002	274 ±19	**263 ±21**	55 ±2	**199 ±21**
9	Drac	DRA1_1	1	433.0 ±0.7	22 ±1	230 ±39	67.7 ±1.5	0.0007 ±0.0001	72 ±12	**70 ±12**	68 ±1	**4 ±12**
10	Drac	DRA1_4.6	4.6	500.1 ±1.2	22 ±1	523 ±52	69.6 ±2.1	0.0014 ±0.0001	141 ±12	**140 ±12**	70 ±2	**74 ±12**

U decay constants: l_{238} = 1.55125x10^{-10} (Jaffey et al., 1971) and l_{234} = 2.82206x10^{-6} (Cheng et al., 2013). Th decay constant: l_{230} = 9.1705x10^{-6} (Cheng et al., 2013).

*$\delta^{234}U = ([^{234}U/^{238}U]_{activity} - 1)$x1000. ** $\delta^{234}U_{initial}$ was calculated based on ^{230}Th age (T), i.e., $\delta^{234}U_{initial} = \delta^{234}U_{measured} \times e^{l234xT}$.

Corrected ^{230}Th ages assume the initial ^{230}Th/^{232}Th atomic ratio of 4.4 ±2.2 x10^{-6}. Those are the values for a material at secular equilibrium, with the bulk earth ^{232}Th/^{238}U value of 3.8. The errors are arbitrarily assumed to be 50%.

***B.P. stands for “Before Present” where the “Present” is defined as the year 1950 A.D.

^{230}Th dating results. The error is 2σ error.

	Cave Name	Sample Name	Sample depth (cm)	^{238}U (ppb)	^{232}Th (ppt)	^{230}Th / ^{232}Th (atomic x10^{-6})	δ^{234}U* (measured)	^{230}Th / ^{238}U (activity)	^{230}Th Age (yr) (uncorrected)	^{230}Th Age (yr) (corrected)	$\delta^{234}U_{initial}$** (corrected)	^{230}Th Age (yr BP)*** (corrected)
1	Campanet	**CAM2_Top**	**0**	549 ±1	4465 ±90	2032.4 ±41.1	131.5 ±1.7	1.0032 ±0.0029	215604 ±2159	**215413 ±2159**	241 ±3	**215349 ±2159**
2	Campanet	**CAM2**	**2.5**	475 ±1	196 ±4	41898.8 ±882.5	176.5 ±1.8	1.0501 ±0.0032	214641 ±2197	**214631 ±2197**	324 ±4	**214569 ±2197**
3	Campanet	**CAM2**	**3.5**	512 ±1	26 ±1	359934.3 ±17910.1	227.6 ±1.9	1.1064 ±0.0037	215438 ±2355	**215436 ±2355**	418 ±4	**215374 ±2355**
4	Campanet	**CAM2**	13	423.0 ±0.7	51 ±1	152054 ±3986	227.1 ±1.6	1.1025 ±0.0025	213572 ±1660	**213569 ±1660**	415 ±4	**213503 ±1660**
5	Campanet	**CAM2**	14	540.5 ±1.2	57 ±1	161412 ±4073	158.3 ±2.1	1.0363 ±0.0029	218237 ±2304	**218234 ±2304**	293 ±4	**218168 ±2304**
6	Campanet	**CAM2**	**31**	456.3 ±0.8	1544 ±31	5477 ±110	237.2 ±1.9	1.1237 ±0.0024	219338 ±1765	**219269 ±1764**	440 ±4	**219203 ±1764**
7	Campanet	**CAM2**	**32.8**	387 ±1	546 ±11	13249.6 ±272.4	253.7 ±1.8	1.1355 ±0.0035	215998 ±2144	**215970 ±2144**	467 ±4	**215908 ±2144**
8	Campanet	**CAM2**	**33.5**	223 ±0	71 ±2	61312.3 ±1479.4	294.5 ±1.5	1.1851 ±0.0032	218882 ±1918	**218875 ±1918**	546 ±4	**218813 ±1918**
9	Campanet	**CAM2**	**34**	247.3 ±0.4	70 ±2	68770 ±1656	288.8 ±2.1	1.1869 ±0.0022	223198 ±1747	**223192 ±1747**	542 ±5	**223126 ±1747**
10	Campanet	**CAM2**	**36**	250.9 ±0.4	108 ±2	45226 ±1010	288.2 ±1.9	1.1815 ±0.0024	220611 ±1729	**220602 ±1729**	537 ±4	**220536 ±1729**
11	Campanet	**CAM2**	**38**	261.6 ±0.4	67 ±2	75491 ±1827	285.6 ±1.9	1.1782 ±0.0026	220405 ±1756	**220399 ±1756**	532 ±4	**220333 ±1756**
12	Campanet	**CAM2**	**41**	333.5 ±0.5	134 ±3	46145 ±1027	234.0 ±2.1	1.1284 ±0.0024	224048 ±2000	**224039 ±2000**	440 ±5	**223973 ±2000**
13	Campanet	**CAM2_bottom**	**41.7**	285.7 ±0.6	1383 ±28	3802 ±77	222.5 ±2.2	1.1167 ±0.0035	224650 ±2555	**224550 ±2554**	419 ±5	**224486 ±2554**
14	Campanet	**CAM3 Top**	**1**	5894.0 ±45.9	213 ±5	432459 ±10038	83.1 ±3.6	0.9482 ±0.0106	213709 ±7603	**213708 ±7603**	152 ±7	**213644 ±7603**
15	Campanet	**CAM3_2**	2	5788.1 ±28.8	18 ±1	5067677 ±320127	79.9 ±2.8	0.9445 ±0.0050	213553 ±3956	**213552 ±3956**	146 ±5	**213486 ±3956**
16	Campanet	**CAM3_5**	5	6751.2 ±21.2	364 ±7	289023 ±5953	84.8 ±1.7	0.9460 ±0.0034	211022 ±2507	**211020 ±2507**	154 ±3	**210954 ±2507**
17	Campanet	**CAM3_8.5**	8.5	6260 ±34	259 ±5	376473.2 ±8165.1	91.1 ±2.5	0.9465 ±0.0075	207012 ±4954	**207010 ±4954**	163 ±5	**206948 ±4954**
18	Campanet	**CAM3_12**	12	59 ±1	2444 ±49	56990.3 ±1160.0	157984.3 ±1669.7	142.4340 ±1.8451	152755 ±4309	**152750 ±4311**	243123 ±3918	**152688 ±4311**
19	Campanet	**CAM3_13**	13	638 ±1	278 ±6	36188.8 ±765.0	93.2 ±1.6	0.9557 ±0.0032	211513 ±2363	**211501 ±2363**	169 ±3	**211439 ±2363**
20	Campanet	**CAM3_23,2**	23.2	607.0 ±1.1	157 ±3	60302 ±1298	77.2 ±1.7	0.9470 ±0.0027	217241 ±2305	**217233 ±2305**	142 ±3	**217167 ±2305**
21	Campanet	**CAM3 Bottom**	**29**	676.1 ±1.9	159 ±3	67447 ±1413	80.7 ±2.2	0.9611 ±0.0039	224556 ±3432	**224550 ±3432**	152 ±4	**224486 ±3432**
22	Campanet	**CAM7_Top**	0.4	7555 ±75	77 ±2	1023568.5 ±25705.1	91.2 ±4.3	0.6295 ±0.0092	92305 ±2183	**92304 ±2183**	118 ±6	**92242 ±2183**
23	Campanet	**CAM7_8**	8	4474.4 ±15.6	42 ±1	1204111 ±43168	111.7 ±2.3	0.6830 ±0.0027	101644 ±742	**101644 ±742**	149 ±3	**101578 ±742**
24	Campanet	**CAM7_10**	10	4214.9 ±15.5	18 ±1	2607248 ±152884	115.2 ±2.3	0.6864 ±0.0028	101882 ±771	**101882 ±771**	154 ±3	**101816 ±771**
25	Campanet	**CAM7_12.5**	12.5	551 ±1	4 ±2	1507572.8 ±561116.1	87.3 ±1.6	0.7098 ±0.0020	112996 ±635	**112995 ±635**	120 ±2	**112933 ±635**
26	Campanet	**CAM7_14**	14	864.4 ±1.7	9 ±3	1113685 ±330426	83.0 ±2.1	0.7108 ±0.0024	114159 ±793	**114158 ±793**	115 ±3	**114092 ±793**
27	Campanet	**CAM7_Bottom**	18.3	537 ±1	11 ±0	546762.3 ±11725.3	69.2 ±1.9	0.7025 ±0.0029	114707 ±910	**114707 ±910**	96 ±3	**114645 ±910**
28	Campanet	**CAM4**	0.4	543.2 ±0.9	16162 ±324	41 ±1	172.8 ±1.6	0.0738 ±0.0006	7075 ±61	**6336 ±526**	176 ±2	**6274 ±526**
29	Campanet	**CAM4**	1	171.8 ±0.2	44 ±1	34190 ±809	384.3 ±1.6	0.5329 ±0.0020	51699 ±260	**51694 ±260**	445 ±2	**51632 ±260**
30	Campanet	**CAM4 Top**	2.3	423 ±1	338 ±7	23498.9 ±479.3	538.8 ±2.3	1.1391 ±0.0038	131091 ±870	**131078 ±870**	780 ±4	**131014 ±870**
31	Campanet	**CAM4**	4.5	858.5 ±2.4	40 ±1	387027 ±11902	421.8 ±2.5	1.0832 ±0.0036	140331 ±1020	**140330 ±1020**	627 ±4	**140264 ±1020**
32	Campanet	**CAM4**	5	935.8 ±2.3	46 ±1	358545 ±9324	418.1 ±2.1	1.0772 ±0.0031	139644 ±880	**139643 ±880**	620 ±4	**139577 ±880**
33	Campanet	**CAM4 Bottom**	15.5	403.8 ±0.9	392 ±8	18352 ±375	407.8 ±2.4	1.0809 ±0.0038	142735 ±1073	**142717 ±1073**	610 ±4	**142653 ±1073**
34	Campanet	**CAM1 Top**		423 ±1	338 ±7	23498.9 ±479.3	538.8 ±2.3	1.1391 ±0.0038	131091 ±870	**131078 ±870**	780 ±4	**131014 ±870**
35	Campanet	**CAM1 Bottom**		403.8 ±0.9	392 ±8	18352 ±375	407.8 ±2.4	1.0809 ±0.0038	142735 ±1073	**142717 ±1073**	610 ±4	**142653 ±1073**
36	Campanet	**CAM5_Top**		522.2 ±1.1	854 ±17	10099 ±207	164.0 ±1.6	1.0013 ±0.0044	195176 ±2399	**195139 ±2398**	284 ±3	**195077 ±2398**
37	Campanet	**CAM5_Bottom**		450 ±2	50 ±1	157260.5 ±3372.0	280.5 ±190.7	1.0699 ±0.0073	174653 ±105518	**174650 ±105511**	459 ±365	**174588 ±105511**
38	Campanet	**CAM6_Top**		592.3 ±1.7	429 ±9	22751 ±465	160.8 ±1.9	0.9995 ±0.0042	195963 ±2369	**195946 ±2369**	280 ±4	**195884 ±2369**
39	Campanet	**CAM6_Bottom**		415.8 ±1.1	20 ±0	362435 ±7601	177.2 ±2.0	1.0326 ±0.0040	204400 ±2472	**204399 ±2472**	316 ±4	**204337 ±2472**
40	Campanet	**CAM8**	0.8	5439.7 ±13.2	75 ±2	1349305 ±40251	545.2 ±2.4	1.1297 ±0.0031	128153 ±722	**128153 ±722**	783 ±4	**128087 ±722**

U decay constants: l_{238} = 1.55125x10^{-10} (Jaffey et al., 1971) and l_{234} = 2.82206x10^{-6}(Cheng et al., 2013). Th decay constant: l_{230} = 9.1705x10^{-6}(Cheng et al., 2013).

*$\delta^{234}U = ([^{234}U/^{238}U]_{activity} - 1)x1000$. ** $\delta^{234}U_{initial}$ was calculated based on ^{230}Th age (T), i.e., $\delta^{234}U_{initial} = \delta^{234}U_{measured} \times e^{l_{234}xT}$.

Corrected ^{230}Th ages assume the initial ^{230}Th/^{232}Th atomic ratio of 4.4 ±2.2 x10^{-6}. Those are the values for a material at secular equilibrium, with the bulk earth ^{232}Th/^{238}U value of 3.8. The errors are arbitrarily assumed to be 50%.

***B.P. stands for "Before Present" where the "Present" is defined as the year 1950 A.D.

^{230}Th dating results. The error is 2σ error.

	Cave Name	Sample Name	Sample depth (cm)	^{238}U (ppb)	^{232}Th (ppt)	^{230}Th / ^{232}Th (atomic x10^{-6})	δ^{234}U* (measured)	^{230}Th / ^{238}U (activity)	^{230}Th Age (yr) (uncorrected)	^{230}Th Age (yr) (corrected)	$\delta^{234}U_{initial}$** (corrected)	^{230}Th Age (yr BP)*** (corrected)
41	Campanet	**CAM8**	**1.5**	5610.5 ±28.3	84 ±2	1244184 ±27411	555.2 ±3.2	1.1361 ±0.0086	127831 ±1761	**127830 ±1761**	796 ±6	**127768 ±1761**
42	Campanet	**CAM8rep**	**1.5**	5386 ±23	52 ±1	1956865.1 ±42833.4	557.8 ±2.8	1.1405 ±0.0073	128283 ±1490	**128282 ±1490**	801 ±5	**128220 ±1490**
43	Campanet	**CAM8**	2	5566.3 ±13.1	213 ±5	494792 ±11181	568.8 ±2.5	1.1500 ±0.0030	128415 ±707	**128415 ±707**	817 ±4	**128349 ±707**
44	Campanet	**CAM8**	**2.5**	6378 ±42	36 ±1	3463645.9 ±135733.7	577.0 ±4.1	1.1796 ±0.0113	132933 ±2362	**132932 ±2362**	840 ±8	**132870 ±2362**
45	Campanet	**CAM8Rep**	**2.5**	6603 ±14	26 ±1	4832020.9 ±107378.3	574.8 ±2.1	1.1537 ±0.0034	128198 ±742	**128198 ±742**	825 ±4	**128136 ±742**
46	Campanet	**CAM8**	3.5	6077.5 ±13.8	15 ±2	7700520 ±877739	584.0 ±2.2	1.1649 ±0.0030	128918 ±673	**128917 ±673**	840 ±4	**128851 ±673**
47	Campanet	**CAM8**	4	6294.8 ±16.8	88 ±3	1372175 ±39279	592.1 ±2.5	1.1681 ±0.0034	128284 ±759	**128283 ±759**	850 ±4	**128217 ±759**
48	Campanet	**CAM8**	**4.7**	7456 ±49	14 ±0	10235591.9 ±239414.4	598.4 ±4.0	1.2021 ±0.0114	133912 ±2364	**133912 ±2364**	873 ±8	**133850 ±2364**
49	Campanet	**CAM8**	5	6352.6 ±15.7	6927 ±140	17622 ±356	560.1 ±2.4	1.1654 ±0.0032	132876 ±766	**132859 ±766**	815 ±4	**132793 ±766**
50	Campanet	**CAM8**	6	418.8 ±0.5	150 ±3	53461 ±1111	539.8 ±2.0	1.1597 ±0.0020	135175 ±535	**135169 ±535**	790 ±3	**135103 ±535**
51	Campanet	**CAM8**	8	795.6 ±1.2	54 ±2	281570 ±8148	539.7 ±2.2	1.1569 ±0.0022	134601 ±598	**134600 ±598**	789 ±3	**134534 ±598**
52	Campanet	**CAM8**	12	479.5 ±0.7	251 ±5	36805 ±752	541.0 ±2.2	1.1663 ±0.0023	136357 ±626	**136348 ±626**	795 ±4	**136282 ±626**
53	Campanet	**CAM8**	**13.2**	658 ±2	13 ±0	947477.1 ±20402.4	545.1 ±2.3	1.1759 ±0.0040	137689 ±945	**137689 ±945**	804 ±4	**137627 ±945**
54	Campanet	**CAM8**	**18.9**	857 ±2	15 ±0	1113641.4 ±24012.7	569.1 ±2.4	1.2011 ±0.0047	138731 ±1089	**138731 ±1089**	842 ±4	**138669 ±1089**
55	Campanet	**CAM8Rep**	**18.9**	873 ±1	7 ±0	2461955.3 ±109249.1	571.5 ±1.8	1.1976 ±0.0019	137560 ±510	**137560 ±510**	843 ±3	**137498 ±510**
56	Campanet	**CAM8**	**19.4**	525.0 ±1.0	64 ±1	163481 ±3345	584.2 ±2.0	1.2116 ±0.0036	138259 ±837	**138256 ±837**	863 ±4	**138194 ±837**
57	Campanet	**CAM8**	20.5	4381.4 ±14.7	14941 ±303	6186 ±126	633.7 ±2.6	1.2794 ±0.0047	143567 ±1085	**143516 ±1085**	950 ±5	**143450 ±1085**
58	Campanet	**CAM8**	22.5	5500.6 ±29.4	9929 ±206	11510 ±240	553.5 ±3.5	1.2601 ±0.0073	155185 ±1928	**155156 ±1927**	858 ±7	**155090 ±1927**
59	Campanet	**CAM8**	24.7	405.7 ±0.8	200 ±4	40391 ±836	476.1 ±2.5	1.2054 ±0.0029	159261 ±999	**159252 ±999**	746 ±4	**159186 ±999**
60	Campanet	**CAM8**	**25.9**	339.0 ±0.5	25 ±1	272912 ±7889	479.2 ±1.6	1.2174 ±0.0059	161745 ±1654	**161743 ±1654**	756 ±4	**161681 ±1654**
61	Campanet	**CAM8Rep**	**25.9**	331 ±0	15 ±0	442573.2 ±9943.0	481.4 ±1.9	1.2127 ±0.0022	159917 ±759	**159916 ±759**	756 ±3	**159854 ±759**
62	Campanet	**CAM8**	**30.7**	175.4 ±0.2	65 ±1	54935 ±1118	492.8 ±1.7	1.2278 ±0.0020	161122 ±679	**161115 ±679**	777 ±3	**161053 ±679**
63	Campanet	**CAM8**	**31.7**	191 ±0	14 ±0	277886.5 ±5910.9	504.1 ±1.9	1.2397 ±0.0029	161530 ±909	**161528 ±909**	795 ±4	**161466 ±909**
64	Campanet	**CAM8**	33	310.5 ±0.5	128 ±3	50417 ±1080	513.2 ±2.3	1.2588 ±0.0024	164404 ±881	**164397 ±881**	816 ±4	**164331 ±881**
65	Campanet	**CAM8**	**34.4**	317 ±0	13 ±0	485389.5 ±10456.3	497.6 ±1.7	1.2431 ±0.0037	164092 ±1094	**164091 ±1094**	791 ±4	**164029 ±1094**
66	Campanet	**CAM8**	**35**	203 ±0	38 ±1	109535.5 ±2269.2	488.6 ±1.9	1.2358 ±0.0037	164376 ±1142	**164373 ±1142**	777 ±4	**164311 ±1142**
67	Campanet	**CAM8**	37.7	236.3 ±0.3	25 ±1	188524 ±8096	464.6 ±1.8	1.2214 ±0.0020	166700 ±754	**166698 ±754**	744 ±3	**166632 ±754**
68	Campanet	**CAM8**	40	184.6 ±0.2	28 ±1	129227 ±5716	430.6 ±2.2	1.1963 ±0.0021	168807 ±888	**168804 ±888**	693 ±4	**168738 ±888**
69	Campanet	**CAM8**	44.2	193.1 ±0.2	10 ±1	391410 ±43085	397.6 ±1.8	1.1770 ±0.0018	172611 ±807	**172610 ±807**	647 ±3	**172544 ±807**
70	Campanet	**CAM8**	**46.7**	210 ±0	484 ±10	7899.2 ±159.9	391.4 ±1.6	1.1040 ±0.0032	152569 ±962	**152527 ±962**	602 ±3	**152465 ±962**
71	Campanet	**CAM8Rep**	**46.7**	213 ±0	509 ±10	7620.3 ±153.8	395.7 ±1.7	1.1066 ±0.0023	152254 ±742	**152210 ±742**	608 ±3	**152148 ±742**
72	Campanet	**CAM8**	**47.5**	189 ±0	208 ±4	17339.3 ±353.6	366.2 ±2.5	1.1594 ±0.0041	176872 ±1641	**176852 ±1641**	603 ±5	**176790 ±1641**
73	Campanet	**CAM8**	50	208.4 ±0.3	58 ±1	69010 ±1729	373.2 ±2.1	1.1661 ±0.0021	176839 ±983	**176833 ±983**	615 ±4	**176767 ±983**
74	Campanet	**CAM8**	**52.5**	234.9 ±0.3	86 ±2	52633 ±1085	374.3 ±1.6	1.1727 ±0.0031	178757 ±1202	**178750 ±1202**	620 ±3	**178688 ±1202**
75	Campanet	**CAM8rep**	**52.5**	221 ±0	72 ±1	58703.1 ±1206.4	371.3 ±1.6	1.1691 ±0.0026	178521 ±1069	**178515 ±1069**	614 ±3	**178453 ±1069**

U decay constants: $l_{238} = 1.55125 \times 10^{-10}$ (Jaffey et al., 1971) and $l_{234} = 2.82206 \times 10^{-6}$ (Cheng et al., 2013). Th decay constant: $l_{230} = 9.1705 \times 10^{-6}$ (Cheng et al., 2013).

*$\delta^{234}U = ([^{234}U/^{238}U]_{activity} - 1) \times 1000$. ** $\delta^{234}U_{initial}$ was calculated based on ^{230}Th age (T), i.e., $\delta^{234}U_{initial} = \delta^{234}U_{measured} \times e^{l_{234}T}$.

Corrected ^{230}Th ages assume the initial $^{230}Th/^{232}Th$ atomic ratio of 4.4 ±2.2 x10^{-6}. Those are the values for a material at secular equilibrium, with the bulk earth $^{232}Th/^{238}U$ value of 3.8. The errors are arbitrarily assumed to be 50%.

***B.P. stands for "Before Present" where the "Present" is defined as the year 1950 A.D.

^{230}Th dating results. The error is 2σ error.

	Cave Name	Sample Name	Sample depth (cm)	^{238}U (ppb)	^{232}Th (ppt)	^{230}Th / ^{232}Th (atomic x10^{-6})	δ^{234}U* (measured)	^{230}Th / ^{238}U (activity)	^{230}Th Age (yr) (uncorrected)	^{230}Th Age (yr) (corrected)	$\delta^{234}U_{initial}$** (corrected)	^{230}Th Age (yr BP)*** (corrected)
1	Es Quartó	**QUA14**	**0.4**	184.6 ±0.2	991 ±20	1940 ±39	138.4 ±1.7	0.6319 ±0.0012	86447 ±326	**86314 ±338**	177 ±2	**86248 ±338**
2	Es Quartó	**QUA14**	1.4	418.2 ±0.7	2122 ±43	2008 ±41	111.4 ±1.7	0.6178 ±0.0017	86960 ±425	**86830 ±434**	142 ±2	**86768 ±434**
3	Es Quartó	**QUA14**	**3.7**	484.1 ±0.6	3188 ±64	1563 ±31	109.3 ±1.5	0.6244 ±0.0012	88636 ±328	**88468 ±348**	140 ±2	**88402 ±348**
4	Es Quartó	**QUA14**	**4.3**	412.6 ±0.5	15102 ±303	292 ±6	88.8 ±1.5	0.6492 ±0.0011	97270 ±355	**96312 ±763**	116 ±2	**96246 ±763**
5	Es Quartó	**QUA14**	**7**	343.8 ±0.5	3986 ±80	948 ±19	71.4 ±1.8	0.6663 ±0.0012	104452 ±457	**104143 ±505**	96 ±2	**104077 ±505**
6	Es Quartó	**QUA14**	**10**	299.4 ±0.4	908 ±18	3603 ±73	59.6 ±1.8	0.6628 ±0.0013	105716 ±473	**105634 ±476**	80 ±2	**105568 ±476**
7	Es Quartó	**QUA14**	**10.6**	321.5 ±0.4	4957 ±99	725 ±15	71.2 ±1.5	0.6779 ±0.0012	107550 ±435	**107140 ±521**	96 ±2	**107074 ±521**
8	Es Quartó	**QUA14**	**11.4**	399.8 ±0.6	17658 ±354	264 ±5	85.9 ±1.9	0.7064 ±0.0015	112367 error	**111210 error**	118 error	**111144 error**
9	Es Quartó	**QUA14**	**13.9**	451.9 ±0.6	10131 ±203	564 ±11	150.6 ±1.6	0.7668 ±0.0013	115621 ±464	**115080 ±599**	208 ±2	**115014 ±599**
10	Es Quartó	**QUA14**	**15.7**	516.6 ±0.7	9753 ±196	649 ±13	83.6 ±1.4	0.7429 ±0.0012	123352 ±495	**122860 ±603**	118 ±2	**122794 ±603**
11	Es Quartó	**QUA14**	**17**	446.4 ±0.6	8000 ±160	714 ±14	117.6 ±1.6	0.7762 ±0.0013	125298 ±547	**124850 ±629**	167 ±2	**124784 ±629**
12	Es Quartó	**QUA14**	18.3	236.7 ±0.4	1792 ±36	1650 ±34	97.1 ±1.7	0.7573 ±0.0033	124482 ±1067	**124288 ±1074**	138 ±3	**124226 ±1074**
13	Es Quartó	**QUA14**	**19**	467.0 ±0.7	3848 ±77	1514 ±30	73.9 ±1.5	0.7565 ±0.0015	130042 error	**129825 error**	107 error	**129759 error**
14	Es Quartó	**QUA14**	**19.6**	388.7 ±0.6	7838 ±157	621 ±12	74.9 ±1.7	0.7596 ±0.0015	130779 ±649	**130248 ±746**	108 ±2	**130182 ±746**
15	Es Quartó	CIA	**1.5**	247 ±0	159 ±3	468.0 ±10.3	205.7 ±1.6	0.0183 ±0.0001	1664 ±14	**1648 ±18**	207 ±2	**1584 ±18**
16	Es Quartó	CIA	**3**	438 ±1	165 ±3	834.9 ±18.4	203.0 ±1.6	0.0191 ±0.0001	1746 ±13	**1737 ±15**	204 ±2	**1673 ±15**
17	Es Quartó	CIA	**3.5**	409 ±1	207 ±4	617.6 ±13.7	203.9 ±1.8	0.0189 ±0.0002	1727 ±15	**1715 ±17**	205 ±2	**1651 ±17**
18	Es Quartó	CIA	**4.5**	300 ±0	364 ±7	274.6 ±6.4	207.3 ±1.8	0.0202 ±0.0002	1840 ±21	**1811 ±30**	208 ±2	**1747 ±30**
19	Es Quartó	CIA	**5.6**	366 ±0	332 ±7	379.6 ±8.4	202.9 ±1.5	0.0209 ±0.0002	1910 ±17	**1888 ±23**	204 ±2	**1824 ±23**
20	Es Quartó	CIA	**8.2**	367.0 ±0.4	230 ±5	594 ±13	203.9 ±1.5	0.0226 ±0.0002	2068 ±16	**2053 ±19**	205 ±2	**1989 ±19**
21	Es Quartó	CIA	**11.6**	407.9 ±0.5	127 ±3	1156 ±26	200.2 ±1.6	0.0218 ±0.0002	1999 ±15	**1992 ±16**	201 ±2	**1928 ±16**
22	Es Quartó	CIA	**14**	433 ±1	48 ±1	3349.0 ±92.4	202.5 ±1.5	0.0224 ±0.0001	2050 ±14	**2048 ±14**	204 ±2	**1984 ±14**
23	Es Quartó	CIA	**16.3**	339.1 ±0.5	156 ±3	838 ±18	203.8 ±1.6	0.0234 ±0.0002	2143 ±16	**2131 ±18**	205 ±2	**2067 ±18**
24	Es Quartó	CIA	**18.8**	423.3 ±0.6	109 ±2	1531 ±35	203.7 ±1.5	0.0238 ±0.0002	2181 ±15	**2174 ±16**	205 ±1	**2110 ±16**
25	Es Quartó	CIA	**21.7**	401.6 ±0.5	118 ±3	1341 ±31	205.3 ±1.6	0.0240 ±0.0002	2189 ±17	**2182 ±18**	207 ±2	**2118 ±18**
26	Es Quartó	CIA	**23.4**	438.8 ±0.6	177 ±4	989 ±23	204.8 ±1.7	0.0242 ±0.0002	2214 ±23	**2204 ±24**	206 ±2	**2140 ±24**
27	Es Quartó	CIA	**28.5**	465.5 ±0.6	1600 ±32	122 ±3	194.3 ±1.5	0.0254 ±0.0002	2345 ±16	**2261 ±61**	196 ±1	**2197 ±61**
28	Es Quartó	CIA	**31.5**	424.2 ±0.6	135 ±3	1356 ±30	207.1 ±1.2	0.0262 ±0.0002	2396 ±14	**2388 ±15**	209 ±1	**2324 ±15**
29	Es Quartó	CIA	**32.5**	468.5 ±0.7	160 ±3	1232 ±27	204.4 ±1.7	0.0256 ±0.0002	2340 ±15	**2332 ±16**	206 ±2	**2268 ±16**
30	Es Quartó	CIA	**34.2**	469 ±1	2619 ±53	79.5 ±1.7	202.9 ±1.8	0.0269 ±0.0002	2469 ±16	**2334 ±97**	204 ±2	**2270 ±97**
31	Es Quartó	CIA	**37.1**	385.0 ±0.5	254 ±5	676 ±14	198.1 ±1.5	0.0271 ±0.0002	2491 ±16	**2474 ±19**	199 ±2	**2410 ±19**
32	Es Quartó	CIA	**34.8**	418.2 ±0.6	1473 ±30	133 ±3	204.8 ±1.8	0.0285 ±0.0002	2608 ±16	**2523 ±62**	206 ±2	**2459 ±62**
33	Es Quartó	CIA	**39.4**	394.7 ±0.5	282 ±6	639 ±13	204.8 ±1.5	0.0277 ±0.0002	2535 ±15	**2518 ±20**	206 ±2	**2454 ±20**
34	Es Quartó	CIA	**41.7**	462 ±1	94 ±2	2239.6 ±47.8	208.7 ±1.8	0.0278 ±0.0001	2534 ±12	**2529 ±12**	210 ±2	**2465 ±12**
35	Es Quartó	**FEN**	**0.8**	242.3 ±0.5	314 ±6	302 ±6	120.5 ±1.9	0.0237 ±0.0002	2332 ±16	**2298 ±29**	121 ±2	**2234 ±29**
36	Es Quartó	**FEN**	**10.2**	376.4 ±0.7	66 ±1	2424 ±54	119.1 ±1.6	0.0256 ±0.0001	2526 ±13	**2522 ±14**	120 ±2	**2458 ±14**
37	Es Quartó	**MUL**	**0.6**	245.2 ±0.5	150 ±3	45 ±4	178.5 ±1.8	0.0017 ±0.0001	156 ±12	**141 ±16**	179 ±2	**77 ±16**
38	Es Quartó	**MUL**	**4.5**	351.2 ±0.4	371 ±8	87 ±3	175.2 ±1.7	0.0056 ±0.0002	519 ±18	**493 ±26**	175 ±2	**429 ±26**
39	Es Quartó	**MUL**	**20.8**	328.4 ±0.5	611 ±12	170 ±4	180.7 ±1.7	0.0192 ±0.0002	1787 ±17	**1742 ±36**	182 ±2	**1678 ±36**
40	Es Quartó	**MUL**	**29.6**	349.7 ±0.5	70 ±2	2025 ±45	168.9 ±1.5	0.0245 ±0.0001	2309 ±13	**2304 ±13**	170 ±1	**2240 ±13**
41	Es Quartó	**QUA**	**1**	510.3 ±1.0	346 ±7	715 ±15	78.1 ±1.6	0.0294 ±0.0001	3016 ±13	**2998 ±19**	79 ±2	**2934 ±19**
42	Es Quartó	**QUA**	**11**	276.7 ±0.6	800 ±16	218 ±5	139.7 ±1.7	0.0383 ±0.0003	3722 ±27	**3648 ±59**	141 ±2	**3584 ±59**
43	Es Quartó	SEAN	0.6	420.2 ±0.6	429 ±9	37 ±2	365.0 ±1.9	0.0023 ±0.0001	185 ±11	**163 ±19**	365 ±2	**97 ±19**
44	Es Quartó	**SEA**	**1.4**	364.8 ±0.5	1107 ±22	15 ±1	176.0 ±1.4	0.0027 ±0.0001	251 ±9	**176 ±54**	176 ±1	**112 ±54**
45	Es Quartó	SEAN	8.4	669.0 ±1.0	121 ±3	540 ±18	156.3 ±1.7	0.0059 ±0.0001	561 ±13	**557 ±13**	157 ±2	**491 ±13**
46	Es Quartó	SEAN	10	765.8 ±1.2	147 ±3	985 ±34	143.5 ±1.7	0.0114 ±0.0003	1096 ±29	**1091 ±29**	144 ±2	**1025 ±29**
47	Es Quartó	**SEA**	**11**	426.9 ±1.0	530 ±11	77 ±2	140.3 ±1.8	0.0058 ±0.0001	553 ±7	**521 ±24**	141 ±2	**457 ±24**

U decay constants: l_{238} = 1.55125x10^{-10} (Jaffey et al., 1971) and l_{234} = 2.82206x10^{-6} (Cheng et al., 2013). Th decay constant: l_{230} = 9.1705x10^{-6} (Cheng et al., 2013).

*$\delta^{234}U = ([^{234}U/^{238}U]_{activity} - 1)$x1000. ** $\delta^{234}U_{initial}$ was calculated based on ^{230}Th age (T), i.e., $\delta^{234}U_{initial} = \delta^{234}U_{measured} \times e^{l234xT}$.

Corrected ^{230}Th ages assume the initial $^{230}Th/^{232}Th$ atomic ratio of 4.4 ±2.2 x10^{-6}. Those are the values for a material at secular equilibrium, with the bulk earth $^{232}Th/^{238}U$ value of 3.8. The errors are arbitrarily assumed to be 50%.

***B.P. stands for "Before Present" where the "Present" is defined as the year 1950 A.D.

^{230}Th dating results. The error is 2σ error.

	Cave Name	Sample Name	Sample depth (cm)	^{238}U (ppb)	^{232}Th (ppt)	^{230}Th / ^{232}Th (atomic x10^{-6})	δ^{234}U* (measured)	^{230}Th / ^{238}U (activity)	^{230}Th Age (yr) (uncorrected)	^{230}Th Age (yr) (corrected)	$\delta^{234}U_{initial}$** (corrected)	^{230}Th Age (yr BP)*** (corrected)
1	Vallgornera	**VALL2**	0.2	1294.6 ±3.1	41 ±1	452066 ±15597	108.8 ±2.0	0.8697 ±0.0025	159998 ±1252	**159997 ±1252**	171 ±3	**159931 ±1252**
2	Vallgornera	**VALL2_Top**	1.8	342.8 ±0.6	12 ±0	485542 ±11926	39.1 ±1.7	1.0199 ±0.0030	377308 ±11561	**377304 ±11561**	113 ±6	**377242 ±11561**
3	Vallgornera	**VALL2**	4.3	289.3 ±0.4	28 ±1	170650 ±5044	32.0 ±1.5	1.0152 ±0.0018	392841 ±9902	**392835 ±9902**	97 ±5	**392769 ±9902**
4	Vallgornera	**VALL2**	5.5	334.2 ±0.5	4 ±1	1295999 ±278065	28.8 ±1.7	1.0207 ±0.0017	436721 ±15916	**436716 ±15915**	99 ±7	**436650 ±15915**
5	Vallgornera	**VALL2**	7	315.9 ±0.4	23 ±1	230927 ±13011	31.1 ±1.5	1.0199 ±0.0021	416922 ±13354	**416916 ±13353**	101 ±6	**416850 ±13353**
6	Vallgornera	**VALL2**	7.6	284.5 ±0.4	10 ±1	503033 ±40961	35.3 ±1.7	1.0281 ±0.0018	429141 ±14893	**429136 ±14893**	118 ±8	**429070 ±14893**
7	Vallgornera	**VALL2**	8.1	372.4 ±0.6	19 ±1	334429 ±20523	40.4 ±1.8	1.0395 ±0.0020	454126 ±19373	**454119 ±19372**	145 ±10	**454053 ±19372**
8	Vallgornera	**VALL2**	8.6	246.9 ±0.3	36 ±1	118137 ±4037	39.7 ±1.5	1.0416 ±0.0020	474894 ±21176	**474883 ±21175**	151 ±11	**474817 ±21175**
9	Vallgornera	**VALL2**	9	770.8 ±1.8	10 ±1	1321617 ±104976	31.0 ±2.0	1.0321 ±0.0026	494581 ±34732	**494572 ±34730**	125 ±15	**494506 ±34730**
10	Vallgornera	**VALL2**	12	811.2 ±2.3	56 ±2	247280 ±6969	25.4 ±2.6	1.0284 ±0.0033	540121 ±73096	**540107 ±73086**	117 ±28	**540041 ±73086**
11	Vallgornera	**VALL2**	15.6	211.6 ±0.2	24 ±1	148538 ±6320	25.4 ±1.5	1.0246 ±0.0019	495996 ±26282	**495984 ±26280**	103 ±10	**495918 ±26280**
12	Vallgornera	**VALL2**	18	335.5 ±0.4	29 ±1	194361 ±7398	25.1 ±1.5	1.0260 ±0.0020	514267 ±32267	**514255 ±32264**	107 ±12	**514189 ±32264**
13	Vallgornera	**VALL2_Bottom**	20.3	349 ±1	11 ±1	549205.7 ±32644.0	23.9 ±1.5	1.0251 ±0.0033	523624 ±48562	**523612 ±48557**	105 ±16	**523550 ±48557**
14	Vallgornera	**VALL3_Top**	1.3	179.6 ±0.2	36 ±1	55306 ±1168	98.3 ±1.6	0.6789 ±0.0017	102887 ±511	**102881 ±511**	131 ±2	**102819 ±511**
15	Vallgornera	**VALL3_7**	7	303.2 ±0.4	35 ±1	96869 ±3959	91.5 ±1.8	0.6770 ±0.0014	103602 ±466	**103599 ±466**	123 ±2	**103533 ±466**
16	Vallgornera	**VALL3_19**	9	311.1 ±0.3	36 ±2	103662 ±5170	131.4 ±1.6	0.7249 ±0.0013	108531 ±435	**108528 ±435**	179 ±2	**108462 ±435**
17	Vallgornera	**VALL3_Bottom**	22.8	278 ±0	47 ±1	70983.7 ±1472.4	119.4 ±1.8	0.7330 ±0.0023	112847 ±691	**112843 ±691**	164 ±2	**112781 ±691**
18	Vallgornera	**VALL4_Top**		425.1 ±1.5	29 ±1	248296 ±7479	27.9 ±3.0	1.0098 ±0.0039	393048 ±20743	**393042 ±20743**	85 ±10	**392976 ±20743**
19	Vallgornera	**VALL4_8.4**	8.4	414.4 ±0.7	59 ±2	118172 ±3082	31.2 ±1.7	1.0126 ±0.0023	387343 ±11065	**387336 ±11064**	93 ±6	**387270 ±11064**
20	Vallgornera	**VALL4_Bottom**		491.6 ±1.3	25 ±1	333060 ±10416	34.9 ±2.4	1.0143 ±0.0031	376661 ±13944	**376657 ±13943**	101 ±8	**376591 ±13943**
21	Vallgornera	**BEN Top**		476.1 ±1.0	1342 ±27	2279 ±46	111.4 ±2.0	0.3897 ±0.0013	46717 ±219	**46644 ±224**	127 ±2	**46580 ±224**
22	Vallgornera	**BEN_5,5**	5.5	206.9 ±1.3	325 ±7	9710 ±223	39.7 ±3.1	0.9258 ±0.0093	232604 ±8527	**232561 ±8523**	77 ±6	**232499 ±8523**
23	Vallgornera	**BEN Bottom**		1041.7 ±4.2	964 ±20	18414 ±384	25.0 ±2.4	1.0339 ±0.0060	688290 error	**688219 error**	174 error	**688155 error**
24	Vallgornera	**FAU**		196 ±1	131 ±3	1371.9 ±29.4	94.8 ±2.3	0.0556 ±0.0003	5674 ±39	**5657 ±41**	96 ±2	**5593 ±41**
25	Vallgornera	**FAU_19.2**	19.2	239.2 ±0.3	70 ±1	3791 ±80	100.2 ±1.6	0.0668 ±0.0003	6825 ±37	**6818 ±37**	102 ±2	**6756 ±37**
26	Vallgornera	**FIO_0,5**	0.5	355 ±1	42 ±1	107736.5 ±2670.0	97.1 ±1.6	0.7790 ±0.0024	131186 ±872	**131182 ±872**	141 ±2	**131120 ±872**
27	Vallgornera	**FIO_10**	10	360 ±1	75 ±2	75699.1 ±1552.9	61.2 ±1.8	0.9569 ±0.0032	238663 ±3239	**238657 ±3239**	120 ±4	**238595 ±3239**
28	Vallgornera	**FIO_2**	2	294 ±1	616 ±12	7542.2 ±154.1	61.3 ±1.7	0.9582 ±0.0034	239613 ±3428	**239558 ±3426**	121 ±3	**239496 ±3426**
29	Vallgornera	**LUC**		874 ±2	508 ±10	29184.5 ±592.8	24.9 ±1.6	1.0277 ±0.0033	539435 ±57216	**539407 ±57201**	114 ±20	**539343 ±57201**
30	Vallgornera	**LUL**		390.9 ±0.8	176 ±4	37229 ±766	25.1 ±1.9	1.0176 ±0.0031	447288 ±24834	**447270 ±24830**	89 ±9	**447206 ±24830**
31	Vallgornera	**MONtse Top**		858.4 ±2.5	177 ±4	83 ±5	101.8 ±2.1	0.0010 ±0.0001	103 ±5	**97 ±6**	102 ±2	**33 ±6**
32	Vallgornera	**MONtse ottom**		204.4 ±0.3	210 ±4	16349 ±333	21.0 ±1.7	1.0198 ±0.0024	509837 ±37361	**509799 ±37349**	88 ±12	**509735 ±37349**
33	Vallgornera	**NAB_Top**		178 ±0	70 ±2	1945.6 ±50.2	98.7 ±1.9	0.0465 ±0.0006	4713 ±59	**4703 ±60**	100 ±2	**4641 ±60**
34	Vallgornera	**NAB_Bottom**		159 ±0	64 ±1	2237.7 ±57.0	97.3 ±1.7	0.0544 ±0.0006	5537 ±65	**5526 ±65**	99 ±2	**5464 ±65**
35	Vallgornera	**NOR_0,5**	0.5	167.2 ±0.3	202 ±4	645 ±14	97.7 ±1.7	0.0472 ±0.0003	4786 ±32	**4754 ±39**	99 ±2	**4692 ±39**
36	Vallgornera	**NOR**		169 ±0	170 ±3	837.8 ±17.9	95.5 ±2.1	0.0510 ±0.0003	5200 ±35	**5174 ±40**	97 ±2	**5110 ±40**
37	Vallgornera	**VALL_Bocí**		279 ±1	348 ±7	13476.3 ±282.3	39.0 ±2.2	1.0203 ±0.0041	378682 ±16049	**378646 ±16044**	114 ±8	**378584 ±16044**
38	Vallgornera	**VALL1_Bottom**		259 ±0	71 ±1	58548.8 ±1201.1	75.8 ±1.8	0.9733 ±0.0029	238600 ±3017	**238592 ±3017**	149 ±4	**238530 ±3017**

U decay constants: $l_{238} = 1.55125 \times 10^{-10}$ (Jaffey et al., 1971) and $l_{234} = 2.82206 \times 10^{-6}$ (Cheng et al., 2013). Th decay constant: $l_{230} = 9.1705 \times 10^{-6}$ (Cheng et al., 2013).

*$\delta^{234}U = ([^{234}U/^{238}U]_{activity} - 1) \times 1000$. ** $\delta^{234}U_{initial}$ was calculated based on ^{230}Th age (T), i.e., $\delta^{234}U_{initial} = \delta^{234}U_{measured} \times e^{l_{234} \times T}$.

Corrected ^{230}Th ages assume the initial $^{230}Th/^{232}Th$ atomic ratio of 4.4 ±2.2 x10^{-6}. Those are the values for a material at secular equilibrium, with the bulk earth $^{232}Th/^{238}U$ value of 3.8. The errors are arbitrarily assumed to be 50%.

***B.P. stands for "Before Present" where the "Present" is defined as the year 1950 A.D.

Annex 7

Core name	Control depths (cm)	Control ages (kyr BP)	sample spacing (-kyr)	sample spacing (+kyr)	Stratigraphic correlation reference	ref. sample spacing (-ky)	ref. sample spacing (+ky)	Uncertainty of reference chronology (1σ [kyr])	Age Uncertainty MSE - 1σ (kyr)	Age Uncertainty MSE + 1σ (kyr)
PP10-17	1303	67.70	0.11	0.11	GICC05modelex NGRIP2	0.05	0.05		1.16	1.16
PP10-17	1335	69.50	0.11	0.11	GICC05modelex NGRIP2	0.05	0.05		1.16	1.16
PP10-17	1375	72.00	0.13	0.31	GICC05modelex NGRIP2	0.05	0.05		1.18	1.36
PP10-17	1403	76.30	0.61	0.24	GICC05modelex NGRIP2	0.05	0.05		1.66	1.29
PP10-17	1417	77.95	0.24	0.27	GICC05modelex NGRIP2	0.05	0.05		1.29	1.32
PP10-17	1467	84.60	0.27	0.19	GICC05modelex NGRIP2	0.05	0.05	neglected	1.32	1.24
PP10-17	1499	87.65	0.19	0.30	GICC05modelex NGRIP2	0.05	0.05		1.24	1.35
PP10-17	1609	103.90	0.30	0.19	GICC05modelex NGRIP2	0.05	0.05		1.35	1.24
PP10-17	1629	105.80	0.19	0.28	GICC05modelex NGRIP2	0.05	0.05		1.24	1.33
PP10-17	1645	108.05	0.28	0.33	GICC05modelex NGRIP2	0.05	0.05		1.33	1.38
PP10-17	1661	110.65	0.33	0.32	GICC05modelex NGRIP2	0.05	0.05		1.38	1.37
PP10-17	1713	119.08	0.65	0.21	ODP 975	0.30	0.30	1.65	2.19	1.93
PP10-17	1735	121.34	0.10	0.30	ODP 975	0.66	0.69	1.73	2.14	2.29
PP10-17	1775	127.40	0.30	0.36	ODP 975	0.14	0.58	1.30	1.61	1.94
PP10-17	1783	128.85	0.36	0.85	ODP 975	0.09	0.18	1.20	1.53	1.95
PP10-17	1791	132.26	0.85	0.85	ODP 975	0.09	0.09	1.17	1.86	1.86
ODP977A	1335.6	69.50	0.43	0.14	GICC05modelex NGRIP2	0.05	0.05		1.48	1.19
ODP977A	1387.6	72.00	0.27	0.10	GICC05modelex NGRIP2	0.05	0.05		1.32	1.15
ODP977A	1542.6	76.30	0.13	0.08	GICC05modelex NGRIP2	0.05	0.05		1.18	1.13
ODP977A	1637.5	77.95	0.18	0.16	GICC05modelex NGRIP2	0.05	0.05		1.23	1.21
ODP977A	1796.3	84.60	0.39	0.18	GICC05modelex NGRIP2	0.05	0.05		1.44	1.23
ODP977A	1956.1	87.65	0.13	1.59	GICC05modelex NGRIP2	0.05	0.05	neglected	1.18	2.64
ODP977A	2004.0	103.90	1.91	0.16	GICC05modelex NGRIP2	0.05	0.05		2.96	1.21
ODP977A	2060.4	105.80	0.16	0.26	GICC05modelex NGRIP2	0.05	0.05		1.21	1.31
ODP977A	2092.3	108.05	0.33	0.37	GICC05modelex NGRIP2	0.05	0.05		1.38	1.42
ODP977A	2125.2	110.65	0.37	0.30	GICC05modelex NGRIP2	0.05	0.05		1.42	1.35
ODP977A	2181.6	115.17	0.38	0.65	ODP 975	0.30	0.30	1.52	1.92	2.10
ODP977A	2209.8	119.08	0.65	0.29	ODP 975	0.30	0.30	1.65	2.20	1.98
ODP977A	2301.0	124.71	0.81	0.51	ODP 975	0.11	0.14	1.46	2.04	1.86
ODP977A	2386.1	128.85	0.23	0.36	ODP 975	0.09	0.18	1.20	1.45	1.59
ODP977A	2424.4	131.70	0.36	0.31	ODP 975	0.09	0.09	1.17	1.51	1.48
ODP977A	2467.4	134.50	0.37	0.39	ODP 975	0.09	0.09	0.57	1.12	1.14
ODP977A	2532.5	139.81	0.23	0.29	ODP 975	0.06	0.06	1.35	1.57	1.60
ODP977A	2577.4	142.07	0.24	0.09	ODP 976	0.14	0.13		1.38	1.22
ODP977A	2937.2	149.01	0.11	0.11	ODP 976	0.16	0.08		1.27	1.19
MD99-2343	2020	63.80	0.43	0.43	GICC05modelex NGRIP2	0.05	0.05		1.48	1.48
MD99-2343	2154	69.50	0.43	0.44	GICC05modelex NGRIP2	0.05	0.05		1.48	1.49
MD99-2343	2210	72.00	0.45	0.67	GICC05modelex NGRIP2	0.05	0.05		1.50	1.72
MD99-2343	2274	76.30	0.67	0.38	GICC05modelex NGRIP2	0.05	0.05		1.72	1.43
MD99-2343	2360	77.95	0.19	0.60	GICC05modelex NGRIP2	0.05	0.05		1.24	1.65
MD99-2343	2470	84.60	0.60	0.20	GICC05modelex NGRIP2	0.05	0.05	neglected	1.65	1.25
MD99-2343	2594	87.65	0.25	0.42	GICC05modelex NGRIP2	0.05	0.05		1.30	1.47
MD99-2343	2834	103.90	0.68	0.44	GICC05modelex NGRIP2	0.05	0.05		1.73	1.49
MD99-2343	2900	105.80	0.29	0.45	GICC05modelex NGRIP2	0.05	0.05		1.34	1.50
MD99-2343	2950	108.05	0.45	0.23	GICC05modelex NGRIP2	0.05	0.05		1.50	1.28
MD99-2343	3064	110.65	0.23	0.45	GICC05modelex NGRIP2	0.05	0.05		1.28	1.50
MD99-2343	3140	115.17	0.59	0.59	ODP 975	0.30	0.30	1.52	2.06	2.06

*B.P. stands for “Before Present” where the “Present” is defined as the year 1950 A.D.

Annex 8

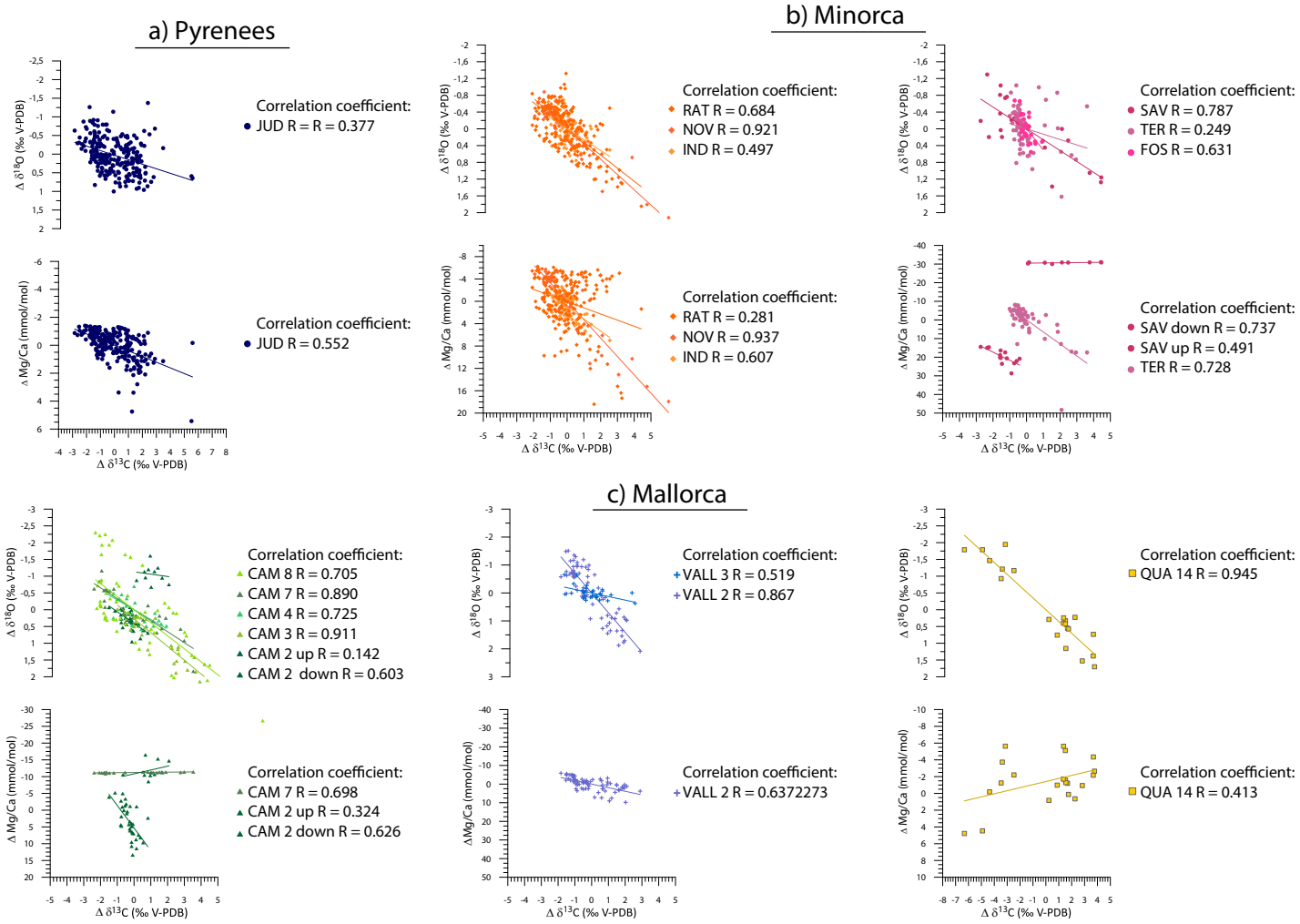

Correlation coefficients

Speleothem	$\delta^{18}O$ vs $\delta^{13}C$	Mg/Ca vs δ13C
JUD	0.377	**0.552**
IND	0.497	**0.607**
NOV	0.921	0.937
RAT	**0.684**	0.281
SAV	0.787	0.737
TER	0.249	**0.728**
FOS	0.631	
VALL 3	0.519	
VALL 2	**0.867**	0.637
CAM 2	0.603	0.626
CAM 3	0.911	
CAM 4	0.725	
CAM 7	**0.890**	0.698
CAM 8	0.705	
QUA 14	**0.945**	0.413

Annex 9

Published paper:
Torner *et al*., 2019

Ocean-atmosphere interconections from the last interglacial to the early glacial:
An integration of marine nd cave records in the Iberian region

Quaternary Science Reviews 226 (2019) 106037

Contents lists available at ScienceDirect

Quaternary Science Reviews

journal homepage: www.elsevier.com/locate/quascirev

Ocean-atmosphere interconnections from the last interglacial to the early glacial: An integration of marine and cave records in the Iberian region

Judit Torner [a, *], Isabel Cacho [a], Ana Moreno [b], Francisco J. Sierro [c], Belen Martrat [d], Julio Rodriguez-Lazaro [e], Jaime Frigola [a], Pedro Arnau [f], Ánchel Belmonte [g], John Hellstrom [h], Hai Cheng [i], R. Lawrence Edwards [i], Heather Stoll [j]

[a] Grup de Recerca Consolidat en Geociéncies Marines, Universitat de Barcelona, Barcelona, Spain
[b] Pyrenean Institute of Ecology, CSIC, Zaragoza, Spain
[c] RG of Oceanic Geosciences, Dept. of Geology, University of Salamanca, Salamanca, Spain
[d] Dept. of Env. Chemistry, Inst. of Env. Assessment and Water Research (IDAEA-CSIC), Barcelona, Spain
[e] Dept. of Stratigraphy and Paleontology, University of Basque Country UPV/EHU, Leioa, Spain
[f] Municipal Museum of Ciutadella, Ciutadella Town Hall, Menorca, Spain
[g] Dept. of Geosciences, University of Zaragoza, Zaragoza, Spain
[h] School of Earth Science, University of Melbourne, Melbourne, VIC, 3010, Australia
[i] Dept. of Geology and Geophysics, University of Minnesota, MN, 55455, USA
[j] Earth Science Department, ETH Zürich, Zurich, Switzerland

ARTICLE INFO

Article history:
Received 17 May 2019
Received in revised form
22 October 2019
Accepted 23 October 2019
Available online 6 November 2019

Keywords:
Interglacials
Western Europe
Speleothems
Sedimentology-marine cores

ABSTRACT

This study explores the climatic variability in the Iberian Peninsula (IP) and its surrounding seas from 140 to 65 kyr BP. Marine sediment cores and cave speleothems are used to reconstruct changes in sea surface water conditions, deep sea current intensities and atmospheric moisture availability based on stable isotopes, trace elements, grain size and XRF-elemental analysis. Oxygen isotopes in both terrestrial and oceanic archives recorded a large-scale precessional climatic rhythm that suggests a common modulation. This signal is interpreted as changes of the isotopic composition in the rainwater source area that is later transmitted into the cave. In terms of millennial-scale variability, the records trace the sequence of events defined for the North Atlantic region. The marine records show an intense sea-surface freshening and cooling related to Heinrich Event 11. During the Last Interglacial (LIG), the sea surface temperature evolution was heterogeneous around the IP with gradients larger than those from today. The LIG ended earlier in the Cantabrian Sea than in the western Mediterranean Sea, which it was coincident with an accelerated aridification phase that marked the glacial inception in a Minorca speleothem at 116.5 kyr BP and preceding the GS25. This was the first of a series of stadials that punctuated the early glaciation and where the sea thermal gradient almost disappeared around the IP. These intense cooling during stadials led the development of drier but intense westerlies over southern European latitudes, reflected in a Pyrenees speleothem record, and favouring enhanced deep convection in the western Mediterranean Sea. In contrast to this stadial regional homogeneity among the studied records, the interstadials periods are distinguished by their rather heterogeneous patterns around the IP pointing to much complex ocean-atmosphere interconnections during warm intervals.

1. Introduction

The study of past warm periods brings the opportunity to better understand the range of natural climate variability without anthropogenic interference (PAGES, P.I.W.G. of P., 2016; Tzedakis et al., 2009). Particularly, the Last Interglacial period (LIG)

* Corresponding author.
E-mail address: j.torner@ub.edu (J. Torner).

https://doi.org/10.1016/j.quascirev.2019.106037
0277-3791/

although it is not the closest analogue to the Holocene in terms of astronomical configuration (Tzedakis et al., 2012, 2009), it is an important focus of ongoing research due to the good preservation of geological records, which show higher temperatures, less ice sheet extent and higher sea level than present day (Bardají et al., 2009; Dutton and Lambeck, 2012; Martrat et al., 2014). Under the ongoing climate change context (IPCC, 2013), where we are experimenting worldwide climate and environmental changes, the last interglacial period becomes a valued climatic scenario to improve our understanding of the climate system operation in a warmer Earth.

Moreover, glacial inceptions and early glacial periods have often received less attention than glacial terminations and interglacial periods, although they are often associated with large-scale but also rapid climatic changes (Dorale et al., 2010; Drysdale et al., 2007). The glacial inception was driven by reduced NH summer insolation in polar and subpolar regions. Even though two maxima in NH summer insolation during the early glacial there was sufficient ice-sheet build up to back to full glacial conditions (PAGES, P.I.W.G. of P., 2016). The interaction of orbital and millennial scale changes that led the planet to enter into a new glacial state is not yet fully understood and is key in determining glacial sequence of events (Drysdale et al., 2007; Tzedakis et al., 2009). This study cover both large-scale and rapid climatic changes from 140 to 65 kyr BP, spanning the Marine Isotopic Stage 5 (MIS 5) entirely and tracing the penultimate deglaciation (MIS 6/5e transition), the LIG-acme and the glacial inception (MIS 5e), and the early glacial period (MIS 5d- MIS 4).

The Iberian Peninsula (IP) is a strategic geographical area to evaluate tele-connections between the North Atlantic and the Mediterranean regions and, subsequently, its climate systems. By one hand, several paleo-oceanographic studies have already proved the strong impact of past Atlantic Meridional Overturning Circulation (AMOC) changes into the IP climatology, although they have focussed very little attention to this specific interglacial-glacial transition (ie. Cacho et al., 2006, 2001, 1999; Frigola et al., 2008, 2007; Jiménez-Amat and Zahn, 2015; Martrat et al., 2015, 2014, 2007, 2004,; Moreno et al., 2005; Rodríguez-Sanz et al., 2017; Sierro et al., 2005). On the other hand, speleothems are proven to be key archives to reconstruct changes in hydrology, air temperature, vegetation response or even atmospheric circulation conditions (Fairchild and Baker, 2012; McDermott, 2004). Several European speleothem records previously studied highlight enhanced moisture availability during the LIG-acme and show regional heterogeneity in the hydrological patterns during the glacial inception in concert with AMOC changes (Bar-Matthews et al., 2000; Couchoud et al., 2009; Demény et al., 2017; Drysdale et al., 2005, 2007; Meyer et al., 2008; Moseley et al., 2015; Vansteenberge et al., 2016). The available IP speleothem information covering the MIS 5 is limited to a stacked-speleothem reconstruction from the north-western region, which recorded changes in water source properties at orbital scale variability (Stoll et al., 2015) and to a low-resolution record from southern IP that shows increased effective precipitation during the MIS 5 (Hodge et al., 2008a). Moreover, two speleothem records from Mallorca Island, in the Balearic Sea, span partially the MIS 5 and highlight dry periods within warm interstadials (Dumitru et al., 2018; Hodge et al., 2008b). An additional value of the speleothem records is their suitability to obtain independent absolute chronologies with U/Th series at high resolution (Cheng et al., 2009; Fairchild and Baker, 2012) that allow testing the assumptions from the marine realm in a more accurate chronological framework.

This study aims to characterise atmospheric changes in relation to the parallel evolution of the oceanic conditions, integrating terrestrial (speleothem) and marine (sediments) archives for the first time in the Iberian region. Atmospheric changes in humidity are reconstructed by means of stable isotopes and Mg/Ca analysis in two new speleothem records: *Indiana* (IND) recovered from Murada cave, in the Minorca Island, which is one of the most southern speleothems records available in Europe for the last interglacial period; and *Judit* (JUD), which grew during the early glacial in the central southern Pyrenees into the *Pot au Feu* cave.

Marine Sea Surface Temperatures (SST) and major changes in the precipitation/evaporation ratio are reconstructed in base to the pair analyses of $\delta^{18}O$ and the Mg/Ca ratios measured in carbonate shells of the planktonic foraminifera *Globigerina bulloides* in three areas surrounding the IP: the Cantabrian Sea (core PP10-17), the Alboran Sea (Site ODP-977A) and the Balearic Sea (core MD99-2343). In addition, changes in the intensity of deep western Mediterranean currents are explored by means of grain size distribution and XRF-geochemical ratios measured in the Balearic core (MD99-2343).

2. Studied areas and material

2.1. Current oceanographic and climatic conditions

The Cantabrian Sea is located north of the IP at the southern part of the Bay of Biscay, which opens westward to the North Atlantic Ocean. The surface water mass in the Cantabrian Sea is characterized by the Eastern North Atlantic Central Water (ENACW), which is the result of winter mixing of surface waters from the northeast Azores to the European margin, mainly driven to this location by the North Atlantic Current (NAC) via the subtropical gyre (STG). The importance of the NAC current remains on its northward heat and salt transport into the Nordic Sea, where deep-water formation occurs (McCartney and Mauritzen, 2001). Expansions and contractions of the subtropical and the subpolar gyres control the NAC heat and salinity supply to high latitudes, finally related with AMOC dynamics (Mary et al., 2017; Pérez-Brunius et al., 2004). Other seasonal-nature current flows eastward along the IP shelf into the Cantabrian Sea, named the Iberian Poleward Current (IPC) (Pingree and Le Cann, 1990). Variations in the regional seasonal salinity, and therefore density of the IPC are produced by freshwater runoff from Spanish and French rivers (Ferrer et al., 2009) (Fig. 1).

The Mediterranean is a semi-enclosed sea where freshwater inputs, as rainfall and fluvial discharge, are exceeded by evaporation leading to a high salinity basin. The western Mediterranean circulation is mostly determined by three major water masses: surface, intermediate and deep (Lionello, 2012; Rohling et al., 2009). Less saline water enters at surface through the Strait of Gibraltar to compensate the negative water balance caused by excessive evaporation in the Mediterranean. This surface water mass flow eastward while progressively increases its salinity and temperature creating the Modified Atlantic Water (MAW) (Pastor et al., 2017; Pierre, 1999; Pinardi and Masetti, 2000; Vargas-Yáñez et al., 2017). The Mediterranean Intermediate Water (MIW) spreads westwards, while mixing with regional waters, to finally outflow through the Strait of Gibraltar (Pinardi and Masetti, 2000). The deepest water mass in the western basin is the Western Mediterranean Deep Water (WMDW) (Millot, 1999). During winters, the north and northwestern winds cause strong cooling and evaporation of surface waters in the Gulf of Lion, increasing its density, and consequently mixing and sinking it into the deep basin. Therefore, the density of this deep-water mass is determined by the temperature and salinity of both the local surface water and the MIW, and also the wind features (Millot, 1999; Rohling et al., 2009). The WMDW flows southwards collecting the continental

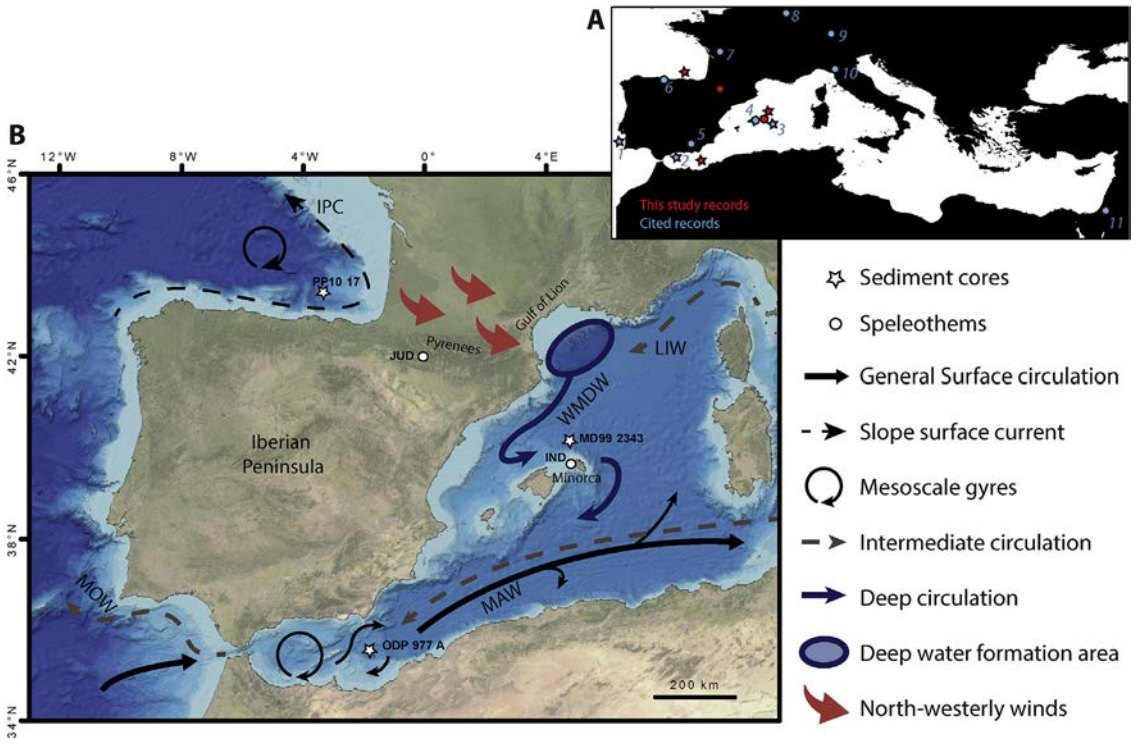

Fig. 1. A) Schematic European map showing the location of this study sites (red) and several discussed sites (blue): 1) MD01-2444 core (Tzedakis et al., 2018), 2) ODP Site 976 (Jiménez-Amat and Zahn, 2015), 3) ODP site 975 (Marino et al., 2015) 4) Campanet cave (Dumitru et al., 2018) and Cala Falcó cave (Hodge et al., 2008b), 5) Gitana cave (Hodge et al., 2008a), 6) Cantabrian caves (Stoll et al., 2015), 7) Villars cave (Genty et al., 2003), 8) Han-sur-Lesse cave (Vansteenberge et al., 2016), 9) Alps caves (Moseley et al., 2015), 10) Corchia cave (Drysdale et al., 2007; Tzedakis et al., 2018) and 11) Soreq cave (Bar-Matthews et al., 2000, 2003). B) Bathymetric map of the studied area showing this study records and the main circulation patterns: North Atlantic Current (NAC); Iberian Poleward current (IPC); Mediterranean Outflow Water (MOW); Levantine Intermediate Water (LIW); Modified Atlantic Water (MAW); West Mediterranean Deep Water (WMDW). (For interpretation of the references to colour in this figure legend, the reader is referred to the Web version of this article.)

sediment discharges, mainly from the Rhone and Ebro rivers, and depositing approximately the 10% of them in the deep basin (Martin et al., 1989). In the Balearic Promontory, the current associated to the WMDW accelerates and induces a re-working, transport and classification of the sediment particles (Cisneros et al., 2019; Frigola et al., 2008; Millot, 1999; Velasco et al., 1996) (Fig. 1).

The studied speleothems were collected in two caves, one from the Minorca Island and the other from the central southern Pyrenees. Minorca is the northern Balearic Island. It has a temperate climate classified according to Köppen as Mediterranean climate with seasonal rainfall, intense storms in autumn and dry summers causing the lack of permanent watercourses. The annual rainfall average is around 500–600 mm and the annual mean temperature is 16–17 °C (AEMET-IM, 2011). The studied Pyrenees area also corresponds to a Mediterranean climate zone. However, the relief influences the climate of this high-altitude area, which can be accurately described as a humid sub-Mediterranean climate. The annual rainfall is around 1000–1200 mm and it occurs mostly as snow. The annual mean temperature is 4–5 °C (AEMET-IM, 2011). Nowadays, the main source areas of moisture that affect the IP and the Balearic Islands are the tropical–subtropical North Atlantic corridor, the IP itself and the Mediterranean Sea (Krklec and Domínguez-Villar, 2014; Nieto et al., 2010 and Gimeno et al., 2010). The eastern IP region is more dominated by Mediterranean moisture source than the Atlantic one (Dumitru et al., 2017; Gimeno et al., 2010).

2.2. Sediment cores

Sediment core PP10-17 was collected in 2010 during SARGASS oceanographic cruise on board *R/V Pourquoi Pas?* from the Cantabrian Sea in the SW Landes Plateau of the Bay of Biscay (43° 58.91′ N; 03°14.02′ W; 2880 m b.s.l.) (Fig. 1B). The lithology of the sediment in the studied sections was olive grey silty clay, continuously deposited with bioturbation from a hemipelagic environment (Brocheray et al., 2014). ODP Site 977A was retrieved on June 1995 during LEG 161 of the Ocean Drilling Program (ODP) on board *JOIDES Resolution*. It was located at south of Cabo de Gata in the Eastern Alboran Sea and its facies represents an open-marine hemipelagic environment (36°01.92′N; 1°57.32′W; 1984 m b.s.l.) (Fig. 1B). The dominant lithology was olive grey clay with nannofossil to nannofossil-rich silty clay moderately bioturbated with the presence of organic-rich layers (ORLs) (Comas et al., 1996). Sediment core MD99-2343 was collected in summer 1999 during LEG 5 of the International Marine Past Global Changes Study program (IMAGES) on board *R/V Marion-Dufresne*. This core was located NE of Minorca Island, in the Balearic Sea (40°29.84′ N; 04°01.69′ E; 2391 m b.s.l.) (Fig. 1B). In particular, it was obtained from the N-NE Minorca peripheral sedimentary contouritic drift, genetically related to the southward flow of the WMDW (Velasco et al., 1996). The studied sections were mostly composed by nannofossils and foraminifera rich greyish and brownish silty clay materials, moderately laminated and bioturbated, with presence of fine levels of pyrite.

2.3. Speleothems

The inactive JUD stalagmite was collected from *Pot au Feu* cave, located on the Irués river valley at the Cotiella massif, southern Central Pyrenees (42°31.48′ N; 0°14.26′ W; 997 m a.s.l.) in

collaboration with the Scientific Speleological Association of Cotiella (ACEC) (Fig. 1B). The host rock is upper Turonian to lower Coniacian packstone with miliolids (López-Mir, 2013). Hydrogeologically the cave belongs to the high mountain free karst aquifer Cotiella-Turbón even though it is a fossil level. JUD has internal banded structure with white-grey crystalline calcite alternated with brown-orange detrital enriched layers and a growth axis of 55 cm length.

The inactive IND stalagmite was collected in November 2011 during the HIDROPAST campaign from Murada cave, southwest Minorca Island (39°57.36 N; 3°57.89' W; 80 m a.s.l.) (Fig. 1B). The host rock consists of Miocene calcarenites that are deeply karstified forming a porous mixed aquifer, where this cave represents a fossil level of karst drainage conduit. IND presents an internal banded structure with white-grey crystalline calcite and its growth axis has 88 cm length.

3. Methods

3.1. Oxygen isotope ($\delta^{18}O$) in foraminifera

Ideally, 8 specimens of the planktonic foraminifera *G. bulloides* were handpicked from a size range of 250–355 μm and sonically cleaned in methanol after shell crushing in order to remove fine sedimentary particles. After few seconds, the supernatant solution was removed and the crushed carbonate shells were dried. A total of 219 and 212 $\delta^{18}O$ measurements were carried out for cores PP10-17 (2 cm resolution) and MD99-2343 (4 cm resolution) respectively. The measurements were accomplished on an IRMS Finnigan-MAT 252 coupled to a CarboKiel-II at the scientific and Technological Centers of University of Barcelona (CCiT-UB). Analytical uncertainties were obtained by means of an in-house carbonate standard, which is calibrated to NBS-19 international standard (Coplen, 1996), and were 0.08‰ VPDB. ODP Site 977A was analysed in a previous study by (Martrat et al., 2004) and it is used here for the estimation of the $\delta^{18}O$ seawater isotopic signal.

3.2. Mg/Ca ratios in foraminifera

Mg/Ca ratios were measured over 40–50 specimens of *G. bulloides* handpicked from a size range of 250–355 μm. Carbonate shells were carefully crushed between two glass plates in order to open the chambers and favour chemical cleaning protocol before the analyses. Samples destined to Mg/Ca analyses were cleaned by means of a full chemical cleaning procedure based on the last modifications on trace elements cleaning protocols developed by Barker et al. (2003) and Pena et al. (2005). The protocol consists on a clay removal first step; a reductive reagent attack to remove potential Mn–Fe oxide contaminant phases; an organic matter attack and finally a weak acid leaching before the dissolution in 3 ml of ultra-pure 1% HNO_3. The reductive attack step was only performed on ODP Site 977A. This cleaning step dissolves preferably Mg rich calcite and consequently the Mg/Ca ratios become lower. Previous studies have demonstrated that Mg/Ca ratios of the reductively cleaned samples are systematically lowered by about 10–15% (Barker et al., 2003, 2005; Yu et al., 2007). Accordingly with these observations, the Mg/Ca ratios estimated in ODP Site 977A samples were corrected with an increase of 15% as it is suggested by Barker et al. (2003). A total of 216, 116 and 163 Mg/Ca ratios have been measured for cores PP10-17 (2 cm resolution), MD99-2343 (10 cm resolution) and ODP Site 977A (5 cm resolution) respectively. Additionally, possible contamination during the laboratory process was controlled by the performance of chemistry blanks in random days. All the samples were analysed with an ICP-MS PerkinElmer model Elan-6000 at the CCiT-UB. An in-house high purity standard solution was used and all data was corrected using a sample-standard bracketing method. The external reproducibility (%, 2-sigma) was 6.59% for core PP10-17, 5.7% for ODP Site 977A and 3.21% for MD99-2343.

Moreover, in order to identify potential contaminated samples and avoid overestimated Mg/Ca–SST, Al/Ca and Mn/Ca ratios were also measured controlling thus the presence of manganese oxides and/or aluminosilicate (Barker et al., 2003; Lea et al., 2005; Pena et al., 2008, 2005). Few samples were discarded according to values above 2σ of each ratio (ODP site 977A: $Mn/Ca \geq 0.41$ and $Al/Ca \geq 0.46$; MD99-2343: $Mn/Ca \geq 0.82$ and $Al/Ca \geq 0.32$; PP10-17: $Mn/Ca \geq 0.49$ and $Al/Ca \geq 0.33$). Furthermore, no co-variations of Al/Ca and Mn/Ca with Mg/Ca ratios were found.

3.3. Grain-size distribution of marine sediments

New grain-size distribution of terrigenous-sourced particles was measured on the Balearic sediment core (MD99-2343) at 10 cm resolution expanding the core record of Frigola et al. (2007) and using the same methodology. Previous to the instrumental measurements, organic matter and carbonates were removed by treatment with excess H_2O_2 and HCl respectively in order to obtain grain-size distribution of the non-carbonate fraction. Samples were analysed with a Coulter LS 230 Laser Particle Size Analyser at the Sedimentology Laboratory of the University of Barcelona. The precision and accuracy were tested performing several control runs using the LS size control G15, which gave a coefficient of variation of 0.03%.

3.4. Elemental composition of marine sediments

Variations in elemental composition of sediments were also determined only in the Balearic sediment core by means of X-Ray Fluorescence analysis using an Avaatech III Core Scanner system (Serial No. 21) at the CORELAB laboratory of the University of Barcelona. This method is advantageous over discrete conventional geochemical methods because it allows rapid, non-destructive and high-resolution analysis of long sediment sequences (Richter et al., 2006; Rothwell and Rack, 2006). The scan was performed on the surface of the split core (at 10 mm resolution) that was previously smoothed to remove irregularities and roughness. Sediment surface was covered with a 4 μm-thick Ultralene film with the aim of 1) eliminating air contact between sediment and the analyser prism, 2) prevents possible contamination and 3) avoid desiccation of sediments (Richter et al., 2006; Tjallingii et al., 2007). Several elements were measured in three separate runs using voltages of 10 KV, 30 KV (Pd-thick filter) and 50 kV (Cu filter), currents of 0.5 mA, 2.0 mA and 2.0 mA, and excitation times of 10 s, 25 s and 35 s respectively. Raw data were processed by the analysis of X-ray spectra by Iterative Least square software (WIN AXIL) package from Canberra Eurisys. In order to reduce signal artefacts related to lithological changes and water content, elemental raw data (cts) was normalized with Al and it is here presented as log-ratios, which account for more robust representation of the element ratios (Weltie and Tiallingii, 2008).

3.5. $^{230}Th/^{234}U$ dating on speleothems

Twenty-four samples were selected for dating taking into account the speleothem layering and morphology, which were milled with 2 mm diameter tungsten carbide micro-drill. In order to acquire preliminary speleothem ages some of the Pyrenean speleothem samples were firstly analysed at the School of Earth Sciences at the University of Melbourne using the technique described by

Hellstrom (2003). The other ages were acquired at the University of Minnesota applying the methodology previously described by (Cheng et al., 2009; Shen et al., 2002). To summarize, carbonate powders samples (100–200 mg) were dissolved in HNO_3 and spiked with an in-house solution with known ^{233}U, ^{236}U and ^{229}Th concentrations. After that, U and Th were isolated from Ca and several trace elements by means of an iron co-precipitation and finally in order to separate U from Th, the samples were loaded in anion exchange resin columns. Several blanks were performed routinely for each laboratory set. All pair of U and Th samples were analysed using a *Neptune* MC-ICP-MS (parallel ion-counting multi collector inductively coupled plasma mass spectrometry).

3.6. Stable isotopes on speleothems

Stable isotopes ($\delta^{18}O$ and $\delta^{13}C$) were measured on 90 and 232 samples drilled from the Minorca and Pyrenees speleothems respectively using a 0.5 mm diameter tungsten carbide dental bur. Around 50 μg of carbonate was sampled at 1 cm resolution on the Minorca speleothem and at 0.25 cm resolution on the Pyrenees speleothem. The top 7 cm of this last speleothem were sampled at 0.125 cm and thus, doubling the resolution. The $\delta^{18}O$ and $\delta^{13}C$ measurements were accomplished on an IRMS (isotope-ratio mass spectrometry) with a Finnigan-MAT 252 mass spectrometer, coupled to a single acid bath CarboKiel-III carbonate preparation device at the Scientific and Technological Centres of the University of Barcelona (CCiT-UB). Analytical uncertainties were obtained by means of an in-house carbonate standard that is calibrated to NBS-19 international standard (Coplen, 1996). The uncertainties were $\leq$0.04‰ VPDB for $\delta^{13}C$ and 0.08‰ VPDB for $\delta^{18}O$.

3.7. Mg/Ca ratios on speleothems

Mg/Ca ratios measurements were carried out on the same sample depths as isotopes analyses on the Pyrenees speleothem, but doubling the isotopes resolution in the Minorca one (180 samples every 0.5 cm). Around 3 mg of carbonate were directly dissolved in 3 ml of ultra-pure 1% HNO3 and centrifuged before the analyses in order to prevent possible lithic or impurities in the solution. Possible contamination was also controlled by means of chemistry blanks in random days. All the samples were analysed with a spectrometer PerkinElmer model Elan-6000 at CCiT-UB. Such as the marine core analysis, an in-house high purity standard solution was measured routinely every four samples to control the accuracy and correct the instrumental drift. Therefore, all calculated ratios were corrected using the SSB method. According to the in-house standard analysis the external reproducibility (%, 2-sigma) obtained among all the analyses was 11.01% for IND and 10.62% for JUD.

4. Results

4.1. Chronology of the marine records

The sequence of marine isotope stages/sub-stages (MISs) and also Greenland Stadials can be well identified in the $\delta^{18}O_{G.bulloides}$ records of the three studied cores, which in addition show an extraordinary resemblance among them (Fig. 2). The age model of ODP Site 977A and PP10-17 are mostly based on previous published chronologies (Martrat et al., 2007; Brocheray et al., 2014 and Rodriguez-Lazaro et al., 2017) with the addition of some tie points for coherence between the three studied records. These additional tie points were assessed on the basis of the alignment of the SST and the $\delta^{18}O_{G.bulloides}$ records with: 1) the Greenland ice core record for the MIS 5 and 4 period using the $\delta^{18}O$ NGRIP2 50 yrs means on the GICC05modelext timescale record (Rasmussen et al., 2014; Seierstad et al., 2014) (Fig. 2A); 2) the $\delta^{18}O_{G.bulloides}$ record from ODP Site 975 to constrain the penultimate deglaciation and the MIS5e (Marino et al., 2015) (Fig. 2B); and 3) the $\delta^{18}O_{G.bulloides}$ record from ODP Site 976 to anchor the oldest part of the age model (Jiménez-Amat and Zahn, 2015) (Fig. 2C). The ODP Site 975 chronology is based in the alignment with an eastern Mediterranean core previously tuned to the radiometrically chronology of the Soreq record, while the ODP 976 site age model was also correlated with speleothem records from European caves (Drysdale et al., 2009; Couchoud et al., 2009), thus both marine records are independent of orbital tuning. Furthermore, the age model of core MD99-2343 was produced in this study by alignment of its $\delta^{18}O_{G.bulloides}$ record with the NGRIP2 record (Rasmussen et al., 2014; Seierstad et al., 2014). Although the potential uncertainties associated with the correlation of SST and $\delta^{18}O_{G.bulloides}$ with the NGRIP2 record due to the effect of light melt water into the surface waters, the alignment was performed since several studies have shown the suitability of the use of the $\delta^{18}O$ ice cores record from Greenland as an isotopic chronostratigraphic reference for age modelling not only for Mediterranean cores (Cacho et al., 1999; Martrat et al., 2007; Rohling et al., 1998; Sierro et al., 2005; Sprovieri et al., 2006) but also for N Atlantic sites (Cayre et al., 1999; Govin et al., 2015). Moreover, cold stadial events were well characterized by the presence of *N. Pachyderma sin*. in the PP10-17 core by Rodriguez-Lazaro et al. (2017), increasing the confidence of the alignment of the Cantabrian core with the Greenland record. In summary, 54 tie points have been used for the tuning of all three sediment records in base of the most relevant structures, particularly for the penultimate deglaciation and the Greenland Stadials (GS) (Table S1). Correlations among the marine records were estimated by linear interpolation using the Analyseries Software package (Paillard et al., 1996). The relative age uncertainties were estimated for every performed alignment following the approach used by Grant et al. (2012) and consisting in the propagation of involved uncertainties by means of the mean squared estimate (MSE) (Table S1). These chronological uncertainties include the reference record age uncertainties (only provided in the case of the ODP 975), the sample spacing from the aligned and reference records and an extra-imposed uncertainty. The extra uncertainty depends of the level of the alignments confidence and consists in this study in the addition of ±0.5 kyr for those alignments whose reference age uncertainty is provided (ODP 975) and ±1 kyr for those where the reference age uncertainties are not provided (NGRIP and ODP976). The obtained age models indicate that PP10-17 samples used in this study spans from 132 to 68 kyr BP, therefore it starts recording the middle of the penultimate deglaciation (Fig. 2D), whereas ODP Site 977A samples exceeds the studied period, from the end of the MIS 6 until the beginning of the MIS 4 (Fig. 2E). MD99-2343 samples spans from 116 to 64 kyr BP, leaving thus the MIS 5e poorly represented in the Balearic Sea (Fig. 2F). The temporal resolution achieved within those three records reach centennial scale, allowing identifying changes and fluctuations that occurred within multi-centennial/millennial time scales. Average sedimentation rates range from 10.6 cm/kyr, 22.8 cm/kyr to 30.2 cm/kyr for cores PP10-17 (Cantabrian), ODP Site 977A (Alboran) and MD99-2343 (Balearic), respectively (Fig. 2G). In the context of the Mediterranean Basin, both Mediterranean sediment cores present high sedimentation rates, which are coherent with other studies from this region (Frigola et al., 2008, 2007; Jiménez-Amat and Zahn, 2015). Note that the highest sedimentation rates occurred during intervals with high $\delta^{18}O$ values, corresponding to cold stadials periods.

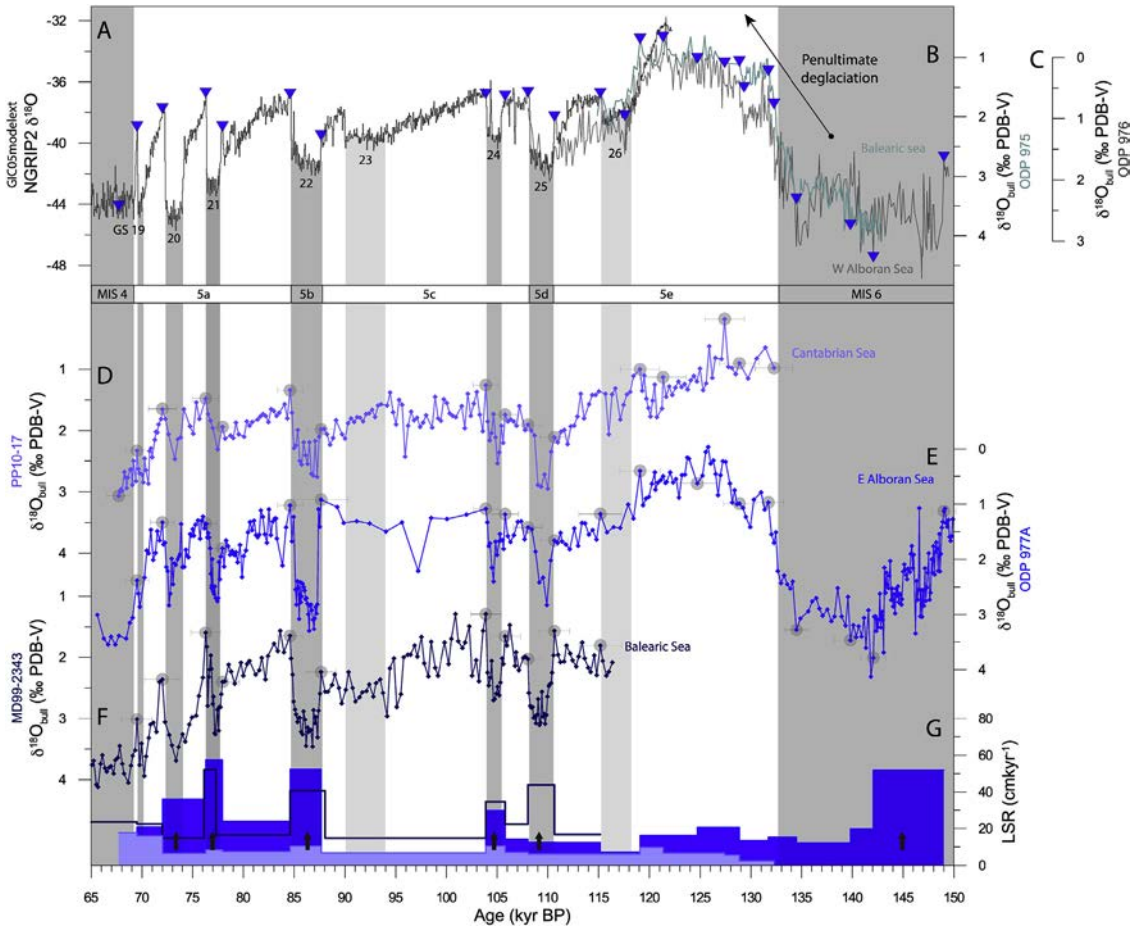

Fig. 2. Age model of marine core records developed by tuning the SST and *G. bulloides* $\delta^{18}O$ record with A) $\delta^{18}O$ NGRIP2 GICC05modelext timescale record (Rasmussen et al., 2014; Seierstad et al., 2014). B) The $\delta^{18}O_{G.bulloides}$ ODP Site 975 record from the Balearic Sea (Marino et al., 2015). C) The $\delta^{18}O_{G.bulloides}$ ODP Site 976 record from the West Alboran Sea (Jiménez-Amat and Zahn, 2015). The blue triangles indicate the new tie points used in this study. Final age models and associated uncertainties are plotted using the $\delta^{18}O_{G.bulloides}$ for D) PP10-17 core modified from Brocheray et al. (2014) and Rodriguez-Lazaro et al. (2017), E) ODP Site 977 modified from Martrat et al. (2007) and F) MD99-2343 core. G) Linear sedimentation rates (LSR). Vertical grey bars show Marine Isotopic Stages and sub-stages (MIS 4–6) and/or Greenland stadials (GS19-26). (For interpretation of the references to colour in this figure legend, the reader is referred to the Web version of this article.)

4.2. Sea surface temperature reconstructions

Mg/Ca ratio measured in carbonate shells of planktonic foraminifera is a frequently used proxy for SST reconstructions (Barker et al., 2005; Elderfield and Gansen, 2000). Although it has been proposed that high-salinity environments such as the Mediterranean Sea could affected foraminifera–Mg/Ca ratios (Ferguson et al., 2008), culture experiments appears to not support it (Hönisch et al., 2013). In contrast, diagenetic overprints have been proposed as the main cause of anomalous high foraminifera-Mg/Ca ratios (Hoogakker et al., 2009). Despite that, secondary high-Mg-calcite overgrowths in foraminiferal shells is lower in deep western Mediterranean samples than in eastern locations due to the presence of less calcite supersaturated bottom waters (van Raden et al., 2011). Furthermore, both reductive and weak acid leaching steps applied in the cleaning procedure have been proved to be efficient removing secondary overgrowths (Pena et al., 2005). Overall, the Mg/Ca ratios obtained in this study appear not to be anomalous high due to they are coherent with other studies for the same location (Català et al., 2019; Jiménez-Amat and Zahn, 2015) and within the ranges of the calibration used to transfer ratios into SST (Cisneros et al., 2016). This equation is appropriated for Mediterranean Mg/Ca-SST estimation since it expands the temperature sensitivity range of the original *G. bulloides* calibration from the N Atlantic (Elderfield and Gansen, 2000) towards the warm end that characterise Mediterranean waters. In this specific region, *G. bulloides* Mg/Ca-SST has been interpreted to reflect spring temperatures, since sediment trap fluxes of *G. bulloides* are maximum during this bloom season (Bárcena et al., 2004; Cisneros et al., 2016; Rigual-Hernández et al., 2012).

The recorded amplitude of the SST changes rise 7.3 °C, 7.5 °C and 8 °C for Cantabrian, Alboran and Balearic seas, respectively. Therefore the Balearic record shows the widest range of variability even though it does not record the last deglaciation, which is only fully recorded in the Alboran record (>5 °C warming) (Fig. 3C, D and E). The SST associated errors are shown in Supplementary Fig. S1. In general, the Cantabrian SST record was about 2–3 °C colder than the western Mediterranean Sea, which is consistent with the current SST pattern, where spring SST mean are 14 °C, 17.6 °C and 16.7 °C for Cantabrian, Alboran and Balearic seas respectively (Picciolo, 2006). The three SST records show strong similarities in the general trend during the overlapped periods despite the warmest temperatures did not occur synchronously among the three studied areas (Fig. 3C, D and E). The MIS 5e and c sub-stages show warm SST while MIS 5a was generally cooler. The cooling phase that ended the MIS 5e was more progressive and smoothed in the Cantabrian region than in the western Mediterranean, where the Balearic record presents the largest SST change (Fig. 3C, D and E:

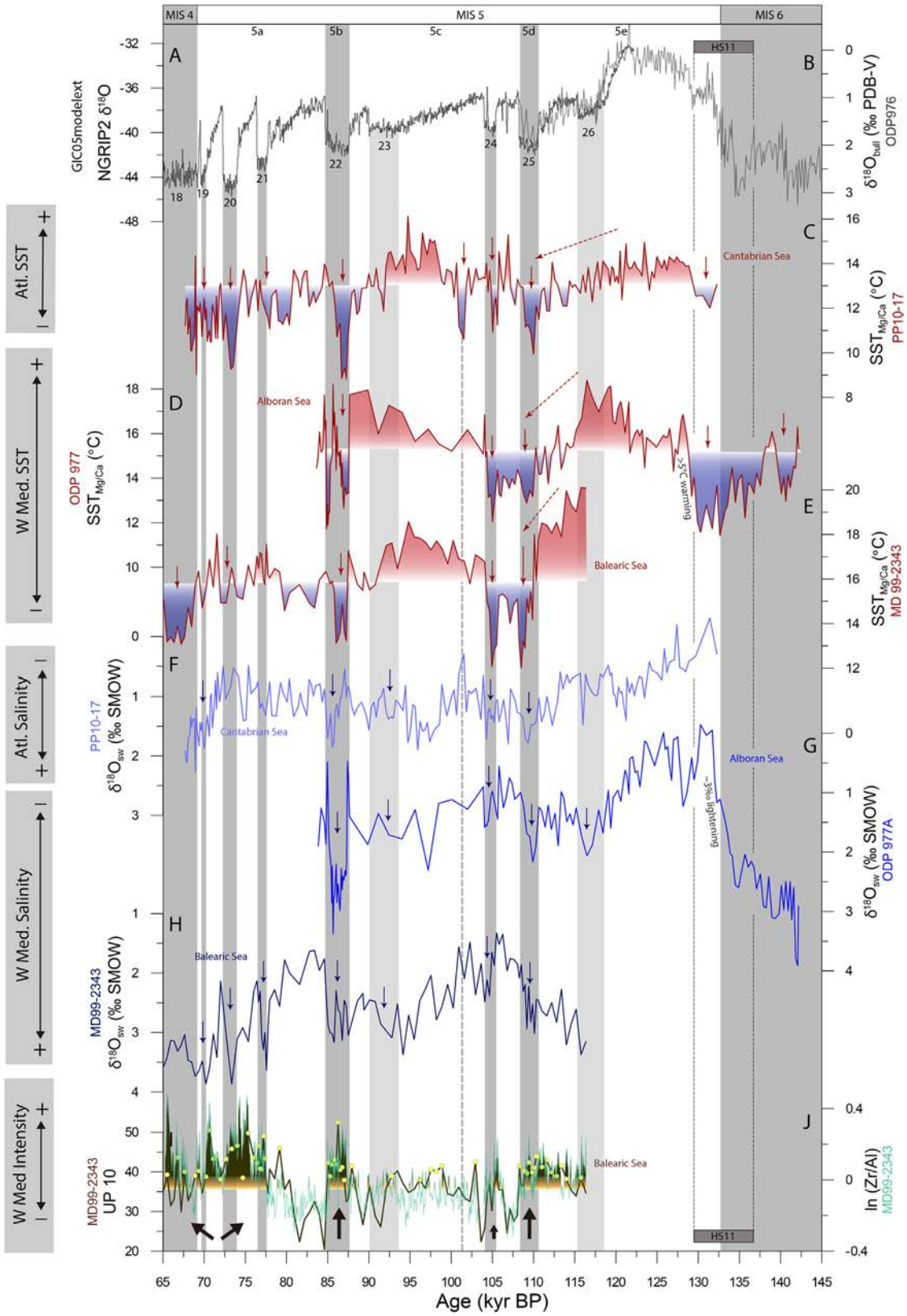

Fig. 3. Marine core results vs. time. Reference records are plotted on top: A) $\delta^{18}O$ NGRIP2 GICC05modelext timescale record (Rasmussen et al., 2014; Seierstad et al., 2014) and B) $\delta^{18}O_{G.bulloides}$ ODP Site 975 record from the Balearic Sea (Marino et al., 2015). This study Mg/Ca-SST records: C) PP10-17 core of the Cantabrian Sea, D) ODP Site 977A of the East Alboran Sea and E) MD99-2343 core of the Balearic Sea. Mean sea surface temperature, 12.7 °C, 14.8 °C and 15.9 °C for Cantabrian, Alboran and Balearic records respectively, are used as colour gradient threshold in plotted curves. This study $\delta^{18}O_{sw}$ records: F) PP10-17 core, G) ODP Site 977A and H) MD99-2343 core. I) MD99-2343 non-carbonate UP10 fraction with samples corresponding to cluster-1 indicated by yellow dots. J) Zirconium geochemical record normalized to aluminum and plotted in logarithmic scale (Zr/Al) of MD99-2343 core. Grey dashed rectangle: Heinrich stadial 11 (HS11). Red arrows: cooling trends. Blue arrows: heavy $\delta^{18}O_{sw}$ events. Black arrows: High deep current intensities. Vertical grey dashed line: Cantabrian cold event. Vertical grey bars: MIS 4–6 and/or Greenland stadials (GS18-26). (For interpretation of the references to colour in this figure legend, the reader is referred to the Web version of this article.)

dashed red arrows). In fact, during the warm sub-stages and especially at the end of the MIS 5e the temperature gradient between the Cantabrian basin and the W Mediterranean sub-basins was relatively high and even higher to those of today (Supplementary Fig. S2). In contrast to the regional heterogeneities of the warm periods, the stadial periods show very distinctive and homogeneous cold conditions among all SST records, except during the GS26 and GS23. These synchronic cold conditions among the three basins achieve similar SST between the Cantabrian and the Alboran or even the Balearic Sea during stadials, especially at GS25 and 24 (Supplementary Fig. S2). Moreover, during the MIS 5c at 101.5 kyr BP occurred an intense cold event in the Cantabrian record that is not reflected in the W. Mediterranean records (Fig. 3C: grey dashed vertical line).

4.3. Sea water $\delta^{18}O$ evolution

The $\delta^{18}O$ signal from *G. bulloides* shells is a combined signal of the water temperature of calcification and also the original seawater $\delta^{18}O_{sw}$ (Waelbroeck et al., 2002). These two variables can be isolated by the use of an independent SST reconstruction, as the Mg/Ca record and, in this way, estimate the original oxygen isotopic composition from seawater ($\delta^{18}O_{sw}$). The $\delta^{18}O_{sw}$ has been estimated using the Shackleton palaeotemperature equation (Shackleton, 1974) and converted in Standard Mean Ocean Water (SMOW) after the correction of Craig (1965). The $\delta^{18}O_{sw}$ record includes the signal from global ice-volume changes, but also local hydrography changes (Rohling, 1999). In the case of the Mediterranean records, variations in the inflow water volume through the strait of Gibraltar due to changes in the relative sea level might amplified the isotopic signal (enrichment) due to increases in water residence time and the evaporative character of the basin (Rohling, 1999, 2014). Hence $\delta^{18}O_{sw}$ changes in the Mediterranean and Cantabrian records are interpreted in terms of variation in regional precipitation/evaporation balance or freshening events related to N Atlantic iceberg melting (Ferrer et al., 2009; Pierre, 1999; Sierro et al., 2005) plus the amplification effect of sea-level changes (Rohling et al., 2014). Overall, heavy/light $\delta^{18}O_{sw}$ values correspond to saltier/fresher sea surface water properties (Pierre, 1999) although the complexity of the factors prevents the application of a simple linear function for paleosalinity reconstructions (Rohling, 1999).

In general, all three cores show high or moderate values during stadials and full glacial (Fig. 3F, G and H: blue arrows) with some exceptions as such the very remarkable rapid freshening event with a ~3‰ lightning in the Alboran-$\delta^{18}O_{sw}$ signal likely reflecting the sea ice melting associated to the H11 that marks the onset of the penultimate deglaciation. The $\delta^{18}O_{sw}$ evolution is also very heterogeneous among the three studied areas. The Cantabrian and Alboran Sea $\delta^{18}O_{sw}$ show more comparable values and significantly lighter than those from the Balearic Sea, reflecting the evaporation character of the Mediterranean basin (Pierre, 1999). Regarding the intensity of the changes, the Alboran Sea $\delta^{18}O_{sw}$ show larger enrichments than the Cantabrian record in relation to the stadial periods. The GS26, 23 and 20 stadials periods show a strong regional contrast, with significant isotopic enrichments in the Balearic core that are not detected in the Cantabrian site, while during the GS25, 24 and 22 the isotopic composition of the sea water was very similar among the basins (Supplementary Fig. S2). It is worth to highlight the extreme freshening event in the Cantabrian record coinciding with the cold Cantabrian event during the MIS 5c at 101.5 kyr BP (Fig. 3F: grey dashed vertical line).

4.4. Sedimentological changes in the Menorca drift and deep current intensity

Contourite drifts are characterized by very high sedimentation rates and hence provide high-resolution records suitable for paleoceanographic studies (Hodell et al., 2009; Oppo et al., 2001; Robinson and McCave, 1994). Deep-water current intensity directly affects the proportion and grain-size of non-cohesive particles deposited in contourite drifts (McCave and Hall, 2006; Mulder et al., 2013; Rebesco et al., 2014). In this sense, the grain-size distribution of the non-carbonate fraction of sediments represents the intensity of bottom currents (McCave et al., 1995). The grain-size record of the last 50 kyr from core MD99-2343 was previously related to deep-water currents intensity changes associated with climate oscillations controlling deep-water formation in the western Mediterranean (Frigola et al., 2008, 2007). Here we focus on the grain-size record from the same core but for the 117-65 kyr time-interval (Fig. 3I). We also use the UP10 index, i.e. volume percentage higher than 10 μm, as proxy of deep-water paleocurrent intensity (Frigola et al., 2007), recently validated with instrumental measurements (Cisneros et al., 2019). In addition, a clustering statistical analysis of grain-size modal distributions was also performed using the k-means method (McQueen, 1967; Povea et al., 2015). Cluster 1 comprises 49% of the samples corresponding to the coarser samples with a main mode located around 10 μm, thus associated to high UP10 values (Fig. 3I: yellow dots). Although the UP10 record has no obvious long-term trend, stadial periods and the MIS 4 are characterized by high UP10 values indicating an increment in the deep current intensity. In contrast, interstadial periods present both high and low UP10 values with relatively high internal oscillations. Particularly, the end of MIS 5e and especially the end of MIS 5a present high UP10 values and almost all samples belongs to the cluster 1 (Fig. 3I). The lowest UP10 percentages indicating weaker deep current intensity are found during these warm intervals.

Currents not only control the grain-size distribution of contourite drifts but also modify the mineralogy of sediments, concentrating heavy respect to lighter minerals (Mulder et al., 2013). As suggested by Bahr et al. (2014), the Zr/Al ratio is used for a semi-quantitative assessment of paleocurrent velocity because it represents the relative enrichment of zircon (heavy mineral) versus aluminosilicates (less dense minerals) under current flow (Fig. 3J). The UP10 record shows an extraordinary fit with the Zr/Al ratio (Fig. 3I and J), corroborating the use of this ratio as deep-water paleocurrent intensity proxy in the studied area. Moreover a Principle Component Analysis (PCA) was carried out with standardized XRF data and only considering elements with a robust signal (i.e. Al, Si, K, Ca, Ti, Fe, Rb, Sr, Zr, and Ba) (Supplementary Fig. S3). PC-1, explaining the 77% of the total variance, can be interpreted as carbonate versus detrital siliciclastic supplies (Ca and Sr opposed to all the other elements). The PC-2 explains 9.49% of the variance and opposes the aluminosilicates elements to barium, which can be related to productivity. Although explaining only a 5.6% of the total variance, the PC-3 is clearly dominated by Zr reinforcing the Zr/Al as a proxy of accumulated heavy minerals due to current intensity sorting.

4.5. Chronology of the speleothem records

Details of radiometric dating, errors and U contents for both speleothems are given in Supplemental Table 2. There are not age inversions for any of the two speleothems when taking into account 2σ errors. The errors associated with the Pyrenean speleothem are larger than those in the Minorca speleothem due to higher presence of detrital material introducing remobilized thorium in the

calcite. Age modelling was determined by StalAge software (Scholz and Hoffmann, 2011). The Pyrenean speleothem presents four possible growth phases identified by coloured detrital layers and changes in the growth axis direction at 35, 406 and 448 mm from the top (Fig. 4A). These visual changes could indicate precipitation/growth breaks but the resolution of the sampling and the errors associated makes difficult to constrain this short hiatuses by U-series ages. Positive excursions occur in the geochemical record (Mg/Ca and $\delta^{13}C$) at each of these potential hiatuses supporting reductions of effective precipitation at these times. Due to speleothem growth hiatuses are not well detected by statistical methods, the Pyrenean record has been divided in four different data series in order to perform a plausible age modelling according to growth gaps. In contrast, the Minorca speleothem does not present visible growth interruptions and the age-depth model is rather linear. Unfortunately, the youngest speleothem (JUD-Pyrenees) started to grow when the other one stopped (IND-Minorca) thus preventing a record overlap. The Pyrenean speleothem ranges from 115 to 68 kyr BP with growth rates between 0.2 and 4 cm/yr. This speleothem grew slower than the Minorca one that presents growth rates between 5 and 12 cm/yr and spans from 125 to 113 kyr BP (Fig. 4B).

4.6. Geochemical records of the speleothems

The mean value of the $\delta^{18}O$ record from the Minorca speleothem IND is −5.79‰ and the overall variation is 1.45‰. The $\delta^{18}O$ record shows a clear general trend to heavier values with time (Fig. 4G). The $\delta^{13}C$ mean value is −6.9‰ and the overall variation is 3.66‰. In contrast to the $\delta^{18}O$, the $\delta^{13}C$ record show relative stable trend until the end of the MIS 5e when values become progressively heavier (Fig. 4H). Mg/Ca ratios show maximum ratios of 15.25 mmol/mol and minimum of 5.32 mmol/mol with a mean average of 8.19 mmol/mol (Fig. 4I). Consistently with the $\delta^{13}C$, Mg/Ca record presents a rather stable evolution with a significant increase in the ratios towards the end of the MIS 5e.

The mean $\delta^{18}O$ value from the Pyrenean speleothem is −7‰, the record shows large oscillations (2.4‰) (Fig. 4D) without any clear relation with the stadial-interstadials evolution. The $\delta^{13}C$ record has a mean value of −5.42‰ and its overall variation range is 6.33‰. In contrast to the $\delta^{18}O$ record, the $\delta^{13}C$ record shows intense enrichments related to the onset and end of the stadials period most of them associated to a speleothem growth hiatus (Fig. 4E). These patterns are consistent with the Mg/Ca record that oscillates between 9.7 mmol/mol and 3.4 mmol/mol with a mean value of 5.5 mmol/mol. This record also shows rapid and intense changes toward higher values associated to the stadial periods mostly with those associated to JUD growth hiatuses (Fig. 4F: black arrows).

5. Discussion

5.1. Interpretation of speleothem geochemical proxies

Several processes control the geochemistry signal in speleothems, starting from the early step when water is evaporating from oceans, until the calcite precipitates inside the cave as speleothem deposits. Some of these processes induce an isotopic fractionation and enrichment-depletion in trace element concentration, which ultimately are used as hydrological and paleoclimate proxies (Fairchild and McMillan, 2007; Fairchild and Treble, 2009; Mc Dermont, 2004; Wong and Breecker, 2015). Due to the high amount of factors controlling the speleothem geochemical signal, a multi-proxy approach is required to provide a climate interpretation. In this study we analyse the $\delta^{18}O$, the $\delta^{13}C$ and the Mg/Ca ratio from each speleothem. Remarkable information coming from this multiproxy approach is the significant difference between the $\delta^{18}O$ trend and the $\delta^{13}C$ and Mg/Ca ratio patterns, thus suggesting a different interpretation (Fig. 4).

Dissolved carbon and its isotopic composition in drip waters derive from several factors controlled by climate conditions: 1) the type of vegetation C3/C4 plants (Dorale et al., 1992) 2) the amount of root respiration in the soil (Genty et al., 2003, 2001; Moreno et al., 2010); and 3) the kinetic fractionation (Fairchild and McMillan, 2007; Richards and Dorale, 2003). All of them are related to water availability and its residence time in the karst system during water percolation. Moreover vegetation/soil activity also depends of temperature (Fairchild and Baker, 2012). Consequently, lowest $\delta^{13}C$ values in speleothems are related to optimum temperature for vegetation/soil activity but also higher water availability and shorter residence times due to an enhanced rainfall amount and ultimately, more atmospheric moisture. By contrast, highest $\delta^{13}C$ values are often attributed to aridity or less atmospheric moisture and cold temperatures. Several mid-latitude speleothem studies have been interpreted $\delta^{13}C$ shifts in terms of changes in regional hydrology and vegetation/soil activity, like for example in the Mallorca Island (Hodge et al., 2008b), in the northeast IP (Bartolomé et al., 2015; Moreno et al., 2010) or in the southwest France (Genty et al., 2003).

In the case of the Mg/Ca ratio, the principal controlling factor seems to be derived from the bedrock composition and groundwater residence times. Assuming that the bedrock composition did not change, variations in the precipitation/evaporation balance in the region should be related to the amount of water infiltrating into the karst system and hence changes in the drip rate and the speleothem growth rate. A prior calcite precipitation (PCP) can occur during the infiltration and dripping due to an early degassing (Fairchild and McMillan, 2007). Consequently, high PCP, long residence time, slow drip rates and slow growth rates will increase the Mg/Ca ratio in the speleothem calcite due to this preferential calcium lost. In consequence, the Mg/Ca ratio in speleothems reflects changes in hydrology; higher Mg/Ca ratios in speleothems suggest drier conditions and vice versa (Fairchild et al., 2000; Moreno et al., 2010). A strong co-variation between Mg/Ca and $\delta^{13}C$ in speleothem records reinforces the interpretation of water availability in the soil thus reflecting atmospheric moisture variability (Fairchild and Treble, 2009). Due to tightly patterns shown by speleothem $\delta^{13}C$ and Mg/Ca records from this study, it can be assumed that these proxies synchronously recorded changes in vegetation productivity and water residence time, thus supporting their use as atmospheric moisture proxies (Fig. 4).

The rainfall $\delta^{18}O$ signal, and consequently the speleothem $\delta^{18}O$ signal, depends on the isotopic composition of ocean water source, the atmospheric air temperature, the amount effect and changes in rainfall patterns (Fairchild and McMillan, 2007, Fairchild et al., 2006; Lachniet, 2009; McDermott, 2004). Moreover kinetic effects also play an important role for oxygen isotope fractionation (Stoll et al., 2015). In mid-latitude speleothems, the $\delta^{18}O$ is commonly interpreted as a combination between temperature and the amount effect (Bartolomé et al., 2015; Vansteenberge et al., 2016). Additionally, at the temporal scale of this study, changes in the marine $\delta^{18}O$ signal of the water source could also play an important role since marine $\delta^{18}O$ changes occurred at global scale in association to the accumulation/melting of large ice sheets and at regional scale by changes in the precipitation/evaporation (Drysdale et al., 2009; Marino et al., 2015).

5.2. Precession signal in $\delta^{18}O$ records

Both, marine and cave $\delta^{18}O$ studied records from the Mediterranean region show a clear precession scale variability where

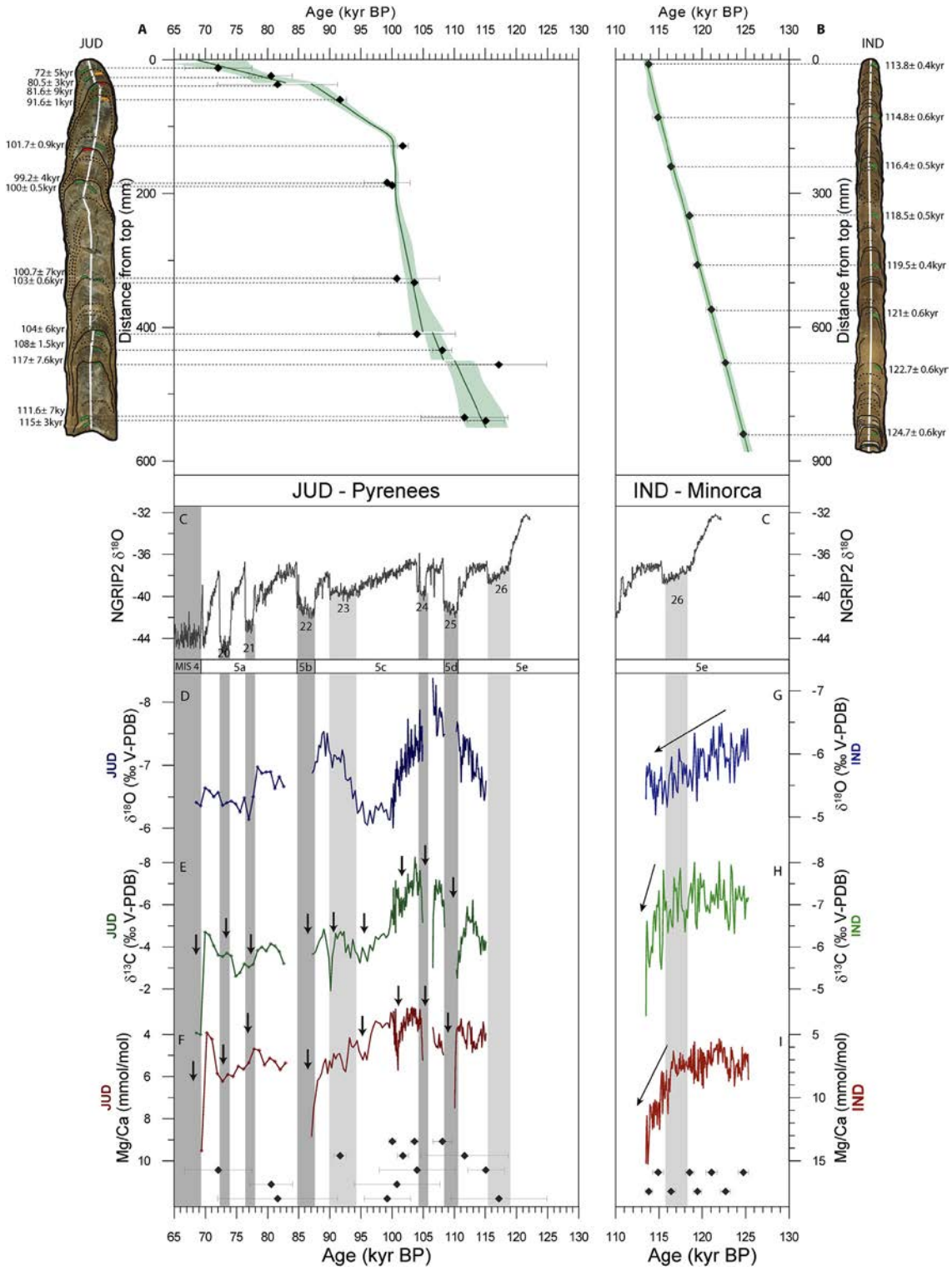

Fig. 4. Age-depth model constructed with StalAge algorithm (Scholz and Hoffmann, 2011) for A) *Judit* speleothem from south central Pyrenees and B) *Indiana* speleothem from Minorca Island. The dark green line represents the age-depth model and the green area marks errors. The interpretation of the internal structure of each speleothem and the dated samples locations are also provided in the lateral images. White line: growth axis. Black lines: growth discontinuities with detrital material. Dashed lines: distinctive layers. Green areas: dated samples used in the age model. Orange areas: replicated dates. Red areas: invalid dates. In the lower panel are plotted the speleothem geochemical results vs. time: C) reference record of $\delta^{18}O$ NGRIP2 (Rasmussen et al., 2014; Seierstad et al., 2014), D) JUD $\delta^{18}O$ values, E) JUD $\delta^{13}C$ values, F) JUD Mg/Ca ratios, G) IND $\delta^{18}O$ values, H) IND $\delta^{13}C$ values and I) IND Mg/Ca ratios. Black arrows: aridity tendency and dry events discussed in the text. U/Th ages are also plotted with 2σ error bars on the bottom. Vertical grey bars: MIS 4–5 and/or GS20-26. (For interpretation of the references to colour in this figure legend, the reader is referred to the Web version of this article.)

lightest values are associated with precession minima and thus insolation maxima in the North Hemisphere (Fig. 5). A precessional rhythm is also present in the $\delta^{18}O_{speleo}$-stacked record from the Cantabrian Margin, north-west IP, where rain is fuelled from the Atlantic region (Stoll et al., 2015). But, the intensities of the $\delta^{18}O$-precession oscillations are significantly different among the records (Fig. 5). In particular, focussing in the precession minimum at 115-95 kyr BP (the central cycle of the studied period), the JUD $\delta^{18}O_{speleo}$ shows a depletion of 2‰ while in the Cantabrian speleothem stack was of about 1.2‰. In the marine realm, the largest oscillation occurred in the Balearic $\delta^{18}O_{sw}$ records, with a depletion of almost 2‰ while in the Alboran $\delta^{18}O_{sw}$ it was of 1.5‰ and any evident $\delta^{18}O_{sw}$–precession depletion occurred in the Cantabrian $\delta^{18}O_{sw}$ record. These marine records support stronger $\delta^{18}O_{sw}$–precession signal into the Mediterranean than the Cantabrian Sea likely related to regional precipitation/evaporation ratio. Pollen sequences also indicate a stronger precession signal in the Mediterranean sector of the IP in relation to the Atlantic sector (Fletcher and Sánchez-Goñi, 2008). The precession driven intensification of the African summer monsoon further strengthened this signal towards the eastern Mediterranean through an enhanced Nile river runoff that also led sapropel formation in this Eastern basin (Rohling et al., 2014). This is reflected in the $\delta^{18}O_{speleo}$ signal from Soreq Cave (Grant et al., 2012; Bar-Matthews et al., 2003, 2000), which for the discussed precession minimum shows an isotopic depletion of 3‰ (Fig. 5 G).

We interpret the described precession signal in the studied $\delta^{18}O_{speleo}$ records to reflect changes in $\delta^{18}O_{sw}$ from the moisture source area. The intensity of the $\delta^{18}O_{speleo}$ oscillations in the speleothem record from central Pyrenees, in relation to the speleothem stack from the Cantabrian source supports the western Mediterranean region as one of the main humidity sources for the studied period. Several studies reveal the IP itself and its proximal marine areas, such as the western Mediterranean Sea, as the principal contributors of moisture to precipitation (Krklec and Domínguez-Villar, 2014; Nieto et al., 2010; Gimeno et al., 2010). The subtropical North Atlantic is identified as an important contributor particularly during autumn and winter, when precipitation is mainly as snow in the Pyrenees, while during the thaw season, Mediterranean source areas became dominant. Our results supports that western Mediterranean source rainwater would account for the enhanced intensity of the precession signal detected in the central southern Pyrenees.

5.3. The penultimate deglaciation and the last interglacial onset

This interval is only represented in the Cantabrian Sea and the Alboran Sea marine records (Fig. 6). One of the most remarkable features during this period is the intense water-surface freshening detected in the two $\delta^{18}O_{SW}$ records (Fig. 6H and I). In the case of the Alboran record, this intense freshening (~132-130 kyr BP) occurred after two small initial pulses (Fig. 6I: Dark blue arrows). This sequence of several pulses has been identified in previous studies from the W-Iberian margin and the westernmost Alboran Sea (Fig. 6H and I) (Jiménez-Amat and Zahn, 2015; Tzedakis et al., 2018). Further west, into the Balearic Sea, the core ODP Site 975 discussed by Rodríguez-Sanz et al. (2017) also recorded this intense late MIS 6 freshening. The Alboran record also shows extreme cold SST contemporary to this freshening event (Fig. 6F). Although this extreme cold SST event is not well recorded in the Cantabrian record (Fig. 6E), the presence of the benthic foraminifer *Cibicides wuellestorfi* found in the same samples of this core by Rodríguez-Lazaro et al. (2017), also indicates glacial conditions. According to N Atlantic records, these freshening was associated to the HE-11, as such shown by an increase in the Si/Sr ratio, a proxy for IRD

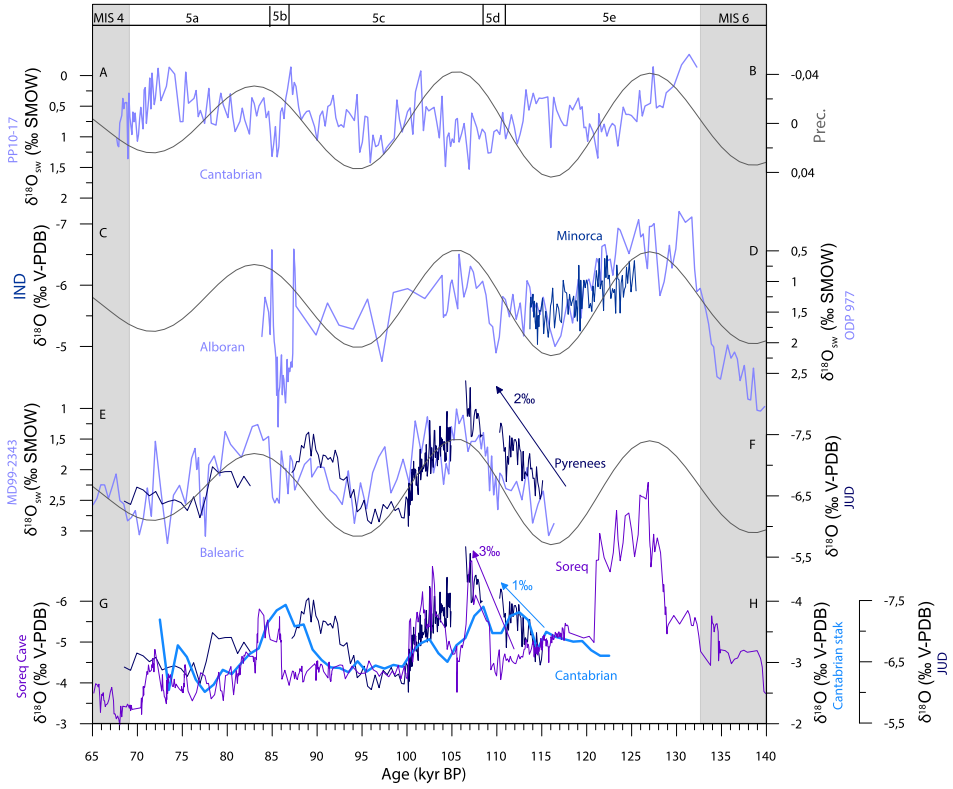

Fig. 5. Precession signal compared with marine and speleothem oxygen isotopes. A) PP10-17 core $\delta^{18}O_{sw}$, B) Precession curve (Laskar et al., 2004), C) IND $\delta^{18}O_{speleo}$ D) ODP Site 977A $\delta^{18}O_{sw}$, E) MD99-2343 core $\delta^{18}O_{sw}$ F) JUD $\delta^{18}O_{speleo}$, G) Soreq cave $\delta^{18}O_{speleo}$ (Bar-Matthews et al., 2000, 2003). H) Cantabrian $\delta^{18}O_{speleo}$ stack (Stoll et al., 2015). Arrows show the $\delta^{18}O_{speleo}$ change in ‰ during half precession cycle. Vertical grey bars: MIS 4 and MIS 6.

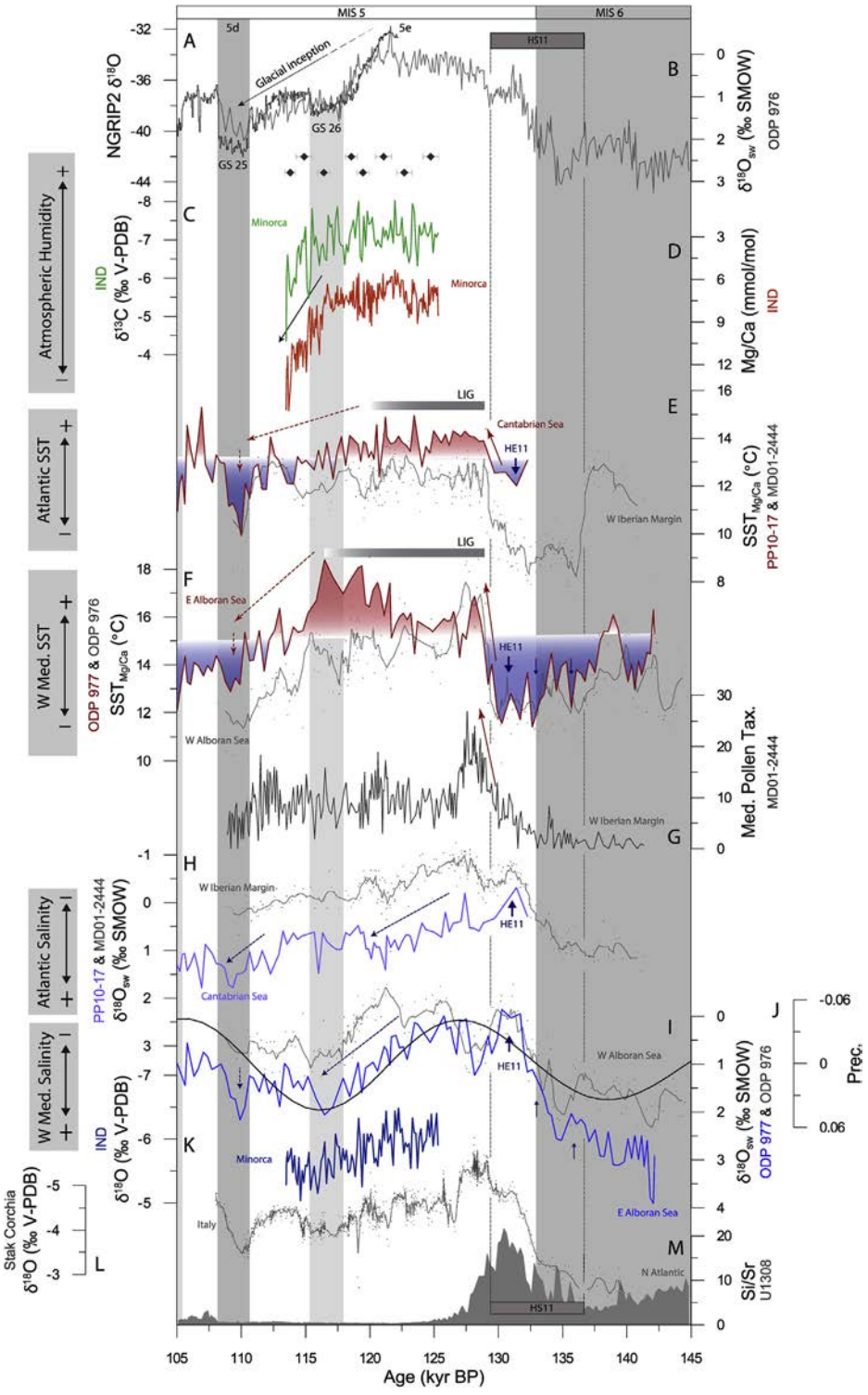

Fig. 6. A comparison of this study records to several published records from 145 to 105 kyr BP. Reference records: A) $\delta^{18}O$ NGRIP2 GICC05modelext timescale record (Rasmussen et al., 2014; Seierstad et al., 2014) and B) $\delta^{18}O_{C.bulloides}$ ODP Site 976 record (Marino et al., 2015). C) IND $\delta^{13}C$ and D) IND Mg/Ca ratios with the U/Th ages plotted with 2σ error bars on the top. E) Mg/Ca-SST of PP10-17 core in red and MD01-2444 core in grey (Tzedakis et al., 2018). F) Mg/Ca-SST of ODP Site 977A in red and ODP Site 976 in grey (Jiménez-Amat and Zahn, 2015). G) Mediterranean pollen taxa record of core MD01-2444 (Tzedakis et al., 2018). H) $\delta^{18}O_{sw}$ of PP10-17 core in blue and MD01-2444 core in grey (Tzedakis et al., 2018). I) $\delta^{18}O_{sw}$ of ODP Site 977A in blue and ODP Site 976 in grey (Jiménez-Amat and Zahn, 2015). J) Precession curve (Laskar et al., 2004). K) IND $\delta^{18}O_{speleo}$. L) Corchia stack $\delta^{18}O_{speleo}$ (Tzedakis et al., 2018). M) Si/Sr-IRD record of U1308 core (Hodell et al., 2008). Grey dashed rectangle: Henrich stadial 11 (HS11). Blue arrows: Penultimate deglaciation cold SST and light $\delta^{18}O_{sw}$ surface waters events related to HS11. Red arrows: Penultimate deglaciation climatic amelioration. Horizontal grey bars: Warm SST plateau or LIG-acme. Black arrow: Glacial inception speleothem aridity tendency. Dashed red arrows: Glacial inception SST falls. Dashed blue arrows: $\delta^{18}O_{sw}$ enrichments trends during the LIG-acme and the glacial inception. Vertical grey bars: MIS 5–6 and/or GS25-26. (For interpretation of the references to colour in this figure legend, the reader is referred to the Web version of this article.)

discharge, from the N Atlantic core U1308 (Fig. 6M) (Hodell et al., 2008). Large ice-sheet meltwater fluxes spreading into the N Atlantic Ocean reduced high latitude sea surface salinity and increased vertical stratification allowing an AMOC weakening (Hodell et al., 2008; Marino et al., 2015; Oppo et al., 2006; Seidenkratz et al., 1996). This freshwater anomaly entered via the Strait of Gibraltar into the western Mediterranean basin, reaching comparable light isotopic values in the Alboran and the Cantabrian basins (Supplementary Fig. S2), while it was progressively vanished along its path toward the eastern Mediterranean basin (Rodríguez-Sanz et al., 2017). Therefore the present study allows detecting the HE-11 impact on surface water properties confirming previous recent studies (Jiménez-Amat and Zahn, 2015; Rodríguez-Lazaro et al., 2017; Rodríguez-Sanz et al., 2017) not only in the western Mediterranean Sea but also in the Cantabrian Sea. Coinciding with the end of the HE-11, a rapid and intense warming occurred in both studied records related to the penultimate deglaciation as previously documented in W-Iberian and Alboran records (Jiménez-Amat and Zahn, 2015; Martrat et al., 2007, 2014; Tzedakis et al., 2018) (Fig. 6E and F: red arrows). It is also highly remarkable the comparable SST and $\delta^{18}O_{SW}$ values in both the eastern (977 site) and the western (976 site) Alboran cores during the HE-11 and the penultimate deglaciation (Fig. 6F and I). These homogenous surface water properties likely reflect a strong surface stratification in the eastern and western Alboran sub-basins, that contrast with the habitual strong mixing that led to a regional gradient in surface properties during other periods (Català et al., 2019). AMOC reinforcement after HE-11 allowed climate amelioration with an increase in precipitation and the consequent development of the Mediterranean forest, as detected through pollen records at the onset of the LIG (Sánchez-Goñi et al., 2012; Tzedakis et al., 2018) (Fig. 6G: red arrow).

5.4. The LIG-acme and the glacial inception

The LIG-acme is defined as the interval within the MIS 5e containing peak values or a plateau in a given record (Govin et al., 2015). Accordingly, it has been established the LIG-acme in base to the plateau of maximum SST (Fig. 6E and F: horizontal grey bars), although the records show significant differences between the Cantabrian and the Alboran Sea. The Cantabrian record present a shorter LIG-acme with more stable SST than the Alboran Sea which show a prominent SST maximum at the end of its LIG-acme. Stability of warm benthic foraminifera and ostracod assemblages was also found in the Cantabrian Sea during this period (Rodriguez-Lazaro et al., 2017). In spite of this, several short-term oscillations can be observed in both seas, being particularly acute in the Alboran record. LIG-acme variability has been previously described in records from the North Atlantic, W-Iberian Margin and even in the central Mediterranean (Oppo et al., 2001, 2006; Sprovieri et al., 2006; Tzedakis et al., 2018). The studied resolution prevents any detailed correlation with these events but the main patterns in the Cantabrian LIG-acme SST record are very comparable to those from the W-Iberian margin (Tzedakis et al., 2018) (Fig. 6E). The largest LIG-acme SST variability occurred in the Alboran Sea where significant differences occurred between the W and E-Alboran sub-basins (977 vs. 976 sites), with a large decoupling by the end of the LIG-acme, when the eastern site recorded the warmest SST. Such warm end of the LIG-acme is also confirmed in Balearic Sea SST record (Fig. 3E) although it does not fully cover the LIG. The Minorca speleothem $\delta^{13}C$ and Mg/Ca records (Fig. 6C and D) indicate the dominance of stable humid conditions during the whole LIG-acme defined by warm SST, although with several short millennial scale oscillations, and in agreement with a general increase in water availability in the Mediterranean region and southern Europe during the LIG (Bar-Matthews et al., 2000; Couchoud et al., 2009; Genty et al., 2013; Meyer et al., 2008; Moseley et al., 2015; Sánchez-Goñi et al., 1999, 2005).

Both Alboran SST and Minorca speleothems $\delta^{13}C$ and Mg/Ca records locate the glacial inception at the end of GS26 (116.5 kyr BP) with a clear intense cooling and aridification phase (Fig. 6C and D: black arrow, note the reverse axis). Thus, the onset of the glacial inception in the western Mediterranean occurred later than in other northern regions, where earlier changes have been associated to the growing ice sheets and changes in the N Atlantic circulation during the GS26 (Supplementary Fig. S4) (Demeney et al., 2017; Genty et al., 2003; Moseley et al., 2015; Sirocko et al., 2005; Tzedakis et al., 2018; Vansteenberge et al., 2016). Moreover, the Cantabrian SST record show a smoothed cooling during the glacial inception, that starts previous to GS26, and therefore also in agreement with the heterogeneous LIG-acme duration discussed in other studies (Bakker et al., 2012, 2014; Hoffman et al., 2017). But in any case, none of the studied SST records support an intense cooling event around the IP associated to the GS26. This is in line with other N Atlantic records that suggest a subtle stadial cooling in the eastern Atlantic but a significant cooling event C25 (GS26 equivalent) in the northern and western subpolar locations (McManus et al., 2002). In contrast, the GS26 is well marked in the Alboran Sea $\delta^{18}O_{sw}$ as an enrichment event also presented in the Corchia stack speleothem record (Tzedakis et al., 2018) and to some extend in the Minorca $\delta^{18}O$ record but it is not detected in the Cantabrian $\delta^{18}O_{sw}$ (Fig. 6H, I and L).

According to all the studied SST records the glacial inception culminated at MIS 5d (GS25) with an intense cooling phase (Fig. 6E and F: red dashed arrows). The global glacial inception should be related to a weakening of the AMOC that caused climate deterioration, changing the strength and position of westerly winds and also the migration of rain belts (Bardají et al., 2009; PAGES, 2016). But the variable timing of the glacial inception may reflect the operation of climate feedbacks with diachronous responses across Europe (Govin et al., 2015).

5.5. The early glacial

During the early glacial period the SST evolution among the three studied areas is dominated by the occurrence of a series of cooling events from 111 to 65 kyr BP in agreement with the GS sequence (Fig. 3A, C, D and E). Furthermore, a weak stadial expression is shown in the SST records from the three regions during GS23, comparable to previously discussed weak GS26. For most of the GS, SST dropped to 13-12 °C in western Mediterranean cores and to 10-9 °C in the Cantabrian Sea, reducing the inter-basin gradients bellow 3 °C and in some extreme cases, as the GS25 and 24, this gradient almost disappeared (Supplementary Fig. S2). Regarding to the Alboran and Balearic Sea, SST values for each GS were identical, indicating strong homogeneous surface properties. In contrast to the overall homogeneous stadial inter-regional response, the Cantabrian record shows the occurrence of a extreme cold and freshening event at 101.5 kyr BP (beginning of the MIS 5c), which is not expressed in the Mediterranean SST records (Fig. 3C: dashed grey line) and it is likely recording a regional feature.

In the continent, the Pyrenean speleothem also supports a rapid atmospheric reorganization associated with stadials. Growth hiatus and intense enrichments in the $\delta^{13}C$ and Mg/Ca signal occurred synchronous to cold stadials supporting the establishment of drier conditions in the Southern Central Pyrenees (Fig. 7B and C: red and green arrows). This is consistent with other European speleothems

records indicating a robust relation between AMOC changes and European precipitation variability during the early glacial (Drysdale et al., 2005, 2007; Genty et al., 2003; Vansteenberge et al., 2016). These Mediterranean dry stadial conditions are consistent with the heavy $\delta^{18}O_{sw}$ events (Fig. 7G and H) overprinted on the large-scale precession signal of the Mediterranean $\delta^{18}O_{sw}$ records previously discussed (Section 5.1). These heavy stadial $\delta^{18}O_{sw}$ events, much intense in the Mediterranean records, should reflect conditions of enhanced evaporation-precipitation balance over the whole basin (Rohling, 1999) that were further strengthened eastward as shown in the $\delta^{18}O_{speleo}$ Soreq record (Fig. 7G, I and J) (Bar-Matthews et al., 2000).

The proxy records for deep-water current intensities in the Balearic core (UP 10 and Zr/Al ratio records in Fig. 7E and F) also show a distinctive signal with relative high values for most of the Stadial periods. The Balearic core location corresponds to a contournitic drift shaped by deep water currents associated with the formation of WMDW in the Gulf of Lion, were westerly winds acts (Frigola et al., 2007; Cisneros et al., 2019). Consistently with the previously described changes for MIS 3 in the same location (Frigola et al., 2008), the overall set of data supports enhanced Stadial formation of WMDW in the Gulf of Lion while cold SST and dry conditions dominated over the whole basin.

These observations highlight an overall rapid interregional coupling in the ocean and atmosphere response during the Stadial intervals. Our results are coherent with the oceanic-atmosphere readjustments observed in model studies after fresh water impose weakening of the AMOC (Ivanovic et al., 2018; Kageyama et al., 2010; Van Meerbeeck et al., 2011). The AMOC weakening reported in these studies support strong westerlies transport of cold and drier air masses due to its path over extended sea ice rather than ocean waters into W Europe and also reducing air temperature

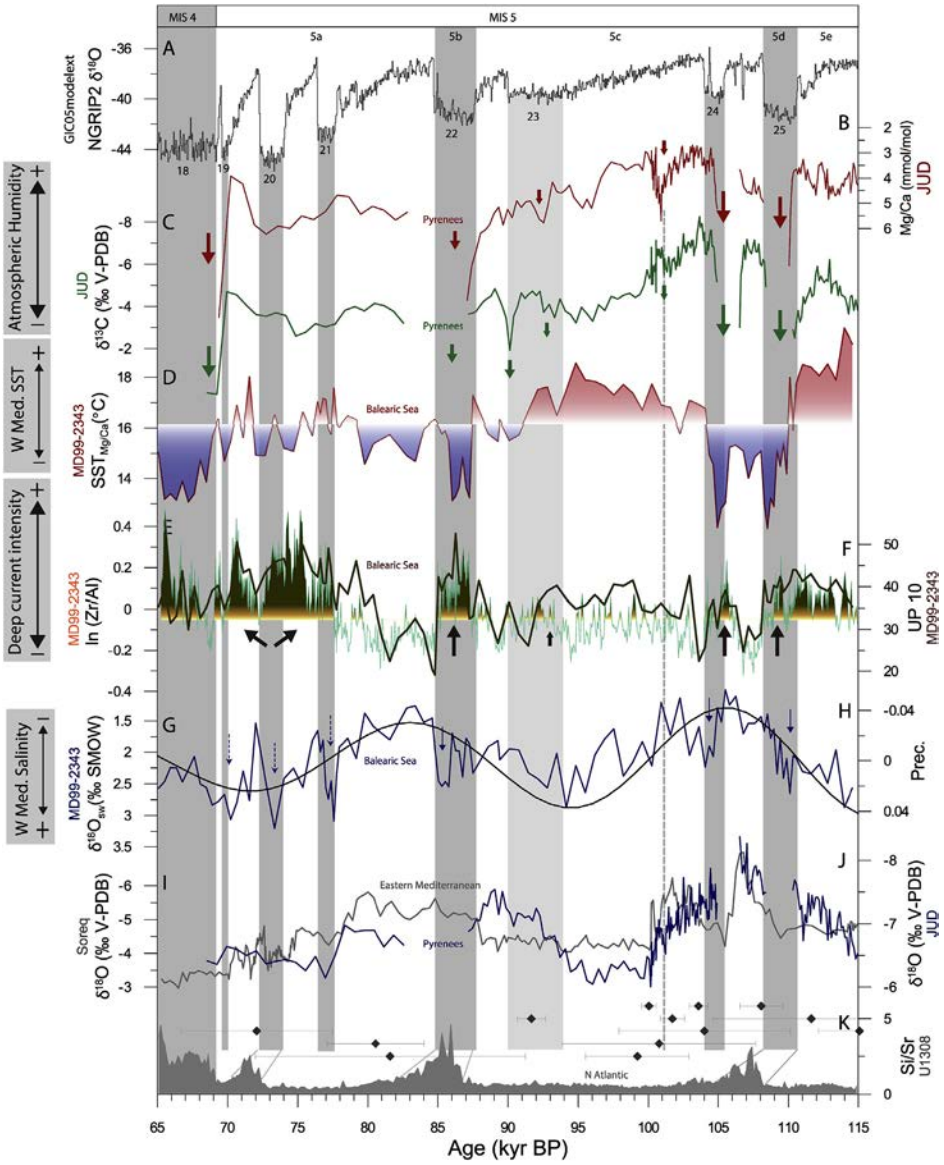

Fig. 7. Comparison of this study records to some published data during the Early glacial. A) reference record $\delta^{18}O$ NGRIP2 (Rasmussen et al., 2014; Seierstad et al., 2014), B) JUD Mg/Ca ratios C) JUD $\delta^{13}C$ record, D) Mg/Ca-SST of MD99-2343 core, E) Zr/Al ratio plotted in logarithmic scale of MD99-2343 core, F) MD99-2343 non-carbonate UP10 fraction, G) $\delta^{18}O_{sw}$ of MD99-2343 core, H) Precession curve (Laskar et al., 2004), I) Stacked Soreq $\delta^{18}O_{speleo}$ record (Bar-Matthews et al., 2000, 2003), J) JUD $\delta^{18}O_{speleo}$ record with the U/Th ages plotted with 2σ error bars on the bottom and K) Si/Sr-IRD record of U1308 core (Hodell et al., 2008). Red and green arrows: dry events discussed in the text. Black arrows: High deep current intensities. Blue arrows: heavy $\delta^{18}O_{sw}$ events. Vertical grey dashed line: Cantabrian cold event. Vertical grey dashed line: Cantabrian cold event. Vertical grey bars: MIS 4–5 and/or GS18-25. (For interpretation of the references to colour in this figure legend, the reader is referred to the Web version of this article.)

in the IP. The Intertropical Convergence Zone (ITCZ) and the atmospheric convection cells were displaced southward, decreasing consequently the moisture availability in mid-latitudes. Moreover extremely cold temperatures surrounding the IP reduced the evaporation on proximal areas, including the western Mediterranean Sea and enhancing the aridity in the region during the cold stadials.

In contrast to the stadial conditions, the SST evolution during the warm interstadials is more heterogeneous among the studied records, showing a diachronic establishment of maximum SST conditions (Fig. 3C, D and E) and reaching large gradients among basins (Supplementary Fig. S2). This regional heterogeneity suggest more complex feedback connections during warm intervals of full AMOC operation, which could probably cause displacements of the polar/subtropical gyres and therefore changes in the surface water properties arriving to the studied areas (Mary et al., 2017). The speleothem record support relatively humid conditions during warm interstadials, consistent with an active AMOC that would bring mild and humid westerly winds over Europe (Ivanovic et al., 2018; Kageyama et al., 2010; Van Meerbeeck et al., 2011). Nevertheless some variability occurred within the Interstadial periods, the Pyrenean record shows a transition in the mid MIS 5c towards less humid conditions. This is consistent with previous observations in a Mallorca speleothem record (Dumitru et al., 2018) and a change from more developed Mediterranean vegetation to steppic pollen taxa detected in southern European pollen records and interpreted as a transition from warm-humid to warm-dry conditions during MIS 5c (Sánchez-Goñi et al., 2005, 1999; Tzedakis, 2003; Wulf et al., 2018).

Overall climatic conditions were slightly different during MIS 5a Stadial and Interstadials periods. SST records during MIS 5a reflect dominant cold conditions in both the Cantabrian and the Mediterranean sectors even for the Interstadial periods (Fig. 3d, f). Acute stadial $\delta^{18}O_{sw}$ enrichments occurred during stadials (GS21, 20 and 19) (Fig. 7D and G: blue dashed arrows), while relatively fresh $\delta^{18}O_{sw}$ dominated in the Cantabrian record (Fig. 3H). Those climatic conditions maintained an overall intense deep-water convection in the Western Mediterranean Sea (Fig. 7E). Nevertheless, dry conditions may have not been as extreme as previous stadials since the Pyrenean speleothem maintained its growth, although at low rate and Mg/Ca and $\delta^{13}C$ record only moderate high values. Moreover, major development of Pyrenean glaciers occurred during this period (Lewis et al., 2009; Peña et al., 2004), also supporting some degree of humidity supply. Therefore, the last hiatus at the MIS 5b and the end of the Pyrenean speleothem growth at the beginning of the MIS 4 could reflect this maximum extension of Pyrenean ice, preventing water seepage into the karst and suggesting the establishment of full glacial conditions.

6. Conclusions

The parallel reconstruction in this study of $\delta^{18}O_{sw}$ and $\delta^{18}O_{speleo}$ records provides a solid base to establish a connection on the appearance of a strong $\delta^{18}O$ precessional-scale signal in both marine and cave records. The enhanced intensity of the precession signal towards the Mediterranean region, let us to argue a relevant contribution of the Western Mediterranean sea as humidity source to the precipitation over the south central Pyrenees which was responsible for the transmission of the $\delta^{18}O_{sw}$ precession signature into the cave.

According to the new generated Cantabrian and Mediterranean $\delta^{18}O_{sw}$ records, the penultimate glaciation ended with an intense light anomaly that reached comparable values in both regions. This situation reflects a major North Atlantic surface freshening associated to the HE-11 melting whose end led to an AMOC reinforcement with an intense SST warming, larger in the Mediterranean region, that marked the onset of the LIG period. The recorded differences in the SST and $\delta^{18}O_{sw}$ evolution during the LIG-acme, indicate a regional decoupling in the climate variability of this overall warm period. The Menorca speleothem records suggest the dominance of relatively humid conditions during this period with several minor oscillations. The LIG-acme end was not synchronous around the IP. The glacial inception started previously in the Cantabrian Sea than in the western Mediterranean were the glacial inception arrived after the GS26, with a rapid cooling in parallel of an aridification phase in Minorca. This regional heterogeneity in SST and $\delta^{18}O_{sw}$ conditions appears to be a characteristic also for the following interstadial periods, indicating a higher complexity in the climate response around the IP during warm periods, pointing to much complex ocean-atmosphere interconnections in contrast to the stadial intervals.

During the stadial intervals, SST records show extreme cold conditions with homogeneous values along the studied records confirming the wide regional impact of the reduced AMOC. The speleothem records suggest the installation of drier conditions during these intervals in the south central Pyrenees, probably as a consequence of the diminished evaporation by the extreme cold conditions in the N Atlantic Ocean and western Mediterranean Sea. Deep convection of WMDW in the Gulf of Lions was also enhanced according to our proxies of deep-water currents intensity in the Minorca drift and likely responding to the overall cold and dry climatic conditions in the basin.

Finally, the Pyrenean speleothem growth ended at the end of the MIS 5a when SST already reached extreme cold values and deep-water currents in the Balearic Sea were particularly strong. A moment associated to the development of full glacial conditions in the region that led into the maximum extension of Pyrenean ice and likely preventing the growth of the studied speleothem.

Acknowledgement

This research was financially supported by CHIMERA (CTM2016-75411-R) and OPERA (CTM2013-48639-C2-1-R) projects, both founded by MINECO, Spain. We thank Generalitat de Catalunya Grups de Recerca Consolidats for grant 2017 SGR 315 to GRC Geociències Marines. We are grateful to M. Guart (Dept. de Dinàmica de la Terra i de l'Oceà, Universitat de Barcelona), M. Romero, T. Padró, B. Baena, J. Perona (Serveis Cientifico-Tècnics, Universitat de Barcelona) and A. Pascual (Dept. of Stratigraphy and Paleontology, University of Basque Country UPV/EHU) for their help with the laboratory work; to X. Rayo for his collaboration with the artwork of maps. I. Cacho thanks the ICREA-Academia programme from the Generalitat de Catalunya. B. Martrat acknowledges support from the CSIC - Ramón y Cajal postdoctoral programme RYC-2013-14073. P. Arnau acknowledges support from the Ciutadella Town Hall. Judit Torner benefited from an FPI-fellowship of MINECO.

Appendix A. Supplementary data

Supplementary data to this article can be found online at https://doi.org/10.1016/j.quascirev.2019.106037.

References

AEMET-IM, 2011. Atlas Climàtico Ibèrico. Temperatura del aire y precipitación (1971-2000). Agencia Estatal de Meteorología, ISBN 978-84-7837-079-5.

Bahr, A., Jimenez-Espejo, F.J., Kolasinac, N., Grunert, P., Hernandez-Molina, F.J., Rohl, U., Voelker, A.H.L., Escutia, C., Stow, D.A.V., Hodell, D., Alvarez-Zarikian, C.A., 2014. Deciphering bottomcurrent velocity and paleoclimate signals fromcontourite deposits in the Gulf of Cadiz during the last 140 kyr: an

inorganic geochemical approach. Geochem. Geophys. 15, 1–16. https://doi.org/10.1002/2014GC005356.Received.
Bakker, P., Renssen, H., 2014. Last interglacial model-data mismatch of thermal maximum temperatures partially explained. Clim. Past 10, 1633–1644. https://doi.org/10.5194/cp-10-1633-2014.
Bakker, P., Van Meerbeeck, C.J., Renssen, H., 2012. Sensitivity of the north atlantic climate to Greenland ice sheet melting during the last interglacial. Clim. Past 8, 995–1009. https://doi.org/10.5194/cp-8-995-2012.
Bar-Matthews, M., Ayalon, A., Gilmour, M., Matthews, A., Hawkesworth, C.J., 2003. Sea – land oxygen isotopic relationships from planktonic foraminifera and speleothems in the Eastern Mediterranean region and their implication for paleorainfall during interglacial intervals 67. Geochem. Cosmochim. Acta 3181–3199.
Bar-Matthews, M., Ayalon, A., Kaufman, A., 2000. Timing and hydrological conditions of Sapropel events in the Eastern Mediterranean, as evident from speleothems, Soreq cave, Israel. Chem. Geol. 169, 145–156. https://doi.org/10.1016/S0009-2541(99)00232-6.
Bárcena, M.A., Flores, J.A., Sierro, F.J., Pérez-Folgado, M., Fabres, J., Calafat, A., Canals, M., 2004. Planktonic response to main oceanographic changes in the Alboran Sea (Western Mediterranean) as documented in sediment traps and surface sediments. Mar. Micropaleontol. 53, 423–445. https://doi.org/10.1016/j.marmicro.2004.09.009.
Bardají, T., Goy, J.L., Zazo, C., Hillaire-Marcel, C., Dabrio, C.J., Cabero, A., Ghaleb, B., Silva, P.G., Lario, J., 2009. Sea level and climate changes during OIS 5e in the Western Mediterranean. Geomorphology 104, 22–37. https://doi.org/10.1016/j.geomorph.2008.05.027.
Barker, S., Cacho, I., Benway, H., Tachikawa, K., 2005. Planktonic foraminiferal Mg/Ca as a proxy for past oceanic temperatures: a methodological overview and data compilation for the Last Glacial Maximum. Quat. Sci. Rev. 24, 821–834. https://doi.org/10.1016/j.quascirev.2004.07.016.
Barker, S., Greaves, M., Elderfield, H., 2003. A study of cleaning procedures used for foraminiferal Mg/Ca paleothermometry. Geochem. Geophys. Geosyst. 4, 1–20. https://doi.org/10.1029/2003GC000559.
Bartolomé, M., Moreno, A., Sancho, C., Stoll, H.M., Cacho, I., Spötl, C., Belmonte, Á., Edwards, R.L., Cheng, H., Hellstrom, J.C., 2015. Hydrological change in southern Europe responding to increasing North Atlantic overturning during Greenland stadial 1. Proc. Natl. Acad. Sci. 112, 6568–6572. https://doi.org/10.1073/pnas.1503990112.
Brocheray, S., Cremer, M., Zaragosi, S., Schmidt, S., Eynaud, F., Rossignol, L., Gillet, H., 2014. 2000years of frequent turbidite activity in the capbreton canyon (Bay of Biscay). Mar. Geol. 347, 136–152. https://doi.org/10.1016/j.margeo.2013.11.009.
Cacho, I., Grimalt, J.O., Canals, M., Sbaffi, L., Shackleton, N.J., Schönfeld, J., Zahn, R., 2001. Variability of the Western Mediterranean sea surface temperature during the last 25,000 years and its connection with the Northern Hemisphere climatic changes. Paleoceanography 16, 40–52. https://doi.org/10.1029/2000PA000502.
Cacho, I., Grimalt, J.O., Pelejero, C., Canals, M., Sierro, F.J., Flores, J.A., Shackleton, N., 1999. Dansgaard-oeschger and Heinrich event imprints in Alboran Sea paleotemperatures. Paleoceanography 14, 698–705. https://doi.org/10.1029/1999PA900044.
Cacho, I., Shackleton, N., Elderfield, H., Sierro, F.J., Grimalt, J.O., 2006. Glacial rapid variability in deep-water temperature and δ18O from the Western Mediterranean Sea. Quat. Sci. Rev. 25, 3294–3311. https://doi.org/10.1016/j.quascirev.2006.10.004.
Català, A., Cacho, I., Frigola, J., Pena, L.D., Lierer, F., 2019. Holocene hydrography evolution in the Alboran Sea: a multi-record and multy-proxy comparison. Clim. Past 15, 1–15.
Cayre, O., Lancelot, Y., Vincent, E., Hall, M.A., 1999. Paleoceanographic reconstructions from planktic formaninfera off the Iberian Margin: temperature, salinity, and Heinrich events. Paleoceanography 14, 384–396.
Cheng, H., Edwards, R.L., Broecker, W.S., Denton, G.H., Kong, X., Wang, Y., Zhang, R., Wang, X., 2009. Ice age terminations. Science 326, 248–252. https://doi.org/10.1126/science.1177840.
Cisneros, M., Cacho, I., Frigola, J., Canals, M., Masqué, P., Martrat, B., Casado, M., Grimalt, J.O., Pena, L.D., Margaritelli, G., Lirer, F., 2016. Sea surface temperature variability in the central-western Mediterranean Sea during the last 2700 years: a multi-proxy and multi-record approach. Clim. Past 12, 849–869. https://doi.org/10.5194/cp-12-849-2016.
Cisneros, M., Cacho, I., Frigola, J., Sanchez-Vidal, A., Calafat, A., Pedrosa-Pàmies, R., Rumín-Caparrós, A., Canals, M., 2019. Deep-water formation variability in the north-western Mediterranean Sea during the last 2500 yr: a proxy validation with present-day data. Glob. Planet. Chang. 177, 56–68. https://doi.org/10.1016/j.gloplacha.2019.03.012.
Comas, M.C., Zahn, R., Klaus, A., 1996. Shipboard scientific party 2 HOLE 816A. Proc. ODP, ink. Repts 161, 299–353. https://doi.org/10.2973/odp.proc.ir.147.104.1993.
Coplen, T.B., 1996. New guidelines for reporting stable hydrogen, carbon, and oxygen isotope-ratio data. Geochem. Cosmochim. Acta 60, 3359–3360. https://doi.org/10.1016/0016-7037(96)00263-3.
Couchoud, I., Genty, D., Hoffmann, D., Drysdale, R., Blamart, D., 2009. Millennial-scale climate variability during the Last Interglacial recorded in a speleothem from south-western France. Quat. Sci. Rev. 28, 3263–3274. https://doi.org/10.1016/j.quascirev.2009.08.014.
Craig, H., Gordon, L., 1965. Deuterium and oxygen 18 variations in the ocean and the marine atmosphere. Stable Isotopes in Oceanographic Studies and Paleotemperatures 9–130.
Demény, A., Kern, Z., Czuppon, G., Németh, A., Leél-Őssy, S., Siklósy, Z., Lin, K., Hu, H.M., Shen, C.C., Vennemann, T.W., Haszpra, L., 2017. Stable isotope compositions of speleothems from the last interglacial – spatial patterns of climate fluctuations in Europe. Quat. Sci. Rev. 161, 68–80. https://doi.org/10.1016/j.quascirev.2017.02.012.
Dorale, J.A., González, L.A., Reagan, M.K., Pickett, D.A., Murrell, M.T., Baker, R.G., 1992. A high-resolution record of holocene climate change in speleothem calcite from Cold Water Cave, Northeast Iowa. Science 258, 1626–1630. https://doi.org/10.1126/science.258.5088.1626.
Dorale, J.A., Onac, B.P., Fornós, J.J., Ginés, J., Ginés, A., Tuccimei, P., Peate, D.W., 2010. Sea-level highstand 81,000 years ago in Mallorca. Science 327, 860–863. https://doi.org/10.1126/science.1181725.
Drysdale, R.N., Hellstrom, J.C., Zanchetta, G., Fallick, A.E., Sánchez-Goñi, M.F., Couchoud, I., 2009. Evidence for obliquity forcing of glacial termination II. Science 325 (5947), 1527–1531. https://doi.org/10.1126/science.1170371.
Drysdale, R.N., Zanchetta, G., Hellstrom, J.C., Fallick, A.E., McDonald, J., Cartwright, I., 2007. Stalagmite evidence for the precise timing of North Atlantic cold events during the early last glacial. Geology 35, 77–80. https://doi.org/10.1130/G23161A.1.
Drysdale, R.N., Zanchetta, G., Hellstrom, J.C., Fallick, A.E., Zhao, J.X., 2005. Stalagmite evidence for the onset of the Last Interglacial in southern Europe at 129 ± 1 ka. Geophys. Res. Lett. 32, 1–4. https://doi.org/10.1029/2005GL024658.
Dumitru, O.A., Forray, F.L., Fornós, J.J., Ersek, V., Onac, B.P., 2017. Water isotopic variability in Mallorca: a path to understanding past changes in hydroclimate. Hydrol. Process. 31, 104–116. https://doi.org/10.1002/hyp.10978.
Dumitru, O.A., Onac, B.P., Polyak, V.J., Wynn, J.G., Asmerom, Y., Fornós, J.J., 2018. Climate variability in the western Mediterranean between 121 and 67 ka derived from a Mallorcan speleothem record. Palaeogeogr. Palaeoclimatol. Palaeoecol. 506, 128–138. https://doi.org/10.1016/j.palaeo.2018.06.028.
Dutton, A., Lambeck, K., 2012. Ice volume and sea level during the last interglacial. Science 337, 216–219. https://doi.org/10.1126/science.1205749.
Elderfield, H., Granssen, G., 2000. Past temperatures and O18 O f surface ocean waters inferred from foraminiferal Mg/Ca ratios. Nature 405, 442–445.
Fairchild, I.J., Baker, A., 2012. Speleothem Science: from Process to Past Environments. Wiley, Hoboken, NJ.
Fairchild, I.J., Borsato, A., Tooth, A.F., Frisia, S., Hawkesworth, C.J., Huang, Y., McDermott, F., Spiro, B., 2000. Controls on trace element (Sr-Mg) compositions of carbonate cave waters: implications for speleothem climatic records. Chem. Geol. 166, 255–269. https://doi.org/10.1016/S0009-2541(99)00216-8.
Fairchild, I.J., McMillan, E.A., 2007. Speleothems as indicators of wet and dry periods. Int. J. Speleol. 36, 69–74. https://doi.org/10.5038/1827-806X.36.2.2.
Fairchild, I.J., Smith, C.L., Baker, A., Fuller, L., Spötl, C., Mattey, D., McDermott, F., 2006. Modification and preservation of environmental signals in speleothems. Earth Sci. Rev. 75, 105–153. https://doi.org/10.1016/j.earscirev.2005.08.003.
Fairchild, I.J., Treble, P.C., 2009. Trace elements in speleothems as recorders of environmental change. Quat. Sci. Rev. 28, 449–468. https://doi.org/10.1016/j.quascirev.2008.11.007.
Ferguson, J.E., Henderson, G.M., Kucera, M., Rickaby, R.E.M., 2008. Systematic change of foraminiferal Mg/Ca ratios across a strong salinity gradient. Earth Planet. Sci. Lett. 265, 153–166. https://doi.org/10.1016/j.epsl.2007.10.011, 2008.
Ferrer, L., Fontán, A., Mader, J., Chust, G., González, M., Valencia, V., Uriarte, A., Collins, M.B., 2009. Low-salinity plumes in the oceanic region of the Basque Country. Cont. Shelf Res. 29, 970–984. https://doi.org/10.1016/j.csr.2008.12.014.
Fletcher, W.J., Sánchez-Goñi, M.F., 2008. Orbital- and sub-orbital-scale climate impacts on vegetation of the western Mediterranean basin over the last 48,000yr. Quat. Res. 70, 451–464. https://doi.org/10.1016/j.yqres.2008.07.002.
Frigola, J., Moreno, A., Cacho, I., Canals, M., Sierro, F.J., Flores, J.A., Grimalt, J.O., 2008. Evidence of abrupt changes in Western Mediterranean Deep Water circulation during the last 50 kyr: a high-resolution marine record from the Balearic Sea. Quat. Int. 181, 88–104. https://doi.org/10.1016/j.quaint.2007.06.016.
Frigola, J., Moreno, A., Cacho, I., Canals, M., Sierro, F.J., Flores, J.A., Grimalt, J.O., Hodell, D.A., Curtis, J.H., 2007. Holocene climate variability in the western Mediterranean region from a deepwater sediment record. Paleoceanography 22, 1–16. https://doi.org/10.1029/2006PA001307.
Genty, D., Baker, A., Vokal, B., 2001. Instra- and inter-annual growth rate of modern stalagmites. Chem. Geol. 176, 191–212. https://doi.org/10.1016/S0009-2541(00)00399-5.
Genty, D., Blamart, D., Ouahdi, R., Gilmour, M., Baker, A., Jouzel, J., Van-Exter, S., 2003. Precise dating of Dansgaard-Oeschger climate oscillations in western Europe from stalagmite data. Nature 421, 833–837. https://doi.org/10.1038/nature01391.
Genty, D., Verheyden, S., Wainer, K., 2013. Speleothem records over the last interglacial. Investigating Past Interglacials, PAGES news 21, 1–2.
Gimeno, L., Nieto, R., Trigo, R.M., Vicente-Serrano, S.M., López-Moreno, J.I., 2010. Where does the iberian Peninsula moisture come From ? An answer based on a Lagrangian approach. J. Hydrometeorol. 11, 421–436. https://doi.org/10.1175/2009JHM1182.1.
Govin, A., Capron, E., Tzedakis, P.C., Verheyden, S., Ghaleb, B., Hillaire-Marcel, C., St-Onge, G., Stoner, J.S., Bassinot, F., Bazin, L., Blunier, T., Combourieu-Nebout, N., El Ouahabi, A., Genty, D., Gersonde, R., Jimenez-Amat, P., Landais, A., Martrat, B., Masson-Delmotte, V., Parrenin, F., Seidenkrantz, M.S., Veres, D., Waelbroeck, C., Zahn, R., 2015. Sequence of events from the onset to the demise of the Last Interglacial: evaluating strengths and limitations of chronologies used in climatic archives. Quat. Sci. Rev. 129, 1–36. https://doi.org/10.1016/j.quascirev.2015.09.018.
Grant, K.M., Rohling, E.J., Bar-Matthews, M., Ayalon, A., Medina-Elizalde, M., Bronk

Ramsey, C., Satow, C., Roberts, A.P., 2012. Rapid coupling between ice volume and polar temperature over the past 150 kyr. Nature 491, 744–747. https://doi.org/10.1038/nature11593.
Hellstrom, J., 2003. Rapid and accurate U/Th dating using parallel ion-counting multi-collector ICP-MS. J. Anal. At. Spectrom. 18, 1346–1351. https://doi.org/10.1039/b308781f.
Hodell, D.A., Channell, J.E.T., Curtis, J.H., Romero, O.E., 2008. Onset of "' hudson strait "' Heinrich events in the Eastern North atlantic at the end of the middle pleistocene transition (640ka). Paleoceanography 23, 1–16. https://doi.org/10.1029/2008PA001591.
Hodell, D.A., Minth, E.K., Curtis, J.H., McCave, I.N., Hall, I.R., Channell, J.E.T., Xuan, C., 2009. Surface and deep-water hydrography on Gardar Drift (Iceland Basin) during the last interglacial period. Earth Planet. Sci. Lett. 288, 10–19. https://doi.org/10.1016/j.epsl.2009.08.040.
Hodge, E.J., Richards, D.A., Smart, P.L., Andreo, B., Hoffmann, D.L., Mattey, D.P., González-ramón, A., 2008a. Effective precipitation in southern Spain (~ 266 to 46 ka) based on a speleothem stable carbon isotope record, 69, 447–457. https://doi.org/10.1016/j.yqres.2008.02.013.
Hodge, E.J., Richards, D., Smart, P., Ginés, A., Mattey, D., 2008b. Sub-millennial climate shifts in the western Mediterranean during the last glacial period recorded in a speleothem from Mallorca, Spain. J. Quat. Sci. 23, 713–718. https://doi.org/10.1002/jqs.1198.
Hoffman, J.S., Clark, P.U., Parnell, A.C., He, F., 2017. Regional and global sea-surface temperatures during the last interglaciation. Science 355, 276–279. https://doi.org/10.1126/science.aai8464.
Hoogakker, B.A.A., Klinkhammer, G.P., Elderfield, H., Rohling, E.J., Hayward, C., 2009. Mg/Ca paleothermometry in high salinity environments. Earth Planet. Sci. Lett. 284, 583–589. https://doi.org/10.1016/j.epsl.2009.05.027.
Hönisch, B., Allen, K.A., Lea, D.W., Spero, H.J., Eggins, S.M., Arbuszewski, J., DeMenocal, P., Rosenthal, Y., Russell, A.D., Elderfield, H., 2013. The influence of salinity on Mg/Ca in plank- tic foraminifers – evidence from cultures, core-top sediments and complementary $\delta^{18}O$. Geochem. Cosmochim. Acta 121, 196–213.
IPCC-, 2013. Climate Change 2013. The Physical Science Basis: Working Group I Contribution to the IPCC Fifth Assessment Report. Cambridge Univ. Press.
Ivanovic, R.F., Gregoire, L.J., Burke, A., Wickert, A.D., Valdes, P.J., Ng, H.C., Robinson, L.F., McManus, J.F., Mitrovica, J.X., Dentith, J.E., 2018. Acceleration of northern ice sheet melt induces AMOC slowdown and northern cooling in simulations of the early last deglaciation. Paleoceanography and Paleoclimatology 33, 807–824. https://doi.org/10.1029/2017PA003308.
Jiménez-Amat, P., Zahn, R., 2015. Offset timing of climate oscillations during the last two glacial-interglacial transitions connected with large-scale freshwater perturbation. Paleoceanography 30, 768–788. https://doi.org/10.1002/2014PA002710.
Kageyama, M., Paul, A., Roche, D.M., Van Meerbeeck, C.J., 2010. Modelling glacial climatic millennial-scale variability related to changes in the Atlantic meridional overturning circulation : a review. Quat. Sci. Rev. 29, 2931–2956. https://doi.org/10.1016/j.quascirev.2010.05.029.
Krklec, K., Domínguez-Villar, D., 2014. Quantification of the impact of moisture source regions on the oxygen isotope composition of precipitation over Eagle Cave, central Spain. Geochem. Cosmochim. Acta 134, 39–54. https://doi.org/10.1016/j.gca.2014.03.011.
Lachniet, M.S., 2009. Climatic and environmental controls on speleothem oxygen-isotope values. Quat. Sci. Rev. 28, 412–432. https://doi.org/10.1016/j.quascirev.2008.10.021.
Laskar, L., Robutel, P., Joutel, F., Gastineau, M., Correia, A.C.M., Levrard, B., 2004. Astrophysics A long-term numerical solution for the insolation. A&A 285, 261–285. https://doi.org/10.1051/0004-6361:20041335.
Lea, D.W., Pak, D.K., Paradis, G., 2005. Influence of volcanic shards on foraminiferal Mg/Ca in a core from the Galápagos region. Geochem. Geophys. Geosyst. 6, 1–13. https://doi.org/10.1029/2005GC000970.
Lewis, C.J., McDonald, E.V., Sancho, C., Peña, J.L., Rhodes, E.J., 2009. Climatic implications of correlated Upper Pleistocene glacial and fluvial deposits on the Cinca and Gállego Rivers (NE Spain) based on OSL dating and soil stratigraphy. Glob. Planet. Chang. 67, 141–152. https://doi.org/10.1016/j.gloplacha.2009.01.001.
Lionello, P., 2012. The Climate of the Mediterranean Region: from the Past to the Future, first ed. Elsevier Inc. https://doi.org/10.1016/B978-0-12-416042-2.00009-4.
López-Mir, B., 2013. Extensional Salt Tectonics in the Cotiella Post-rift Basin (South-central Pyrenees): 3D Structure and Evolution. PhD of Department of Geodinamics and Geophysics, University of Barcelona.
Marino, G., Rohling, E.J., Rodríguez-Sanz, L., Grant, K.M., Heslop, D., Roberts, A.P., Stanford, J.D., Yu, J., 2015. Bipolar seesaw control on last interglacial sea level. Nature 522, 197–201. https://doi.org/10.1038/nature14499.
Martin, J.M., Elbaz-Poulichet, F., Guieu, C., Loÿe-Pilot, M.D., Han, G., 1989. River versus atmospheric input of material to the mediterranean sea: an overview. Mar. Chem. 28, 159–182. https://doi.org/10.1016/0304-4203(89)90193-X.
Martrat, B., Grimalt, J.O., Lopez-Martínez, C., Cacho, I., Sierro, F.J., Flores, J.A., Zahn, R., Canals, M., Curtis, J.H., Hodell, D.A., 2004. Abrupt temperature changes in the western mediterranean over the past 250,000 years. Science 306, 1762–1765. https://doi.org/10.1126/science.1101706.
Martrat, B., Grimalt, J.O., Shackleton, N.J., De Abreu, L., Hutterli, M.A., Stocker, T.F., 2007. Four climate cycles of recurring deep and surface water destabilizations on the Iberian margin. Science 317, 502–507. https://doi.org/10.1126/science.1139994.
Martrat, B., Jimenez-Amat, P., Zahn, R., Grimalt, J.O., 2014. Similarities and dissimilarities between the last two deglaciations and interglaciations in the North Atlantic region. Quat. Sci. Rev. 99, 122–134. https://doi.org/10.1016/j.quascirev.2014.06.016.
Martrat, B., Tzedakis, P.C., Margari, V., Skinner, L., Hodell, D.A., Grimalt, J.O., 2015. Oceanic processes as potential trigger and amplifying mechanisms for Heinrich events. PAGES Mag 23, 1–2.
Mary, Y., Eynaud, F., Colin, C., Rossignol, L., Brocheray, S., Mojtahid, M., Garcia, J., Peral, M., Howa, H., Zaragosi, S., Cremer, M., 2017. Changes in Holocene meridional circulation and poleward Atlantic flow: the Bay of Biscay as a nodal point. Clim. Past 13, 201–216. https://doi.org/10.5194/cp-13-201-2017.
McCartney, M.S., Mauritzen, C., 2001. On the origin of the warm inflow to the Nordic Seas. Prog. Oceanogr. 51, 125–214. https://doi.org/10.1016/S0079-6611(01)00084-2.
McCave, I.N., Hall, I.R., 2006. Size sorting in marine muds: processes, pitfalls, and prospects for paleoflow-speed proxies. Geochem. Geophys. Geosyst. 7 https://doi.org/10.1029/2006GC001284.
McCave, I.N., Manighetti, B., Robinson, S.G., 1995. Sortable silt and fine sediment size composition slicing - parameters for paleocurrent speed and paleoceanography. Paleoceanography 10, 593–610. https://doi.org/10.1029/94PA03039.
McDermott, F., 2004. Palaeo-climate reconstruction from stable isotope variations in speleothems: a review. Quat. Sci. Rev. 23, 901–918. https://doi.org/10.1016/j.quascirev.2003.06.021.
McManus, J.F., Oppo, D.W., Keigwin, L.D., Cullen, J.L., Bond, G.C., 2002. Thermohaline circulation and prolonged interglacial warmth in the north atlantic. Quat. Res. 58, 17–21. https://doi.org/10.1006/qres.2002.2367.
McQueen, J.B., 1967. Some methods for classification and analysis of multivariate observations, statistics and probability. Univ. of California. Press Proc. Fifth Berkeley Symp. on Math. Statist. and Prob. 1, 281–297.
Meyer, M.C., Spötl, C., Mangini, A., 2008. The demise of the Last Interglacial recorded in isotopically dated speleothems from the Alps. Quat. Sci. Rev. 27, 476–496. https://doi.org/10.1016/j.quascirev.2007.11.005.
Millot, C., 1999. Circulation in the western Mediterranean sea. J. Mar. Syst. 20, 423–442. https://doi.org/10.1016/S0924-7963(98)00078-5.
Moreno, A., Cacho, I., Canals, M., Grimalt, J.O., Sánchez-Goñi, M.F., Shackleton, N., Sierro, F.J., 2005. Links between marine and atmospheric processes oscillating on a millennial time-scale. A multi-proxy study of the last 50,000 yr from the Alboran Sea (Western Mediterranean Sea). Quat. Sci. Rev. 24, 1623–1636. https://doi.org/10.1016/j.quascirev.2004.06.018.
Moreno, A., Stoll, H., Jiménez-Sánchez, M., Cacho, I., Valero-Garcés, B., Ito, E., Edwards, R.L., 2010. A speleothem record of glacial (25-11.6 kyr BP) rapid climatic changes from northern Iberian Peninsula. Glob. Planet. Chang. 71, 218–231. https://doi.org/10.1016/j.gloplacha.2009.10.002.
Moseley, G.E., Spötl, C., Cheng, H., Boch, R., Min, A., Edwards, R.L., 2015. Termination-II interstadial/stadial climate change recorded in two stalagmites from the north European Alps. Quat. Sci. Rev. 127, 229–239. https://doi.org/10.1016/j.quascirev.2015.07.012.
Mulder, T., Hassan, R., Ducassou, E., Zaragosi, S., Gonthier, E., Hanquiez, V., Marchès, E., Toucanne, S., 2013. Contourites in the Gulf of Cadiz: a cautionary note on potentially ambiguous indicators of bottom current velocity. Geo Mar. Lett. 33, 357–367. https://doi.org/10.1007/s00367-013-0332-4.
Nieto, R., Gimeno, L., Drumond, A., Hernandez, E., 2010. A Lagrangian identification of the main moisture sources and sinks affecting the Mediterranean area. WSEAS Trans. Environ. Dev. 6, 365–374.
Oppo, D.W., Keigwin, L.D., Mcmanus, J.F., Cullen, J.L., 2001. Persistent suborbital climate variability in marine isotopestage 5 and Termination II. Paleoceanography 16, 280–292.
Oppo, D.W., Mcmanus, J.F., Cullen, J.L., 2006. Evolution and demise of the last interglacial warmth in the subpolar North Atlantic. Quat. Sci. Rev. 25, 3268–3277. https://doi.org/10.1016/j.quascirev.2006.07.006.
Paillard, D., Labeyric, L., Yiou, P., 1996. Machintosh program performs time-series analysis. Eos Trans. AGU 77, 376.
PAGES, P.I.W.G. of P, 2016. Interglacials of the last 800,000years. Rev. Geophys. 54, 162–219. https://doi.org/10.1002/2015RG000482.Received.
Pastor, F., Valiente, J.A., Palau, J.L., 2017. sea surface temperature in the mediterranean: trends and spatial patterns (1982–2016). Pure Appl. Geophys. https://doi.org/10.1007/s00024-017-1739-z.
Pena, L.D., Cacho, I., Calvo, E., Pelejero, C., Eggins, S., Sadekov, A., 2008. Characterization of contaminant phases in foraminifera carbonates by electron microprobe mapping. Geochem. Geophys. Geosyst. 9 https://doi.org/10.1029/2008GC002018.
Pena, L.D., Calvo, E., Cacho, I., Eggins, S., Pelejero, C., 2005. Identification and removal of Mn-Mg-rich contaminant phases on foraminiferal tests: implications for Mg/Ca past temperature reconstructions. Geochem. Geophys. Geosyst. 6 https://doi.org/10.1029/2005GC000930.
Peña, J.L., Sancho, C., Lewis, C., Mcdonald, E.E., 2004. Datos cronológicos de las morrenas terminales del glaciar del Gállego y su relación con las terrazas fluvioglaciares (Pirineo de Huesca). Geogr. Física Aragón. Asp. Gen. y temáticos Univ. Zaragoza e Inst. Fernando el Católico 71–84, 849621429X.
Pérez-Brunius, P., Rossby, T., Watts, D.R., 2004. Absolute transports of mass and temperature for the north atlantic current– subpolar front system. J. Phys. Oceanogr. 34, 1870–1883. https://doi.org/10.1175/1520-0485(2004)034<1870:ATOMAT>2.0.CO;2.
Picciolo, A.R., 2006. National oceanographic data center. AIBS Bull. 13, 38. https://doi.org/10.2307/1292958.

Pierre, C., 1999. The oxygen and carbon isotope distribution in the Mediterranean water masses. Mar. Geol. 153, 41–55. https://doi.org/10.1016/S0025-3227(98)00090-5.

Pinardi, N., Masetti, E., 2000. Variability of the large scale general circulation of the Mediterranean Sea from observations and modelling: a review. Palaeogeogr. Palaeoclimatol. Palaeoecol. 158, 153–173.

Pingree, R.D., Le Cann, B., 1990. Structure, strength and seasonality of the slope currents in the Bay of Biscay region. J. Mar. Biol. Assoc. U. K. 70, 857–885.

Povea, P., Cacho, I., Moreno, A., Men, M., Fernando, J.M., 2015. A new procedure for the lithic fraction characterization in marine sediments from high productivity areas : optimization of analytical and statistical procedures. Limnol Oceanogr. Methods 13, 127–137. https://doi.org/10.1002/lom3.10013.

Rasmussen, S.O., Bigler, M., Blockley, S.P., Blunier, T., Buchardt, S.L., Clausen, H.B., Cvijanovic, I., Dahl-Jensen, D., Johnsen, S.J., Fischer, H., Gkinis, V., Guillevic, M., Hoek, W.Z., Lowe, J.J., Pedro, J.B., Popp, T., Seierstad, I.K., Steffensen, J.P., Svensson, A.M., Vallelonga, P., Vinther, B.M., Walker, M.J.C., Wheatley, J.J., Winstrup, M., 2014. A stratigraphic framework for abrupt climatic changes during the Last Glacial period based on three synchronized Greenland ice-core records: refining and extending the INTIMATE event stratigraphy. Quat. Sci. Rev. 106, 14–28. https://doi.org/10.1016/j.quascirev.2014.09.007.

Rebesco, M., Hernández-Molina, F.J., Van Rooij, D., Wåhlin, A., 2014. Contourites and associated sediments controlled by deep-water circulation processes: state-of-the-art and future considerations. Mar. Geol. 352, 111–154. https://doi.org/10.1016/j.margeo.2014.03.011.

Richards, Dorale, 2003. Uranium-series Chronology and Environmental Applications of Speleothems. School of Geograph. Sci., Univ. of Bristol, 1529-6466/00/0052-0010$10.00.

Richter, T.O., van der Gaast, S., Koster, B., Vaars, A., Gieles, R., de Stigter, H.C., De Haas, H., van Weering, T.C.E., 2006. The Avaatech XRF Core Scanner: technical description and applications to NE Atlantic sediments. Geol. Soc. Lond. Spec. Publ. 267, 39–50. https://doi.org/10.1144/GSL.SP.2006.267.01.03.

Rigual-Hernández, A.S., Sierro, F.J., Bárcena, M.A., Flores, J.A., Heussner, S., 2012. Seasonal and interannual changes of planktic foraminiferal fluxes in the Gulf of Lions (NW Mediterranean) and their implications for paleoceanographic studies: two 12-year sediment trap records. Deep. Res. Part I Oceanogr. Res. Pap. 66, 26–40. https://doi.org/10.1016/j.dsr.2012.03.011.

Robinson, Simon G., McCave, I.N., 1994. Orbital forcing of bottom-current enhanced sedimentation on Feni Drift, NE Atlantic, during the mid-Pleistocene. Paleoceanography 9, 943–972.

Rodriguez-Lazaro, J., Pascual, A., Cacho, I., Varela, Z., Pena, L.D., 2017. Deep-sea benthic response to rapid climatic oscillations of the last glacial cycle in the SE Bay of Biscay. J. Sea Res. 130, 49–72. https://doi.org/10.1016/j.seares.2017.06.002.

Rodríguez-Sanz, L., Bernasconi, S.M., Marino, G., Heslop, D., Müller, I.A., Fernandez, A., Grant, K.M., Rohling, E.J., 2017. Penultimate deglacial warming across the Mediterranean Sea revealed by clumped isotopes in foraminifera. Sci. Rep. 7, 1–11. https://doi.org/10.1038/s41598-017-16528-6.

Rohling, E.J., Foster, G.L., Grant, K.M., Marino, G., Roberts, A.P., Tamisiea, M.E., Williams, F., 2014. Sea-level and deep-sea-temperature variability over the past 5.3 million years. Nature 508, 477–482. https://doi.org/10.1038/nature13230.

Rohling, E.J., Abu-Zied, R.H., Casford, J.S.L., Hayes, A., Hoogakker, B. a a, 2009. The Marine Environment: Present and Past, the Physical Geography of the Mediterranean. Oxford University Press, Oxford, pp. 33–67.

Rohling, E.J., 1999. Environmental control on Mediterranean salinity and 5180. Paleoceanography 14 (6), 706–715.

Rohling, E.J., Hayes, A., De Rijk, S., Kroon, D., Zachariasse, W.J., Eisma, D., 1998. Abrupt cold spells in the northwest Mediterranean. Paleoceanography 13, 316–322. https://doi.org/10.1029/98PA00671.

Rothwell, G.R., Rack, F.R., 2006. New techniques in sediment core analysis: an introduction. Geol. Soc. Lond. Spec. Publ. 267, 1–29. https://doi.org/10.1144/GSL.SP.2006.267.01.01.

Sánchez-Goñi, M.F., Eynaud, F., Turon, J.L., Shackleton, N.J., 1999. High resolution palynological record off the Iberian margin: direct land-sea correlation for the Last Interglacial complex. Earth Planet. Sci. Lett. 171, 123–137. https://doi.org/10.1016/S0012-821X(99)00141-7.

Sánchez-Goñi, M.F., Loutre, M.F., Crucifix, M., Peyron, O., Santos, L., Duprat, J., Malaizé, B., Turon, J.L., Peypouquet, J.P., 2005. Increasing vegetation and climate gradient in western Europe over the last glacial inception (122-110 ka): data-model comparison. Earth Planet. Sci. Lett. 231, 111–130. https://doi.org/10.1016/j.epsl.2004.12.010.

Sánchez-Goñi, M.F., Bakker, P., Desprat, S., Carlson, A.E., Van Meerbeeck, C.J., Peyron, O., Naughton, F., Fletcher, W.J., Eynaud, F., Rossignol, L., Renssen, H., 2012. European climate optimum and enhanced Greenland melt during the last interglacial. Geology 40, 627–630. https://doi.org/10.1130/G32908.1.

Scholz, D., Hoffmann, D.L., 2011. StalAge: an algorithm designed for construction of speleothem age models. Quat. Geochronol. 6, 369–382. https://doi.org/10.1016/j.quageo.2011.02.002.

Seidenkrantz, M., Bornmalm, L., Johnsen, S.J., Knudsen, K.L., Kuijpers, A., Lauritzen, S., Leroy, S.A.G., Mergeai, I., Schweger, C., Vliet-lanoe, B.V.A.N., Alberta, T., 1996. Two-step deglaciation at the oxygen isotope stage 6/5e transition: the zeifen-kattegat climate oscillation. Quat. Sci. Rev. 15, 63–75.

Seierstad, I.K., Abbott, P.M., Bigler, M., Blunier, T., Bourne, A.J., Brook, E., Buchardt, S.L., Buizert, C., Clausen, H.B., Cook, E., Dahl-Jensen, D., Davies, S.M., Guillevic, M., Johnsen, S.J., Pedersen, D.S., Popp, T.J., Rasmussen, S.O., Severinghaus, J.P., Svensson, A., Vinther, B.M., 2014. Consistently dated records from the Greenland GRIP, GISP2 and NGRIP ice cores for the past 104ka reveal regional millennial-scale δ18O gradients with possible Heinrich event imprint. Quat. Sci. Rev. 106, 29–46. https://doi.org/10.1016/j.quascirev.2014.10.032.

Shackleton, N.J., 1974. Attainment of isotopic equilibrium between ocean water and the benthonic foraminifera genus Uvigerina: isotopic changes in the ocean during the last glacial. Colloq. Int. du C.N.R. S 203–209.

Shen, C., Edwards, R.L., Cheng, H., Dorale, J.A., Thomas, R.B., Moran, S.B., Weinstein, S.E., Edmonds, H.N., 2002. Uranium and thorium isotopic and concentration measurements by magnetic sector inductively coupled plasma mass spectrometry. Chem. Geol. 185, 165–178.

Sierro, F.J., Hodell, D.A., Curtis, J.H., Flores, J.A., Reguera, I., Colmenero-Hidalgo, E., Barcena, M.A., Grimalt, J.O., Cacho, I., Frigola, J., Canals, M., 2005. Impact of iceberg melting on Mediterranean thermohaline circulation during Heinrich events. Paleoceanography 20, 1–13. https://doi.org/10.1029/2004PA001051.

Sirocko, F., Seelos, K., Schaber, K., Rein, B., Dreher, F., Diehl, M., Lehne, R., Jäger, K., Krbetschek, M., Degering, D., 2005. A late Eemian aridity pulse in central Europe during the last glacial inception. Nature 436, 833–836. https://doi.org/10.1038/nature03905.

Sprovieri, R., Di Stefano, E., Incarbona, A., Oppo, D.W., 2006. Suborbital climate variability during Marine Isotopic Stage 5 in the central Mediterranean basin: evidence from calcareous plankton record. Quat. Sci. Rev. 25, 2332–2342. https://doi.org/10.1016/j.quascirev.2006.01.035.

Stoll, H., Mendez-Vicente, A., Gonzalez-Lemos, S., Moreno, A., Cacho, I., Cheng, H., Edwards, R.L., 2015. Interpretation of orbital scale variability in mid-latitude speleothem d 18 O : significance of growth rate controlled kinetic fractionation effects. Quat. Sci. Rev. 127, 215–228. https://doi.org/10.1016/j.quascirev.2015.08.025.

Tjallingii, R., Röhl, U., Kölling, M., Bickert, T., 2007. Influence of the water content on X-ray fluorescence corescanning measurements in soft marine sediments. Geochem. Geophys. Geosyst. 8, 1–12. https://doi.org/10.1029/2006GC001393.

Tzedakis, C., 2003. Timing and duration of Last Interglacial conditions in Europe: a chronicle of a changing chronology. Quat. Sci. Rev. 22, 763–768. https://doi.org/10.1016/S0277-3791(03)00004-0.

Tzedakis, P.C., Raynaud, D., McManus, J.F., Berger, A., Brovkin, V., Kiefer, T., 2009. Interglacial diversity. Nat. Geosci. 2, 751.

Tzedakis, P.C., Wolff, E.W., Skinner, L.C., Brovkin, V., Hodell, D.A., McManus, J.F., Raynaud, D., 2012. Can we predict the duration of an interglacial? Clim. Past 8, 1473–1485. https://doi.org/10.5194/cp-8-1473-2012.

Tzedakis, P.C., Drysdale, R.N., Margari, V., Skinner, L.C., Menviel, L., Rhodes, R.H., Taschetto, A.S., Hodell, D.A., Crowhurst, S.J., Hellstrom, J.C., Fallick, A.E., Grimalt, J.O., McManus, J.F., Martrat, B., Mokeddem, Z., Parrenin, F., Regattieri, E., Roe, K., Zanchetta, G., 2018. Enhanced climate instability in the north atlantic and southern Europe during the last interglacial. Nat. Commun. 9, 4235. https://doi.org/10.1038/s41467-018-06683-3.

Van Meerbeeck, C.J., Renssen, H., Roche, D.M., Wohlfarth, B., Bohncke, S.J.P., Bos, J.A.A., Engels, S., Helmens, K.F., Sánchez-goñi, M.F., Svensson, A., Vandenberghe, J., 2011. The nature of MIS 3 stadial e interstadial transitions in Europe : new insights from model e data comparisons. Quat. Sci. Rev. 30, 3618–3637. https://doi.org/10.1016/j.quascirev.2011.08.002.

van Raden, U.J., Groeneveld, J., Raitzsch, M., Kucera, M., 2011. Mg/Ca in the planktonic foraminifera Globorotalia inflata and Globigerinoides bulloides from Western Mediterranean plankton tow and core top samples. Mar. Micropaleontol. 78, 101–112. https://doi.org/10.1016/j.marmicro.2010.11.002.

Vansteenberge, S., Verheyden, S., Cheng, H., Edwards, R.L., Keppens, E., Claeys, P., 2016. Paleoclimate in continental northwestern Europe during the Eemian and early Weichselian (125-97 ka): insights from a Belgian speleothem. Clim. Past 12, 1445–1458. https://doi.org/10.5194/cp-12-1445-2016.

Vargas-Yáñez, M., García-Martínez, M.C., Moya, F., Balbín, R., López-Jurado, J.L., Serra, M., Zunino, P., Pascual, J., Salat, J., 2017. Updating temperature and salinity mean values and trends in the Western Mediterranean: the RADMED project. Prog. Oceanogr. 157, 27–46. https://doi.org/10.1016/j.pocean.2017.09.004.

Velasco, J.P.B., Baraza, J., Canals, M., Balón, J., 1996. La depresión periférica y el lomo contourítico de Menorca: evidencias de la actividad de corrientes de fondo al N del talud Balear. Geogaceta 20, 359–362.

Waelbroeck, C., Labeyrie, L., Michel, E., Duplessy, J.C., McManus, J.F., Lambeck, K., Balbon, E., Labracherie, M., 2002. Sea-level and deep water temperature changes derived from benthic foraminifera isotopic records. Quat. Sci. Rev. 21, 295–305. https://doi.org/10.1016/S0277-3791(01)00101-9.

Weltje, G.J., Tjallingii, R., 2008. Calibration of XRF core scanners for quantitative geochemical logging of sediment cores: theory and application. Earth Planet. Sci. Lett. 274, 423–438. https://doi.org/10.1016/j.epsl.2008.07.054.

Wong, C.I., Breecker, D.O., 2015. Advancements in the use of speleothems as climate archives. Quat. Sci. Rev. 127, 1–18. https://doi.org/10.1016/j.quascirev.2015.07.019.

Wulf, S., Hardiman, M.J., Staff, R.A., Koutsodendris, A., Appelt, O., Blockley, S.P.E., Lowe, J.J., Manning, C.J., Ottolini, L., Schmitt, A.K., Smith, V.C., Tomlinson, E.L., Vakhrameeva, P., Knipping, M., Kotthoff, U., Milner, A.M., Müller, U.C., Christanis, K., Kalaitzidis, S., Tzedakis, P.C., Schmiedl, G., Pross, J., 2018. The marine isotope stage 1–5 cryptotephra record of Tenaghi Philippon, Greece: towards a detailed tephrostratigraphic framework for the Eastern Mediterranean region. Quat. Sci. Rev. 186, 236–262. https://doi.org/10.1016/j.quascirev.2018.03.011.

Yu, J., Elderfield, H., Greaves, M., Day, J., 2007. Preferential dissolution of benthic foraminiferal calcite during laboratory reductive cleaning. Geochem. Geophys. Geosyst. 8 https://doi.org/10.1029/2006GC001571.